UNIVERSITÄT
ZU KÖLN

Computational study of aqueous geochemical fluids at high temperature and pressure

Inaugural-Dissertation

zur

Erlangung des Doktorgrades

der Mathematisch-Naturwissenschaftlichen Fakultät der

Universität zu Köln

vorgelegt von

Rajorshi Chattopadhyay

aus Kolkata, India

Köln, 2024

Acknowledgments

I would like to express my heartfelt gratitude to Prof. Dr. Sandro Jahn for his unwavering support and scientific supervision for all the projects. His support in preparation of talks and presentations for conferences, scientific writing, constructive criticism and discussions have played an important role in inculcating scientific fervour in me. I also want to thank my colleague, Dr. Maximilian Schulze for everything he has done for me over the years, starting from providing guidance during my internship in 2020, scientific pep-talks to discussing and sharing potential research ideas. Moreover, I am equally thankful to the supervisor of Masters' project, Prof. Dr. Mruganka Kumar Panigrahi for introducing me to the field of computational geochemistry and fostering a sense of self-discipline. I extend my gratitude to all other professors in my thesis review and defense committee.

My appreciation also goes to the faculty and staff in the Institute for Geology and Mineralogy, University of Cologne for providing a serene working environment along with state of the art resources and infrastructure conducive to high-class scientific research. I deeply thank Deutsche Forschungsgemeinschaft (DFG) for funding my PhD project (SPP 2238 - Dynamics of Ore Metals Enrichment (DOME)) and Gauss Centre for Supercomputing (GCS) for providing computation time through the John von Neumann Institute for Computing (NIC) on the Supercomputer JURECA and JUWELS at Jülich Supercomputing Centre (JSC). I owe gratitude to all my friends back in India and in Germany for their camaraderie. My sincere gratitude goes to fellow players and coaches at Uni Sports Table Tennis Club for introducing me to the fascinating game of table tennis. This helped me keep my spirits high throughout the PhD journey.

Nothing would have been possible without the support and motivation of my parents, Enakshi Chattopadhyay (mother), Debashis Chattopadhyay (father), Dr. Deboki Chattopadhyay (sister), Mihir Kumar Chattopadhyay (grandfather) and all other members of my family. My deepest gratitude goes to my guruji, Pandit Amitabh Chatterjee for motivating me to keep pursuing music alongside my studies. Lastly I would like to thank my '4 year younger self' for being brave and curious enough to relocate to a new country and set out on this arduous scientific journey.

Table of Contents

List of Tables

List of Figures

Acronyms

AIMD Ab Initio Molecular Dynamics. iii, iv, xi, xii, xxi, 5, 15, 19, 25, 27, 29, 49, 71–74, 78–81, 84–86, 90–92, 94–98, 100–102, 104, 105, 107, 108

AO Atomic Orbital. 18

BLYP Becke, Lee, Yang, and Parr. xiii, xxi, 17, 20, 21, 25–28, 32, 34, 35, 37, 38, 40–47, 49, 50, 108, 110, 111, 114–117, 119

CIP Contact Ion Pair. xii, 92–96, 98, 104

CMD Classical Molecular Dynamics. iii, xxi, 5, 11, 12, 34, 37, 44, 52, 105

CN Running Coordination Number. vii, ix, x, xiii, 28, 33–36, 49, 81, 85, 88, 90, 91, 97, 107, 111, 112

CV Collective Variable. 22, 23, 92

DC Dang and Chang. xi, 74, 75, 107

DEW Deep Earth Water. viii, x, 57, 58, 125

DFT Density Functional Theory. vii, xxi, 16–19, 21, 44–46, 71, 74, 77, 113

DZ Double-Zeta. 18

DZV Double Zeta Valence. 79

DZVP Double Zeta Valence Potential. 18, 27

E Energy. 8

EOS Equation Of State. viii, x, 57, 58, 68, 69, 72, 80, 97, 106, 125

EXAFS Extended X-ray Absorption Fine Structure. xii, 96–98

FES Free Energy Surface. xii, 22, 23, 79, 80, 92–94, 101, 102, 107

FT Fourier Transform. 29, 30

GGA Generalised Gradient Approximation. xxi, 20, 25, 26, 45, 46, 49

GPW Gaussian Plane Wave. 28, 79

GTH Goedecker-Teter-Hutter. 19, 27

HF Hartree-Fock. vi, vii, x, 34, 40, 44–46, 48, 49, 113

HKF Helgeson-Kirkham-Flowers. xii, 72, 96–98, 104, 106

IR Infrared. 25

LJ Lennard Jones. vi, ix, 10, 12, 13, 54, 71, 74

LREE Light Rare Earth Element. 70, 71

LSDA Local Spin Density Approximation. 20

MD Molecular Dynamics. iii, ix, xx, 5–7, 9, 10, 14, 21, 22, 30, 52, 53, 67, 68, 71, 73, 100, 105, 106, 108

meta-GGA meta-Generalised Gradient Approximation. 21, 25, 43, 49

MLWF Maximally Localized Wannier Function. 75–77

MOLOPT Molecularly Optimized. 18, 79

MP Møller–Plesset. vi, vii, 40, 45, 113

MSD Mean Squared Displacement. viii, 54, 56, 124

N Number of particles. 8

NNP Neural Network Potential. 108

NQE Nuclear Quantum Effect. 45

P Pressure. 8

PBC Periodic Boundary Conditions. iii, 9, 56

PBE Perdew, Burke and Ernzerhof. 17, 20, 25, 26, 45, 46, 79

PES Potential Energy Surface. 15, 22

PIM Polarizable Ion Model. vii, xi, xii, xxi, 72, 74–77, 80, 82, 84–92, 94–102, 104, 106–108

PMF Potential of Mean Force. 80, 92

QC Quantum Chemical. xxi, 14, 68, 106

QNM Quasi-Normal Mode. vi, ix, x, xiii, 29–31, 39–41, 116, 117, 119

REE Rare Earth Element. 4, 5, 70, 71, 97, 107

revPBE revised Perdew, Burke, and Ernzerhof. 20, 25, 26

SCAN Strongly Constrained and Appropriately Normed. 21, 25, 26

SPC/E Extended Simple Point Charge. iii, vi, viii–xi, xiv, xxi, 12, 13, 27, 52–54, 56–69, 78, 80, 106, 121–126, 128–130

SShIP Solvent Shared Ion Pair. xii, 86, 88, 92–94, 96, 98, 102, 104

SSIP Solvent separated Ion Pair. xii, 92, 93, 107

STO Slater-Type Orbital. 18

SV Split-Valence. 18

T Temperature. 8

TS Transition State. xii, 93, 94

TZ Triple-Zeta. 18

UEG Universal Electron Gas. 20

V Volume of simulation box. 8

VACF Velocity Autocorrelation Function. 29, 30

VDOS Vibrational Density Of States. 27, 29

VDZ Valence Double Zeta. 18

VTZ Valence Triple Zeta. 18

WMetaD Well-tempered Metadynamics. 22, 23, 79, 81, 92, 94, 100

XAS X-ray Absorption Spectroscopy. xii, 71, 96–98

XC Exchange and Correlation. iii, vi, vii, x, xxi, 17, 19, 20, 25–28, 32, 34, 35, 37, 38, 40, 42, 47–49, 79, 108, 113

XRD X-Ray Diffraction. vi, 34, 44

Abstract

Aqueous fluids play a critical role in the evolution of the Earth - starting from the atmosphere to the deep Earth. They are important carriers of heat energy and matter thereby playing an important role in several chemical reactions that determine the geochemistry of the Earth's interior. Hydrothermal solutions in the Earth reduce the melting point of rocks leading to the formation of volcanoes and plate tectonics. Lower water activity compared to CO_2 in the Venusian crust leads to an increase in the melting point of rocks at elevated pressure which hinders plate tectonics. In a way, it is because of the aqueous fluid induced dynamic nature that several lifeforms have sustained on our planet. Hydrothermal fluids also play a dominant role in mobilising several strategically important elements followed by their precipitation resulting in the formation of ore deposits. Elements mobilised and deposited by aqueous fluids depend on the chemical composition and the prevalent thermodynamic conditions. As a result detailed understanding of the chemical structure and composition of hydrothermal fluids under geological conditions is warranted. Several spectroscopic studies have been conducted over the years to delineate the speciation of aqueous fluids. These have been accompanied by high temperature and high pressure experiments with devices like hydrothermal autoclaves, pressure vessels or heated/hydrothermal diamond anvil cells that aim to determine different physical and transport properties of aqueous fluids. However, these experiments are limited in their temperature, pressure and composition ranges.

Ever since computers became available for unclassified scientific research, consistent effort has been made to implement fundamental laws of physics (like Newton's Laws of Motion, Schrödinger Equation) thereby providing insights into the structure and dynamics of natural systems on the atomistic scale. Development of more advanced and efficient hardware has made use of Molecular Dynamics (MD) simulations realizable in studying different fluid rock interaction processes. These studies not only complement available experimental data but also provide an alternate framework to verify various assumptions and simplifications in existing theoretical models of fluids. In addition to these, MD simulations can provide insights into the structure and composition of aqueous geochemical fluids at conditions difficult to simulate in laboratories.

In this thesis different types of MD simulations have been used to study geochemical

fluids with different compositions at supercritical conditions. Different target properties are calculated and compared against available experimental data using Density Functional Theory (DFT) based Ab Initio Molecular Dynamics (AIMD) simulations and Classical Molecular Dynamics (CMD) simulations. This provides discernment in the precision and accuracy of these techniques at geological conditions. In the different chapters of the thesis, we study properties of important solvents as well as solutes and the impact of different simulation parameters on them. In Chapter 3, we show that the Generalised Gradient Approximation (GGA) Exchange and Correlation (XC) functional like Becke, Lee, Yang, and Parr (BLYP) and meta-GGA XC functional like r2SCAN predicts similar structural properties of aqueous H_2SO_4 and Na_2SO_4 solutions at supercritical conditions. Using r2SCAN gives better estimates of the different vibrational modes of oxidized sulfur species as compared to the BLYP functional. However, the predicted vibrational frequencies are still underestimated in comparison to experimental data. Both the functionals reproduce the temperature-induced shifts in different vibrational modes. Electrical conductivity of NaCl solutions in supercritical conditions are calculated with ReaxFF and pairwise Extended Simple Point Charge (SPC/E) models in Chapter 4. We show that although ReaxFF is a polarizable, dissociative forcefield fitted on lots of Quantum Chemical (QC) data, its accuracy is not good in predicting a property (in this case electrical conductivity) not explicitly present in the training dataset. In Chapter 5, a new ab initio based Polarizable Ion Model (PIM) interaction potential is developed at supercritical conditions. We discuss fundamental issues related to transferability of interaction potentials and establish the superiority of the newly developed interaction potential in predicting structural and thermodynamic properties of La^{3+} in chloride bearing hydrothermal fluids.

Overall, although state of the art techniques are precise and give important information about the geochemistry of supercritical fluids, significant scope of improvement exists. The thesis also serves to give an overview of fundamental issues related to the 'art' of interaction potential development that has to be kept in mind in future projects. This includes cardinal questions like XC functional to be used in generation of training data, types of data to be included in the training set and functional form of the potential to be fitted.

Chapter 1

Introduction

1.1 What are aqueous hydrothermal aqueous fluids

Aqueous fluids are ubiquitous - from high in the atmosphere to deep in the Earth's interior and are critical to the evolution of the planet. They influence tectonic, petrologic and ore forming processes. Ability of fluids to flow and to store and transport matter and thermal energy makes them irreplaceable mediators of chemical reactions in varied geologic settings. As a result fluid circulation and fluid rock interaction reactions take place under variety of geochemical settings starting from ambient surface temperatures to extreme subsurface temperatures and pressures. Physical and chemical properties of aqueous fluids vary depending on the thermodynamic conditions thereby providing valuable information about the geological setting and the type of fluid rock interactions [1].

Hydrothermal fluids typically refer to fluids that have been heated to temperatures above ambient conditions in the Earth's interior due to natural processes [2]. They therefore have several compounds and gases dissolved in them. Circulation of seawater in the oceanic crust is one of the important sources of hydrothermal fluids [3, 4]. As seawater circulates through the cracks and fissures of the underlying crust, it goes through extensive high temperature water mediated reactions and phase separations. These reactions result in removal of abundant constituents of sea water like magnesium, oxygen and sulfur and addition of new elements like silicon, magnesium and iron [5]. It is these hydrothermal alterations that determine the subsequent fluid history of subduction zones and magmatic arcs [6]. The composition of wall rocks and the stable mineral assemblages in them are proxy of the crustal depth at which they are formed and the different hydrothermal alterations taking place. For example,

in shallow to intermediate depths below a recharge zone, reducing conditions are prevalent resulting in release of H_2 the and formation of Fe_2O_3 via the following reaction [7],

$$2\,(\mathsf{FeO^+})_{\mathsf{rock}} + \mathsf{H_2O} \longrightarrow (\mathsf{Fe_2O_3})_{\mathsf{rock}} + \mathsf{H_2} \tag{1.1}$$

At greater depths where temperatures and pressures are high, dissolution of non polar gases in liquid solvent may lead to the formation of a coexisting vapour phase [7]. Fluid circulation in zones of high temperature (also called reaction zones) lead to intense chemical reactions with the wall rock till they are discharged through sea-floor vents (also called discharge zones). The composition of fluids in these sea-floor vents reflect fluid routes, composition of rocks and other physical properties of fluid-rock reactions [6].

Another source of hydrothermal fluids are of magmatic origin. They show a close genetic relationship with magmas which are important sources of volatiles and heat source for mobilising different elements. Composition of dissolved volatiles in magma include (but not limited to) water (H_2O), sulfur (S) and other halogens. Exsolution of volatiles occur as the magma ascends to lower depths undergoing decompression and cooling. Concentration of different elements in the fluid phase is determined by the fluid-melt partitioning of the volatiles which is a function of temperature, pressure, oxygen fugacity and melt composition [8]. Partial melting of basement rocks also occur in subduction zones where oceanic crust subducts below continental crust transporting huge amount of materials to lower mantle conditions. During the subduction process, water rich minerals such as amphibole, serpentine, lawsonite, phengite and other hydrous solid phases become unstable releasing water into the system [9, 10, 11, 12]. Subduction zone hydrothermal fluids can be broadly of two types depending on their depths of formation. Hydrothermal fluids formed in shallow depths are water rich with low solubility of silicates and salt. On the contrary, fluids at greater depths can have very high concentrations of salts, gases and rock components thereby showing compositional similarity to melts [1]. These fluids play important role in mineral alteration reactions [13] and also influence the heat transport and electrical conductivity patterns of mantle wedge setting [14].

Hydrothermal fluids can also be generated in geothermal systems. Tremendous amount of primordial heat energy is caged in the Earth's interior. This is slowly being released from the core and mantle through the crust to the atmosphere. Magmas at depths heat up groundwater that ascends towards the Earth's forming reservoirs of hot water and steam

at relatively shallow depths in localized geothermal provinces [15]. During this journey it reacts with the wall rock and accumulates several volatiles. The enormous amounts of energy stored in these fluids also make them good candidates for clean and renewable energy source [16]. Different sources of hydrothermal fluids are illustrated in Figure 1.1

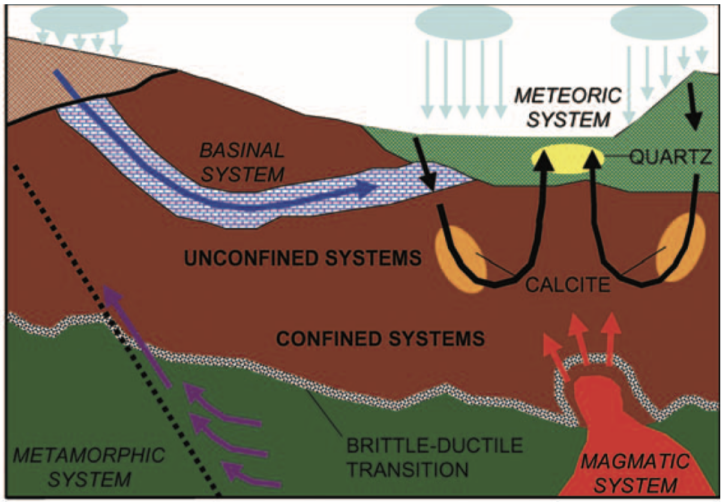

Figure 1.1: Different geologic settings where aqueous hydrothermal fluids are formed. Figure reprinted from Kesler [17]

1.2 Why study aqueous hydrothermal fluids

Ore deposits are regions in the Earth's crust where the concentration of one or more elements are higher than background levels and they can be extracted and sold profitably. Hydrothermal fluids facilitate the transport of mass and thermal energy in the crust leading to formation of ore deposits. Ore metals are generally carried in fluids as complex ions [18]. Fluid inclusions in ore deposits consist of large amounts of H_2O and CO_2 and minor amounts of H_2S, CH_4 and N_2. Dissolved cations include Na^+, K^+, Ca^{2+}, Mg^{2+} and Fe^{2+} along with anions like Cl^-, SO_4^{2-} and HCO_3^- [19]. Circulation of hydrothermal fluids have been discovered in all major ocean floor spreading centers starting from Gakkel Ridge in Arctic to the East Pacific Rise [20]. The composition of fluids in mid-oceanic ridge settings depend on a number of factors like the composition of the host rocks, thermal gradient of the oceanic lithosphere and spreading rate [21]. In systems dominated by basalt, sulfide rich hot fluids form 'black smokers'. Presence of cold sea-water induces several chemical reactions bringing

about compositional changes in the fluids by depositing minerals like anhydrite and forming altered minerals like chlorite that strips the fluids of their Mg content in exchange for Ca [20, 22]. As the fluids enter high temperature zones in the recharge zones, temperatures above the critical point of seawater are encountered where properties like viscosity and static dielectric constant are reduced. Circulation of fluids in this region results in splitting of the single phase fluid into a low salinity and a high salinity fluid that determine the concentrations of dissolved phases like silica [23]. Presence of non polar gases like CO_2 and CH_4 result in the formation of a vapour phase rich in these gases [13] which result in the destabilization and deposition of several metals like Au [24].

Hydrothermal fluids mobilise Rare Earth Elements (REEs) forming ore deposits that are of hydrothermal origin. Insights into REE speciation may be obtained from Pearson's rules [25]. These rules state that a 'hard' (not polarizable) cation will coordinate with a hard anion and vice versa. Since REEs carry charge of +3 and have short radii, they are hard cations and hence their tendency of form stable aqueous complexes follow the order: $F^- > OH^- > NO_3^- > Cl^- > Br^-$ [25]. Pioneering experimental work on REE speciation at ambient and high temperatures have been done by different groups [26, 27, 28, 29]. These are generally associated with peralkaline silicate rocks and carbonatites as in case of Bayan Obo which is the largest REE deposit known today [30]. Fluid inclusion studies show that this ore deposit was formed by precipitation from fluids containing 7-10 wt% NaCl at temperatures of 300°C to 400°C [31]. Other REE deposits of hydrothermal origin include Gallinas Mountains deposits in New Mexico [29] formed from 12-18 wt% NaCl at temperatures of 300°C to 400°C and Karonge deposits in Burundi formed from >25 wt% NaCl at temperatures of >420°C [32]. Although Pearson's rule indicates high tendency of REEs to form fluoride complexes, these complexes are highly insoluble even at high temperatures and are hence not preferred for REE transportation [33]. Hence, while Cl^- are important transporters of ore metal, F^- act as good binders that precipitate REEs as minerals like fluocerite and bastnäsite [30].

Aqueous fluids determine the physico-chemical characteristics of the Earth's interior. Magnetotelluric studies often reveal the presence of zones of high electrical conductivities in the mantle wedge above subduction zones [34, 35] and in the deep crust below young fold belts like the Himalayas [36, 37]. These anomalies are generally attributed to the co-existence of partial melts and aqueous fluids. Presence of fluids and silicate melts also control the viscosity and density of slab fluids thereby determining their buoyancy and mobility [38].

1.3 Aim of the thesis

In this PhD thesis we study different geochemical fluids at high temperature and pressure conditions with Classical Molecular Dynamics (CMD) and Ab Initio Molecular Dynamics (AIMD). We try to give an overall understanding of the applicability and precision of Molecular Dynamics (MD) simulations in providing important insights into the structural, transport as well as thermodynamic properties of these complex systems in conditions difficult to replicate in laboratories. We also fit an altogether new potential for La^{3+} in Cl^{-} bearing hydrothermal fluids from AIMD simulations. The newly developed potential along with enhanced sampling technique is used to study the thermodynamics of ion association reactions in hydrothermal fluids. Issues like finite sampling time and transferability of interaction potentials are discussed in detail. We begin with a discussion on the physics behind MD simulations, different types of interaction potentials used in the thesis and other technical aspects of MD simulations in Chapter 2. Since a variety of different post-processing tools are used, these are discussed in detail in the respective chapters. In Chapter 3 and chapter 4, we study molecular structure and transport properties of important solvents that mobilise REEs in hydrothermal conditions. Having discussed the accuracy of different MD simulation techniques in predicting solvent properties, we study speciation and thermodynamics of REEs in hydrothermal fluids using a newly fitted ab initio based interaction potential in Chapter 5. Each of the chapters are written in the form of manuscript containing brief introductions and conclusions of their own.

Chapter 2

Methods

2.1 Molecular Dynamics (MD) simulations: Introduction and brief history

The use of computer simulations became widespread in 1950s when electronic machines developed during and after Second World War started to be used for unclassified scientific research. Earlier, these machines were being used only for heavy military research and code-breaking.

One of the oldest formulated scientific problems is the famous N-body problem which involves predicting the positions and velocities of N celestial bodies interacting with each other via mutual gravitational force. The analytical reformulations of Newton's Laws of Motion by Euler, Lagrange, Hamilton provided a theoretical framework for solving a simplified version of this problem - the 2-body problem. However, it was quickly realized that the problem was analytically insolvable for three or more bodies. In the 1960s, many theoretical models were being developed to understand properties of different materials and comprehend experimental observations (Example: crystal properties like magnetism, different properties of liquids and gases). These models (Example: Gas equations, Ising model for ferromagnets, Debye-Hückel theory for electrolytes) had to make several approximations as equilibrium properties of these systems could not be computed exactly. The success of all these models depended on our knowledge of the inter-atomic forces in these materials and the accuracy to which these forces were accounted for. Since knowledge of inter-atomic forces was sparse for most of the materials, these models could only make predictions with significantly large

error bars [39]. Also, there was no other independent way to verify these theoretical formulations since disagreement of theoretical results with available experiments would put the entire theory along with all the approximations in question. Computer simulations filled in this void and provided an alternate pathway to verify theoretical model and often gained additional information about the system.

Computer simulations can be used to obtain 'exact' results for a given model without relying on the approximations. This is of utmost importance for theoreticians who now have a tool to examine the system under investigation directly without relying on closed-form solutions which come with several (often uncontrolled) approximations. It is now possible to compare data from simulations against experimental data. If they disagree, we know that the representation of inter-atomic forces is not accurate enough. On the other hand disagreement between simulations and theoretical data mean possible flaws in the theory. Computer simulations have therefore been widely used to investigate systems whose progress has been hampered by the lack of tests to assess quality of approximate models, one such example being dense liquids. Before the advent of computer simulations, this system was being studied using mechanical simulations of macroscopic spherical balls. The main problem that had to be addressed was how to arrange these balls so that this system can model liquids. The problem became intractable when more balls were added into the system.

Liquids were one of the first systems to be simulated when computers were made available for unclassified research. The first simulation of dense liquid was carried out by Metropolis, Teller, Rossenbluth on the MANIAC computer at Los Alamos using the Metropolis Monte Carlo algorithm. The first MD simulations were reported in 1956 by Alder and Wainwright [40] who studied the dynamics of hard spheres at Livermore. MD simulations of real liquids (argon) were first done by Rahman [41] at Argonne. Ever since that, there has been a lot of development of both hardware and software which have opened the floodgates for several interesting research works using computer simulations.

2.1.1 Basic theory

The basic theoretical framework of MD simulations is based on Newton's Laws of Motion. We start with a simulation box containing some atoms/ions/molecules with known initial values of positions and velocities. We also choose a thermodynamic ensemble to keep certain macroscopic properties constant throughout the simulation. The most commonly used

ensembles include the NVT ensemble in which the Number of particles (N), Volume of simulation box (V) and Temperature (T) of the system are held constant, the NPT ensemble in which the N, Pressure (P) and T of the system are held constant or the NVE ensemble where N, V and Energy (E) of the system are held constant. Given a way to calculate the forces between the particles, we can solve the Newton's Law for each particle i at a given time t as:

$$m_i \vec{a_i}^t = \vec{f_i^t} \tag{2.1}$$

where m_i is the mass of particle i. $\vec{a_i}^t, \vec{f_i}^t$ are the accelerations and forces acting on particle i at time t.

In order to propagate the system in time, Equation 2.1 has to be solved numerically. Several discretization algorithms exist for this. The mostly widely used algorithm in several MD engines [42, 43, 44] is called the Velocity Verlet algorithm [45, 46]. This is described next.

Given the position, $\vec{x_i}^t$, velocity, $\vec{v_i}^t$, acceleration, $\vec{a_i}^t$ of particle i at a time instant t, $\vec{x_i}^{t+\Delta t}$ can be calculated from Taylor expansion of $\vec{x}(t)$ about t,

$$\vec{x_i}^{t+\Delta t} = \vec{x_i}^t + \vec{v_i}^t \Delta t + \frac{\vec{a_i}^t (\Delta t)^2}{2} \tag{2.2}$$

Similarly, $\vec{x_i}^{t-\Delta t}$ can be calculated as,

$$\vec{x_i}^{t-\Delta t} = \vec{x_i}^t - \vec{v_i}^t \Delta t + \frac{\vec{a_i}^t (\Delta t)^2}{2} \tag{2.3}$$

Addition of Equations 2.2 and 2.3 gives,

$$\vec{x_i}^{t+\Delta t} = 2\vec{x_i}^t - \vec{x_i}^{t-\Delta t} + \vec{a_i}^t (\Delta t)^2 + \mathcal{O}((\Delta t)^4) \tag{2.4}$$

where $\mathcal{O}$ stands for order of approximation. Similarly, subtraction of Equations 2.2 and 2.3 gives,

$$\vec{v_i^t} = \frac{\vec{x_i}^{t+\Delta t} - \vec{x_i}^{t-\Delta t}}{2\Delta t} + \mathcal{O}((\Delta t)^2) \tag{2.5}$$

This algorithm is called the Verlet algorithm. The discretization error associated is fourth order for positions and second order for velocities although velocities are not required

to integrate the equations of motion. However, velocity is calculated as a difference between two quantities having same order of magnitude. When using computers which always operate with finite numerical precision, this can lead to loss of accuracy and significant round-off errors. Also Verlet algorithm is not self-starting and another algorithm is needed to calculate the first few terms.

A mathematical equivalent of the Verlet algorithm, called the Velocity Verlet algorithm [45, 46] is given by,

$$\vec{x_i}^{t+\Delta t} = \vec{x_i}^{t} + \vec{v_i}^{t}\Delta t + \frac{\vec{a_i}^{t}(\Delta t)^2}{2} \tag{2.6}$$

$$\vec{v_i}^{t+\Delta t} = \vec{v_i}^{t} + \frac{(\vec{a_i}^{t+\Delta t} + \vec{a_i}^{t})\Delta t}{2} \tag{2.7}$$

Equation 2.7 is obtained from Equations 2.4 and 2.5 after some substitutions. It should be noted that unlike the ordinary Verlet algorithm, the Velocity Verlet algorithm is self-starting. For performance improvement, several MD engines implement this algorithm after applying certain tricks to allow proper scaling. Some examples are the Beeman algorithm [47] and Barnes-Hut algorithm [48]. Equation 2.6 and 2.7 are solved for all the particles in the system to obtain their positions and velocities in the next time interval $t + \Delta t$. A thermostat and/or a barostat is then invoked (depending on the chosen ensemble) to regulate temperature and pressure of the system by scaling the velocities and simulation box lengths respectively. Different types of commonly used thermostats include Berendsen thermostat [49], Andersen thermostat [50], Nosè-Hoover thermostat [51], Bussi-Donadio-Parrinello thermostat [52]. Different types of barostats include Berendsen barostat [49], Andersen barostat [50], Parrinello-Rahman barostat [53].

As evident from Equations 2.6 and 2.7, calculation of forces is essential for the scheme to self-start. MD simulations can be of different types depending on the techniques used for calculation of forces.

2.1.2 Periodic Boundary Conditions (PBC)

A simulation box with fixed walls is not a good model to study large (infinite) systems like liquids. To solve this problem the Periodic Boundary Conditions (PBC) are imposed. With PBCs, an infinite system can be represented by a single unit cell which is then replicated

an infinite number of times in three dimensions. Figure 2.1 shows the application of this scheme in two dimensions. In the course of the simulation, when a particle leaves the unit cell, its image in the neighbouring box enters the unit cell in the exact same way. The number density in the central box is thus conserved throughout the simulation (also imposed by NVT, NPT or NVE ensembles). The minimum-image convention is used for particle bookkeeping in which each individual particle in the simulation interacts with the closest image of the remaining particles in the system.

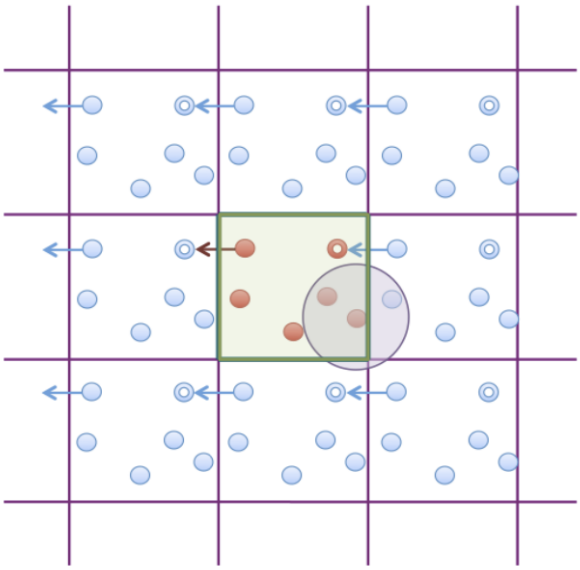

Figure 2.1: PBC in 2-dimensions with minimum-image convention [54]. The highlighted cell is the starting simulation box provided to the MD engine. Each particle interacts with the nearest image of the others with a set cutoff distance $\left(\text{generally} = \frac{boxlength}{2}\right)$ indicated by the sphere. Arrows indicate the instantaneous velocities of the particles

It is also important to understand if properties of small, infinitely periodic system and the macroscopic system are the same. This depends on the range of the interatomic potential being used. For the widely used Lennard Jones (LJ) potential [55] with the following analytical form,

$$V = \sum_{i,j} 4\epsilon_{ij} \left[\left(\frac{\sigma_{ij}}{r_{ij}} \right)^{12} - \left(\frac{\sigma_{ij}}{r_{ij}}^{6} \right) \right] \tag{2.8}$$

simulations can be done with boxes with edge length (L) of $\sim 6\sigma$ so that the particles are invisible to their nearest images. In Equation 2.8, ϵ_{ij}, σ_{ij} are the parameters of the potential and r_{ij} is the interatomic distance. However, if a potential is long-ranged (i.e $V \propto r_{ij}^{-\mu}$ where

μ is less than the dimensionality of the system), there will be substantial interaction between a particle and its neighbouring image [54]. This imposes symmetry in the system which does not exist in a isotropic fluid.

2.2 Classical Molecular Dynamics (CMD)

For a simple system containing N atoms, the total potential energy U of the system can be written as a sum of contributions (v_i) from individual atoms, pairs, triplets and higher order terms as [54]:

$$U = \sum_i v_1(\vec{r_i}) + \sum_i \sum_{j>i} v_2(\vec{r_i}, \vec{r_j}) + \sum_i \sum_{j>i} \sum_{k>j>i} v_3(\vec{r_i}, \vec{r_j}, \vec{r_k}) + ... \tag{2.9}$$

where the summation is over all unique pairs (i.e $ij = ji$), unique triplets and so on. The first term represents external forces on the system. The remaining terms are the interatomic interactions. The second term in Equation 2.9, v_2, also called the pair potential is the most important term. This term depends on the pair separation $|\vec{r_i} - \vec{r_j}|$ and is also abbreviated as $v_2(r_{ij})$. The v_3 term in Equation 2.9 involving triplets of atoms become important for some systems like highly dense liquids. Estimates of this term have been made for inert gases in their solid-state face centered cubic (f.c.c) lattices [56, 57]. Four body and higher terms, collectively called the many-body terms are small in comparison v_2 and v_3.

Although explicit treatment of many-body terms become important for many systems, particularly those that involve chemical reactions [58, 59, 60, 61, 62], we can safely neglect them for aqueous ionic systems by defining an 'effective' pair potential where these terms are usually considered implicitly. Evaluation of these three body and higher order terms use up significant amount of computation time and are hence rarely included in simulations. Effective pair potentials are of the form:

$$U = \sum_i v_1(\vec{r_i}) + \sum_i \sum_{j>i} v_2^{eff}(r_{ij}) \tag{2.10}$$

The effective pair potentials have an implicit description of the many-body terms and gives remarkably good predictions of properties of liquids like pure water and water+NaCl [63, 64, 65] systems, while consuming significantly lower computational resources. One

consequence of this approximation is that the effective pair potential needed to reproduce experimental data may turn out to depend on density, temperature etc., while the true two-body pair potential ($v_2(r_{ij})$) does not. As evident from the discussion above, CMD treats particles in the system as hard rigid spheres with fixed radii. The electronic degrees of freedom are not treated explicitly and are approximated in the parameters of the classical potential.

In this PhD thesis, simple effective pair potentials, many-body potentials as well as reactive potentials have been used. These potentials are briefly described next.

2.2.1 Extended Simple Point Charge (SPC/E) model

Any empirical forcefield describes interactions between the atoms with the following interaction terms:

$$U_{total} = U_{bond} + U_{angle} + U_{vdW} + U_{sr} + U_{Coulomb} \tag{2.11}$$

where U_{bond} is the pairwise bonding energy, U_{angle} is the three-body angular energy, U_{vdW} is the van der Waal's energy arising due to dipole-induced dipole and higher order multipole interactions, U_{sr} is the short-range energy due to repulsion between overlapping electron clouds at short distances and $U_{Coulomb}$ is the Coulomb energy between charged species. We use the rigid SPC/E model [66] to describe the solvent water molecules in Chapter 4. This includes all the interactions in Equation 2.11 except the U_{angle} term making it a pairwise interaction model. Solute Na^+ and Cl^- ions are modelled with the forcefield described by Smith and Dang [67]. The LJ potential [55] is used to describe the short range repulsion and van der Waals interactions between atom pairs (Equation 2.12). A graphical representation of the LJ potential is shown in Figure 2.2 (left).

$$U_{sr} + U_{vdW} = \sum_{i,j} 4\epsilon_{ij} \left[\left(\frac{\sigma_{ij}}{r_{ij}} \right)^{12} - \left(\frac{\sigma_{ij}}{r_{ij}} \right)^{6} \right] \tag{2.12}$$

The model treats atoms as hard rigid spheres with fixed charges. Hence Coulomb interactions in Equation 2.11 are calculated as, $U_{Coulomb} = \sum_{i,j} \left(\frac{q_i q_j}{r_{ij}} \right)$ where q_i is the charge of the atom.

The O-H bond length in water is fixed at 1 Å whereas the H-O-H angle is fixed at 109.47°.

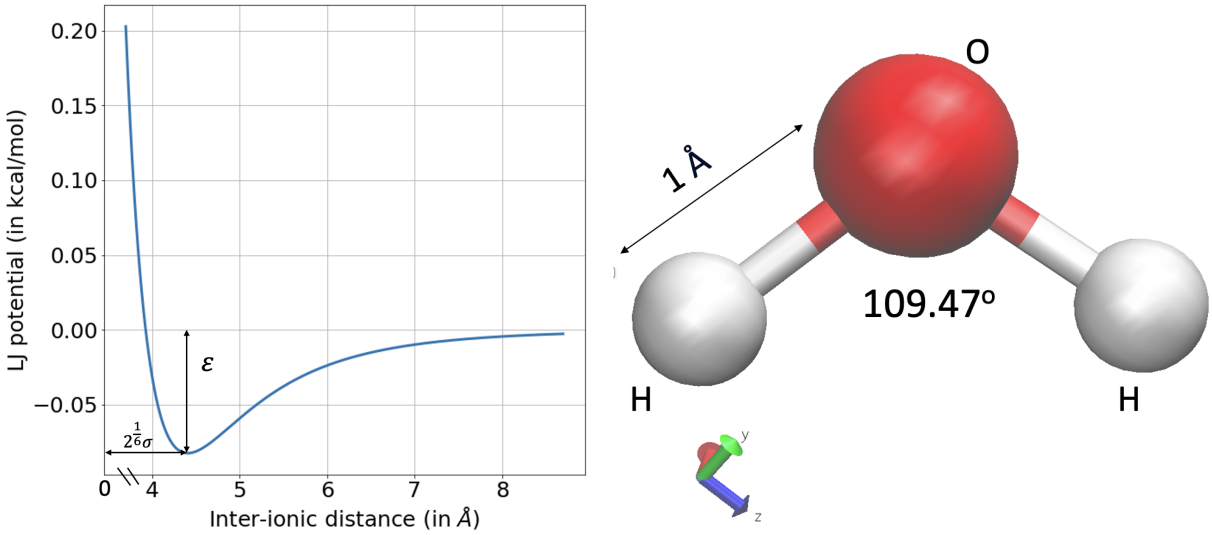

Figure 2.2: Left: Short range repulsion and long range interactions represented by LJ potential. ϵ is the energy minimum of the potential whereas the distance corresponding to the minimum is given by $2^{\frac{1}{6}}\sigma$ Right: Three body rigid water molecule modelled with the SPC/E model. Oxygen atoms are represented by the red balls whereas hydrogen atoms are shown with grey balls. It has to be noted that although the figure represents atoms with spheres of finite radii, they are treated as point charges in the simulation

Figure 2.2 (right) shows a water molecule used in the simulations. The bond and valence angle energy terms (U_{bond}, U_{angle}) are often described by simple harmonic functions of the form:

$$U = \frac{1}{2}ka^2 \tag{2.13}$$

where k is a fitted parameter of the potential describing the frequency of the harmonic function and $a = r_{ij}$ or θ_{ijk} depending bond or angle energy respectively. Since SPC/E is a rigid model, the SHAKE algorithm [68] is used to fix the bond lengths and bond angles throughout the MD simulation.

SPC/E water model has been shown to give very accurate results for a wide variety of systems [63]. The Na-Cl interaction parameters have also been shown to give accurate results for dilute to concentrated brines upto high temperatures [64].

2.2.2 ReaxFF

ReaxFF [61] is a many-body, bond-order dependent reactive forcefield. This was developed to fill the gap between first principle Quantum Chemical (QC) methods and mathematically simpler empirical forcefield based methods. While QC methods can be applied to all systems, their computational expense makes them inapplicable for large systems (containing more than a few hundred atoms). Empirical forcefields on the otherhand describe the potential energy surface with a set of simple functions. Bonding and valence angle interactions are usually described by harmonic equations. Due to their mathematical simplicity, they can be applied to large systems with thousands of atoms. Empirical forcefields have been successfully applied in several chemical environments including aqueous, inorganic, proteins and hydrocarbon systems [61, 62, 60]. However, because of their empirical nature, empirical forcefields are generally fitted against data generated from experiments and/or other QC methods (also called the training set). Hence they should only be applied to systems which are similar to the ones present in the training set. Since harmonic functions are used to describe bonds, these forcefields can only describe systems near their equilibrium configuration. The shape of the potential function makes it impossible to find parameter values near the dissociation limit.

In ReaxFF, the connectivity between the species can change in the course of the MD simulation allowing formation and breaking of bonds. The functional form of the potential allows energy and forces to be continuous throughout these chemical processes. Each element is represented by only one type irrespective of the chemical reactions involved. This makes ReaxFF potentials transferable across different systems. Similar to non reactive empirical forcefields, ReaxFF also breaks down the total energy into different components as,

$$U_{system} = U_{bond} + U_{over} + U_{under} + U_{angle} + U_{pen} + U_{tors} + U_{conj} + U_{vdW} + U_{Coulomb} \quad (2.14)$$

where U_{over}, U_{under} are the energy overcoordination and undercoordination terms, respectively. U_{tors} is the energy of torsion angle and U_{conj} is the contribution of conjugated systems to total energy. U_{pen} is an additional energy penalty term relevant in systems having multiple double bonds. The mathematical expressions for the energy terms in Equation 2.14 can be found in van Duin et al. [61]. ReaxFF also includes polarizability by introducing atomic

charge fluctuations. At each step, a charge equilibration is used to calculate the charges 'on the fly'. Generally, Electronegativity Equalisation Method (EEM) [69] is used to compute the atomic charges.

ReaxFF has been used extensively to model different chemical systems for almost one and a half decade now. They have been parameterized to describe combustible systems [70], heterogeneous catalysis [71] and several aqueous systems [60, 62]. ReaxFF for water has been highly successful in predicting thermophysical properties and diffusion properties of OH^- and H_3O^+ ions [62, 72]. In Chapter 4 of the thesis, we have used the recently developed parameter set by Fedkin et al. [60] for electrolytes to study electrical conductivity of NaCl solutions. The potential has been shown to give reliable results at room temperature as well as high temperature conditions [60, 73].

2.3 Ab Initio Molecular Dynamics (AIMD)

Suppose we have a simulation box containing several atoms and we want to study the properties of these atoms. One of the fundamental properties of interest is the energy of the system and how the energy varies when the positions of the atoms change in the course of the simulation (given by the Potential Energy Surface (PES)). An important observation is that the nuclei which contains many protons and neutrons are much heavier than the electrons (mass of proton/neutron is ∼1800 times mass of electron). Hence, electrons respond much more rapidly to changes in their surroundings than nuclei [74]. As a result, we can decouple electronic degrees of freedom from the nuclear degrees of freedom. For a given set of nuclear positions, we solve the electronic equations of motion to find the lowest energy state, called the ground state of the electrons. This separation of the nuclear and electronic motion is called the Bonn-Oppenheimer approximation [74]. If we have the set of nuclear positions $\vec{R_1}, \vec{R_2}, ...\vec{R_M}$, we can write the ground state energy E as a $E(\vec{R_1}, \vec{R_2}, ...\vec{R_M})$. This function is known as the adiabatic potential energy surface.

The fundamental equation governing the motion of the electrons is the time-independent non-relativistic Schrödinger equation [75] given by,

$$\hat{H}\psi = E\psi \tag{2.15}$$

where $\hat{H}$ is the Hamiltonian operator and ψ is a solution of Equation 2.15 or eigenstates of

the Hamiltonian. Each of these solutions ψ_n, represents a electronic state of the state with energy E_n. For a system with N electrons interacting with each other, the Hamiltonian can be written as,

$$\left[\frac{\hbar^2}{2m}\sum_{i=1}^{N}\nabla_i^2 + \sum_{i=1}^{N}V(\vec{r_i}) + \sum_{i=1}^{N}\sum_{j>i}U(\vec{r_i},\vec{r_j})\right]\psi = E\psi \tag{2.16}$$

where m is the mass of electron, h is the Planck's constant. The terms in the bracket define, in order, the kinetic energy of the electrons, interaction potential energy between the nuclei and the electrons and the interaction potential energy between the electrons. The ground state electronic wave function ψ is a function of all $3N$ electronic coordinates i.e. $\psi = \psi(\vec{r_1}, \vec{r_2}, ..., \vec{r_N})$. Solving Equation 2.16 is difficult because of the number of coordinates involved. For large systems with few hundreds of electron, the problem becomes intractable. The most critical term in $\hat{H}$ is the third term which accounts for the electron-electron interactions. Since this term depends on pairs of electronic coordinates, Equation 2.16 cannot be solved for each individual electronic wavefunctions, $\psi_i(\vec{r})$, independent of the others. This means that the Schrödinger equation [75] is a many-body problem.

Density Functional Theory (DFT) provides a theoretical framework to calculate ground state energy of the system in terms of electron density bypassing the need to obtain the full $3N$ dimensional electronic wavefunction. DFT is based on two fundamental mathematical theorems by Walter Kohn and Pierre Hohenberg and derivation of a set of equations by Walter Kohn and Lu Jeu Sham [76] in mid 1960s. The first theorem provided by Hohenberg and Kohn [77] is: The ground-state energy from Schrödinger equation is an unique functional of the electron density. This means that the electron density uniquely determines the energy and wavefunction of the system. The immediate advantage is that we can now think of the solution of Schrödinger equation as a function of 3 spatial variables instead of $3N$ electronic coordinates [74].

The second Hohenberg-Kohn theorem [77] defines an important property of the functional - The electron density that minimizes the energy of the overall functional is the true electron density corresponding to the full solution of the Schrödinger equation [74]. The energy functional can be written as [74]:

$$E[\psi_i] = E_{known}[\psi_i] + E_{XC}[\psi_i] \tag{2.17}$$

where ψ_i's are the one electron wavefunctions that fully define the electron density ($n(\vec{r})$). Here, $E_{known}[\psi_i]$ are the terms that can be written in simple analytical forms and everything else as E_{XC}. The $E_{known}[\psi_i]$ terms include electron kinetic energies, the Coulomb interactions between electrons and the nuclei, the Coulomb interactions between electron pairs and Coulomb interactions between pairs of nuclei. The $E_{XC}[\psi_i]$ term includes all the 'quantum mechanical effects'.

The Kohn-Sham (KS) [76] equations show that the correct electron density can be obtained by solving a set of equations in which each equation depends on one electron wavefunctions, ψ_is. These equations have the following form [74]

$$\left[\frac{\hbar^2}{2m}\nabla_i^2 + V(\vec{r_i}) + V_H(\vec{r_i}) + V_{XC}(\vec{r_i})\right]\psi_i(\vec{r}) = \epsilon_i\psi_i(\vec{r}) \tag{2.18}$$

On the left hand side of the KS equations, there are three terms, V, V_H, V_{XC}. The first term also appeared in Equation 2.16 and defines the interaction between electrons and atomic nuclei. The second term is called the Hartree potential and describes the Coulombic repulsions between each electron and the electron density defined by all the electrons. This also includes a self-interaction term because every electron is also a part of the total electron density. This is unphysical and is taken care of in the V_{XC} term. V_H is given by [74],

$$V_H(\vec{r}) = e^2 \int \frac{n(\vec{r'})}{|\vec{r} - \vec{r'}|}\, d^3r' \tag{2.19}$$

The third term, V_{XC} contains the electron exchange and correlation contributions. This can be defined as a 'functional derivative' of the exchange-correlation energy [74],

$$V_{XC}(\vec{r}) = \frac{\delta E_{XC}(\vec{r})}{\delta n(\vec{r})} \tag{2.20}$$

In this PhD thesis different Exchange and Correlation (XC) functionals like Becke, Lee, Yang, and Parr (BLYP) [78, 79], r2SCAN [80], Perdew, Burke and Ernzerhof (PBE) [81] have been used. These will be discussed in greater detail later.

DFT is implemented in several quantum chemistry codes like CPMD[1] , VASP[2], CP2K [3] , ABINIT[4]. In this PhD thesis, all AIMD simulations were done using CP2K code [42].

[1] `https://www.cpmd.org`
[2] `https://www.vasp.at`
[3] `https://www.cp2k.org`
[4] `https://abinit.github.io/abinit_web/`

2.3.1 Basis sets

Basis sets (χ_i) are a set of mathematical functions that are used to build the wavefunction. A DFT calculation starts by expressing the Kohn-Sham one-electron orbitals ($\psi_i(\vec{r})$) as a linear combination of these basis set functions as [82]:

$$\psi_i = \sum_i c_{ri}\chi_i \tag{2.21}$$

The coefficients c_{ri} in Equation 2.21 are determined self-consistently during the calculation.

Basis sets have been created from Slater, Gaussian, plane wave and delta functions. Each Atomic Orbital (AO) can be represented as a linear combination of one or more Slater-Type Orbitals (STOs). An STO centered on atom a has the form, $Nr_a^{n-1}e^{-\zeta r_a}Y_l^m(\theta_a, \phi_a)$ [82].

A Double-Zeta (DZ) basis set is obtained by replacing each STO with two STOs that have different orbital exponent value ζ [83]. Similarly, a Triple-Zeta (TZ) basis set is obtained by replacing each STO with 3 STOs with different orbital exponents.

A Split-Valence (SV) basis set uses two (or more) STOs for each valence AO but only one STO for each inner shell [84]. SV basis sets can be Valence Double Zeta (VDZ), Valence Triple Zeta (VTZ) according to the number of STOs used for each valence AO. In this PhD thesis, Molecularly Optimized (MOLOPT) Double Zeta Valence Potentials (DZVPs) [85] have been used. Optimizing basis sets for different systems is a specialized field of research and so we do not describe this is detail.

2.3.2 Pseudopotentials

The periodic table contains several heavy elements with many electrons. It is technically quite challenging to describe all the electrons using basis sets. Moreover, the valence electrons take part in most of the chemically interested phenomenon like chemical bonding polarization. Also, the greater the number of electrons, the greater will be the associated electron correlation. This problem was first solved by Hellmann in 1930s who proposed to replace the core electrons with analytical functions that describe the effective nuclear-electronic core to the valence electrons [74]. These functions are called the pseudopotentials. Another purpose served by pseudopotentials is that they implicitly account for relativistic effects of core

electrons in heavy elements.

Designing and optimizing pseudopotentials for different chemical systems is itself a field of research. Once properly optimized, these element-specific functions are transferable across different systems and thermodynamic conditions [74]. In this PhD thesis, all AIMD simulations were carried out using Goedecker-Teter-Hutter (GTH) pseudopotentials [86] which are implemented in CP2K code [42]. These pseudopotentials have been shown to give reliable results for aqueous systems at room temperature as well as supercritical conditions [87, 88, 89, 90].

2.3.3 Exchange and Correlation (XC) functionals

As discussed in Section 2.3, V_{XC} term in Equation 2.18 contains all the energy contributions due to quantum mechanical effects. A good description of these effects is important for the accuracy of the DFT calculations. One important classification of the XC functionals is given by John Perdew and co-workers [91] and is called the Jacob's ladder. This is shown in Figure 2.3. Higher rungs represent functionals that include more and more physical information as steps towards the 'perfect method' in which the Schrödinger equation is solved without approximation.

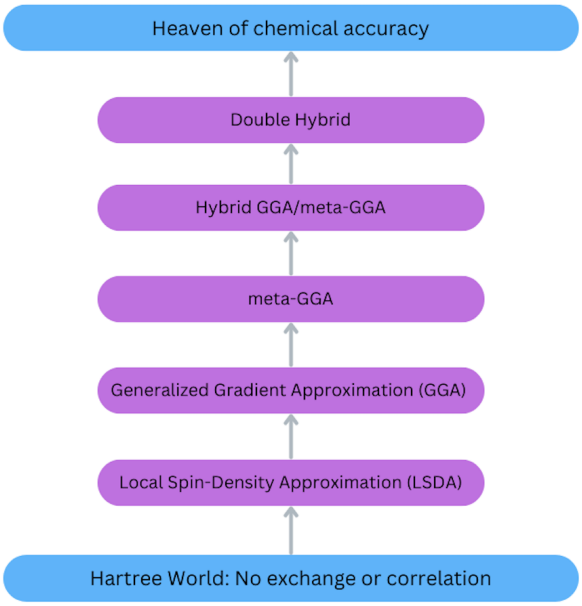

Figure 2.3: Jacob's Ladder comprising five rungs of increasing sophistication of XC functionals

Another way to categorize XC functionals is whether they are empirical or non empirical. Non empirical functionals have been constructed to satisfy certain constraints in order to make use of the known exact constraints on the true Kohn-Sham functionals. Non empirical functionals from higher rung satisfy more constraints. Empirical functionals on the other-hand are fitted against selected experimental or ab initio data and contain many parameters that are introduced and adjusted during the fitting procedure. Since these functionals often violate various properties of the Kohn-Sham functional, it is not always reasonable to expect better results with XC functionals from higher rung of ladder, especially if the functional from the higher rung is empirical.

The simplest exchange correlation functional depends only on the electron density and occupy the first rung of the Jacob's ladder. This is called the Local Spin Density Approximation (LSDA) and is exact for an infinite Universal Electron Gas (UEG) [92]. However they are highly inaccurate for molecular systems having delocalized electron densities. The LSDA exchange functional has an exact analytic form but there is no exact analytic form for the LSDA correlation functional, and the three most popular parameterisations (VWN5 [93], PZ81 [94], and PW92 [95] use fits to accurate Quantum Monte Carlo data [96] computed by Ceperley and Alder in the late 1970s.

In order to improve on the systematic errors of LSDA, it is necessary to account for the inhomogeneous electron densities. This is done by introducing the the density gradient ($\nabla\rho$) and the resulting XC functional, called the Generalised Gradient Approximation (GGA) occupies the second rung of the Jacob's Ladder. The functional form of GGAs include a correction for inhomogeneity in addition to contribution from UEG exchange energy. For detailed mathematical formulation of GGAs, one can refer to [97, 81, 98, 99]. Popular GGA exchange functionals include B88 [78], PW91 [100], PBE [81], revPBE [101], RPBE [102], and PBEsol [103], while popular GGA correlation functionals include P86 [104], LYP [79], PW91 [100], PBE [81], and PBEsol [103]. These components can be combined to define GGA XC functionals, and the PBE XC (PBE exchange + PBE correlation) is perhaps the most popular one. Besides PBE, other successful GGA density functionals include BP86 (B88 + P86), BLYP (B88 + LYP), PW91 (PW91 + PW91), revPBE (revPBE + PBE), RPBE (RPBE + PBE), and PBEsol (PBEsol + PBEsol).

In order to further increase accuracy, two additional ingredients can be included - Laplacian of electron density ($\nabla^2\rho$) or kinetic energy density. Since both the terms include second

derivative terms, they are related and generally one or the other is included in the functionals. The kinetic energy density has been used in many modern functionals to add flexibility to the functional form. These functionals are called the meta-Generalised Gradient Approximation (meta-GGA) and they define the third rung of the Jacob's Ladder. For detailed mathematical formulations of meta-GGA, interested readers can refer to literature [105, 106, 107]. Popular non-empirical meta-GGA exchange-correlation functionals are almost exclusively from Perdew and co-workers, and include PKZB [108], TPSS [109], and revTPSS [110], as well as the newer MS0 [111],MS1 [112], MS2 [112], MVS [113], and Strongly Constrained and Appropriately Normed (SCAN) [114] functionals.

meta-GGAs like SCAN have shown good accuracy even for systems that are known to be challenging for DFT. Examples include predicting accurate geometries and energetics of ice and silicon phases [115] and for polymorphs of MnO_2 [116]. However, SCAN's utility in large scale projects is hampered by its sensitivity to density of integration grids. Since highly dense integration grids have to be used, computational efficiency is heavily reduced. Recently, a new meta-GGA called r2SCAN was proposed by Furness et al. [80]. r2SCAN addresses the integration grid issues faced by SCAN while retaining the chemical accuracy of SCAN. In Chapter 3, we compare the accuracy of BLYP and r2SCAN functionals in predicting vibrational spectra and structural properties of hydrothermal sulfate bearing fluids.

2.4 Enhanced sampling techniques

One of the drawbacks of MD simulations is the limited timescale that can be reached. This happens because the timestep of MD simulations must be smaller than the fastest motion in the system. So, even with classical force fields the maximum timescales that can be reached is of the order of microseconds. This is a problem because several interesting dynamical processes involve metastable states that are separated by high energy barriers leading to kinetic bottlenecks. Proper sampling of these states would take unreasonably high computation resources. To overcome this, enhanced sampling techniques are used that introduce biases in the simulation forcing the system out of energy troughs thus achieving better sampling of all the states. For example, suppose we want to study the energetics of dissociation reactions like $LaCl_3$ dissociating to $LaCl_2^+$ and Cl^-. Since this reaction has a high energy barrier, occurrence of this reaction in an unbiased simulation is rare, leading to

poor statistics. Hence enhanced sampling techniques like thermodynamic integration [117], Well-tempered Metadynamics (WMetaD) [118] and adaptive force bias [119] are used that forces the system out of these energy basins. In Chapter 5 of this thesis we have used WMetaD technique to calculate dissociation constants of La-Cl complexes.

2.4.1 Metadynamics

The probability distribution of different states obtained from MD contains all the thermodynamic information of the system being studied. However, the full PES is a unintelligible $3N$ dimensional function. For this reason, a coarse grained representation of the molecular system is warranted which is achieved by a set of Collective Variables (CV). CV (denoted by $s(q)$ where q are the positions and velocities of the particles) is defined as a non linear function of the atomic coordinates and hence allows analysis of the system in lower dimensions while retaining all the physicochemical information of the system. The CVs must be able to distinguish between the different metastable states of the system and should ideally be low in number. When analysing a system in terms of CVs, potential energy ($U(\vec{R})$) can be replaced with Free Energy Surface (FES, G(s) where s is the CV). Hence, the probability of observing a particular CV can be written as,

$$P(s)ds \propto e^{\frac{-G(s)}{k_B T}} ds \tag{2.22}$$

If the energy differences between the metastable states of the system are $\sim$ thermal energy ($k_B T$) of the system, unbiased MD simulation gives good sampling of all the important states of the system. In such a case, $G(s)$ along a particular CV can be calculated by binning the sampled CV values into a histogram and determining their probabilities of occurrence ($N(s)$) as shown in Equation 2.23. However in most systems this is not the case and biasing of the CVs is required to achieve proper sampling of the metastable states.

$$G(s) = -k_B T log N(s) \tag{2.23}$$

A bias potential $V(s)$ is then constructed on this CV which takes the following form upon convergence, [120]

$$V(s) = -\left(1 - \frac{1}{\gamma}\right) G(s) \tag{2.24}$$

and the system evolves under the following FES:

$$G^*(s) = G(s) + V(s) = \frac{G(s)}{\gamma} \tag{2.25}$$

where $G^*(s)$ is the biased FES, γ is the bias factor which is a simulation parameter used in biasing the CVs.

In metadynamics, the time dependent bias potential at time t can be written as,

$$V(s,t) = \int_0^t \omega e^{-\sum_{i=1}^{N_{CV}} \left(\frac{(s_i(q(t)) - s_i(q(t')))^2}{2\sigma_i^2} \right)} dt' \tag{2.26}$$

where ω is the energy rate, N_{CV} is the number of CVs and σ_i is the width of the i^{th} CV. As evident from Equation 2.26, the bias potential at any given time t is an integral of all Gaussian-shaped bias potentials deposited from time $0 - t$. The energy rate is constant and is defined as the ratio of the Gaussian height (W) and the deposition stride (τ_G). The time evolution of the bias potential can be written as,

$$\dot{V}(s,t) = \omega e^{-\sum_{i=1}^{N_{CV}} \left(\frac{(s_i(q(t)) - s_i(q(t')))^2}{2\sigma_i^2} \right)} \tag{2.27}$$

However, systems evolving under Equations 2.26, 2.27 shows poor convergence of the FES. Also, since the height of the Gaussians are fixed, it tries to sample the entire CV space and can push the system to thermodynamically irrelevant states [120]. Both these problems are tackled by a modification of metadynamics, called the Well-tempered Metadynamics (WMetaD).

In WMetaD, the bias is updated in slightly different way as [118],

$$\dot{V}(s,t) = \omega e^{\frac{-V(s(t),t)}{k_B \Delta T}} e^{-\sum_{i=1}^{N_{CV}} \left(\frac{(s_i(q(t)) - s_i(q(t')))^2}{2\sigma_i^2} \right)} \tag{2.28}$$

where ΔT is an input parameter measured in temperature units.

Equation 2.28 implies that the heights of the deposited Gaussians are scaled by a factor that is inversely dependent on the bias potential evaluated at that point. Hence, in energy basins where a sizable bias potential has already been added, the next Gaussians will be of decreasing heights thus preventing overfilling of the energy basin.

Chapter 3

Vibrational and structural properties of aqueous H_2SO_4 and Na_2SO_4 systems from ambient to supercritical conditions: A comparative study between BLYP and r2SCAN functionals

3.1 Introduction

Sulfur is one of the most important elements in the Earth's crust. It plays a very important role various domains like determining mineral dissolution, precipitation as well as crystal growth in ambient to supercritical geo-fluids, acid mine waters and oxidation of coal [121, 122, 123, 124, 125, 126]. Fluid inclusion experimental studies show that inorganic ligands like sulfate and bisulfate play an important role in the mobilization, transport and precipitation of strategically important elements [127]. Sulfate-rich hydrothermal fluids have resulted in the formation of several ore deposits around the globe like the Capitan Pluton and Gallinas Mountains in New Mexico [128]. Sulfate in seawater acts as an important oxidizing agent and influences the redox budget of the Earth [129]. Records of sulfur and oxygen isotopes in seawater are used in paleo-environment detection like sedimentary, riverine or microbial

systems [129]. Apart from this, sulfate is also an important ligand in other geological settings like see-floor vents, magmatic hydrothermal fluids and subduction fluids [128]. The molecular properties of the sulfate anion such as coordination environment, vibrational states and symmetry determine its behaviour in hydrothermal geo-fluids. Raman and Infrared (IR) spectroscopy are often used to determine in-situ sulfur speciation and concentrations [130, 131]. The vibrational frequencies of the most abundant sulfur species (sulfate-SO_4^{2-}, bisulfate-HSO_4^-) obtained from Raman and IR spectroscopy studies are summarized in Table A1 in Appendix A.

AIMD has become a widely used technique to study geochemical fluids - providing reasonable tradeoff between accuracy and computational cost. These simulations have been incredibly successful in providing important insights into different aqueous systems [89, 88, 132, 133] under conditions difficult to replicate in laboratories. However, AIMD models have their own shortcomings and accurate models that capture all structural and thermodynamic properties of aqueous systems remain elusive. Moreover, this approach is limited by the fact that predictions depend on the XC functional being used. For example, the most widely used XC functionals called PBE [81] and BLYP [78, 79] (which are GGA [97] functionals) predict energetics of gas phase water clusters reasonably well [134, 135] but predict significantly overstructured bulk water at ambient conditions with very slow diffusion compared to experiments [136]. These effects may be 'corrected' by introducing a temperature shift of ∼50-100 K [137] or by using other GGA functionals like the revised Perdew, Burke, and Ernzerhof functional with Grimme dispersion correction (revPBE-D3) [81, 101, 138]. At elevated temperature and pressure, Fowler and Sherman [133] report excellent agreement of bulk densities of NaCl solutions with PBE functional. GGA functionals also give relatively good estimates of infrared spectrum of liquid water [137] although a systematic redshift with respect to experimental data remain. Increasing the sophistication of the XC functional can solve some of the shortcomings of GGA functionals but with increased computational overhead. Sophisticated functionals like the SCAN [114] functional (which is a meta-GGA functional [105, 106]) gives better estimates of the IR spectrum of liquid water [139] and also predict accurate hydration shell structure of ions like Na^+, K^+, Ba^{2+}, Cl^- in solution [140, 141, 142, 143], as compared to GGA functionals. This stems from the fact that GGA functionals suffer from delocalization error [144] and have issues reproducing interactions between charged species [140]. However, SCAN predicts shorter O-O distances as compared to

experiments and revPBE-D3 GGA functional for pure water [141]. Using more sophisticated functionals like hybrid-GGA [145] may give improved predictions but are so expensive that even with state of the art hardware they are restricted to short simulations with very few atoms. The accuracy and precision of different XC functionals are therefore system-specific and also depend on the properties under investigation.

Introduction of complex ions (like SO_4^{2-}, HSO_4^-) complicates the already arduous task of making accurate predictions for pure water system. So far, computational studies involving more complex ions such as HSO_4^- have been mostly restricted to structural properties in aqueous solutions up to ambient conditions (298 K-310 K) [146, 147, 148, 149] or to vibrational spectra of the ions in the gas phase [150, 151] and in aqueous solution at ambient conditions [148, 152]. For SO_4^{2-} ions, computational studies have been performed to understand structural properties at ambient conditions [153, 154, 155, 156, 157] and at higher temperatures[158]. Computational studies of vibrational spectroscopy have been done for different hydrated gas phase clusters [159, 160, 161], aqueous solutions at 298 K (free ion) [162], high temperature supercritical fluids containing $MgSO_4$ [89, 163] and Na_2SO_4 [90]. Vibrational frequencies of the most abundant sulfur species (sulfate, bisulfate) obtained from computational studies are shown in Table A2.

Since increasing sophistication of XC functionals (and hence computational cost) does not guarantee increased accuracy, a systematic study of the predictive capacities of different XC functionals for complex ion bearing aqueous systems at ambient temperatures and hydrothermal conditions is warranted. In this study, we use two different XC functionals of different sophistication levels, namely BLYP and r2SCAN, to predict various structural and vibrational properties of sulfur-bearing species in liquid and supercritical water. The reliability of PBE GGA functional in calculating vibrational modes of sulfur bearing species in hydrothermal conditions has been shown by Jahn and Schmidt [89] ($MgSO_4$ solutions at 500 K), Schmidt and Jahn [90] (Na_2SO_4 solutions at 1000 K). In this paper we investigate whether the temperature-induced trends in vibrational frequencies can be systematically reproduced by a GGA functional (BLYP in this case) with reasonable computational overhead. The recently proposed r2SCAN functional improves the numerical efficiency while retaining the accuracy of SCAN functional [80]. We perform simulations from ambient conditions to supercritical conditions in order to understand the molecular structures of aqueous H_2SO_4, Na_2SO_4 solutions and the effects of solvent on the vibrational properties of these

species. We use mode projection analysis to resolve the vibrational modes of sulfur bearing species from the total Vibrational Density Of States (VDOS). This is of great importance for the systems being studied due to the presence of several closely spaced vibrational modes from different species [152]. The results are compared against experimental data or other computational studies wherever available. The XC functionals are judged based on their preciseness in predicting structural and vibrational properties thereby helping in judicious usage of computational resources in future projects.

3.2 Methods

3.2.1 Simulation protocol

AIMD simulations are performed with 1.13 m aqueous sulfuric acid solutions in 3D periodically replicated simulation boxes. The concentration and temperature of the simulations are chosen to match the experimental conditions of Schmidt and Seward [131] thereby allowing direct comparison with results from our simulations. Four different simulation boxes are prepared as shown in Table 3.1. First, a simulation box containing only water molecules is equilibrated at room temperature and density of $\sim$1 g/cm^3 with the SPC/E model [66]. Boxes 1 and 2 are then created by replacing some of the water molecules with geometry optimized H_2SO_4 molecule resulting in box 1 containing 100 H_2O, 2 H_2SO_4 molecules and box 2 containing 50 H_2O, 1 H_2SO_4 molecule. In order to understand the effect of cations on speciation and vibrational spectrum, water molecules are replaced with geometry optimized Na_2SO_4 molecule to create boxes 3 and 4 containing 100 H_2O, 2 Na_2SO_4 molecules and 50 H_2O, 1 Na_2SO_4 molecule respectively. The edge lengths of all the simulation boxes are adjusted to have a density of $\sim$1 g/cm^3 (boxes 1,3 - 14.6 Å, boxes 2,4 - 11.8 Å) .

The DZVP basis sets [85] along with the GTH pseudopotentials [86] are used for all species. A plane wave cutoff of 1000 Ry is used for simulations with the BLYP functional whereas 1200 Ry is used for simulations with the r2SCAN functional [164]. The timestep for the simulations is set to 0.5 fs. We run production AIMD simulations in the NVT ensemble for atleast 30-50 ps after 4 ps of initial equilibration. The simulations are performed at ambient conditions, 473 K and 673 K for each XC functional. The target temperatures for ambient conditions are set to 320 K for BLYP and 330 K for r2SCAN functional, consistent

Table 3.1: Details of simulation boxes

Box no.	Contents	Cell length (in Å)	ρ (in g/cm^3), Molality
1	100 H_2O, 2 H_2SO_4	14.6	1.06, 1.12
2	50 H_2O, 1 H_2SO_4	11.8	1.0, 1.12
3	100 H_2O, 2 Na_2SO_4	14.6	1.11, 1.12
4	50 H_2O, 1 Na_2SO_4	11.8	1.05, 1.12

with previous NVE simulations of pure water with the respective XC functionals [87, 139]. Boxes 1 and 3 are used for simulations with the BLYP XC functional. In order to account for higher computational expense, box 2 and 4 are used for simulations with the r2SCAN functional. Nosé–Hoover thermostat is used to control the temperature at the target value. All simulations are performed with the Gaussian Plane Wave (GPW) methodology using the CP2K simulation package [42]. Structural and vibrational properties are computed with the production trajectories.

3.2.2 Post-processing tools

3.2.2.1 Pair correlation functions

The atomic structure is studied using pair correlation functions defined as:

$$g_{ij}(r) = \left\langle \frac{dn_r^{ij}}{4\pi r^2 \rho_j dr} \right\rangle \tag{3.1}$$

where dn_r^{ij} is a function calculating the number of particles of type j within a shell of thickness dr at a distance r from a particle of type i. ρ_j is the particle density $\left(= \frac{N_j}{V} \right)$ of j. The angular brackets denote ensemble average over the entire trajectory. $g_{ij}(r)$ is a measure of local particle density at position r with respect to ideal gas conditions. Pair correlation functions for different species were calculated using TRAVIS code [165]. The first maximum of the function defines the bond length whereas the first minimum defines the first coordination shell. Running Coordination Number (CN) are determined by counting the number of atoms till the first minimum.

3.2.2.2 Mode projection analysis

Vibrational spectra calculated from AIMD simulations are based on the Fourier Transform (FT) of normalised Velocity Autocorrelation Functions (VACFs) as shown in Equations 3.2, 3.3

$$C(t) = \left\langle \frac{\sum_i \vec{v^i}(t'+t)\vec{v^i}(t')}{\sum_i \vec{v^i}(t')\vec{v^i}(t')} \right\rangle \tag{3.2}$$

$$F(\omega) = \int_0^{t_{max}} cos(\omega t) C(t)\, dt \tag{3.3}$$

where $\vec{v^i}$ in Equation 3.2 is the velocity vector of particle i. The summation in Equation 3.2 are over all atoms of a tetrahedral sub unit. $F(\omega)$ is the spectral density, ω is the angular frequency and angular brackets indicate ensemble average. For each atom, the vector autocorrelation of the velocity is calculated and sum of all the correlation functions of a molecule is Fourier transformed to get the power spectrum of that molecule. However, FT of the total velocity of atoms gives the complete molecular VDOS that includes translational, rotational and long-range acoustic contributions making band assignment difficult. Therefore, the spectroscopically distinct contributions must be isolated from the complete VDOS. This can be achieved using mode projection analysis.

Mode projection analysis is based on the observation that high frequency vibrational modes of SO_4^{2-} tetrahedra remain normal mode like throughout different degrees of polymerization. The frequency of these vibrational modes depend on the degree of polymerization of the sub units and the thermodynamic conditions. To uncover these high frequency modes in different environments, the total VDOS is distributed among various Quasi-Normal Modes (QNMs). The QNMs of a group of atoms is calculated by taking FT of ACF of velocity projected along respective QNMs. Mathematically, this is achieved by Equation 3.4 as,

$$C^i_{QNM}(t) = \left\langle v^i_{QNM}(t'+t) v^i_{QNM}(t') \right\rangle \tag{3.4}$$

where v^i_{QNM} is the magnitude of projected velocity along respective QNMs for the i^{th} tetrahedron. Projection of atomic motions onto QNMs isolates the spectroscopically distinct contributions because the quasi-local vibrations behave like the molecular normal-modes based on symmetry [166]. For example, the four Raman-active normal modes of

SO_4^{2-} tetrahedra having T_d symmetry can be approximated with four QNMs with degeneracies: symmetric stretch ($\upsilon_1(a_1)$), asymmetric stretch ($\upsilon_3(f_2)$), symmetric bend ($\upsilon_2(e)$), asymmetric bend ($\upsilon_4(f_2)$) where a_1, e, f_2 denote totally symmetric, doubly degenerate and triply degenerate respectively. In the first step of mode decomposition, for each MD frame the atoms of individual sub units are grouped together (in our case S,O atoms of SO_4^{2-} or HSO_4^-). Velocities of individual S atoms are then subtracted from velocities of each of the four oxygen atoms of SO_4^{2-} or HSO_4^- to eliminate the low-frequency translation modes. In the third step, velocities of individual atoms are decomposed along QNMs strictly based on symmetry, as discussed later. Finally, FT of VACF of the projected velocities gives the frequency of the QNMs. This computational technique has been successfully used to assign frequencies to different molecular vibrations in SiO_4 bearing melts and glasses [166, 167]. The same analysis code as in Spiekermann et al. [167] is used as the symmetries of the considered species in the H_2O-SiO_2 system are similar to those of interest here.

Decomposition of velocity: Two important QNMs are studied for the SO_4^{2-} tetrahedra: symmetric stretch ($\upsilon_1(a_1)$) and asymmetric stretch ($\upsilon_3(f_2)$). The instantaneous velocity vectors of all four oxygen atoms of tetrahedron i can be projected onto the $\upsilon_1(a_1)$ QNM as:

$$V_{\upsilon_1}^i = \sum_{j=1}^{4} v_{ij}^{||} \tag{3.5}$$

where $v_{ij}^{||}$ is the magnitude of velocity of j^{th} oxygen atom projected along normalized displacement vector S_i-O_j. Similarly, projection along $\upsilon_3(f_2)$ QNM is achieved as follows:

$$V_{\upsilon_3}^{i,1} = v_{i,1}^{||} + v_{i,2}^{||} - v_{i,3}^{||} - v_{i,4}^{||} \tag{3.6}$$

The other two degenerate modes (2,3) are obtained by exchanging oxygen 2 with oxygens 3 and 4 respectively. These QNMs are shown in Figure 3.1.

For HSO_4^- molecule, 3 important vibrational modes are studied which can be approximated by the following QNMs: symmetric SO_3 stretch ($\upsilon_1(a_1)$), asymmetric SO_3 stretch ($\upsilon_3(e)$) and S-OH stretch ($\upsilon_4(a_1)/\upsilon_{SOH}(a_1)$). Projection along $\upsilon_1(a_1)$ QNM is done as follows:

$$V_{\upsilon_1}^i = \sum_{j=1}^{3} v_{ij}^{||} \tag{3.7}$$

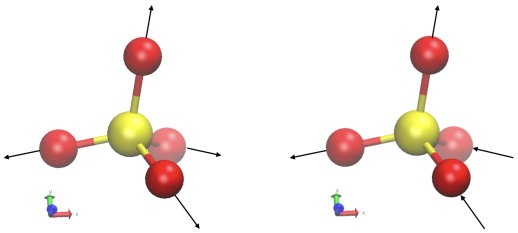

Figure 3.1: QNMs of sulfate ion (Yellow: sulfur, Red: oxygen). Left: Symmetric stretching mode ($\upsilon_1(a_1)$), Right: Asymmetric stretching mode ($\upsilon_3(f_2)$). Arrows indicate directions of projected velocity of each oxygen atom

whereas the projection along $\upsilon_3(e)$ QNM is achieved by,

$$V_{\upsilon_3}^{i,1} = v_{i,1}^{||} + v_{i,2}^{||} - v_{i,3}^{||} \tag{3.8}$$

The other degenerate mode (2) is obtained by exchanging oxygen 2 with oxygen 3. Finally, $\upsilon_4(a_1)$ mode of the bisulfate ion is studied by first identifying the O atom to which the proton is attached and then projecting the velocity of this O atom along the respective S-O normalized displacement vector. These QNMs are shown in Figure 3.2.

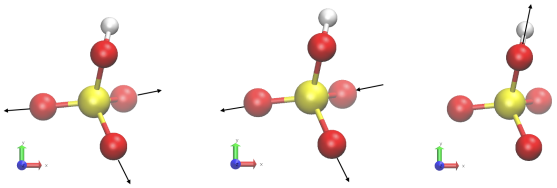

Figure 3.2: QNMs of bisulfate ion (Yellow: sulfur, Red: oxygen, White: hydrogen). Left: Symmetric stretching mode ($\upsilon_1(a_1)$), Middle: Asymmetric stretching mode ($\upsilon_3(e)$) Right: S-OH stretching mode ($\upsilon_4(a_1)$). Arrows indicate directions of projected velocity of each oxygen atom

3.3 Results

This section is divided into two parts. In the first part we present structural data obtained from simulations of aqueous H_2SO_4 solution and aqueous Na_2SO_4 solutions whereas in the next part, vibrational spectra are presented. In the remaining paper 'S' is used to denote the sulfur atom of sulfate/bisulfate/sulfuric acid, 'O_w' is used to denote the water oxygen

atoms and 'O_b', 'H_b' are used to denote the oxygen atoms bonded to the sulfur atom and hydrogen atom of bisulfate ion respectively.

3.3.1 Structure

3.3.1.1 Aqueous H_2SO_4 solution

The pair correlation functions, $g_{SOw}(r)$ from the two XC functionals at ambient conditions are shown in Figure 3.3. Distances and coordination numbers predicted by the XC functionals for different systems are listed in Table 3.2. $g_{SOw}(r)$ for aqueous H_2SO_4 solution at ambient conditions is shown in Figure 3.3. Figures for higher temperatures are shown in Figure A4 in Appendix A.

From Table 3.2 it can be inferred that r2SCAN predicts a shorter S-O_w distance at all temperatures, as compared to BLYP. However, the size of the first hydration shell is smaller for BLYP as compared to r2SCAN at ambient conditions. This also results in lower number of hydration water molecules in case of the former. The difference is $\sim$5 water molecules at ambient conditions which reduces to $\sim$1 water molecule at elevated temperatures due to similar sizes of hydration shells predicted by the two XC functionals. BLYP shows increase in S-O_w distance with temperature whereas r2SCAN shows and initial increase from ambient to 473 K followed by decrease at 673 K. Hydration water molecules and size of the hydration shell increase with increasing temperature for both the functionals. At ambient conditions, an overstructured hydration shell indicated by the high second maximum and low second minimum (Figure 3.3) is observed with BLYP functional.

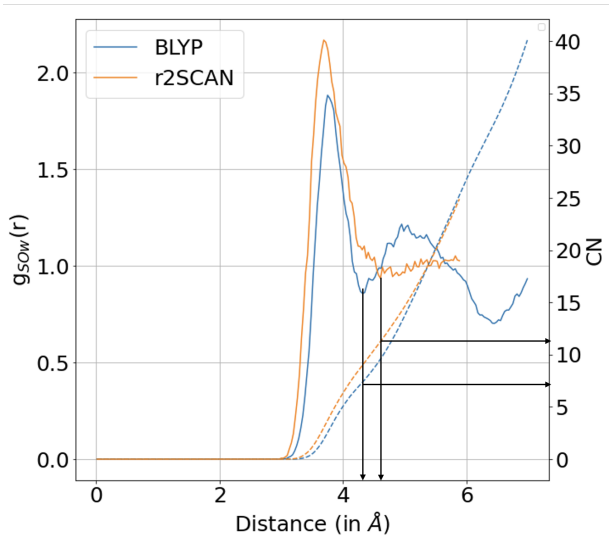

Figure 3.3: Pair correlation functions $g_{SOw}(r)$ and CN for aqueous H_2SO_4 solution at ambient conditions. Solid lines represent $g_{ij}(r)$ whereas dashed lines are used to plot CN. Vertical arrows are dropped at the first minimum of $g_{SOw}(r)$ and the corresponding CNs are marked by the horizontal arrows

Table 3.2: Nearest neighbour distances and coordination numbers obtained from simulations at different conditions. HF: Hartree-Fock, XRD: X-Ray Diffraction

Temperature	System	XC functional	Species	First maximum (in Å)	First minimum (in Å)	CN	Second maximum (in Å)	Second minimum (in Å)	CN	Third maximum (in Å)
Ambient	Aq. H_2SO_4	BLYP	S-O_w	3.74	4.31	7.0	5.00	6.45	32.0	-
		r2SCAN	S-O_w	3.67	4.67	12.0	-	-	-	-
		Hybrid-GGA [147]	S-O_w	3.76	-	10.0	-	-	-	-
		HF [148]	S-O_w	-	-	8.0	-	-	-	-
	Aq. Na_2SO_4	BLYP	S-O_w	3.67	4.40	10.0	4.90	5.56	21.0	-
		r2SCAN	S-O_w	3.71	4.71	13.0	-	-	-	-
		HF [156]	S-O_w	3.84	-	11.0	-	-	-	-
		CMD [154]	S-O_w	3.56	-	13.0	-	-	-	-
		XRD [168]	S-O_w	3.67-3.89	-	7.0-12.0	-	-	-	-
		BLYP	S-Na	3.11	4.40	2.5	4.97	6.00	3.0	-
		r2SCAN	S-Na	3.05	3.17	0.3	3.50	4.40	2.0	-
473 K	Aq. H_2SO_4	BLYP	S-O_w	3.79	4.94	15.0	-	-	-	-
		r2SCAN	S-O_w	3.77	4.95	14.0	-	-	-	-
	Aq. Na_2SO_4	BLYP	S-O_w	3.70	4.63	12.0	-	-	-	-
		r2SCAN	S-O_w	3.75	4.60	12.0	-	-	-	-
		BLYP	S-Na	3.21	3.31	0.3	3.43	4.40	1.0	6.0
		r2SCAN	S-Na	3.00	3.21	0.3	3.40	4.40	1.0	-
673 K	Aq. H_2SO_4	BLYP	S-O_w	3.84	5.29	19.0	-	-	-	-
		r2SCAN	S-O_w	3.76	5.29	18.0	-	-	-	-
	Aq. Na_2SO_4	BLYP	S-O_w	3.75	4.95	15.0	-	-	-	-
		r2SCAN	S-O_w	3.68	5.00	15.0	-	-	-	-
		BLYP	S-Na	3.15	3.35	0.5	3.45	4.08	1.0	-
		r2SCAN	S-Na	3.09	3.51	0.5	3.61	4.12	1.0	-

3.3.1.2 Aqueous Na_2SO_4 solution

Pair correlation functions $g_{SO_w}(r)$, $g_{SNa}(r)$ at ambient conditions are shown in Figure 3.4 for both functionals. Plots for higher temperatures are shown in Figure A5. Data for all temperatures are listed in Table 3.2.

From Table 3.2, it can be seen that BLYP predicts increase in S-O_w distances from ambient to supercritical temperatures whereas r2SCAN predicts an initial increase in distance from ambient to 473 K followed by decrease at 673 K. Similar to aqueous H_2SO_4 solution, r2SCAN shows larger hydration shell thereby accommodating more water molecules at ambient conditions (∼13 for r2SCAN vs ∼10 for BLYP). At elevated temperatures hydration shell sizes and water molecules are similar for the two XC functionals. BLYP envisages increase in hydration water molecules with temperature whereas r2SCAN predicts decrease at 473 K followed by increase at 673 K. Further, BLYP shows a second hydration shell characterized by prominent second maximum and minimum at ambient conditions (Figure 3.4 (left)).

Figure 3.4 (right) illustrates $g_{SNa}(r)$ for the two functionals at ambient conditions. Pair correlation functions from higher temperature simulations are shown in Figure A5. $g_{SNa}(r)$ shows several peaks, particularly at elevated temperatures for both the XC functionals. Both the functionals predict S-Na CN ∼2 at ambient conditions. For identification of ligands (discussed in detail later), these peaks are divided into 2 groups - peaks at distances $<$ ∼3.20 Å, peaks at distances $>$ ∼3.20 Å and $<$ ∼4.00 Å. BLYP simulations at ambient conditions show one sharp distinct peak at ∼3.11 Å and several shoulders at distances between ∼3.20 Å and ∼4.00 Å. Both BLYP and r2SCAN predict decreasing coordination numbers with temperature. Notably, both functionals also show a prominent third peak at ∼5 Å, particularly at ambient conditions and at 473 K.

At 473 K and 673 K, S-Na coordination numbers of ∼1 is observed with both BLYP and r2SCAN functionals. Since BLYP simulations have two sulfate ions, this can mean both the sulfate ions may exist as $NaSO_4^-$ species, or one of them is Na_2SO_4 while the other one is an uncomplexed SO_4^{2-} ion. To resolve this, pair correlation functions $g_{S_iNa}(r)$ $(i = 1, 2)$ are calculated where S_is are the sulfur atoms of the two sulfate ions. The results are shown in Figures A6, A7. At 473 K, distinct peak at ∼3.20 Å indicates one of the sulfate ions exist as $NaSO_4^-$ species whereas the other one is an uncomplexed SO_4^{2-} ion. However, at 673 K both the ions exist as $NaSO_4^-$ species. Snapshots of these complexes are shown in Figures A6, A7. Similar analysis at ambient conditions reveals the formation of Na_2SO_4 species for

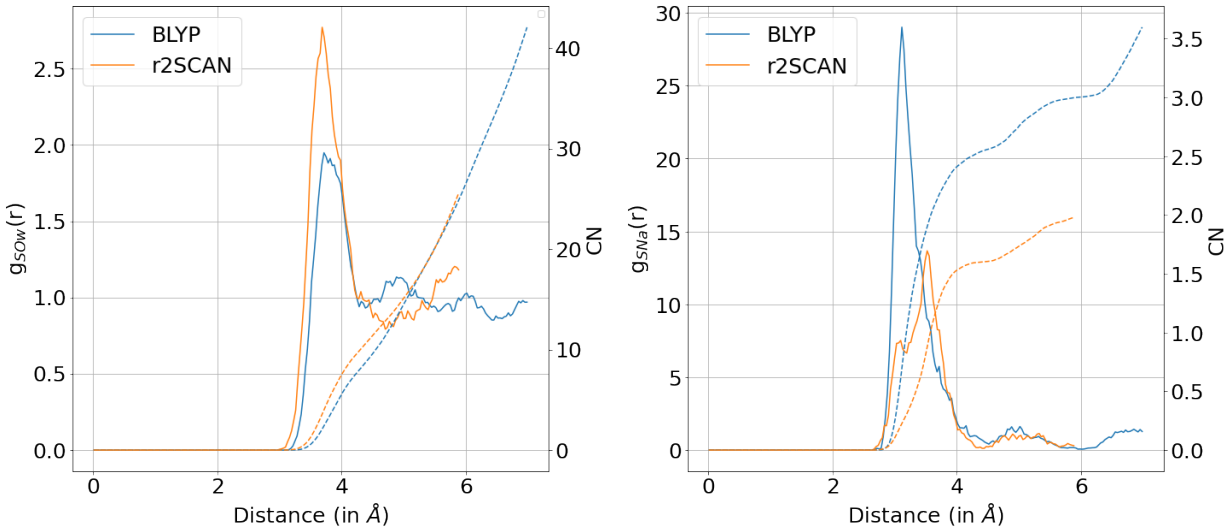

Figure 3.4: Pair correlation functions $g_{SOw}(r)$ (left), $g_{SNa}(r)$ (right) with CN for aqueous Na_2SO_4 solution at ambient conditions. Solid lines represent $g_{ij}(r)$ whereas dashed lines are used to plot CN

both the functionals.

3.3.1.3 Hydrogen bond analysis

Figure 3.5 shows a snapshot of the first hydration shell of bisulfate from aqueous H_2SO_4 system. H-bonds with three different donor-acceptor pairs were seen in the system:

- O_w-H_w—O_b
- O_b-H_b—O_w (only in bisulfate and undissociated sulphuric acid)
- O_b-H_b—O_b (only in box 1 where the two Ob's belong to different bisulfate molecules)

For aqueous Na_2SO_4 system, H-bonds only between donor O_w and acceptor O_b were considered.

H-bonds were identified using simple geometric H-bond criteria [169] where a pair of O atoms is considered H-bonded when $r_{OO} < 3.5$ Å and $\phi_{OHO} > 120°$, where r_{OO} is the interatomic distance and ϕ_{OHO} is the donor-H-acceptor angle. These criteria have been shown to give accurate results for several aqueous systems from ambient to supercritical conditions [169, 170, 171, 172, 72].

Table 3.3: Number of H-bonds

System	XC functional	Sulfate (acceptor)	Bisulfate (acceptor)	Bisulfate (donor)	Acid (acceptor)	Acid (donor)
Aq. H_2SO_4	BLYP	10.29	7.12	1.05	4.13	2.12
	r2SCAN	11.32	8.22	1.01	-	-
CMD [146]		9.5	5.5	-	-	-
Experiment [173]		12	-	-	-	-
Aq. Na_2SO_4	BLYP	7.05	-	-	-	-
	r2SCAN	10.43	-	-	-	-

The average number of H-bonds for sulfate species obtained using different XC functionals in aqueous H_2SO_4 and aqueous Na_2SO_4 systems at ambient conditions are shown in Table 3.3.

r2SCAN predicts higher number of H-bonds for both HSO_4^- and SO_4^{2-} ions in aqueous H_2SO_4 and Na_2SO_4 systems. This difference may be due to differences in simulation temperatures of the XC functional. Lower number of H-bonds are obtained for sulfate tetrahedra in Na_2SO_4 system as compared to H_2SO_4 system with both BLYP and r2SCAN functionals.

Previous experiments show a 12 H-bonds coordinated sulfate ion in aqueous solution containing Fe^{3+} at ambient conditions [173]. Canales et al. [146] have studied aqueous H_2SO_4 system with CMD. They predict ~9.5 H-bonds for SO_4^{2-} ion and ~5.5 H-bonds for HSO_4^- ion. However, it seems that only acceptor H-bonds are calculated for HSO_4^- ion. Calculated number of H-bonds in HSO_4^- ion is higher for both the XC functionals as compared to CMD [146].

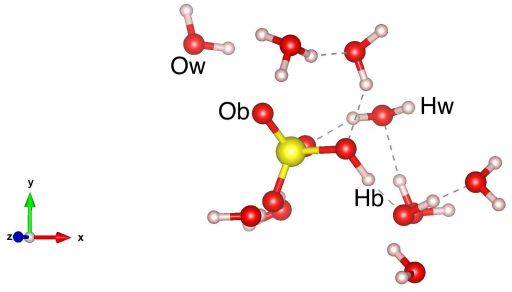

Figure 3.5: First hydration shell of bisulfate ion (O_w-oxygen atom of water molecule, H_w-hydrogen atom bonded to O_w, O_b-oxygen atom bonded to sulfur, H_b-hydrogen atom bonded to O_b)

3.3.2 Vibrational Spectra

3.3.2.1 Aqueous H_2SO_4 solution

In dilute aqueous solutions SO_4^{2-} occurs primarily as a tetrahedral species with T_d symmetry. The undistorted T_d geometry has 9 modes of 4 fundamental internal vibrations with the following representation (Equation 3.9). All the modes are Raman active [162].

$$\Gamma = a_1(\upsilon_1) + e(\upsilon_2) + 2f_2(\upsilon_3 + \upsilon_4) \tag{3.9}$$

In the presence of the hydrogen in HSO_4^-, the tetrahedral symmetry is broken resulting in $C_{3\upsilon}$ anionic centre. This symmetry group shows 9 modes in 6 fundamental internal vibrations with the following representation (Equation 3.10). All the modes are Raman active [174].

$$\Gamma = 3a_1(\upsilon_1 + \upsilon_3 + \upsilon_4) + 3e(\upsilon_2 + \upsilon_3 + \upsilon_4) \tag{3.10}$$

In this paper we calculate the wavenumbers of symmetric stretch ($\upsilon_1(a_1)$), doubly degenerate antisymmetric stretch ($\upsilon_3(e)$), S-OH stretch ($\upsilon_4(a_1)$) of HSO_4^- ions and symmetric stretch ($\upsilon_1(a_1)$), triply degenerate antisymmetric stretch ($\upsilon_3(f_2)$) of SO_4^{2-} ions. For notational simplicity we drop the degeneracy term in the remaining paper and name the modes as $\upsilon_{1/3/4}$ followed by the ion type. The wavenumbers of these modes obtained with different XC functionals for all the systems studied are listed in Table 3.4. The spectra obtained with r2SCAN functional for aqueous H_2SO_4 solution are shown in Figure 3.6. Spectra obtained with BLYP are shown in Figure A8.

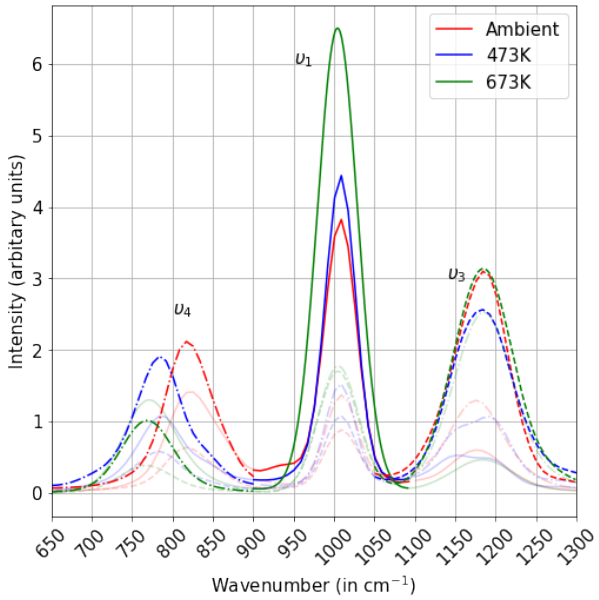

Figure 3.6: QNMs of HSO_4^- ions from r2SCAN in aqueous H_2SO_4 solution at different studied temperatures. υ_1: solid lines, υ_3: dashed lines, υ_4: dashed-dotted lines

Table 3.4: Wavenumbers (in cm^{-1}) of QNMs at different conditions. Ranges of experimental and computational data at ambient conditions are from Tables A1, A2. MP: Møller–Plesset

Temperature	System	XC functional	υ_1 bisulfate	υ_3 bisulfate	υ_4 bisulfate	υ_1 sulfate	υ_3 sulfate
Ambient	Aq. H_2SO_4	BLYP	955	1096	790	-	-
		r2SCAN	1010	1184	815	-	-
		MP2 level	1043-1052	1147-1195	752-910	-	-
		HF level (gas phase)	1037	-	770-850	-	-
		HF level (bulk phase)	1028	1175	867	-	-
		Experiment	1035-1052	1165-1230	876-905	977-983	1098-1110
	Aq. Na_2SO_4	BLYP	-	-	-	880	1028
		r2SCAN	-	-	-	930	1077
		Hybrid GGA (PBE0)	-	-	-	961-991	1111
		HF level (gas phase)	-	-	-	930	1019-1110
		HF level (bulk phase)	-	-	-	968	1118
		Experiment	-	-	-	980.5-981.3	1104
473 K	Aq. H_2SO_4	BLYP	954.5	1117	753	-	-
		r2SCAN	1007	1181	782	-	-
		Experiment [131]	1042	1146	863	-	-
	Aq. Na_2SO_4	BLYP	-	-	-	873	1019
		r2SCAN	-	-	-	925	1066
		Experiment [130, 175]	-	-	-	975-981	-
673 K	Aq. H_2SO_4	BLYP	952	1127	732	-	-
		r2SCAN	1001	1182	765	-	-
		Experiment [131]	1047	1150	∼835 (broad)	-	-
	Aq. Na_2SO_4	BLYP	-	-	-	870	1007
		r2SCAN	-	-	-	919	1063
		Experiment[130]	-	-	-	978	-

Mode projection analysis is used to assign peaks to respective vibrational modes of HSO_4^- ion which has the highest abundance at these conditions. Both the functionals predict 3 distinct vibrational modes at all conditions in agreement to experimental data [131]. Wavenumbers determined with r2SCAN are higher for all the 3 vibrational modes of HSO_4^- ion as compared to BLYP, at all conditions. Further, υ_1 and υ_4 modes show redshifts with temperature, for both the functionals. The υ_4 mode shows a much stronger temperature dependence as compared to the υ_1 mode. While υ_3 mode predicted by r2SCAN remains roughly constant for r2SCAN simulations, it shows a prominent blueshift for BLYP simulations.

3.3.2.2 Aqueous Na_2SO_4 solution

Vibrational spectra of sulfate ions calculated from trajectories obtained from aqueous Na_2SO_4 simulations for BLYP and r2SCAN functionals are listed in Table 3.4. The spectra obtained with r2SCAN functional are shown in Figure 3.7. Spectra obtained with BLYP functional are shown in Figure A9.

Both the functionals predict 2 distinct stretching modes of SO_4^{2-} ions which has highest abundance at all the studied conditions. As in case of aqueous H_2SO_4 solutions, r2SCAN envisages higher wavenumbers than BLYP for both υ_1 and υ_3 modes. Both the functionals show redshift of the modes with temperature.

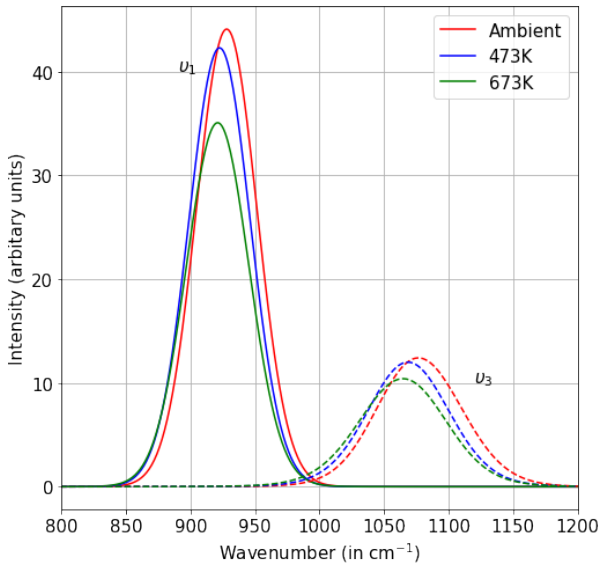

Figure 3.7: QNMs of SO_4^{2-} ions from r2SCAN in aqueous Na_2SO_4 solution at different studied temperatures. υ_1 modes are shown with solid lines whereas the υ_3 modes are shown with dashed lines

3.4 Discussion

3.4.1 Speciation and structure

In order to classify species as sulfate, bisulfate or sulfuric acid, each H atom is attached to its nearest oxygen atom. Sulfuric acid follows a two step dissociation process in aqueous solutions.

$$H_2SO_4 \longrightarrow HSO_4^- + H^+ \tag{3.11}$$

$$HSO_4^- \rightleftharpoons SO_4^{2-} + H^+ \tag{3.12}$$

While the first dissociation reaction is almost complete, equilibrium is established between sulfate and bisulfate at ambient conditions. All the functionals predict negligible amounts of undissociated acid. This is consistent with previous experimental and computational work which obtain undissociated acid only at concentrations higher than 80 wt % [174, 122, 147]. Simulations also predict that bisulfate is the dominant species for both the XC functionals and the dissociation from bisulfate to sulfate is negligible (∼3,% for both BLYP, r2SCAN). The time-averaged mole fraction of different species with the two XC functionals are shown in Table A3. The time averaged mole fraction of undissociated H_2SO_4 increases with increase in temperature for both the XC functionals, consistent with experimental studies [131] as shown in Figure 3.8 (for exact numerical data see Table A3. Convergence plots are shown in Figures A1, A2, A3). However, bisulfate remains the most abundant species at high temperature in agreement with experimental studies with same sulfuric acid concentration [131] (Table A3). Due to high viscosity of water at ambient conditions, dynamics of the system is sluggish [176, 149]. Therefore, we cannot guarantee that equilibrium has been reached in our simulations. The mole fraction numbers should hence be taken for qualitative understanding only.

Na_2SO_4 solutions do not exhibit proton exchange reactions throughout the simulation time. Hence, sulfate is the most abundant species for both BLYP and r2SCAN functionals at ambient conditions as well as higher temperatures.

As shown in Table 3.2 in r2SCAN predicts a larger hydration shell with higher coordi-

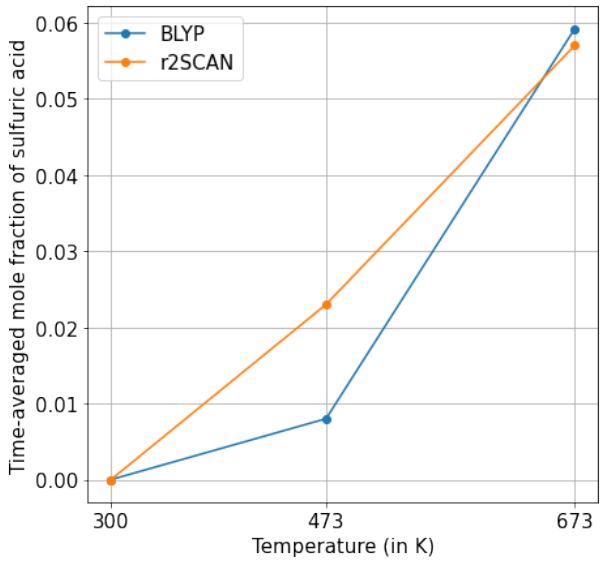

Figure 3.8: Time-averaged mole fraction of undissociated sulfuric acid with temperature

nation number as compared to BLYP, at ambient conditions. Similar to simulations with pure water [87], BLYP shows an overstructured hydration shell. This generally happens because dispersion forces are completely absent in the BLYP functional. Previous studies have concluded that the lack of dispersion forces results in high repulsive forces leading to positive interaction energies in rare gas and hydrogen dimers [87, 177, 178, 179]. The presence of high second maximum and minimum (Figure 3.3) indicates that the interactions between S and O_w are long-ranged and are significant even beyond 7 Å. This long ranged nature of the S-O_w interactions result in lower first maximum in case of BLYP as compared to r2SCAN (Figure 3.3). Using meta-GGA functionals softens the hydration shell resulting in higher coordination numbers. Also, complexation by Na^+ cations significantly reduces this effect as observed in case of aqueous Na_2SO_4 solutions (Figure 3.4 (left)). However, we cannot comment on possible reasons for this behaviour as this would require extensive investigation of interaction energy of various clusters in aqueous H_2SO_4 and Na_2SO_4 solutions. At elevated temperatures, overstructuring of hydration shell is no longer observed leading to better agreement between BLYP and r2SCAN S-O_w pair correlation functions for both aqueous H_2SO_4, Na_2SO_4 solutions (Figures A4, A5).

Previous studies of aqueous H_2SO_4 solution at ambient conditions with hybrid-GGA functionals predict ∼10 hydration water molecules [147]. S-O_w distance obtained from BLYP functional is closer to prediction of more sophisticated hybrid-GGA functionals.

A geometric criterion based on ionic distances [180] was used to resolve the origin of

the peaks in $g_{SNa}(r)$ shown in Figure 3.4 and Figure A5. For a monodentate ligand where S and Na are separated by a bridging O_b atom, $r_{Na-S} \approx r_{Na-O} + r_{S-O}$, whereas for a bidentate ligand, where Na is complexed to two O_b atoms, $r_{NaS} < r_{NaO_b} + r_{SO_b}$ (where r_{ij} is the distance between atom i, j). For this analysis r_{SO_b} was taken as 1.40 Å whereas r_{NaO_b} was taken as 2.30 Å (first maximum of $g_{NaO_b}(r)$). The peaks at distances < 3.20 Å, are accordingly assigned to bidentate ligands whereas those at distance ≈ 3.50 Å are assigned to monodentate ligands. The heights of the peaks in the pair correlation functions indicate the relative population of these two different ion pairs. Snapshots of monodentate and bidentate ion pairs are shown in Figure A10.

As shown in Table 3.2, BLYP, r2SCAN, HF predict S-O_w distances within the range of XRD data at ambient conditions. Hydration water molecules is within the experimental range for both the functionals. However, this comparison is not straightforward due to difficulties in defining clear minima in the anion-water correlation functions. Wan et al. [181] predicts hydration numbers of 12-13 for sulfate ion at low temperature, in agreement to r2SCAN. CMD studies of aqueous Na_2SO_4 solutions at similar conditions underestimate S-O_w distance. Studies with polarizable and non-polarizable classical forcefields also show several distinct peaks in $g_{SNa}(r)$ function [155], in agreement to our results. Vchirawongkwin et al. [156] predicts an overstructured hydration shell of sulfate ion in water with HF level of theory. DFT simulations with the BLYP functional reduces the overstructuring indicated by shorter second maximum and shallower second minimum (Figure 3.4). However, it is not possible to comment whether this difference is due to the underlying level of theory used or due to the absence of counterions in Vchirawongkwin et al [156].

3.4.2 Vibrational spectra

The temperature variations of the different modes for both the systems are shown in Figure 3.9. The lower wavenumbers predicted by BLYP functional is because of the longer S-O_b bond lengths and hence weaker bonds predicted by BLYP as compared to r2SCAN for both the systems. This is shown in Figure 3.10. Such correlation of bond length and vibrational frequencies has also been shown in sulfur bearing systems at high temperature by Schmidt and Jahn [90].

For aqueous H_2SO_4 system, both BLYP and r2SCAN underestimate the frequencies of the υ_4 mode as compared to experimental data, at all studied temperatures. However, as listed in

Table 3.4, the underestimation is lower for r2SCAN (∼75 wavenumbers) than BLYP (∼100 wavenumbers). Previous computational studies on hydrated gas phase HSO_4^- ions with MP2 level of theory [150] show wide range for the υ_4 mode (Table 3.4) that encompasses the experimental range thereby giving better estimation of this mode. However, this comparison is not straightforward as the computations have been done on isolated gas phase complexes with harmonic approximation. Prediction of HF level of theory are higher and closer to experiments than DFT (for both gas phase as well as bulk phase). This is because of lower S-O_bH bond lengths predicted by HF (∼1.58 Å [148] from HF vs ∼1.61 Å from DFT). Table 3.5 compares the rate of decrease of frequency of υ_4 mode with temperature. Rate of decrease of frequency predicted by r2SCAN is closer to experimental data than BLYP. It should be noted that we do not consider Nuclear Quantum Effects (NQEs) in this study. Inclusion of NQEs have been shown to produce significant red shift of the O-D stretching mode in water [139]. Although the blueshift from BLYP to r2SCAN is an improvement, inclusion of NQEs may lead to red shift of this mode.

Both BLYP and r2SCAN underestimate the υ_1 mode in aqueous H_2SO_4 system as compared to experiments, at all the studied temperatures. However, BLYP underestimates the wavenumber by ∼ 90 wavenumbers whereas for r2SCAN the difference is ∼ 35 wavenumbers. Shorter S-O_b bond lengths (∼1.45 Å [148] from HF vs ∼1.49 Å from DFT) lead to data from HF level of theory being closer to experimental data than BLYP and r2SCAN at ambient conditions. υ_1 mode calculated at ∼500 K with PBE GGA functional in Jahn and Schmidt [89] in aqueous $MgSO_4$ system (∼ 900 cm^{-1}) also shows underestimation due to longer bonds.

BLYP also underestimates the υ_3 mode by ∼ 100 wavenumbers at ambient conditions and ∼ 30 wavenumbers at elevated temperatures, in aqueous H_2SO_4 system. Underestimation of υ_3 mode has also been reported in Jahn and Schmidt [89] with PBE GGA functional. Predictions of r2SCAN are within the experimental range for υ_3 mode at ambient conditions. Predictions of υ_3 by r2SCAN is as good as MP2 or HF levels of theory. At elevated temperatures, r2SCAN shows an overestimation of ∼ 30 wavenumbers for the υ_3 mode. Overall, r2SCAN provides better estimation of the vibrational modes of HSO_4^- ion when compared against available experimental data at ambient conditions as well as elevated temperatures (Tables 3.4).

The υ_4 mode of bisulfate ion is of particular interest as it shows a distinct temperature dependence [182]. Also, the frequent exchange of the H atom between solute and solvent

makes it a probe for solute-solvent interactions.

A qualitative understanding of the strength of H-bonds can be obtained by calculating the continuous survival probability as:

$$S(\tau) = \left\langle \frac{h_{ij}(t)h_{ij}(t+\tau)}{h_{ij}(t)} \right\rangle \tag{3.13}$$

where $h_{ij}(t)$ is the H-bond population operator which is 1 when there is a H-bond between species i, j and otherwise 0. $h_{ij}(t+\tau)$ is 1 when a H-bond at time t survives continuously till time $t+\tau$ and otherwise 0. The angular brackets represent an average over all time origins. Both BLYP and r2SCAN predict decrease in frequency of this mode with temperature, consistent with experiments [182]. Figure 3.11 (left) shows that the strength of the S-O_b-H_b—O_wH bonds involving this H atom decrease with increasing temperature for both the functionals. As discussed in Walrafen et al. [182], reduction in strength of the H-bonds with temperature, allows the proton to stretch further thereby weakening the S-OH bond. This is also indicated by the lengthening of the S-OH bond length with temperature as shown in Figure 3.10 (left). This results in redshift of the υ_4 mode with temperature. However, neither BLYP nor r2SCAN can reproduce the increase in frequency of υ_1 mode with temperature [182].

In case of aqueous Na_2SO_4 systems, both BLYP and r2SCAN underestimate the symmetric and asymmetric stretching modes of SO_4^{2-} tetrahedra at all temperatures. However, as evident from Table 3.4, the underestimation for r2SCAN is lower than BLYP. For the υ_1 mode underestimation is ∼100 wavemnumbers for BLYP functional vs ∼50 wavenumbers for r2SCAN functional. For the υ_3 mode underestimation is ∼80 wavemnumbers for BLYP functional vs ∼30 wavenumbers for r2SCAN functional. As in aqueous H_2SO_4 system, frequencies from aqueous sulfate solutions with HF level of theory are closer to experimental data at ambient conditions due to shorter bond lengths predicted by HF as shown in Figure 3.10 (right) (∼1.47 Å [162] from HF vs ∼1.50 Å from DFT). Underestimation of the υ_1 mode of SO_4^{2-} tetrahedra by PBE GGA functional is also seen in aqueous $MgSO_4$ solutions at high temperature ($\sim 900\,\mathrm{cm}^{-1}$) [89]. Both r2SCAN and BLYP reproduce the decreasing frequency of symmetric stretch with temperature, in agreement with experimental data from Schmidt [130], shown in Figure 3.9. This behavior may be due to the decreasing strength of S-O_b—H_w-O_wH bonds with increasing temperature as shown in Figure 3.11 (right). It is interesting to note that the υ_1 mode in aqueous H_2SO_4 solutions [182] shows blueshift with

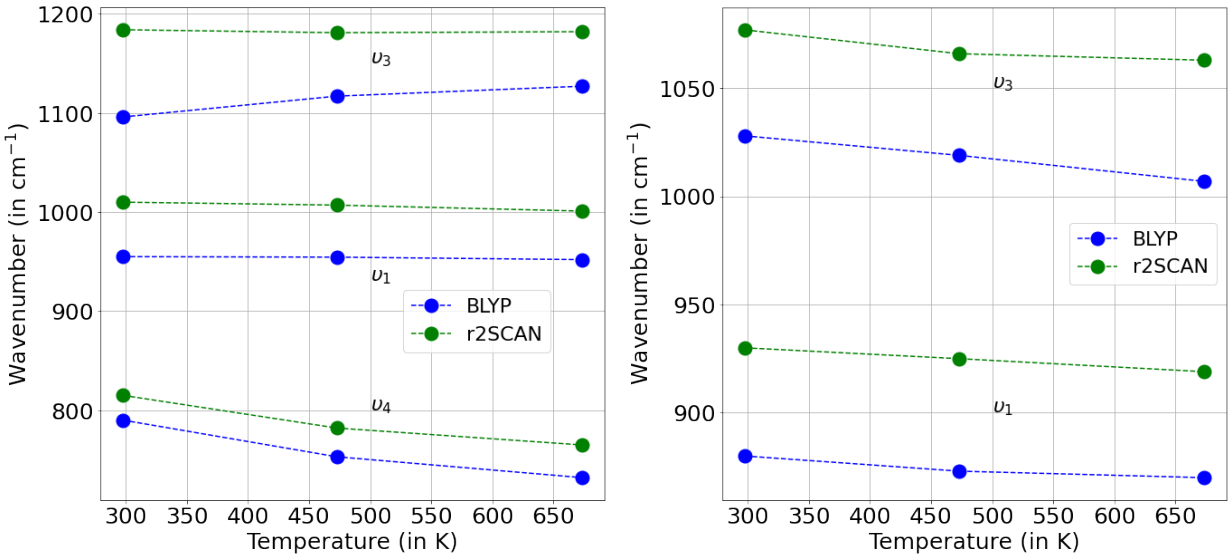

Figure 3.9: Wavenumbers of different vibrational modes obtained from aqueous H_2SO_4 solutions (left) and aqueous Na_2SO_4 solutions (right)

Table 3.5: Rate of decrease of frequency of υ_4 mode of HSO_4^- ion from different XC functionals and experiment

XC functional	Rate (in cm^{-1}/K)
BLYP	-0.161
r2SCAN	-0.141
Experiment [131]	-0.145

temperature whereas the υ_1 mode in aqueous Na_2SO_4 shows redshift with increasing temperature [130]. Table 3.4 shows that more sophisticated hybrid GGA functionals like PBE0 give more accurate vibrational spectrum of bulk phase SO_4^{2-} tetrahedra at ambient conditions. However, as shown in Table 3.6, PBE0 predicts the sharpest decrease in frequency of υ_1 mode of SO_4^{2-} tetrahedra as compared to experimental data [130] and other XC functionals. The rate predicted by BLYP is closest to experimental data among all the XC functionals considered.

As discussed in the results section, at 473 K, the two sulfate tetrahedra exist as $NaSO_4^-$ and SO_4^{2-} ions. As a result the tetrahedra show characteristic bands in the spectra as shown in Figure A11. Cation complexation leads to a blueshift of the υ_3 by ∼15 wavenumbers due to the polarizing power of the cations. This is in contrast to experiments conducted by Daly et al. [183] where it is shown that the presence of Na^+ cations does not produce shifts in the spectrum of unassociated sulfate tetrahedra. Previous experiments with aqueous $MgSO_4$

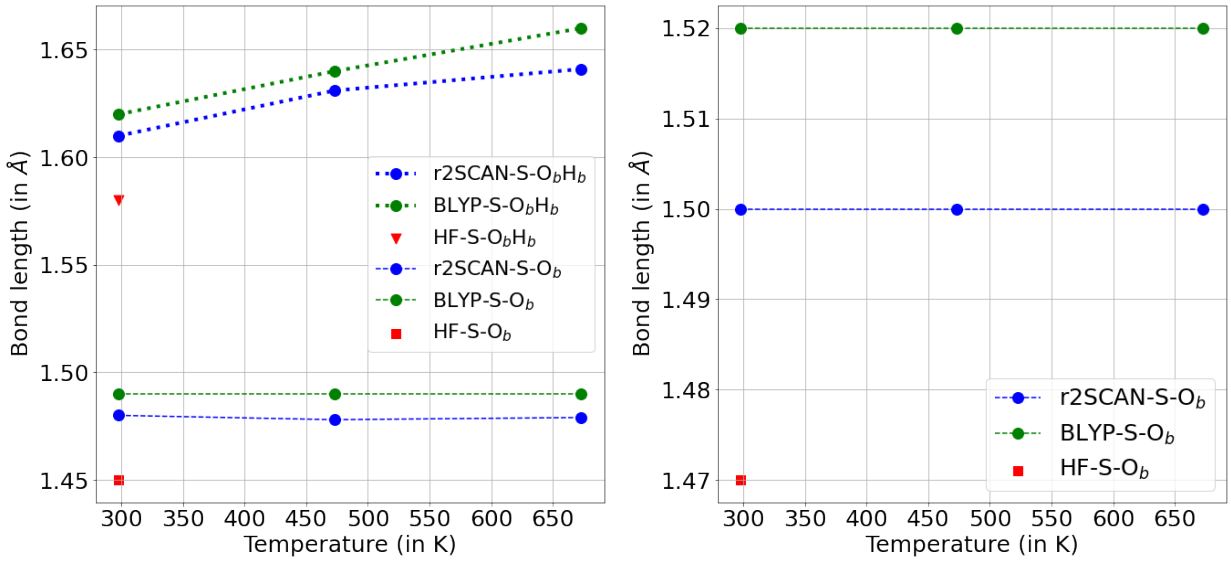

Figure 3.10: S-O_b bond lengths in aqueous H_2SO_4 solutions (left) and aqueous Na_2SO_4 solutions (right) from the two XC functionals and HF level of theory [162, 148]

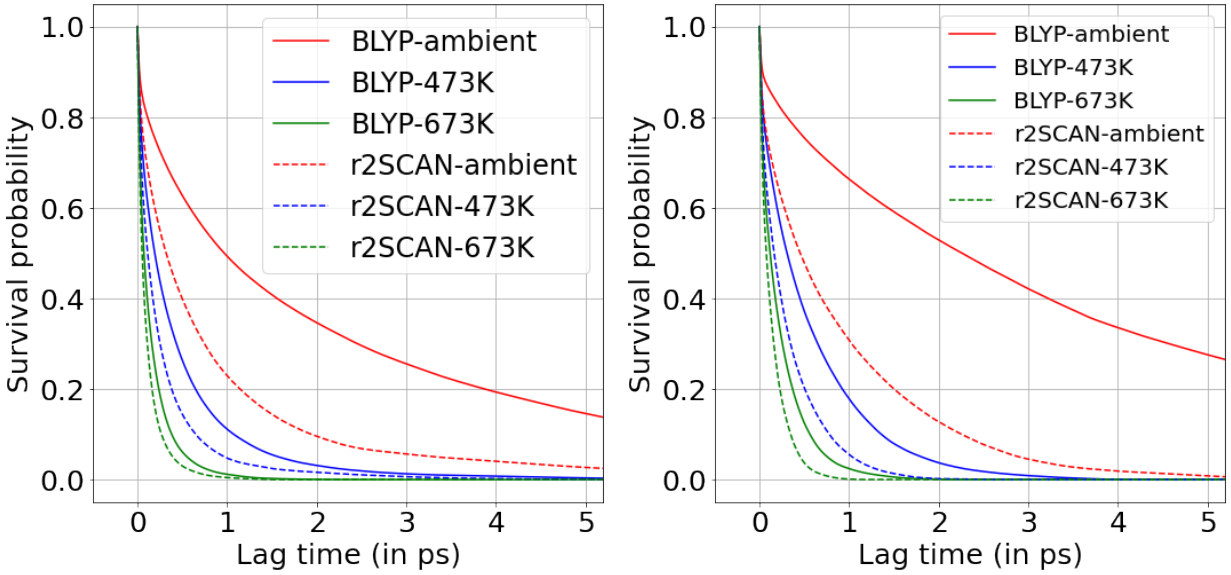

Figure 3.11: Survival probability of H-bonds with different XC functionals at different conditions in aqueous H_2SO_4 solutions (left) and aqueous Na_2SO_4 solutions (right)

Table 3.6: Rate of decrease of frequency of υ_1 mode of SO_4^{2-} tetrahedra from different XC functionals and experiment

XC functional	Rate (in cm^{-1}/K)
BLYP	-0.025
r2SCAN	-0.032
PBE0 [163]	-0.037
Experiment[130]	-0.015

solutions predict a blueshift of υ_1 mode by $\sim$12 wavenumbers due to ion pair formation [184, 126].

3.5 Conclusions

In this paper we have carried out AIMD simulations with aqueous H_2SO_4 and Na_2SO_4 systems. The systems were studied with 2 different XC functionals (BLYP (GGA) and r2SCAN (meta-GGA)) at 3 different temperatures (ambient, 473 K and 673 K). Structural and vibrational properties of sulfur bearing species were determined and compared against experimental data.

A disagreement in the $g_{SOw}(r)$'s from the two functionals was observed at ambient conditions for both the systems. However, at higher temperatures both BLYP and r2SCAN predict similar $g_{SOw}(r)$ and hence similar neighbour distances and CNs. Both the functionals also predict the presence of bidentate as well as monodentate ion pairs in aqueous Na_2SO_4 solutions at all conditions.

Both the functionals underestimate the frequencies of all the studied vibrational modes (except υ_3 in aqueous H_2SO_4 solutions) at all temperature points. However, the underestimation is lower for r2SCAN at subcritical as well as supercritical conditions due to shorter bond lengths, leading to better agreement with experimental data. Both functionals reproduce the decreasing frequency of υ_4 mode in aqueous H_2SO_4 and υ_1 mode in aqueous Na_2SO_4, with temperature. Interestingly, BLYP gives better estimate of the rate of decrease of frequency of υ_1 mode in aqueous Na_2SO_4 system as compared to r2SCAN and PBE0. Also, scaled vibrational frequencies from HF level of theory are in better agreement with experimental data at ambient conditions.

Overall, structural predictions of BLYP are as good as r2SCAN, particularly at higher temperatures at much lower computational costs. Using r2SCAN gives better estimates of

the different vibrational modes as compared to BLYP but they are still underestimated in comparison to experimental data. Both the functionals reproduce the temperature-induced shifts in different vibrational modes.

Chapter 4

Electrical conductivity of NaCl solutions at supercritical conditions - Insights from molecular dynamics simulations

4.1 Introduction

Aqueous fluids play an important role in characterizing the thermophysical properties of several subsurface geochemical systems. Regions of anomalously high electrical conductivity have been reported in the lower crust and in the arc and subduction zone settings [185, 186, 187, 188]. Several systems have been studied to explain the occurrence of these zones, including but not limited to minerals [189, 190], partial melts [191, 192], and saline fluids [193, 194, 195, 196]. However, most of these zones represent contributions from all these systems, with aqueous fluids playing a dominant role, especially in subduction zones [186, 190]. Pure water has relatively low electrical conductivity [197, 198]. Dissolved salts enhance the conductivity of these fluids in conditions of the lower crust and upper mantle. Fluid inclusion studies from subduction zones suggest that NaCl is the dominant solute under these conditions [199]. In addition to this, hydrothermal fluids containing dissolved carbonate, sulfate, or chloride salts of Na^+ along with smaller amounts of K^+, Ca^{2+}, Ba^{2+} and Mg^{2+} facilitate cooling and melt-

ing in subduction zones that lead to the formation of new continental crust [200]. Several magnetotelluric surveys [36, 201] have been conducted to understand the nature of aqueous fluids in high temperature and high pressure geologic environments. However, interpretation of these data is difficult because of the lack of electrical conductivity data for such fluids.

The electrical conductivity of NaCl solutions is a complex function of temperature, pressure and concentration. Over the years, determination of electrical conductivity of NaCl solutions at supercritical conditions has been the aim of several experimental studies [202, 203, 204, 205, 206, 207] because of the importance of this chemical system across various scientific and engineering domains. Measurements of electrical conductivity along isobars ranging from 0.025 GPa-1 GPa show an initial increase up to about 400°C followed by a decrease [202, 203, 204, 205]. When measured along isotherms, conductivity increases rapidly with an increase in pressure at low fluid densities (<0.5-0.6 g/cm^3) [203, 206, 207]. The rate of increase gradually reduces with density [206, 207] and eventually a decrease in conductivity is observed starting at a fluid density of about 0.8 g/cm^3 [203]. The density at which this conductivity maximum is observed depends on the concentration of the NaCl solution [203, 204]. Guo and Keppler [208] extended the ranges of temperature and pressure to 900°C, 5 GPa respectively and also observed a non monotonic pressure dependence of electrical conductivity at these conditions. Quist and Marshall [203] qualitatively explained these behaviour using density and ion pair effects [203] whereas Lee et al. [209] attributed these to residence times of water molecules in hydration shell in supercritical fluids. Infact, the influence of ion association is particularly dominant at high temperatures because of the extremely low dielectric constant of water [205].

MD simulations help us explain experimental observations from an atomistic scale. MD simulations allow explicit treatment of ions and water molecules helping us understand the mechanism of electrical conduction at a nanoscale. CMD simulations with pairwise interaction potentials have been successfully used to study several properties of electrolytes under conditions difficult to simulate in laboratories. For example, self-diffusion coefficients of Na^+ and Cl^- ions have been calculated in a range of conditions starting from room temperature to supercritical conditions [210, 209], NaCl ion association in supercritical brines [64], electrical conductivity in a wide range of conditions [209, 211, 212, 213, 214, 215, 216]. The most popularly used water model called the SPC/E model is extremely successful in reproducing bulk properties of pure water [63]. However, a systematic underestimation of

electrical conductivity in ambient conditions [217] is observed with these simple potentials. Pairwise interaction potentials are also limited by their inability to represent bonded interactions in the limit of dissociation, thereby failing to model reactive systems involving extensive formation and breakage of chemical bonds like the Grotthuss mechanism of proton diffusion in water [218]. This is remedied by reactive forcefields like the ReaxFF [61] which are empirically fitted to model such reactive systems [62, 70, 72]. Recently, a new ReaxFF parameter set was developed by Fedkin et al. [60] for aqueous electrolytes. This potential successfully reproduced structural and transport properties of electrolytes at ambient conditions [60]. However empirical forcefields come with a caveat - systematic errors may arise if these forcefields are extrapolated to systems too far beyond what they have been fitted on. Therefore, MD simulations with such forcefields must be adequately bench marked to understand their extrapolation capabilities.

In this chapter we examine the influence of two dominant factors governing electrical conductivity at temperatures of 200°C-800°C and pressures of 1-5 GPa - ion self-diffusion and ion association. Total electrical conductivity is broken down into contributions from ion diffusion and ion association to assess the influence of each of them in determining temperature and pressure induced variations. We choose the ReaxFF and SPC/E models in our simulations to systematically investigate the role of functional complexities of underlying forcefields in electrical conductivity predictions. Electrical conductivities calculated from the two interaction models are compared against available experimental data and the models are judged based on their predictive capabilities at supercritical conditions.

4.2 Methods

4.2.1 Simulation protocol

MD simulations of ∼1.05 m aqueous NaCl solutions are performed in 3D periodically replicated simulation boxes to match concentrations used in experimental study by Guo and Keppler [208]. Two different simulation boxes are prepared as shown in Table 4.1. Box 1 is used for simulations with SPC/E model. In order to account for higher computational expense, box 2 is used for simulations with the ReaxFF model. To prepare the boxes, first a simulation box containing only water molecules is equilibrated at 298 K and 1 bar using

Table 4.1: Details of simulation boxes including solute molality and weight percent

Box no.	Contents	Molality	Weight %
1	1960 H_2O, 36 Na-Cl pairs	1.02	5.63
2	757 H_2O, 14 Na-Cl pairs	1.02	5.63
3	729 H_2O	-	-
4	2197 H_2O	-	-

Table 4.2: LJ potential parameters with partial charges

Species	ϵ_{ij} (in kJ/mol)	σ_{ij} (in Å)	q_i (in e)
Na^+	0.54431	2.350	1.0
Cl^-	0.4187	4.400	-1.0
O	0.6500	3.166	-0.8476
H	0.0	0.0	0.4238

the SPC/E model [66]. The final simulation boxes are obtained by replacing some of the water molecules with Na-Cl ion pairs resulting in box 1 containing 1960 water molecules, 36 Na-Cl pairs and box 2 containing 757 water molecules, 14 Na-Cl pairs. To calculate the static dielectric constant (ϵ) of the solvent, simulations are conducted with pure water using boxes 3 and 4 containing 729 and 2197 water molecules respectively. The interaction parameters for calculating pairwise van der Waals interactions, short range interactions and Coulomb interactions in the SPC/E model are listed in Table 4.2. The timestep for the SPC/E simulations is 0.5 fs. Since the ReaxFF is a dissociative forcefield and accounts for several intramolecular degrees of freedom, a shorter timestep of 0.25 fs is used. The simulation boxes are equilibrated for 10^6 timesteps in the NPT ensemble. Production simulations are then conducted in the NVT ensemble for 20 ns in case of the SPC/E model and for 5 ns with the ReaxFF model. Nosé–Hoover thermostat and barostat are used to control the temperature and pressure at the target values. The production simulation trajectories are used to calculate electrical conductivities, Mean Squared Displacement (MSD) and ion association. Additional production simulations are conducted in the NPT ensemble to calculate the density of NaCl solutions. All simulations were conducted with the LAMMPS simulation package [43].

4.2.2 Post-processing tools

4.2.2.1 Electrical conductivity and its decomposition

The electrical conductivity (σ) of NaCl solutions is calculated using the Green-Kubo relation [219, 220]:

$$\sigma = \frac{1}{3Vk_BT}\int_0^\infty \langle \vec{j}(0)\vec{j}(t)\rangle \, dt \tag{4.1}$$

where

$$\vec{j}(t) = \sum_i q_i \vec{v}_i \tag{4.2}$$

where $\vec{j}(t)$ is the charge current at time t, V is the volume of the simulation cell, k_B is the Boltzmann constant, T is the temperature, q_i is the partial charge and $\vec{v}_i$ is the velocity vector of ion i. The angular brackets denote ensemble average over the entire trajectory. Equation 4.1 is derived using the linear response theory and hence does not require an external electric field to be applied in the simulations.

The Green-Kubo integral in Equation 4.1 can be written as a summation of contributions from the individual ionic species I given by:

$$\sigma_I = \frac{1}{3Vk_BT}\int_0^\infty \langle \vec{j}_I(t)\vec{j}(0)\rangle \, dt \tag{4.3}$$

This can be further splitted into self and cross-correlation terms [221].

$$\sigma_I = \frac{\rho_I q_I^2 D_I}{k_BT} + \sum_L \frac{q_I q_L}{Vk_BT}\int_0^\infty C_{IL}(t)\, dt \tag{4.4}$$

where ρ_I is the number density of ion I and D_I is the self-diffusion coefficient obtained by integrating the velocity autocorrelation function of species I.

$$D_I = \frac{1}{3N_I}\int_0^\infty \left\langle \sum_{i\epsilon I} \vec{v}_i(0)\vec{v}_i(t) \right\rangle dt \tag{4.5}$$

where N_I is the number of species of type I. It has be to noted that since classical forcefields do not explicitly account for the electronic degrees of freedom, σ is approximated by ionic conductivity.

Another way to calculate the self-diffusion coefficients of ions is from MSD of ions as:

$$D_I = \frac{1}{2dN_I} \lim_{t\to\infty} \frac{\langle \sum_{i\epsilon I} |\vec{r}_i(t) - \vec{r}_i(0)|^2 \rangle}{t} \tag{4.6}$$

where d is the dimensionality of the system and $\vec{r}_i(t)$ is the position vector of the i^{th} ion of type I at time t. It has been shown previously that both of these methods yield very similar results [216]. To make credible comparisons between the two methods, we calculate the ion self-diffusion coefficients with the two methods for 1 m NaCl solution at 298 K, 1 bar. The results are very similar and are shown in Table B1 in Appendix B.

C_{IL} is the velocity cross-correlation function between the ions of type I and L given by Equation 4.7

$$C_{IL}(t) = \frac{1}{3} \left\langle \sum_{i\epsilon I} \sum_{l\epsilon L} \vec{v}_i(0)\vec{v}_l(t) \right\rangle \tag{4.7}$$

When I and L are identical $i = l$ term is excluded. For infinitely dilute solutions C_{IL} can be neglected and Equation 4.4 reduces to the Nernst-Einstein relation for ionic conductivity. Equation 4.1 is integrated till 1-5 ps for SPC/E and 10-20 ps for the ReaxFF simulations. In order to achieve convergence, average over two successive time chunks of 400 ps for the SPC/E model and 2000 ps for the ReaxFF model are taken as final conductivity value (Figure B1). The ReaxFF simulations require larger time chucks and longer integration times because of the nature of the underlying autocorrelation functions. The ReaxFF being a dissociative forcefield accounts for several intramolecular degrees of freedom and hence more data points are required for better averaging. The SPC/E model on the otherhand produces much smoother autocorrelation functions that converge to 0 faster than the ReaxFF.

4.2.2.2 Static dielectric constant (ϵ)

Under PBC, ϵ of isotropic fluids can be calculated as:

$$\epsilon = 1 + \frac{\left(\langle |\vec{M}|^2 \rangle - \langle |\vec{M}| \rangle^2 \right)}{3\epsilon_0 V k_B T} \tag{4.8}$$

where

$$\vec{M} = \sum_{molecules} \vec{\mu}_i \tag{4.9}$$

is the total dipole moment of the system obtained by summation of individual dipole moments μ_i. Since the ReaxFF simulations does not guarantee zero net charge on water molecules, the dipole moment was calculated with respect to the centre of mass (COM) with instantaneous charges. This makes the calculated dipole moments independent of the absolute positions of atoms. Simulations of pure water are done with second generation ReaxFF water forcefield [62]. This forcefield is generated by refitting the parameters related to the vdW force, hydrogen bonding, and Coulomb forces thereby giving improved description of the weak interactions between hydrocarbons and water as compared to the first generation ReaxFF water forcefield [222] used in developing the water-electrolyte interaction parameters [60].

4.3 Results

Figure 4.1 (left) shows D_I of Na^+, Cl^- ions obtained from the two models by integrating the velocity autocorrelation function. Numerical values of D_I of ions are listed in Table B2 and convergence plots are shown in Figures B2, B3. D_I of cations and anions from both the models increase with increasing temperature and decrease with increasing pressure. The ReaxFF model predicts higher D_I of cations than anions at all conditions. For the SPC/E model, anion D_I are higher at lower pressures (∼1-2 GPa). At higher pressures cation D_I are higher, similar to the ReaxFF model.

Figure 4.1 (right) compares bulk densities predicted by the ReaxFF and SPC/E models against Equation Of State (EOS) from Mantegazzi et al. [223] (For numerical values refer to Table B3). Predictions of density from the three models follow the following order: $\rho_{ReaxFF} < \rho_{SPC/E} \approx \rho_{EOS}$. The underestimation of bulk densities by the ReaxFF is particularly high at low pressures (∼10%) but reduces to ∼1% at higher pressures.

Figure 4.2 shows ϵ obtained from the two models compared against Deep Earth Water (DEW) model [224]. Both models predict increase in ϵ with pressure and decrease with temperature. Numerical values of ϵ obtained from the different models are listed in Table B4 and convergence plots are shown in Figure B4. Predictions of ϵ from the three models follow the the ascending order: $\epsilon_{ReaxFF} < \epsilon_{SPC/E} < \epsilon_{DEW}$.

Table 4.3 lists σ of 1.05 m NaCl solution calculated using the SPC/E and ReaxFF models along three isotherms. Figure 4.3 compares σ along different isotherms (a,b) and isobars (c,d). σ predicted by the ReaxFF model are always lower than those of the SPC/E model.

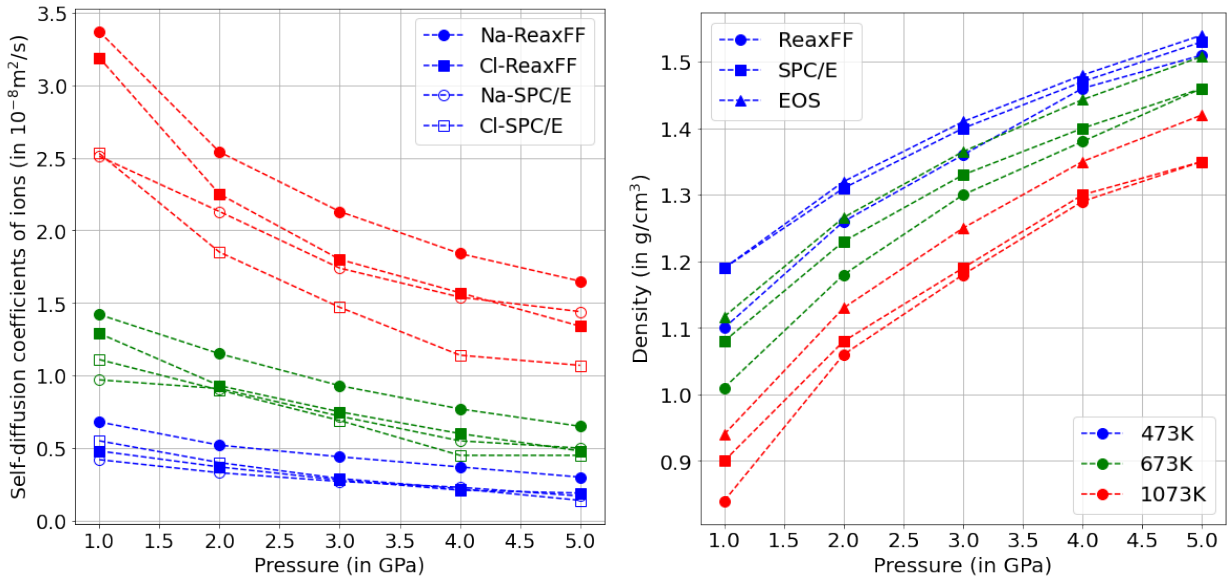

Figure 4.1: Left: Self-diffusion coefficients of cations and anions in 1.05 m brine obtained from the SPC/E and ReaxFF models along isotherms. Right: Bulk density of 1.05 m brine obtained from the SPC/E, ReaxFF models compared against EOS from Mantegazzi et al. [223] along isotherms

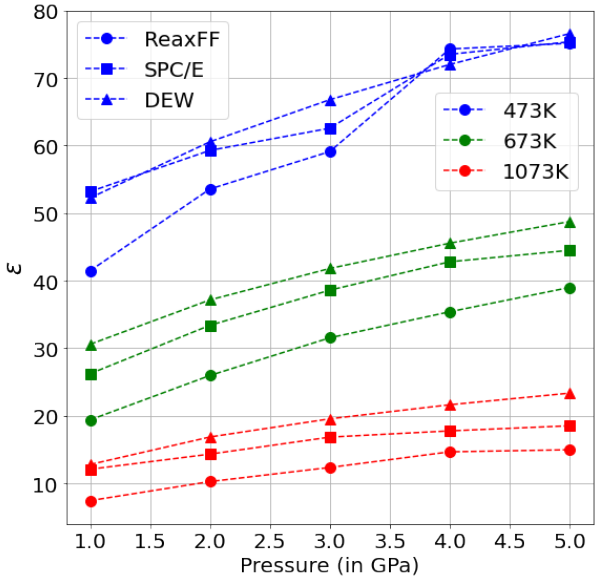

Figure 4.2: ϵ of water obtained from the SPC/E, ReaxFF models compared against the DEW model [224] along isotherms

Table 4.3: σ (in S/m) of 1.05 m brine along 473 K, 673 K, 1073 K isotherms. Number in the bracket is the error in the least significant digit. Error is calculated from variability of data once convergence is achieved. Convergence plots are shown in Figure B1

Temperature	Pressure	SPC/E	ReaxFF
473 K	1.0 GPa	24(1)	10(1)
	2.0 GPa	20(1)	14(1)
	3.0 GPa	16(1)	15.4(7)
	4.0 GPa	12.6(6)	13.4(3)
	5.0 GPa	9.7(3)	12(2)
673 K	1.0 GPa	32(1)	10.4(7)
	2.0 GPa	28.7(7)	16(2)
	3.0 GPa	27.0(3)	15(1)
	4.0 GPa	23.8(6)	20.5(2)
	5.0 GPa	20.6(9)	16(2)
1073 K	1.0 GPa	29(3)	15.2(8)
	2.0 GPa	28(4)	17.5(5)
	3.0 GPa	32(1)	16(1)
	4.0 GPa	28(1)	18.8(5)
	5.0 GPa	25(2)	18(1)

As shown in Figure 4.3 (b), the SPC/E model predicts monotonic decrease in σ with pressure at 473 K and 673 K, in agreement with previous simulation studies [211]. At 1073 K, this monotonic trend is no longer seen and a peak in σ at $\sim$3 GPa is seen from the SPC/E model. σ from the ReaxFF model at 473 K increases up to $\sim$3-4 GPa and then decreases (Figure 4.3 (a)). At 673 K, the ReaxFF model predicts increasing σ (within the errors of the model) with pressure whereas at 1073 K σ is almost constant (within the errors of the model).

From Figure 4.3 (c,d) it can be inferred that both the models show an initial increase in σ with temperature (within error bars). For the SPC/E model, a prominent decrease in conductivity is observed at higher temperatures along 1 GPa and 2 GPa isobars whereas no such systematic trends can be delineated from conductivity obtained from the ReaxFF model. This is due to the varying influence of ion self-diffusion and ion association which is discussed in detail in the next section.

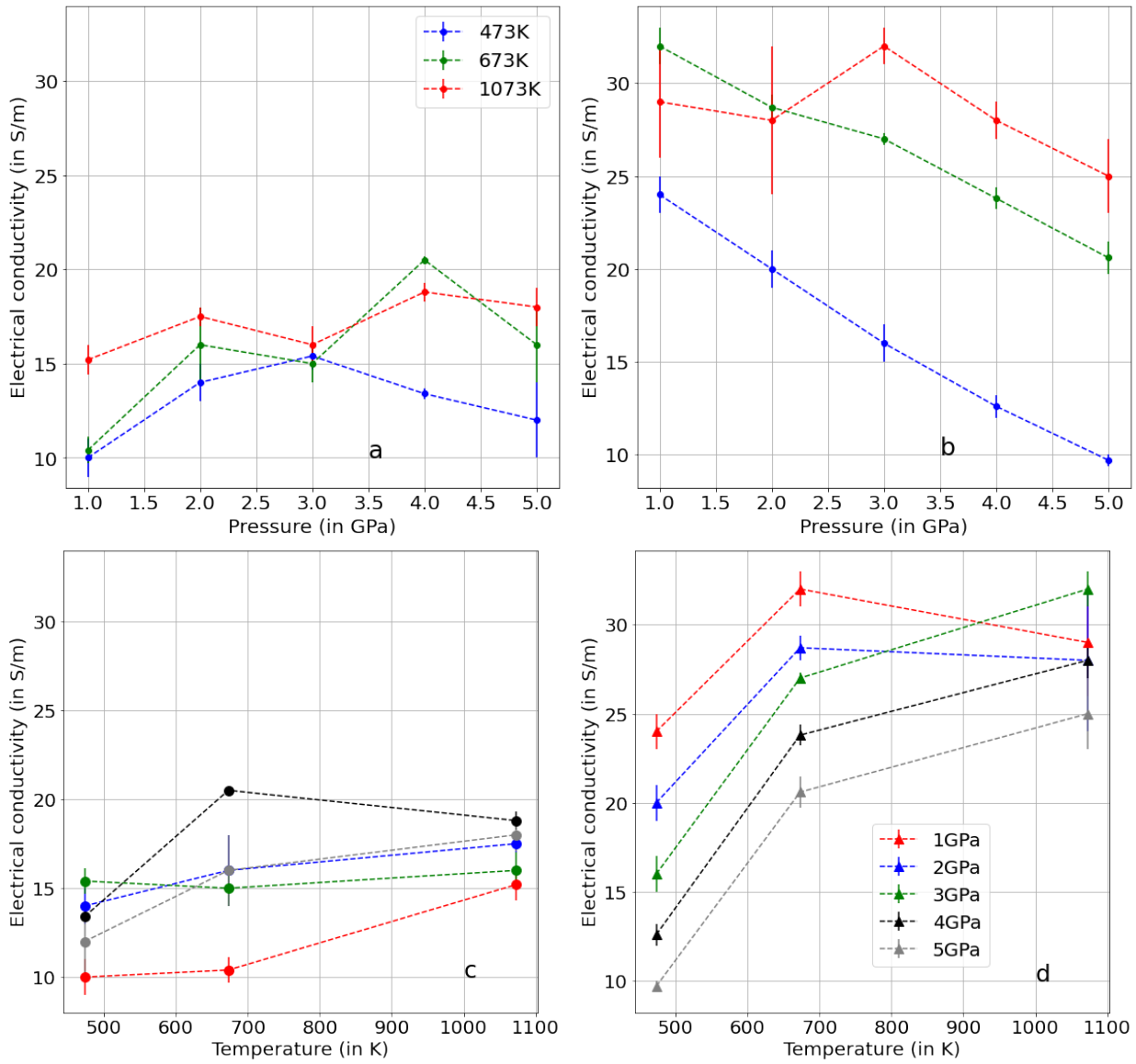

Figure 4.3: a,b - σ of 1.05 m brine obtained from the ReaxFF (a) and SPC/E (b) models along different isotherms. c,d - σ of 1.05 m brine obtained from the ReaxFF (c) and SPC/E (d) models along different isobars

4.4 Discussion

4.4.1 Influence of ion diffusion and ion association on electrical conductivity

4.4.1.1 Pressure dependence

Previous computational studies of the ReaxFF brine at ambient conditions [60] agree with the underestimation of anion self-diffusion observed in this study. For the SPC/E model, higher anion D_I at lower pressures (∼1-2 GPa) is in agreement with data at ambient conditions [215] and data till 80 °C [210]. Sakuma et al. [211] also calculated D_I at high temperatures and pressures up to 2 GPa with a non-dissociative interaction potential. Their data predict higher D_I for anions than cations for 0.6 m and 1.8 m NaCl solutions at 673 K and 973 K.

The trends in D_I (Figure 4.1 (left)) are correlated to the trends in bulk density predicted by the two models shown in Figure 4.1 (right). Lower densities predicted by the ReaxFF model lead to higher D_I for both cations and anions, as compared to the SPC/E model. However, although densities predicted by the two models converge at higher pressures, significant differences exist between the D_I at these conditions, particularly for cations. Hence differences in densities alone cannot explain the differences in D_I predicted by the ReaxFF and SPC/E models. It has to be noted that the SPC/E and ReaxFF models have completely different functional forms for short range and long range interactions which will have effects on the calculated transport properties.

The decomposition of σ calculated from the ReaxFF and SPC/E models is shown in Figure 4.4 (for numerical values refer to Tables B5, B6 respectively). This breakdown separates velocity autocorrelation and cross correlation contributions of σ that can be attributed to ion self-diffusion effects and ion-pairing effects respectively. Since ion self-diffusion is a function of density, its contribution to σ is also density dependent. The contributions of cross correlation terms for like ions are close to zero for both the ReaxFF and SPC/E models at all the studied pressures and temperatures due to short correlation times of the underlying velocity correlation functions. For the SPC/E model, cross correlation contribution of oppositely charged ions is also close to zero at 473 K and 673 K making σ completely diffusion controlled. Since contribution of ion self-diffusion to σ decreases with increase in pressure

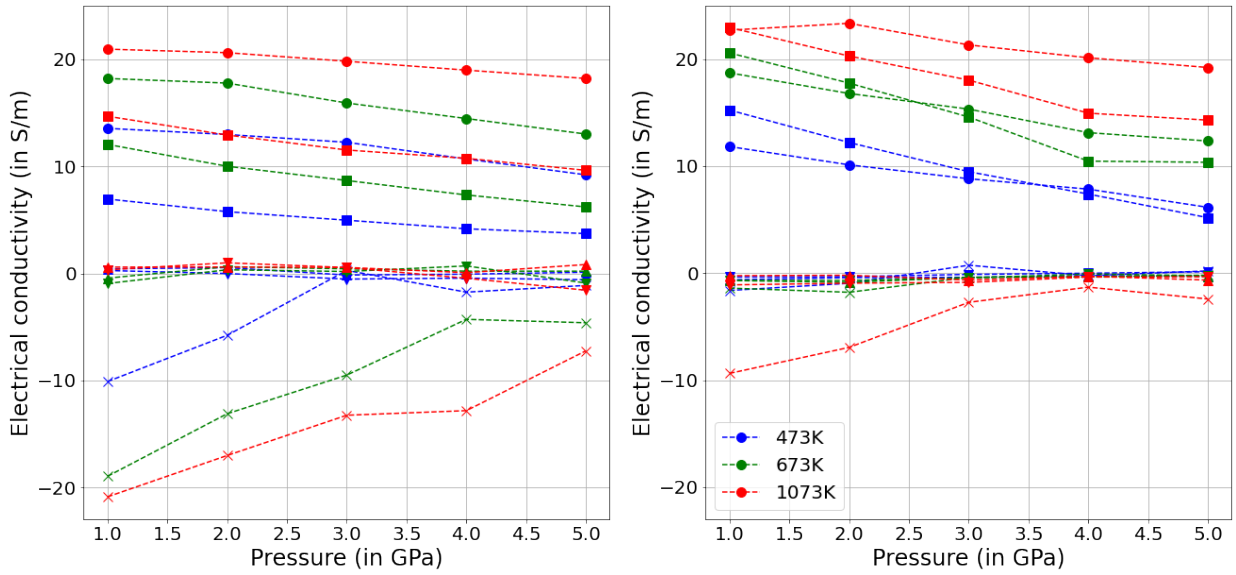

Figure 4.4: Decomposition of σ of 1.05 m brine from the ReaxFF model (left) and the SPC/E model (right) along isotherms. Symbols are used to show different components of σ - dot: cation self-diffusion, square: anion self-diffusion, inverted triangle: cation cross correlation, triangle: anion cross correlation, cross: cation-anion cross correlation

(Figure 4.5 (right)), the SPC/E model predicts decrease in σ with pressure at 473 K and 673 K (Figure 4.3 (b)). At 1073 K, Figure 4.4 (right) shows significantly higher negative contribution of oppositely charged ion pairs which reduces with increasing pressure in the SPC/E simulations. The high negative contribution of ion pairing at high temperature and low pressures (1073 K, ∼1-3 GPa) is because of the low ϵ of water that promotes ion pair formation (and hence lower percentages of free ions as shown in Table 4.4) at these conditions. With increase in pressure along 1073 K isotherm, ϵ of water increases (Figure 4.2) thereby increasing the ability of water to stabilize isolated charges. Reducing positive contribution of ion self-diffusion (Figure 4.5 (right)) along with reducing negative contribution of ion pairing results in a conductivity maximum at ∼3 GPa along 1073 K isotherm, as shown in Figure 4.3 (b).

In case of the ReaxFF model, there is a significantly higher negative contribution of cross correlation of oppositely charged ions along all the three studied isotherms (Figure 4.4 (left)). In contrast to the SPC/E model, σ in the ReaxFF model is governed by both ion self-diffusion as well as ion pairing, particularly at low pressures. The negative contribution decreases with pressure along all the three isotherms due to reasons discussed above. This is corroborated by data in Table 4.4 that shows increasing percentages of free cations and anions

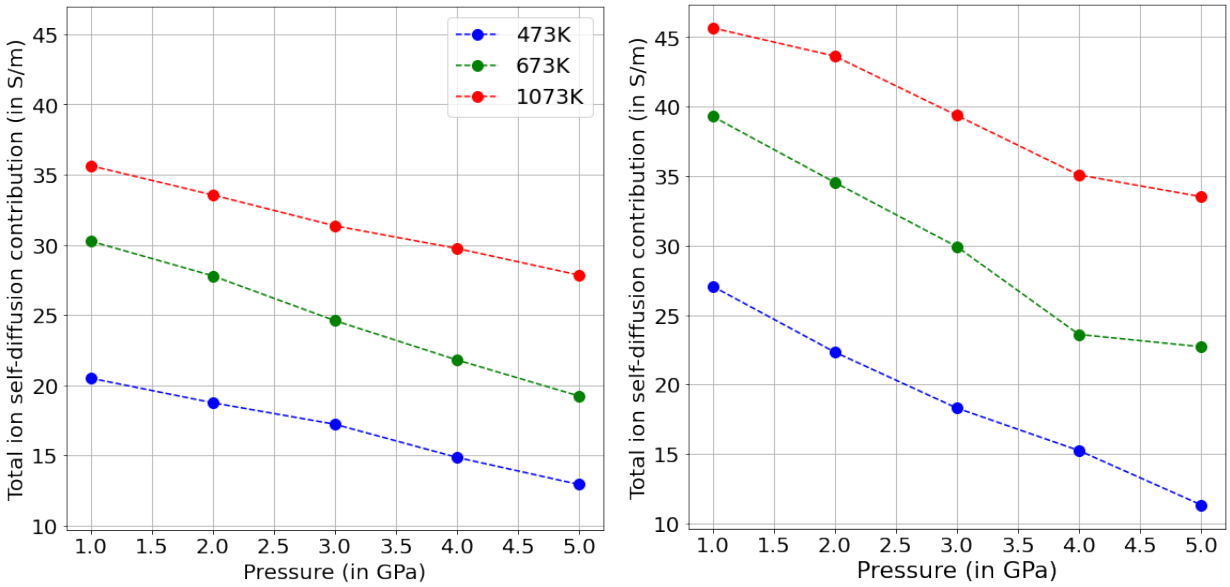

Figure 4.5: Contribution of ion self-diffusion to σ in 1.05 m brine from the ReaxFF model (left) and the SPC/E model (right) along isotherms

with pressure along all three isotherms for the ReaxFF model. The positive contribution from ion self-diffusion also decreases with increase in pressure due to decrease in D_I of ions at higher bulk densities (Figures 4.1 (right), 4.5 (left)). The interplay of these two factors result in a conductivity maxima at ∼3-4 GPa in the ReaxFF model along all the studied isotherms, as shown in Figure 4.3 (a).

It is worth noting that the contribution of ion self-diffusion to σ is a function of not only D_I of the ions but also ionic charges and density of the system (Equation 4.4). Hence higher D_I of ions in the ReaxFF model does not necessarily translate to higher contribution to σ (Figure 4.5). The higher D_I is offset by lower densities and lower charges predicted by the ReaxFF model. Na^+ and Cl^- ions are treated as hard spheres with fixed formal charges of $+1$ and -1 respectively in the SPC/E model. The ReaxFF model, on the other hand allows long range charge transfers leading to partial charges on the ions. Average charges on ions obtained from the ReaxFF simulations are shown in Table B7.

Overall, higher ϵ predicted by the SPC/E model results in higher free ion percentages as compared of the ReaxFF along all three isotherms (Table 4.4). As a result, σ from the SPC/E model is primarily diffusion driven at lower temperatures. In case of the ReaxFF model, ion association is higher and σ is shown to be governed by diffusion as well as ion association along all isotherms.

Table 4.4: Percentage of free ions in 1.05 m brine at different conditions from the SPC/E and ReaxFF models. Values are determined by identifying Na and Cl bearing clusters with inter-ionic distances <4.2 Å using a topological approach implemented in the TRAVIS code[165]

Temperature	Pressure	SPC/E (Cl^-,Na^+)	ReaxFF (Cl,Na)
473 K	1.0 GPa	78,67	35,34
	2.0 GPa	79,68	54,53
	3.0 GPa	79,70	66,66
	4.0 GPa	80,72	77,77
	5.0 GPa	80,73	80,79
673 K	1.0 GPa	65,62	17,22
	2.0 GPa	69,65	29,34
	3.0 GPa	71,65	37,41
	4.0 GPa	71,66	45,48
	5.0 GPa	72,66	53,55
1073 K	1.0 GPa	43,42	24,25
	2.0 GPa	53,51	26,30
	3.0 GPa	56,54	28,34
	4.0 GPa	59,55	31,37
	5.0 GPa	60,56	34,40

4.4.1.2 Temperature dependence

One of the important kinetic models used to explain temperature dependence of σ of liquids is the Arrhenius Law,

$$\sigma = \sigma_0 e^{-\frac{\Delta H}{k_B T}} \tag{4.10}$$

where σ_0 is the pre-exponential factor and ΔH is the activation enthalpy of the conduction process.

From Equation 4.10, it can be seen that a pure kinetically driven conduction mechanism would increase the conductivity with increase in temperature. Figure 4.6 (a,c) shows that the contribution of ion self-diffusion increases with increase in temperature for both the models in agreement with Equation 4.10. Both the SPC/E and ReaxFF models show an increase in negative contribution of ion pairing with increase in temperature at all pressures (Figure 4.6 (b,d)). This behaviour is due to the decreasing ϵ of water with temperature favouring more ion pair formation (Table 4.4, Figure 4.2). However, ion pairing is negligible at pressures > 2 GPa for the SPC/E model as shown in Figure 4.6 (d). As a result, σ is

primarily diffusion driven at pressures > 2 GPa and increases with increase in temperature (Figure 4.3 (d)) . Along 1 GPa and 2 GPa isobars, a reversal of temperature dependence of σ is seen from low to high temperatures. This is because of the dominance of ion diffusion at lower temperatures and ion association at higher temperatures. For similar reasons, the ReaxFF model also shows an increase in conductivity (within error bars) from 473 K-673 K along all the isobars (Figure 4.3 (c)). At higher temperatures, high negative contribution of ion pairing is observed and trend in total conductivity is determined by rate of increase of contributions from ion pairing and ion self-diffusion.

4.4.2 Comparison to experimental data

For 1.05 m NaCl solutions both the SPC/E and ReaxFF models underestimate σ when compared to the experimental data of Guo and Keppler [208] (Figure 4.7). This underestimation is particularly large at high temperature and high pressure conditions. Experimental data from Guo and Keppler [208] show a change in the pressure dependence from low to high temperatures. While σ shows a monotonic decrease with pressure at 473 K, at 673 K and 1073 K σ increases to a maximum at ∼3-4 GPa followed by decrease at higher pressures (Figure 4.7). Figure 4.7 (left) shows that the SPC/E model predicts monotonic decrease in σ with pressure consistent with the decreasing trend obtained in experiments [208] at 473 K. At 673 K, σ obtained from the ReaxFF model shows an overall increase within the errors of the model as shown in Figure 4.7 (middle). However, the SPC/E model predicts monotonically decreasing σ with pressure at 673 K. At 1073 K, σ calculated from the SPC/E model shows an initial increase (within error bars) followed by decrease, consistent the with experimental data from Guo and Keppler [208] (Figure 4.7 (right)) whereas σ from the ReaxFF model is almost constant within the errors of the model.

The large underestimation by the ReaxFF model may due to the partial charges on the ions because σ has an explicit square dependence on ionic charges. Blazquez et al. [217] similarly argued that although empirical forcefields with partial charges give better estimation of self-diffusion coefficients, formal charges are required to reproduce absolute values of σ. To check whether partial charges affect ReaxFF model results, we recalculated σ with formal charges in Equation 4.4. We find that the use of formal charges result in a maximum increase of ∼13 S/m in σ as shown in Figure B7. However, underestimation with respect to data from the SPC/E simulations and experiments is seen even with formal

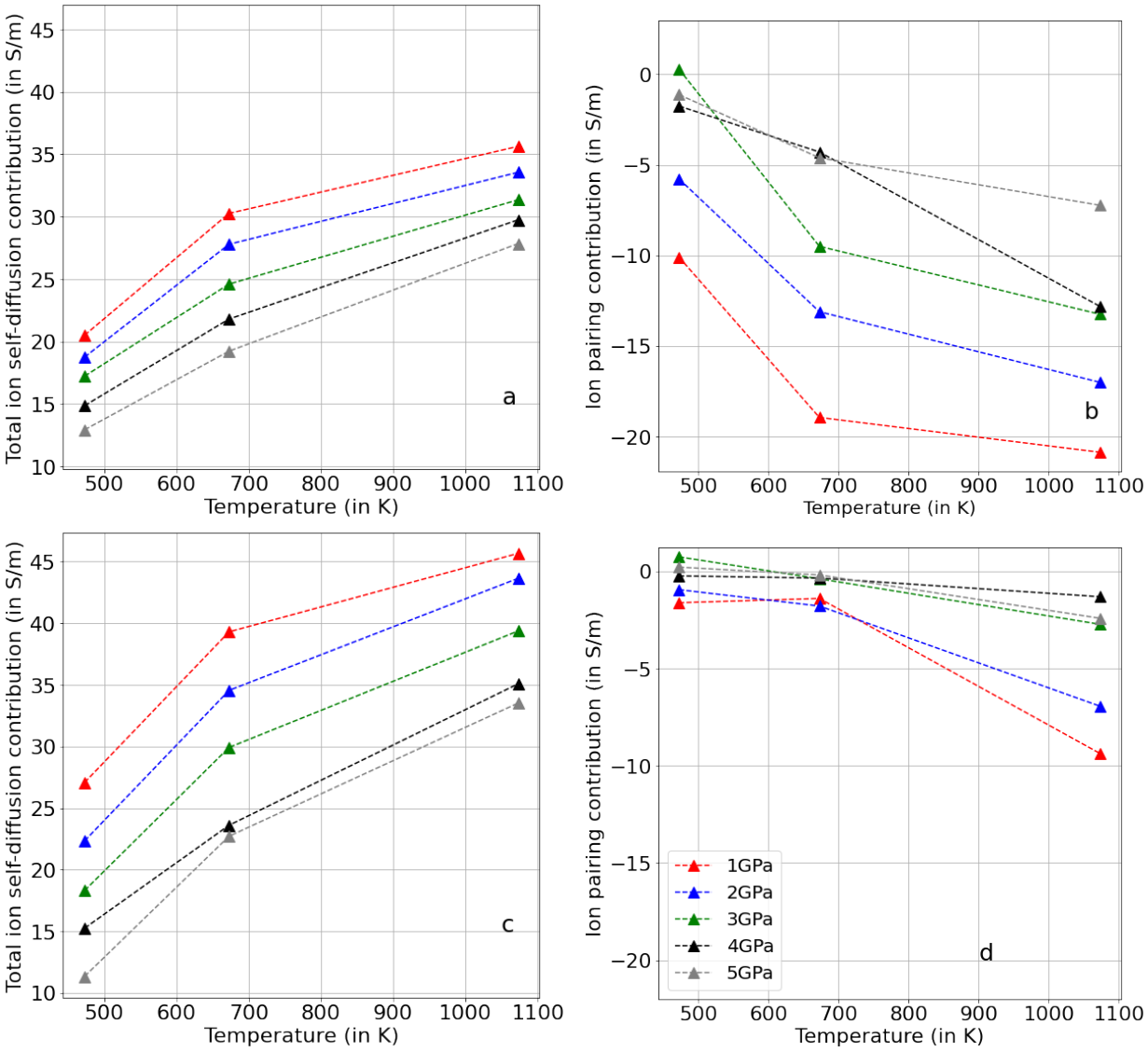

Figure 4.6: Contribution of ion diffusion and ion pairing to σ in the ReaxFF (a,b) and SPC/E (c,d) models along different isobars in 1.05 m brine

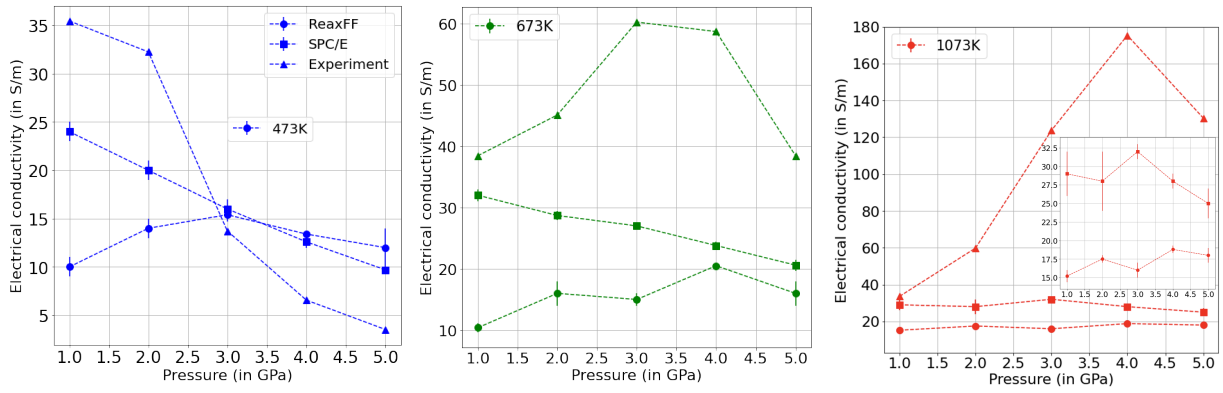

Figure 4.7: Comparison of σ from simulations with experiments from Guo and Keppler [208] along different isotherms. Inset shows the magnified view of σ obtained from the SPC/E and ReaxFF models at 1073 K

charges.

Sinmyo and Keppler [205] predict two distinct temperature and pressure regimes based on temperature dependence of σ of 5 wt % NaCl solutions. They predict increasing conductivity with temperature up to about 400°C. At higher temperatures the behaviour is pressure dependent - at low pressures (<1 GPa), σ decreases with increase in temperature whereas it increases with temperature at high pressures (>3 GPa). Figure 4.8 shows variations in σ obtained from the ReaxFF and SPC/E models at similar conditions. It is interesting to note that the SPC/E model reproduces the experimentally predicted change in temperature dependence from low to high pressures whereas for the ReaxFF model no systematic trend can be delineated. The distinct change in temperature dependence observed in the SPC/E simulations motivates breakdown of the studied temperature and pressure ranges into two distinct regimes depending on the main factor governing σ - ion self-diffusion dominant regime and ion association dominant regime as shown in Figure 4.8 (right, inset).

Since data from the SPC/E model shows a roughly linear decrease with pressure, we linearly extrapolated it and compared it to data from Bannard [202] at 473 K and 673 K as shown in Figure B8. Their data predict almost constant conductivity along isotherms till 0.2 GPa. Extrapolation of data obtained from the SPC/E simulations to such low pressures underestimate the conductivity of NaCl solutions.

Although MD simulations predict correct trends in σ at high temperature and pressure conditions, there is substantial underestimation of the absolute values when compared to experimental data (Figure 4.7). Since σ is intricately dependent on properties like charge,

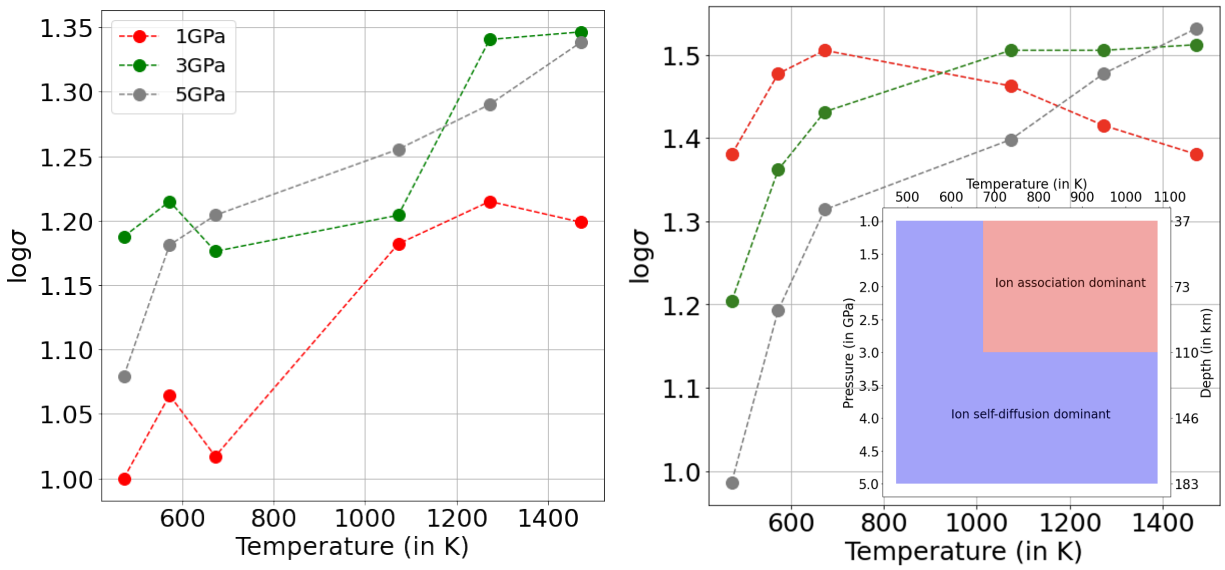

Figure 4.8: σ from the ReaxFF (left) and SPC/E (right) models. Inset on the right shows two distinct temperature and pressure regimes of σ. Distinction is made based on main factor governing σ. To convert pressure to crustal depth, lithostatic conditions are assumed with uniform density of $2.8\,\mathrm{g/cm^3}$

density and self-diffusion coefficients, accurate prediction of these properties are required for precise calculation of σ. Both the models, ReaxFF and SPC/E predict lower bulk densities of NaCl solutions as compared to EOS (Figure 4.1 (right)). Traditional empirical forcefields with fixed charges, like the SPC/E model used in this work have been quite successful but have also failed to reproduce properties such as solubilities, viscosities and activity coefficients [225]. Transport properties of ions are also among properties that these forcefields have failed to reproduce accurately [226]. Several groups [227, 228, 229, 230] have suggested to use scaled charges for cations and anions. Although this scheme improves predictions of several properties, there is no single set of charges that describe all properties correctly. In this work we show that although the ReaxFF includes an 'on-the-fly' scheme to determine charges, no significant improvement in predictions of absolute values of σ is observed. This points to other fundamental issues related to MD simulations with empirical potentials. The SPC/E is parameterized to reproduce experimental heat of vaporization [66] and are non-dissociative in nature. The ion-water interaction parameters are fitted to gas phase binding enthalpy data of ion-water clusters [67]. On the contrary, the ReaxFF water potential is fitted on QC water interactions data, including H–H, HO–OH and O=O bond dissociation energies, charge distributions, angle bending energies and binding energies of water clusters

[231]. It is also fitted to reproduce energetics of several H-transfer reaction pathways and is dissociative in nature [231]. The ReaxFF parameters for electrolytes are fitted on gas phase energies of ion-water clusters and EOS of different crystalline phases [60]. None of the models used in this work are fitted to explicitly reproduce properties in high temperature and pressure conditions targeted in this paper. In fact, classical potential that reproduces all properties of pure water is still elusive [232]. Since underestimation of σ by the ReaxFF model is attributed to the formation of ion clusters with different residence lifetimes, the issue of finite sampling due to short simulation times cannot be neglected.

4.5 Conclusion

In this chapter we have calculated the electrical conductivity of 1.05 m NaCl solution at supercritical conditions using the ReaxFF and SPC/E models. Our simulations establish density and ion association as the two main factors governing σ with the later responsible for the observed non monotonic behaviour of σ at supercritical conditions. However, the influence of these factors in σ is different for the two models. For the SPC/E model, conductivity is entirely diffusion driven at lower temperatures with ion association effects showing up at high temperatures whereas for the ReaxFF model, σ is governed by both ion self-diffusion and ion association at all the studied temperature and pressure conditions. The ReaxFF model predicts lower bulk densities of NaCl solutions in supercritical conditions. It also envisages higher association of NaCl in supercritical water leading to lower σ as compared to the SPC/E model. Both the models underestimate σ when compared to recent high temperature and pressure experimental data. However, the SPC/E model reproduces the experimentally observed change in temperature dependence of σ from low to high pressures. Fundamental issues like transferability of potential and finite sampling have to be taken into account when using these models at supercritical conditions. Overall, it is not possible to identify one interaction model as more accurate than the other in terms of electrical conductivity prediction. While both the models agree on the conduction mechanism at supercritical conditions, accuracy in predicting electrical conductivity trends depend on the target thermodynamic conditions of the NaCl solution.

Chapter 5

Development of ab initio based polarizable forcefield for La^{3+} in chloride-bearing hydrothermal fluids

5.1 Introduction

REEs are a group of 17 (including scandium (Sc) and yttrium (Y)) silvery-white heavy metals. Compounds containing REEs have immense applications in electronic and electrical equipments, lasers, glass, semiconductors and magnetic materials. Due to their increasing importance in economic developments and potential of their supplies being at risk [233, 234], they have been classified as critical elements by the U.S. Geological Survey (USGS).

Hydrothermal processes control the mineralogy and grade distribution of several important REE deposits like Gallinas Mountain in New Mexico [29], Thor Lake in Canada [235]. The mobility of elements in hydrothermal fluids is primarily controlled by the chemical composition and speciation, which have been shown to be controlled by temperature and pressure [236]. Commonly formed REE complexes include carbonates, sulfates, fluorides, chlorides [26, 33]. Therefore, accurate knowledge of speciation of REEs in dilute to concentrated hydrothermal brines is necessary to improve existing geochemical models and complement existing mineral recovery and extraction processes.

Lanthanum (La), which is classified as a Light Rare Earth Element (LREE) is generally enriched by hydrothermal processes forming primary ore deposits. Several minerals like

bastnasite, monazite, zircon, apatite are important sources of REEs in primary ore deposits [237]. Although LREEs form stronger complexes with F^- with increasing temperature, Cl^- is considered to be the main transporter of LREEs mainly because of its higher availability in hydrothermal fluids [238]. Several experimental and theoretical studies have been conducted to determine the properties of La^{3+} aqua and chloride complexes at room temperature (Table 1 in Guan et al. [238]). Experimental as well as MD studies have confirmed the hydration structure of La^{3+} at room temperature to be tricapped trigonal prism with 9 water molecules. Different types of forcefields have been developed for aqueous La^{3+} at room temperatures including polarizable forcefield for lanthanoids [239, 240, 241], AMOEBA [242, 243, 244] based forcefield, 12-6 LJ and 12-6-4 LJ potential [245], LJ and Buckingham potential for lanthanoids in aqueous solutions [28] and MDCHO [246, 247] model. Ikeda et al. [248] and Terrier et al. [249] predicted the same hydration properties of La^{3+} using AIMD. At hydrothermal conditions, a change in coordination geometry is observed but no decrease in hydration number is seen [236].

Several MD studies have been conducted to understand the structure of La^{3+} chloro complexes at room temperature. Beuchat et al. [250] constructed a new potential and predicted $La(H_2O)_9$ complexes in 1 m solutions and solutions of higher concentrations. Petit et al. [251] used a combination of simple pair potential based molecular dynamics and AIMD and predicted an average configuration of $La(H_2O)_8Cl_2$ in 14 M solutions. Bühl et al. [252] used AIMD along with thermodynamic integration to calculate binding energies of La-chloro complexes in water at room temperature. Rudolph and Irmer [253] studied the effects of different solvents on La-Cl complexation using Raman spectroscopy and DFT. They found that significantly higher amounts of $LaCl_n$ (n = 1-3) were being formed in the presence of HCl in pure water. Several studies have been conducted for the La-Cl-H_2O system at room temperature using different experimental techniques. For a comprehensive list of all such studies, readers are referred to Table 1 in Guan et al. [238].

Although the La-Cl-H_2O system is well studied at room temperature, studies targeting hydrothermal temperatures and pressures are quite scarce in available literature. Mayanovic et al. [254] performed in-situ X-ray Absorption Spectroscopy (XAS) of La^{3+} in Cl-bearing solutions till 500 °C. They predicted a gradual increase in Cl-complexation from 0 at 25 °C to 3.1 at 500 °C. The formation constants of La-Cl complexes are well studied at room temperature [26]. In the absence of experiments at high temperatures, earlier studies relied

on extrapolations of room temperature data using species based EOS like the Helgeson-Kirkham-Flowers (HKF) model [255]. Haas et al. [256] fitted a set of parameters for the HKF model at 25 °C, 1 bar. Migdisov et al. [27] performed high temperature solubility experiments and published a set of HKF parameters that can be used till 300 °C. As far as computational studies are concerned, Guan et al. [238] is the only study available in literature. They performed AIMD simulations up to 500 °C and reported speciation and association constants at wide range of temperature, pressure and concentration.

AIMD simulations rely on quantum mechanical calculations to calculate forces between atoms. As a result, these simulations demand extremely high computational resources. In order to account for this high computational demand, AIMD is restricted to short simulation times and small simulation boxes with only few hundred atoms. Due to their simple underlying interaction model, classical force fields are much more efficient and can overcome some of the shortcomings of AIMD while providing sufficient geochemical insights into fluid properties at hydrothermal conditions, which cannot be attained easily in laboratories [64]. The reliability and accuracy of molecular simulations not only depends on the representation of ionic charge but also on the polarization of ionic charge by solvent molecules. The later becomes particularly important when dealing with highly charged ions having high polarization power in concentrated solutions [59]. Many different polarizable forcefields exist, each having a different representation of polarizability [62, 257, 258]. In this paper, we fit ab initio based Polarizable Ion Model (PIM) for La-Cl-H_2O system. This model includes an explicit treatment of polarizability of ions while still modelling them as hard spheres with fixed charges (discussed in detail later). Although this results in slightly higher computation expense than simple pair potential based forcefields, PIM is still more efficient than AIMD allowing us to address finite size effects. Since our aim is to calculate thermodynamic properties at hydrothermal conditions, the forcefield is fitted from snapshots of AIMD simulations at hydrothermal conditions (773 K, 5 kbar). We use the newly fitted potential to study the speciation of La^{3+} in dilute to concentrated brines at 773 K, 5 kbar. We also use enhanced sampling techniques to calculate association constants of different La-Cl complexes in hydrothermal conditions. We calculate association constants from simulation boxes of different sizes in order to understand the effects of box size on association constants. To check the transferability of this new potential, production simulations are done at 473 K, 400 bar. To understand the importance of ionic polarizability, additional simulations are performed

with pair potential based non polarizable forcefields [28] and a comparison is made between the two different models. The results are compared to available AIMD/experimental data, wherever available.

5.2 Parameterization of force field

5.2.1 Model

The total energy of the system comprises four terms:

$$V_{total} = V_{charge} + V_{disp} + V_{rep} + V_{pol} \tag{5.1}$$

The V_{charge} term is calculated calculated between ion pair I and J from Coulomb's Law:

$$V_{charge} = \sum_{I,J} \frac{q_I q_J}{r_{IJ}} \tag{5.2}$$

where q_I, q_J are the formal charges of the respective ions and r_{IJ} is the distance between the ions. The V_{disp} term includes contributions from the dipole-dipole and dipole-quadrupole terms,

$$V_{disp} = -\sum_{I,J>I} \left(f_6^{IJ}(r_{IJ}) \frac{C_6^{IJ}}{r_{IJ}^6} + f_8^{IJ}(r_{IJ}) \frac{C_8^{IJ}}{r_{IJ}^8} \right) \tag{5.3}$$

The short-range corrections are described using the Tang-Tonnies functions f_n^{IJ}, which are of the form [259],

$$f_n^{IJ}(r_{IJ}) = 1 - e^{-b_D^{IJ} r_{IJ}} \sum_{k=0}^{n} \frac{(b_D^{IJ} r_{IJ})^k}{k!} \tag{5.4}$$

The V_{rep} term accounts for the short range repulsion and is modelled by exponential as,

$$V_{rep} = \sum_{I,J} A^{IJ} e^{-B^{IJ} r_{IJ}} \tag{5.5}$$

Finally, the many-body electrostatic effects are described by the induced dipole ($\vec{\mu_I}$) terms. These are treated as additional degrees of freedom and obtained at each MD step by

Table 5.1: LJ potential parameters with partial charges

r_{OH} (in Å)	r_{OM} (in Å)	H-O-H angle (in °)	ϵ_O (in kcal/mol)	σ_O (in Å)	q_H (in e)	α_M (in Å^3)
0.9752	0.215	104.52	0.1825	3.2340	0.5190	1.444

minimizing the polarization energy,

$$V_{pol} = \sum_I \frac{1}{2\alpha^I}|\vec{\mu_I}| + \sum_{I,J}[(q^I\mu_\alpha^J g^{IJ}(r_{IJ}) - q^J\mu_\alpha^I g^{JI}(r_{IJ}))T_{IJ}^\alpha - \mu_\alpha^I\mu_\beta^J T_{IJ}^{\alpha\beta}] \tag{5.6}$$

where α^I is the ion polarizability and T are the multipole interaction tensors. Tang-tonnies type damping functions as short-range corrections are of the form [259],

$$g^{IJ}(r_{IJ}) = 1 - c^{IJ}e^{-b^{IJ}r_{IJ}}\sum_{k=0}^{4}\frac{(b^{IJ}r_{IJ})^k}{k!} \tag{5.7}$$

This model, called the Polarizable Ion Model (PIM) has been shown to accurately describe Cl^- bearing aqueous solutions of several ions [59]. The solvent water molecules are described by the polarizable model described by Dang and Chang (DC) [258] which is compatible with PIM. DC water is a rigid 4-site rigid model, with an additional virtual site M along the symmetry axis of the molecule which carries a negative partial charge and the induced dipole as shown in Figure 5.1. The short range repulsion and dispersion interactions are described by LJ interaction on the oxygen atom only. The parameters of the DC model are summarized in Table 5.1. This model has been shown to correctly reproduce the trends in several thermophysical properties of bulk water from ambient to high temperature conditions [260].

In this work, we fit most of the parameters directly from AIMD snapshots thereby reducing the risk of error compensation and retaining the physical meaning of the parameters. The different adjustable parameters and fitting procedure is described in the following section.

5.2.2 Calculation of parameters

First principle calculations using DFT describes the electron density of the system as a whole. Due to the delocalized nature of the orbitals, it is not possible to assign the orbitals to individual molecules/ions. It has been shown that Maximally Localized Wannier Func-

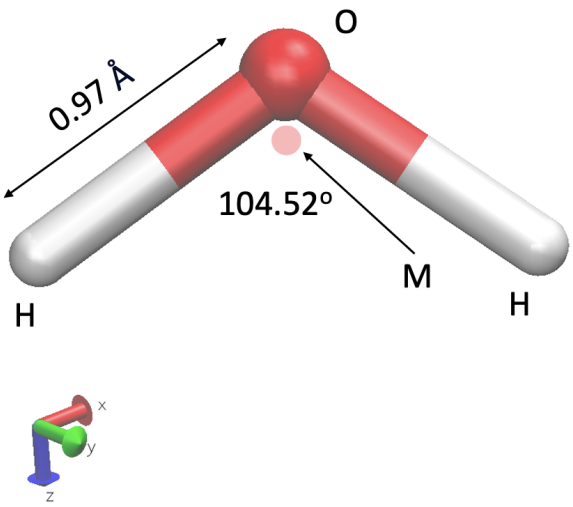

Figure 5.1: Four body rigid water molecule modelled with the DC model. The transparent red point is the virtual site, called the M site which carries the polarizability and the partial charge

tions (MLWFs) obtained by unitary transformation of Kohn-Sham orbitals can be used to systematically derive the ionic polarizabilities (α^I) as well as dispersion parameters C_6^{IJ} and C_8^{IJ} of PIM [261, 262]. MLWFs are constructed by choosing a phase that minimizes the overall spread of the Wannier functions [263].

5.2.2.1 Polarizability

For closed shell systems where every MLWF contributes two electrons, the molecular or atomic dipole moment is given by,

$$\vec{\mu^I} = \sum_{i \epsilon I} \left(Z_i \vec{R_i} - 2 \sum_{n \epsilon i} \vec{r_n^w} \right) \tag{5.8}$$

where the outer summation runs over atoms i belonging to fragment I. The inner summation runs over MLWFs whose centers are localized in the vicinity of the nuclear position $\vec{R_i}$ of i. Z_i is the charge of nucleus i, and $\vec{r_n^w}$ is the position of the center of the n^{th} MLWF. If the externally applied electric field is small, induced dipole moment shows a linear response. Isotropic polarizability (α^I) of ions is the slope of this linear plot. More details of this method can be found in Molina et al. [264], Tazi et al. [59].

The gas phase polarizabilities of ions are not equal to those obtained in solution. This

Table 5.2: Ionic polarizabilities used in PIM fitting

Ion	Polarizability (in Å^3)
Cl^-	3.05
La^{3+}	1.12

is due to the existence of a confining potential, which affects the electron density around a given species, and originates from both Coulombic interactions and the exclusion of electrons from the region occupied by the electron density of the first-neighbour solvation shell. Molina et al. [264] have shown that while this effect is significant for anions, it is small for cations. Accordingly, in this work we have used the ionic polarizability of Cl^- obtained in hydrothermal solution and gas phase values for La^{3+} ions. The values used in the model are listed in Table 5.2. These values are in good agreement with previously calculated polarizability values for these ions [264, 265, 266]. Consistent with Tazi et al. [59], we have taken the ionic polarizability of Na^+ as 0.

5.2.2.2 Dispersion terms: C_6^{IJ}, C_8^{IJ}

These parameters were calculated directly from the MLWFs with the method of Silvestrelli [267]. In this method, dispersion interactions are calculated between each pair of MLWFs. The long-range interactions between separated fragments of matter is calculated based on the formulations of Andersson et al. [268] as,

$$E_{xc}^{lr} = \frac{6e}{4(4\pi)^{1.5} m 0.5} \int_{V_1} \int_{V_2} \frac{(\rho_1(\vec{r_1})\rho_2(\vec{r_2}))^{0.5}}{\rho_1(\vec{r_1})^{0.5} + \rho_2(\vec{r_2})^{0.5}} \, d\vec{r_1} \, d\vec{r_2} \times \frac{1}{|\vec{r_1} - \vec{r_2}|^6} \tag{5.9}$$

where $\rho(\vec{r_i})$ is the charge density of fragment i, m is the electronic mass and V_i is the volume occupied by fragment i. For large separations R, this scales as $E^{lr} = -C_6/R^6$ where the C_6 coefficient for the interaction between two MLWFs k and l can be computed as

$$C_6^{kl} = \frac{3}{32\pi^{1.5}} \int_{r_1 \leq r_c} \int_{r_2 \leq r_c} \frac{w_k(\vec{r_1}) w_l(\vec{r_2})}{w_k(\vec{r_1}) + w_l(\vec{r_2})} \, d\vec{r_1} \, d\vec{r_2} \tag{5.10}$$

where r_c is the cutoff radius chosen to capture the long range interactions in electron gas. The analytical form of r_c and w_r are taken from [267]. Assuming an isotropic distribution of MLWF centers around nuclei I, J at fixed distances, dispersion coefficients can be calculated as,

$$C_6^{IJ} = \sum_{k\epsilon I, l\epsilon J} C_6^{kl} \tag{5.11}$$

$$C_8^{IJ} = \sum_{k\epsilon I, l\epsilon J} 5(d_k^2 + d_l^2) C_6^{kl} \tag{5.12}$$

where $d_{k,l}$ are the distances of the MLWF centers to their respective nuclei and C_6^{kl} is computed for each pair of MLWFs.

5.2.2.3 Dipole fitting

The parameters of short range damping of charge dipole interactions (b^{IJ}, c^{IJ} in Equation 5.7) is fitted by minimizing the errors on dipole moments calculated from PIM with respect to those obtained from DFT on training configurations. Mathematically, this can be written down as,

$$\chi_\mu^2 = \frac{1}{N_{conf} N_{atom}} \sum_{conf} \sum_{atom} \frac{|\vec{\mu}^{classical} - \vec{\mu}^{DFT}|^2}{|\vec{\mu}^{DFT}|^2} \tag{5.13}$$

where N_{conf} is the number of configurations in training set, N_{atom} is the number of atoms in each snapshot, $\vec{\mu}^{classical}$ are the dipole moments obtained from PIM and $\vec{\mu}^{DFT}$ are the reference dipole moments obtained from MLWFs. χ^2 is the relative Mean Square Error (MSE).

5.2.2.4 Force fitting

Lastly, the parameters of the short range repulsion term (V_{rep}) are fitted following a similar procedure. The forces calculated from PIM are compared against those obtained from DFT on representative configurations thereby reducing their relative error. Mathematically, this can be described as:

$$\chi_F^2 = \frac{1}{N_{conf} N_{atom}} \sum_{conf} \sum_{atom} \frac{|\vec{F}^{classical} - \vec{F}^{DFT}|^2}{|\vec{F}^{DFT}|^2} \tag{5.14}$$

$\vec{F}^{classical}$ are the atomic forces obtained from PIM and $\vec{F}^{DFT}$ are the reference atomic forces obtained from DFT.

The iterative fitting approach is shown using a flowchart in Figure 5.2.

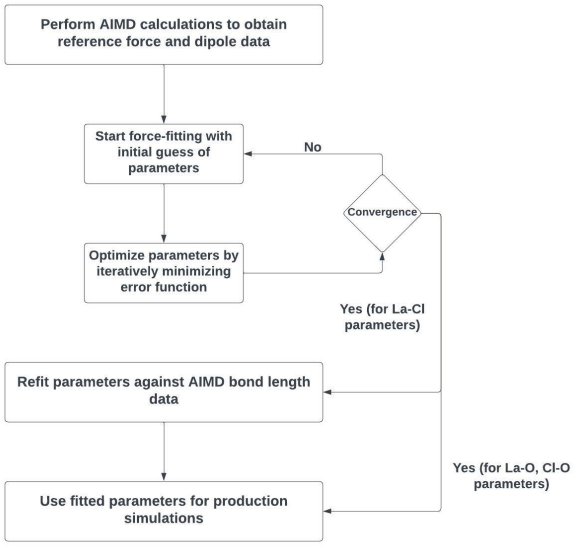

Figure 5.2: Iterative fitting procedure

5.2.3 Simulations for parameter fitting

The aqueous La-Cl system is broken down into 3 subsystems - crystalline $LaCl_3$, aqueous La-O and aqueous Cl-O. Parameters were fitted for each of them independent of the others. Simulation boxes used for generation of training sets with AIMD are listed in Table 5.3 and discussed in detail below.

La-Cl, La-La and Cl-Cl interaction parameters are fitted from forces and dipole moments of crystalline $LaCl_3$. The snapshots that constitute the training set are taken from AIMD simulations of 3×3×3 supercell of crystalline $LaCl_3$ (box 1 in Table 5.3). The supercell is equilibrated at 300 K for ∼4 ps. Production simulations are then carried out for ∼10 ps. Additional equilibration and production simulations are carried out at 773 K with the same time settings. In order to have a comprehensive sampling of the phase space, snapshots are taken from both sets of production trajectories, constituting a training set with ∼30 configurations.

La-O, Cl-O interaction parameters are fitted from the forces and dipole moments of aqueous La^{3+} and aqueous Cl^- respectively, obtained from AIMD simulations with box 2 and 3 in Table 5.3. To prepare the boxes, first a box containing only water molecules is equilibrated at a density of ∼0.8 g/cm^3 with the SPC/E model [66]. One water molecule

Table 5.3: Details of the simulation boxes used for generation of training sets

Box no.	Subsystem	Contents	Edge lengths (in Å)
1	$LaCl_3$ crystal	32 La^{3+}, Cl^-	26.1332×15.0880×8.7432
2	aqueous La^{3+}	84 H_2O, 1 La^{3+}	14.2784
3	aqueous Cl^-	84 H_2O, 1 Cl^-	14.2784

is then replaced with a La^{3+} ion to prepare box 2 and with a Cl^- ion to prepare box 3 both containing 84 H_2O molecules. The edge lengths of the boxes (=14.2784 Å) are set to match the density of water at the target temperature and pressure values (773 K, 5 kbar, ∼0.87 g/cm^3). The boxes are equilibrated for ∼4 ps followed by production simulations for ∼15 ps. Snapshots from production simulations are used to create the training sets for La-O and Cl-O subsystems, each containing ∼100 configurations.

The DZV-MOLOPT basis sets [85] are used along with the PBE XC functional for all the species. All equilibration and production simulations are carried out in the NVT ensemble with a timestep of 0.5 fs. Nosé–Hoover thermostat is used to control the temperature at the target value. All AIMD simulations are done using the CP2K [42] simulation package using GPW method.

Association constants at infinite dilution are calculated from FES as [269]:

$$K_{eq}^{\infty} = c_{MD} \int_{r_i}^{r_c} 4\pi r^2 g^{\infty}(r)\, dr \tag{5.15}$$

where $c_{MD} = 6.022 * 10^{-4}$Å^{-3}, $g^{\infty}(r)$ is the radial distribution function in the limit of infinite dilution and r_c is the distance criteria separating the associated state and dissociated state, r_i is the distance criteria defining the initial associated state. $g^{\infty}(r)$ is calculated from FES as [127, 269, 270]:

$$\Delta G = -k_B T ln\left[4\pi r^2 g^{\infty}(r)\right] \tag{5.16}$$

Before applying Equation 5.16, the ΔG computed from WMetaD simulations is aligned to the analytical solution of two point charges q_i, q_j interacting via a screened electrostatic potential and short range potential, $SR(r)$ as,

$$\phi(r) = \frac{q_i q_j}{4\pi\epsilon_0\epsilon_r r} + SR(r) \tag{5.17}$$

where ϵ_0 is the permittivity of free space, ϵ_r is the permittivity of the solvent and $\phi(r)$ is the Potential of Mean Force (PMF). This problem has a well-known analytical solution and the free energy as a function of the particle distance r can be written as,

$$\Delta G(r) = \phi(r) - k_B T ln(4\pi r^2) \tag{5.18}$$

where the second term arises from the Jacobian of transformation of free energy from Cartesian to spherical coordinates and is called the configurational entropy. Equation 5.18 can be used to convert from FES to PMF and vice-versa depending on the enhanced sampling technique being used. For a detailed statistical mechanical discussion on this, interested readers may refer to Chialvo et al. [270]. This technique has been used to calculate association constants in previous studies [127, 269, 270].

5.2.4 Production simulations

The fitted PIM parameters are used to investigate the speciation and association constants of La-Cl complexes at 773 K, 5 kbar conditions. The boxes used for production simulations to study speciation as a function of brine concentration are described in Table 5.4 (Box 1-4). The edge lengths of the boxes are adjusted to match the densities obtained from EOS in Driesner et al. [271]. To prepare the boxes, first a box containing only water molecules is equilibrated at a density of $\sim$0.8 g/cm^3 with the SPC/E model [66]. Boxes 1,7 are prepared by replacing some of the water molecules with a geometry optimized $LaCl_3$ molecule. The boxes at higher concentrations (boxes 2,3,4) are then prepared by successively replacing more water molecules with Na^+ and Cl^- ions so as to maintain charge neutrality. The boxes are equilibrated in the NVT ensemble for $\sim$5 ps-10 ps followed by $\sim$5 ns of production simulation. The timestep chosen for the simulations is 0.5 fs. To compare the fitted potential against available pair potential based non polarizable forcefields, simulations (referred to as N-POL MD simulations in the remaining paper) are carried out with the same boxes using the parameters reported in Migliorati et al. [28]. To check the transferability of the fitted potential to subcritical conditions, additional production simulations are performed at 473 K, 400 bar. This temperature and pressure are chosen to ensure similar solvent densities as the fitted conditions and to facilitate direct comparison with AIMD data from Guan et al. [238]. Interaction potential parameters for the Na-Cl-H_2O subsystem are taken from Tazi et al. [59].

Table 5.4: Details of simulation boxes

Box no.	Contents	Density (in g/cm^3)	Molality
1	227 H_2O, 1 La^{3+}, 3 Cl^-	0.90	0.734
2	315 H_2O, 1 La^{3+}, 12 Na^+, 15 Cl^-	1.10	2.64
3	291 H_2O, 1 La^{3+}, 24 Na^+, 27 Cl^-	1.14	5.15
4	265 H_2O, 1 La^{3+}, 37 Na^+, 40 Cl^-	1.20	8.38
5	55 H_2O, 1 La^{3+}, 3 Cl^-	1.03	3.02
6	55 H_2O, 1 La^{3+}, 3 Cl^-	1.11	3.02
7	339 H_2O, 1 La^{3+}, 3 Cl^-	1.05	0.495

Pair correlation functions are calculated for different pairs of species to study their relative atomic structures using Equation 5.19. Distance corresponding to the first minimum of the pair correlation functions is the size of the first coordination shell. CN were calculated by counting the number of particles till the first minimum.

$$g_{ij}(r) = \left\langle \frac{dn_r^{ij}}{4\pi r^2 \rho_j dr} \right\rangle \tag{5.19}$$

where dn_r^{ij} is a function calculating the number of particles of type j within a shell of thickness dr at a distance r from a particle of type i. ρ_j is the particle density $\left(= \frac{N_j}{V} \right)$ of j. The angular brackets denote ensemble average over the entire trajectory. Pair correlation functions for different species are calculated using TRAVIS code [165].

In order to calculate association constants of different La-Cl complexes, WMetaD is performed in the NVT ensemble for ∼6 ns. Hills of height 1 kJ/mol and width of 0.02 are deposited every 10^2 timesteps to get good sampling of associated and dissociated states within reasonable simulation time. To facilitate direct comparison with AIMD data from Guan et al. [238] at studied conditions, box 5 and box 6 in Table 5.4 are used for these simulations. WMetaD simulations are also performed with box 1, box 7 to understand the effects of box size on association constant. These simulations are conducted using PLUMED package together with CP2K code [42].

5.3 Results

5.3.1 One parameter study

In order to understand the effect of different potential parameters on La-Cl distances, simulations are conducted by varying one of A^{IJ} or B^{IJ} in Equation 5.5 or c^{IJ} in Equation 5.7. La-Cl distances as a function of parameter value is shown in Figure 5.3.

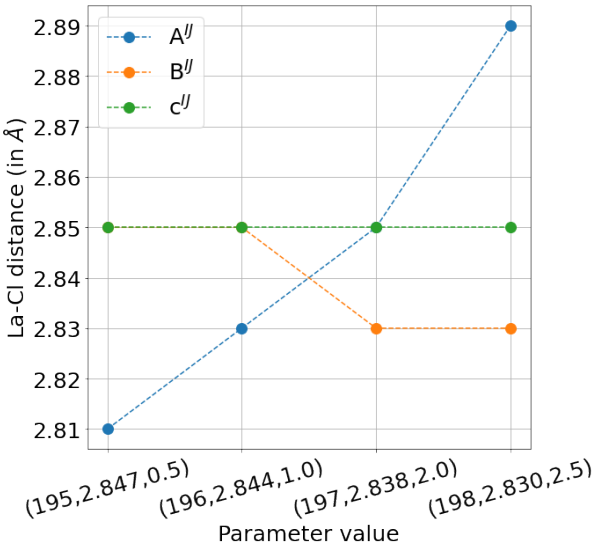

Figure 5.3: Variation of La-Cl distance with values of different PIM parameters. Set of numbers used as labels of the x-axis are the values of parameters A^{IJ}, B^{IJ}, c^{IJ} respectively

From Figure 5.3 it can be inferred that A^{IJ} (Equation 5.5) has the strongest correlation with La-Cl distance whereas no change in distance is seen with variation of c^{IJ} (Equation 5.6). Therefore, A^{IJ} was included in the iterative fitting routine (Figure 5.2) and c^{IJ} for La-Cl interactions was set to 1.0.

5.3.2 Validation

The final PIM parameters obtained with the iterative fitting procedure is given in Table 5.5.

The MSEs obtained on the different subsystems for forces and dipole moments is listed in Table 5.6. Plots comparing fitted and computed dipole moments and forces for aqueous Cl-O subsystem is shown in Figure 5.4, 5.5 respectively whereas the remaining plots are shown in Figures C1,C2,C3,C4 in Appendix C.

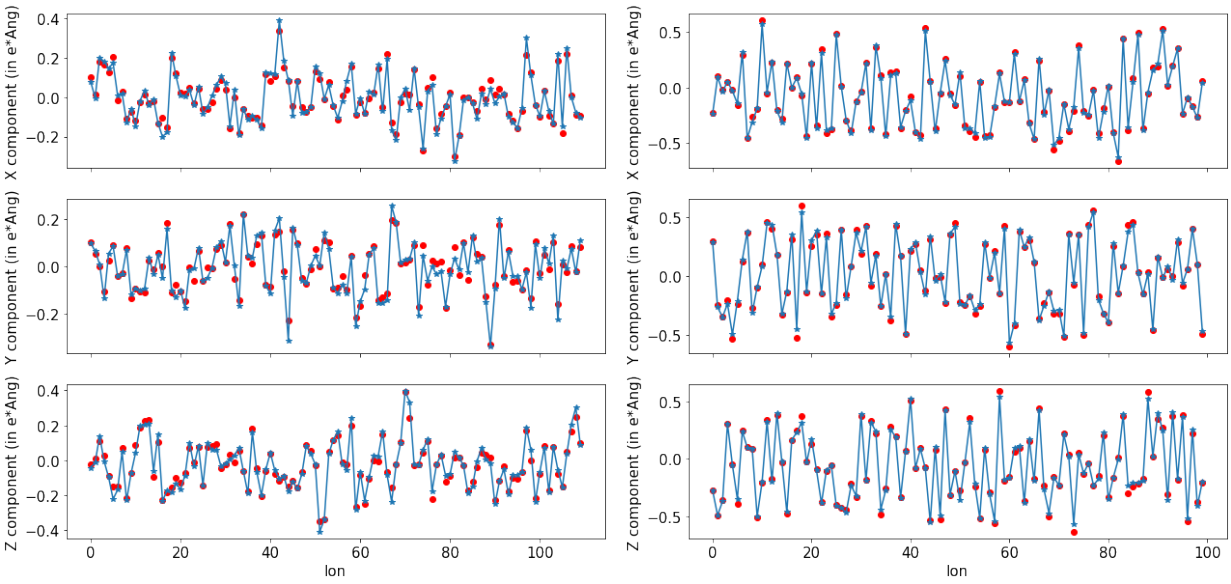

Figure 5.4: Comparison of fitted (dots) and computed dipole moments (solid line) of Cl^- ion (left) and water molecules (right) in aqueous Cl-O subsystem

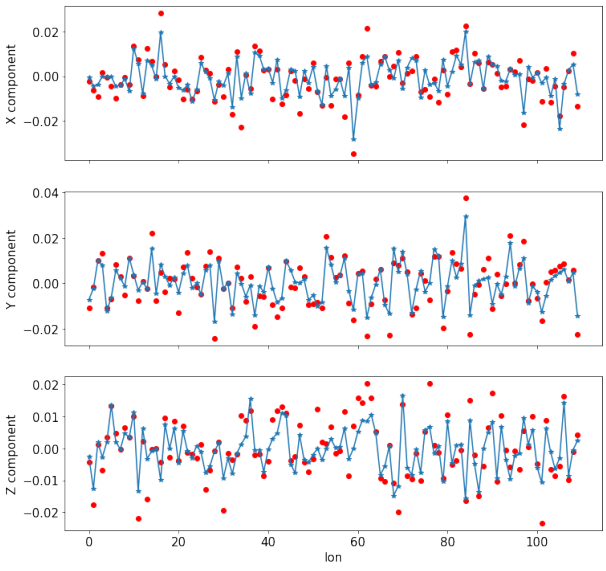

Figure 5.5: Comparison of fitted (dots) and computed atomic forces (solid line) on Cl^- ion in aqueous Cl-O subsystem

Table 5.5: Fitted parameters of PIM

Subsystem	Ion pair (I, J)	A^{IJ} (Ha)	B^{IJ} ($Å^{-1}$)	C_6^{IJ} ($HaÅ^6$)	C_8^{IJ} ($HaÅ^8$)	b_D^{IJ} ($Å^{-1}$)	b^{IJ} ($Å^{-1}$)	c^{IJ}
$LaCl_3$ crystal	La-La	1.5643	5.3542	2.8889	5.7830	5.3542	-	-
$LaCl_3$ crystal	La-Cl	194.6102	2.9768	4.4840	10.1427	2.9768	2.4498	1.0
$LaCl_3$ crystal	Cl-Cl	18.6488	2.4573	7.1163	17.9533	2.4573	-	-
aqueous La^{3+}	La-O	132.1557	3.3156	1.4961	2.7856	2.8447	3.7756	1.0242
aqueous Cl^-	Cl-O	973.7683	3.8222	2.2225	4.3390	0	3.0998	-0.7204
aqueous Cl^-	Cl-H	-	-	-	-	-	5.7893	3.8516

Table 5.6: χ^2 error on forces and dipole moments

Subsystem	Component	χ^2 error
$LaCl_3$ crystal	La^{3+} force	0.767
$LaCl_3$ crystal	Cl^- force	2.451
$LaCl_3$ crystal	La^{3+} dipole	0.7433
$LaCl_3$ crystal	Cl^- dipole	0.0369
aqueous La^{3+}	La^{3+} dipole	0.1603
aqueous La^{3+}	Water dipole	0.0065
aqueous La^{3+}	La^{3+} force	0.3983
aqueous Cl^-	Cl^- dipole	0.0963
aqueous Cl^-	Water dipole	0.0070
aqueous Cl^-	Cl^- force	0.5743

In order to check the performance of the fitted PIM, calculated bond lengths and coordination numbers are compared against available AIMD data. For proper validation of La-O and Cl-O parameters, production PIM simulations are carried out with boxes 2 and 3 in Table 5.3 and compared against corresponding AIMD data. La-Cl parameters are validated by comparing production PIM simulation with box 5 in Table 5.4 against AIMD data reported in Guan et al. [238]. Comparison of bond lengths calculated from the two models is shown in Table 5.7:

La-Cl, La-O and Cl-O pair correlation functions from PIM and AIMD are shown in Figures 5.6, 5.7. Figure 5.6 shows the advantage of PIM over N-POL MD. N-POL MD predicts strong La-Cl attraction that allows negligible ion exchange throughout the simulation. This

Table 5.7: Comparison of bond lengths and coordination numbers

Species	Bond length from PIM (in Å)	Bond length from AIMD (in Å)	CN from PIM	CN from AIMD
La-Cl	2.85	2.780	1.66	2.00
La-O	2.516	2.550	8.04	8.30
Cl-O	3.183	3.083	10.43	10.36

point is illustrated and discussed in greater detail later.

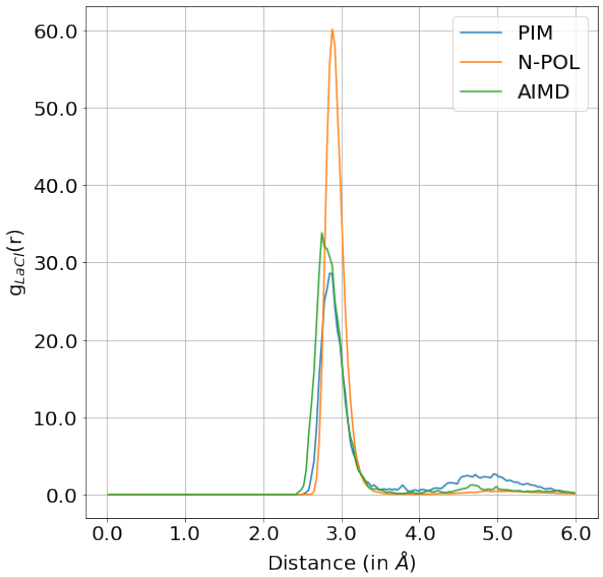

Figure 5.6: Comparison of pair correlation functions ($g_{LaCl}(r)$) obtained from PIM and AIMD

Good agreement between bond lengths predicted by AIMD and fitted PIM (difference is $< 5\%$ for all pair of species) instills confidence in our potential. We now calculate structural properties and association constants with the new potential, at supercritical and subcritical conditions.

5.3.3 Speciation and structure

Supercritical conditions: Pair correlation functions between different species, from PIM and N-POL MD at 773 K, 5 kbar are listed in Table 5.8. $g_{LaCl}(r)$ and $g_{LaO}(r)$ obtained at 773 K from box 1 with both models are shown in Figure 5.8. Remaining pair correlation functions are shown in Figure C5.

N-POL MD predicts longer La-Cl and La-O distances as compared to PIM. Number of

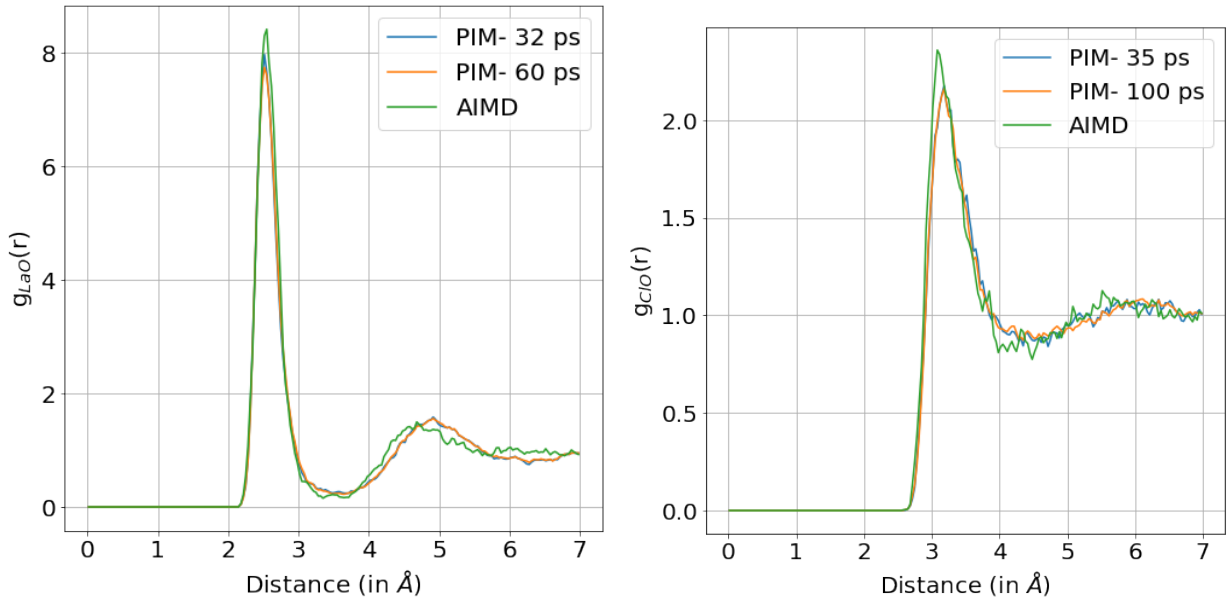

Figure 5.7: Pair correlation functions (left: $g_{LaO}(r)$, right: $g_{ClO}(r)$) obtained from PIM and AIMD. In order to assess convergence, correlation functions for PIM has been shown for 2 different simulation times

coordinating Cl^- ligands in the first coordination shell of La^{3+} increases with increase in concentration for both the models. Increase in Cl^- ligands is accompanied by decrease in number of hydration water molecules. As a result the total number of coordinating species around the central La^{3+} ion is ∼7 for PIM. For N-POL MD, total coordination number is ∼8 for boxes 1 and 2 whereas it is ∼7 for boxes 3 and 4. Contrary to PIM, N-POL MD with box 1 shows almost no La-Cl dissociation resulting in high CN. La-Cl pair correlation functions from PIM also show a prominent second coordination shell due to the formation of Solvent Shared Ion Pairs (SShIPs). Second coordination shells from N-POL MD simulations are characterized by lower maxima than PIM.

Figure 5.9 shows $g_{LaNa}(r)$ at 773 K in high concentration solutions. Both N-POL MD and PIM predict ∼5-6 Cl^- ligands in the first coordination shell for concentrations > 5 m. This is accompanied by ∼7-10 and ∼5-7 Na^+ cations within a distance of ∼7 Å for PIM and N-POL respectively. PIM also predicts shorter La-Na distances as compared to N-POL MD.

Subcritical conditions: Pair correlation functions between different species, from PIM and N-POL MD at 473 K, 200 bar are listed in Table 5.9. $g_{LaCl}(r)$ and $g_{LaO}(r)$ obtained at 473 K from box 1 with both models are shown in Figure 5.10. Remaining pair correlation functions are shown in Figure C6.

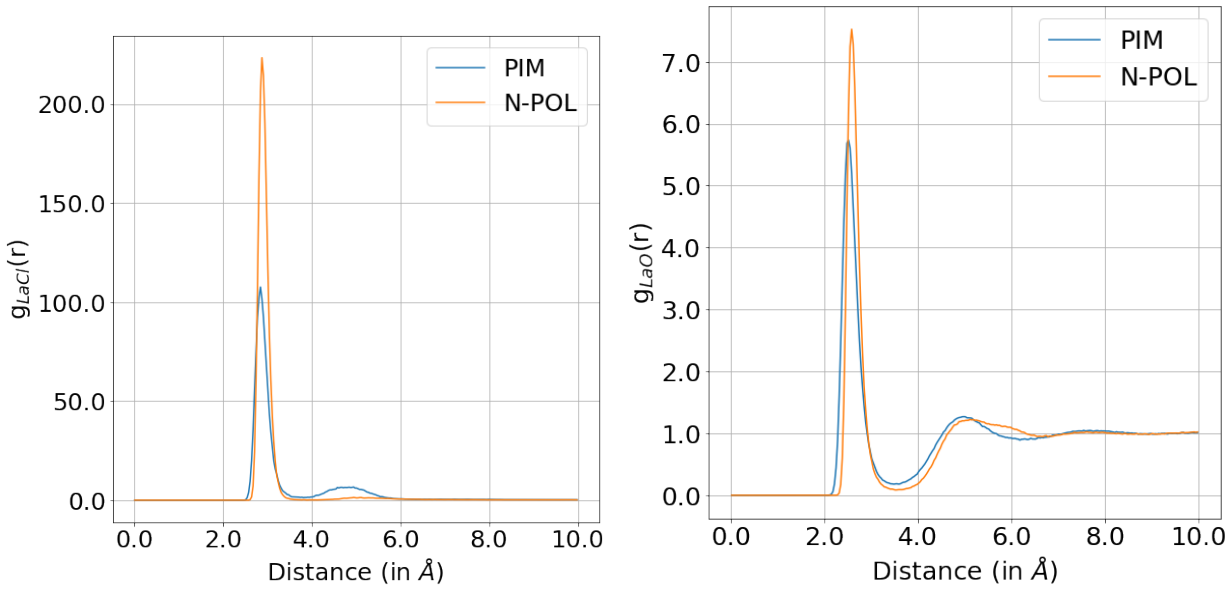

Figure 5.8: Left: $g_{LaCl}(r)$ obtained at 773 K with PIM and N-POL MD with box 1 Right: $g_{LaO}(r)$ obtained at 773 K with PIM and N-POL MD with box 1

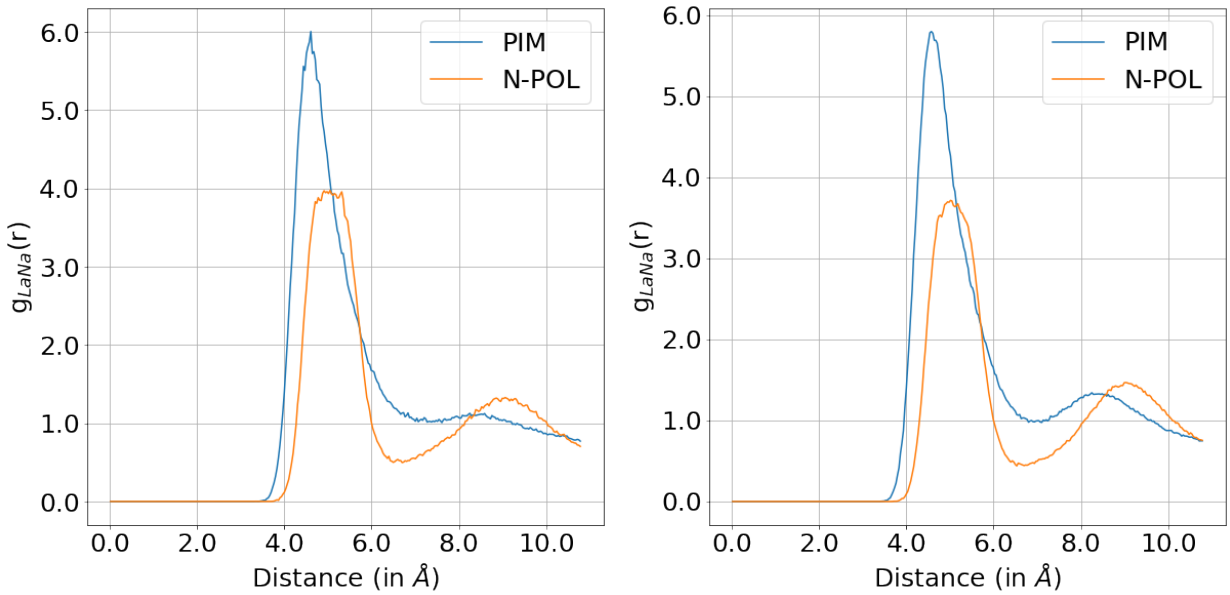

Figure 5.9: Left: $g_{LaNa}(r)$ obtained at 773 K with PIM and N-POL MD with box 3 Right: $g_{LaNa}(r)$ obtained at 773 K with PIM and N-POL MD with box 4

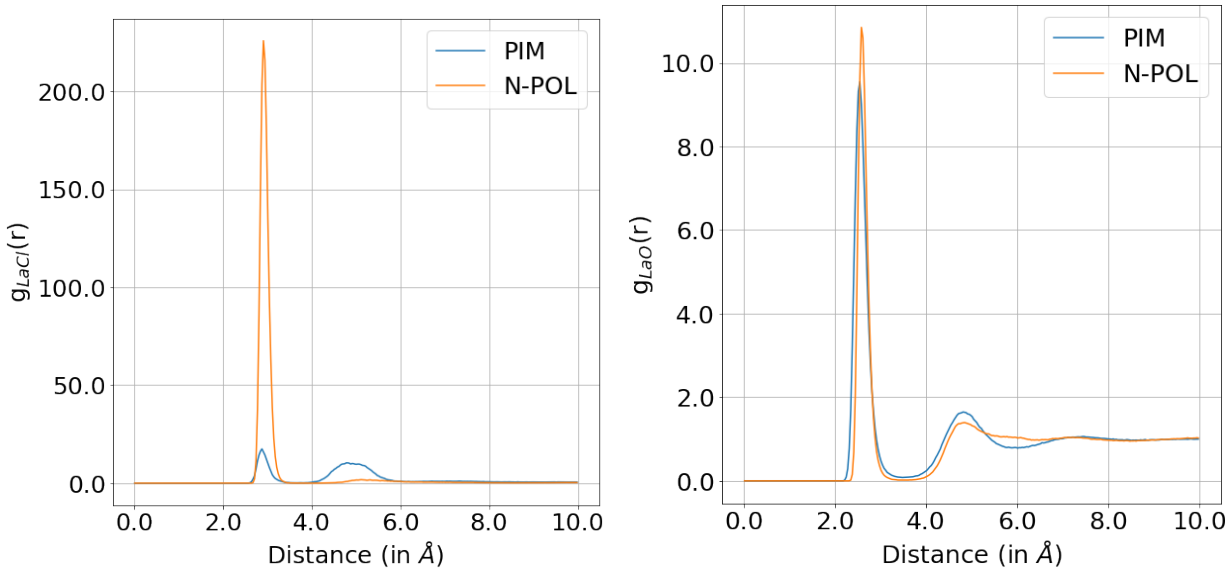

Figure 5.10: Left: $g_{LaCl}(r)$ obtained at 473 K with PIM and N-POL MD with box 1 Right: $g_{LaO}(r)$ obtained at 473 K with PIM and N-POL MD with box 1

N-POL MD predicts longer La-O distances whereas PIM predicts longer La-Cl distances except in box 1. La-Cl CN increases with increase in concentration for both the models. At low concentrations PIM predicts completely hydrated La^{3+} ion with ∼8 water molecules in the first hydration shell. At higher concentrations, water molecules are replaced by ∼8 Cl^- ions. N-POL MD on the contrary shows a gradual increase in La-Cl coordination from ∼2 at low concentrations to ∼5 at higher concentrations. This is accompanied by a gradual decrease in La-O coordination from ∼7 at low concentrations to ∼3 at higher concentrations. Total CN is ∼8 for PIM whereas it is ∼9-10 for N-POL MD. As in case of supercritical conditions, La-Cl pair correlation functions from PIM show a prominent second coordination shell due to the formation of SShIPs. Second coordination shells from N-POL MD simulations are characterized by lower maxima than PIM.

Figure 5.11 shows $g_{LaNa}(r)$ at 473 K in high concentration solutions. PIM shows very high La-Cl and La-Na CNs that increase with increasing concentration, in solutions with concentration > 5 m. High La-Cl and La-Na CNs are also seen in N-POL MD simulations in concentrated solutions but are lower than PIM.

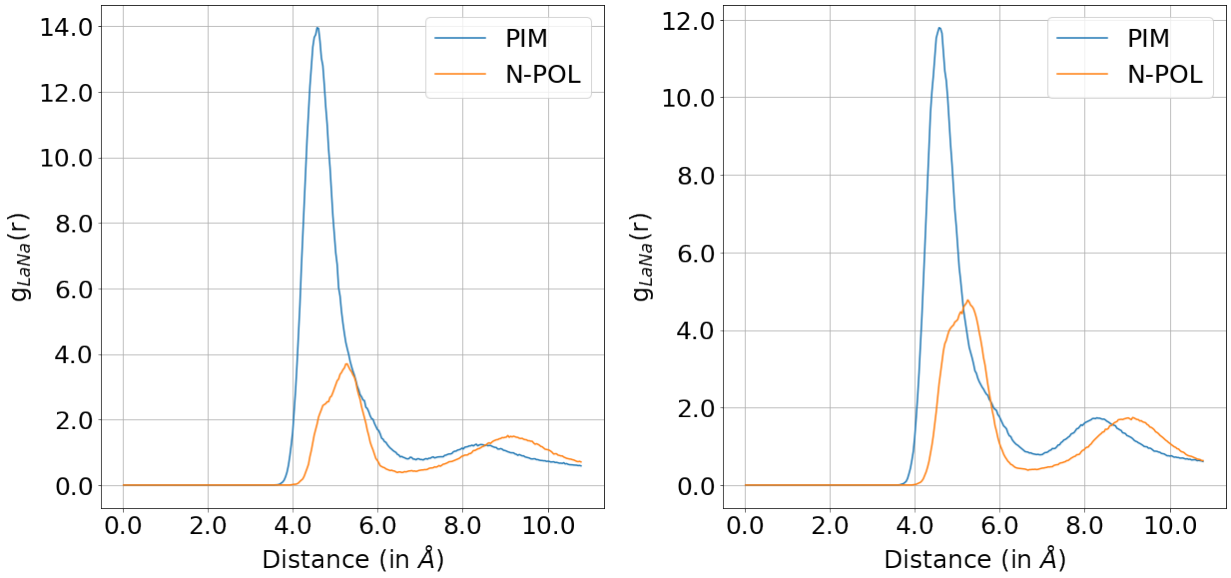

Figure 5.11: Left: $g_{LaNa}(r)$ obtained at 473 K with PIM and N-POL MD with box 3 Right: $g_{LaNa}(r)$ obtained at 473 K with PIM and N-POL MD with box 4

Table 5.8: Nearest neighbour distances and running coordination numbers for different ion pairs obtained from simulations at 773 K. CNs are rounded off to the nearest integers. Total CNs (see main text) are rounded off after addition. Naming convention used for different simulations is: box number-Model

Temperature	Box	Species	First maximum (in Å)	First minimum (in Å)	CN	Second maximum (in Å)	Second minimum (in Å)	CN	Third maximum (in Å)	Third minimum (in Å)	CN
773 K	1-PIM	La-Cl	2.83	4.00	1.5	4.84	6.00	2.0	-	-	-
		La-O	2.51	3.5	6.0	5.00	6.17	27.0	-	-	-
	AIMD [238]	La-Cl	2.76	-	2.0	-	-	-	-	-	-
		La-O	2.58	-	5.8	-	-	-	-	-	-
	2-PIM	La-Cl	2.88	4.00	3.0	5.00	6.00	5.0	-	-	-
		La-O	2.51	3.50	4.5	5.00	6.24	27.0	-	-	-
	3-PIM	La-Cl	2.86	4.00	5.0	4.97	5.54	7.0	6.30	-	-
		La-O	2.48	3.50	2.0	5.12	5.54	11.0	6.13	7.00	30.0
		La-Na	4.60	7.00	7.00	-	-	-	-	-	-
	4-PIM	La-Cl	2.88	4.00	6.0	5.00	5.54	8.0	6.24	-	-
		La-O	2.48	3.50	1.0	5.21	5.61	9.0	6.28	7.00	23.0
		La-Na	4.60	7.00	10.0	-	-	-	-	-	-
	1-N-POL MD	La-Cl	2.88	4.00	2.3	-	-	-	-	-	-
		La-O	2.58	3.50	6.0	5.15	6.67	35.0	-	-	-
	2-N-POL MD	La-Cl	2.90	4.00	4.8	-	-	-	-	-	-
		La-O	2.58	3.50	3.0	5.60	6.80	35.0	-	-	-
	3-N-POL MD	La-Cl	2.88	4.00	5.0	6.92	-	-	-	-	-
		La-O	2.57	3.50	2.0	5.90	7.04	36.0	-	-	-
		La-Na	5.00	6.60	5.0	-	-	-	-	-	-
	4-N-POL MD	La-Cl	2.88	4.00	5.4	6.92	-	-	-	-	-
		La-O	2.61	3.50	2.0	5.80	7.00	31.0	-	-	-
		La-Na	5.00	6.70	7.0	-	-	-	-	-	-

Table 5.9: Nearest neighbour distances and running coordination numbers for different ion pairs obtained from simulations at 473 K. Naming convention used for different simulations is: box number-Model

Temperature	Box	Species	First maximum (in Å)	First minimum (in Å)	CN	Second maximum (in Å)	Second minimum (in Å)	CN	Third maximum (in Å)	Third minimum (in Å)	CN
473 K	1-PIM	La-Cl	2.87	4.00	0.0	4.88	6.00	2.0	-	-	-
		La-O	2.53	3.50	8.0	4.82	6.00	28.0	-	-	-
	AIMD [238]	La-Cl	2.86	-	1.0	-	-	-	-	-	-
		La-O	2.55	-	7.2	-	-	-	-	-	-
	2-PIM	La-Cl	2.98	4.00	0.0	5.00	6.00	4.0	-	-	-
		La-O	2.53	3.50	8.0	4.76	6.00	28.0	-	-	-
	3-PIM	La-Cl	2.92	4.00	7.0	6.25	8.00	20.0	-	-	-
		La-Na	4.60	7.00	10.0	-	-	-	-	-	-
	4-PIM	La-Cl	2.93	4.00	8.0	6.25	8.00	28.0	-	-	-
		La-Na	4.60	7.00	14.0	-	-	-	-	-	-
	1-N-POL MD	La-Cl	2.90	4.00	2.0	-	-	-	-	-	-
		La-O	2.58	3.50	7.0	4.78	6.50	33.0	-	-	-
	2-N-POL MD	La-Cl	2.90	4.00	2.0	5.14	6.00	3.0	7.18	9.00	6.0
		La-O	2.58	3.50	7.0	4.75	6.00	28.0	-	-	-
	3-N-POL MD	La-Cl	2.91	4.00	4.0	5.38	6.00	5.0	6.89	9.00	11.0
		La-O	2.59	3.50	4.4	5.0	6.72	33.0	-	-	-
		La-Na	5.00	6.60	3.0	-	-	-	-	-	-
	4-N-POL MD	La-Cl	2.92	4.00	5.0	6.83	9.00	18.0	-	-	-
		La-O	2.60	3.50	3.0	5.0	7.00	30.0	-	-	-
		La-Na	5.00	6.60	8.0	-	-	-	-	-	-

5.3.4 Association constants

WMetaD is used to calculate the reaction constants and the energy barriers associated with different La-Cl association reactions by using Equation 5.15. r_c is taken as half of the edge length of the respective simulation boxes (∼6.10-6.30 Å for boxes 5,6 and ∼10.00-10.80 Å for boxes 1,7 in Table 5.4). r_i is taken as ∼2.8 Å in all biased simulations corresponding to the distance of first minimum in FES. These are listed in Table 5.10 (PMF data from Guan et al. [238] is used to recalculate $logK_{eq}^{\infty}$ using Equation 5.15). To make credible comparison, association constants obtained from small simulation boxes were compared against AIMD data. Effects of box sizes are discussed later. La-Cl complexes show step-wise association reactions as,

$$\mathsf{LaCl}_{n-1}{}^{4-n} + \mathsf{Cl}^{-} \longrightarrow \mathsf{LaCl}_{n}{}^{3-n} \tag{5.20}$$

The reactions for successive values of n starting from $n = 1$ in Equation 5.20 are referred to as reaction 1,2,3 respectively in the remaining paper.

Energy barriers for dissociation are approximated by the difference in G between the first energy maximum and first energy minimum in the FES as shown in Figure 5.12 (right). Relative stabilities of different metastable states are estimated by calculating free energy difference between them as shown in Figure 5.12 (right).

WMetaD is carried out with La-Cl inter-ionic distance of the dissociating Cl^- as the CV. The other Cl^- ligands are prevented from dissociating or associating by restraining them to a fixed distance either close to or far away from the La^{3+} ion. For example, in case of reaction 2, one Cl^- ligand is restrained at ∼3 Å, the other is allowed to associate while the third one (to be associated in the next step) is restrained at ∼8-10 Å. This is illustrated in Figure 5.12 (left, inset). In dilute solutions ions generally exist in equilibrium as Contact Ion Pairs (CIPs - ion pairs where anion and cation are in close contact), Solvent Shared Ion Pairs (SShIPs - ion pairs where anion and cation share hydration water molecules) and Solvent Separated Ion Pairs (SSIPs - ion pairs where anion and cation form their individual hydration shells) as shown in Figure 5.13. These can be distinguished from each other using the La-Cl inter-ionic distance thereby allowing proper sampling of all the metastable states.

Figure 5.12 shows the FES of reaction 2 obtained from PIM and N-POL MD at super-critical and subcritical conditions. FES for other reactions from PIM and N-POL MD are

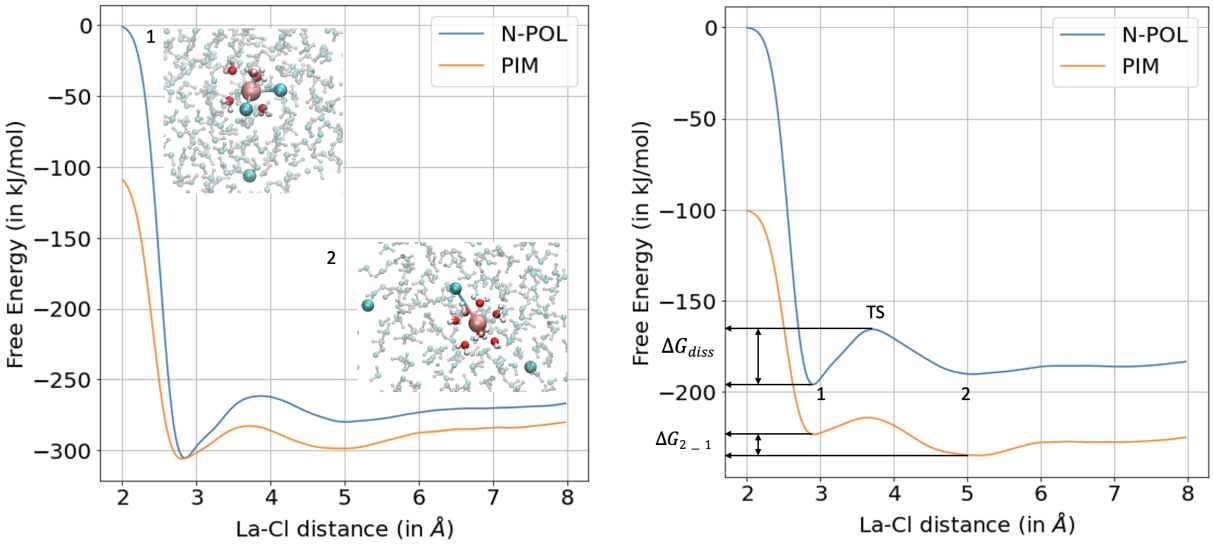

Figure 5.12: Left: FES of $LaCl^{2+} + Cl^{-} \longrightarrow LaCl_2^{+}$ reaction at 773 K. Inset 1 shows the associated state where two Cl^{-} ions (green) are coordinated to the central La^{3+} ion (brown) while the third one is restrained at a long distance. Inset 2 shows the dissociated state where one of the coordinating Cl^{-} ions is at a long distance. Right: FES of $LaCl^{2+} + Cl^{-} \longrightarrow LaCl_2^{+}$ reaction at 473 K. ΔG_{diss} is the energy barrier for dissociation calculated as the difference in free energy between state 1 (associated state) and the high energy Transition State (TS). ΔG_{2-1} is the energy difference between states 2 and 1

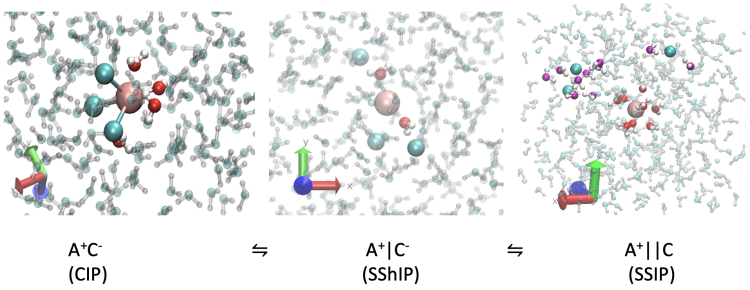

Figure 5.13: Different ion pairs obtained from simulations. Brown balls represent La^{3+} ion whereas green balls represent Cl^{-} ions. In case of CIPs and SSIPs, red balls represent hydration water molecules of La^{3+}, and magenta balls represent hydration water molecules of Cl^{-} ions. For SShIPs red balls are the shared hydration water molecules

shown in Figures C7, C8. All FES primarily show two metastable states indicated by energy minima at ∼3 Å and at ∼5 Å (marked by 1 and 2 in Figure 5.12 (right)). State 1 is attributed to the CIPs whereas state 2 is populated by SShIPs and these metastable states are separated by a high energy Transition State (TS). A change in relative stabilities of CIPs and SShIPs predicted by the two models from subcritical to supercritical conditions is observed, as shown in Figure 5.14.

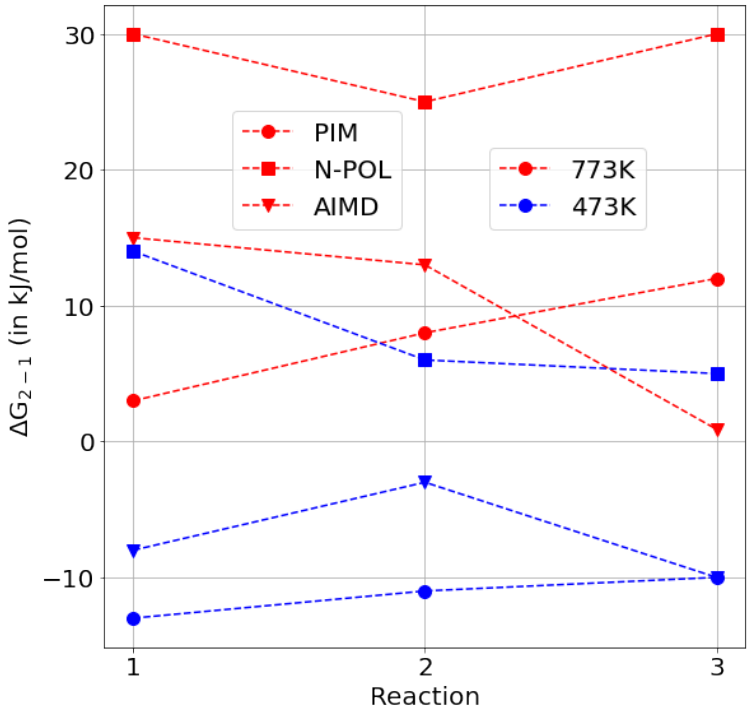

Figure 5.14: Comparison of relative stabilities of CIPs and SShIPs given by ΔG_{2-1} between N-POL MD, PIM and AIMD [238] at different conditions

From Table 5.10, high values of energy barrier for dissociation as compared to thermal energy (k_BT), can be seen. This creates kinetic bottleneck in unbiased simulations thereby explaining the motivation of using WMetaD for this system. Further, it can be inferred that PIM predicts lower energy barriers for dissociation as compared to N-POL MD for all the reactions at subcritical as well as supercritical conditions. PIM predicts increase in energy barriers for successive dissociation reactions at both conditions. N-POL MD predicts almost constant energy barriers at 773 K. At 473 K, an increase in energy barrier from reaction 1 to 2 followed by decrease in reaction 3 is seen.

Both the models predict positive values of $logK_{eq}^{\infty}$ for all the stepwise association reactions due to the tendency of ions to associate in water at high temperatures. In general calculated

Table 5.10: Energy barriers and reaction constants of La-Cl association reactions from different models at supercritical conditions (773 K) and subcritical conditions (473 K)

Temperature	Reaction	Method	Energy barrier (in k_BT)	$logK_{eq}^{\infty}$
773 K	$La^{3+} + Cl^- \longrightarrow LaCl^{2+}$	PIM	2.97	2.86
		N-POL	6.19	3.51
		AIMD [238]	4.65	2.72
	$LaCl^{2+} + Cl^- \longrightarrow LaCl_2^+$	PIM	3.57	2.20
		N-POL	6.17	2.64
		AIMD [238]	4.10	1.66
	$LaCl_2^+ + Cl^- \longrightarrow LaCl_3$	PIM	4.07	1.53
		N-POL	6.22	1.77
		AIMD [238]	3.51	0.53
473 K	$La^{3+} + Cl^- \longrightarrow LaCl^{2+}$	PIM	2.25	2.29
		N-POL MD	7.12	2.45
		AIMD [238]	3.73	1.81
	$LaCl^{2+} + Cl^- \longrightarrow LaCl_2^+$	PIM	2.46	1.60
		N-POL MD	7.47	1.60
		AIMD [238]	4.60	1.19
	$LaCl_2^+ + Cl^- \longrightarrow LaCl_3$	PIM	3.10	0.97
		N-POL MD	6.67	0.76
		AIMD [238]	3.90	0.18

values of $logK_{eq}^{\infty}$ with PIM are lower for all the association reactions at subcritical as well as supercritical conditions as compared to N-POL MD. This is because of deep energy basins predicted by N-POL MD for CIPs which make them more exothermic than PIM. Both models show increase in $logK_{eq}^{\infty}$ with increase in temperature. It has to noted that FES and $logK_{eq}^{\infty}$ have a many to one relation. Therefore, accurate prediction of the underlying FES is of paramount importance to retrieve reliable association constants.

5.4 Discussion

5.4.1 Speciation and structure : Comparison with available AIMD and experimental data

The newly fitted PIM predicts La-Cl bond distances closer to AIMD data as compared to N-POL MD (Table 5.8) at both the studied conditions. However, distances from both PIM

and N-POL MD are shorter than the 2.90-3.02 Å range predicted by experiments at similar conditions [238]. Increase in La-Cl bond lengths at higher concentrations of Cl^- and in the presence of a second cation (Na^+ in this case) is seen for both the models consistent with AIMD simulations at ambient conditions [251, 250] and at higher temperatures [238]. Both the models also predict decrease in La-Cl bond lengths with increase in temperature consistent with experiments [238] and AIMD [238] at similar conditions. N-POL MD simulations with box 1 at both conditions show almost no La-Cl dissociation resulting in CN > 2. The presence of high energy barriers for dissociation ($\sim 7\, k_B$T, Table 5.10) at both conditions is the reason why La-Cl dissociation is kinetically unfavourable in N-POL MD. Similar conclusions were drawn by Zhang and Yan [127] with a different set of pair potential at similar temperature conditions. This is remedied by PIM which softens the La-Cl interactions resulting in significant dissociation at both conditions, consistent with AIMD simulations and Extended X-ray Absorption Fine Structure (EXAFS) data [238] at similar conditions. At 473 K ΔG_{2-1} is negative for PIM reactions (Figure 5.14) meaning SShIP is more stable state as compared to CIP. This is also seen in unbiased simulations (PIM with box 1, Table 5.9) where almost all Cl^- ligands preferentially populate the second coordination shell at a distance of $\sim$5 Å.

Figure 5.15 shows comparison of total number of ligands and number of Cl^- ligands in the first coordination shell. With increase in temperature, static dielectric constant of water decreases promoting ion association. This effect is seen in PIM where an increase in $\sim$1 Cl^- ion is observed from subcritical to supercritical conditions, consistent with AIMD data [238], EXAFS studies [238], XAS studies [254] and HKF model data [27]. N-POL MD predicts higher Cl^- coordination and negligible change with temperature. In terms of absolute number of Cl^- ligands, PIM data is in good agreement with HKF model [26] generated using solubility data from Migdisov et al. [27] and EXAFS data [238], whereas an overestimation of $\sim$1 ligand is observed for N-POL MD. With decrease in temperature, PIM shows an increase in total ligands of $\sim$1 in agreement to EXAFS data [238]. XAS data [254] predicts increase in $\sim$3 ligands. However, XAS generally overestimates coordination numbers indicated by the 10-fold coordinated La^{3+} predicted at subcritical conditions [254]. N-POL MD predicts negligible change in total ligands with temperature. In terms of absolute number of total ligands in first coordination shell, PIM data is in good agreement with EXAFS [238] and AIMD [238] data whereas an overestimation by $\sim$1 ligand is predicted by N-POL MD.

PIM also shows better agreement with XAS studies [254] in terms of total number of ligands as compared to N-POL MD at 773 K. In general, La-O distances predicted by PIM are shorter than AIMD and experiments [238] at similar conditions.

High La-Cl CNs ranging from ∼5-6 at 773 K and ∼4-8 at 473 K is seen in concentrated solutions with PIM as well as N-POL MD (Table 5.8, 5.9). AIMD and EXAFS studies [238] predict a maximum of 4 Cl^- ligands at 773 K and ∼1-2 Cl^- ligands at 473 K. However, it should be noted that the AIMD simulations were performed with a maximum of only two Na^+ cations. In this respect both PIM and N-POL MD seems to be overestimating the CNs at higher concentrations. An analysis of the individual trajectories revealed the formation of large La-Cl-Na clusters in these high concentration solutions as shown in Figure 5.16 indicating a strong tendency of crystallization. Although precipitation of REEs (mostly REE fluorites) from highly concentrated NaCl solutions has been attributed to the formation of several REE ore deposits [29], our simulations cannot confirm whether precipitation takes place because of the lack of gravitational force in the simulations (and hence phases do not readily segregate) and the inability to differentiate between different phases in visualised trajectories. NaCl EOS from Driesner et al. [271] predict single phase fluid at concentrations of ∼5 m and ∼8 m at 773 K. At 473 K, single phase fluid is predicted at ∼5 m concentration whereas a two phase fluid+halite system is predicted at ∼8 m concentration. Also, it should be noted that the La-Na pair correlation functions (Figure 5.9, 5.11) do not converge even at 10 Å distance. This indicates that there are significant correlations between La^{3+} and periodic images of Na^+ due to small simulation boxes which may affect La-Na coordination numbers.

5.4.2 Ion association thermodynamics: Comparison with available AIMD and experimental data

In general, association constants predicted by AIMD, N-POL MD and PIM follow the order, $logK^{\infty}_{eq,N-POL} > logK^{\infty}_{eq,PIM} > logK^{\infty}_{eq,AIMD}$. This is illustrated in Figure 5.17. Although PIM gives better $logK^{\infty}_{eq}$ values as compared to N-POL, the disagreement with AIMD is still large (∼1 log units in some cases). Table 5.11 shows the cumulative association constants, $log\beta$ obtained from N-POL MD, PIM, AIMD [238] and HKF model parameterized with solubility data from Migdisov et al. [27] till ∼350 °C. This is obtained by cumulative addition of

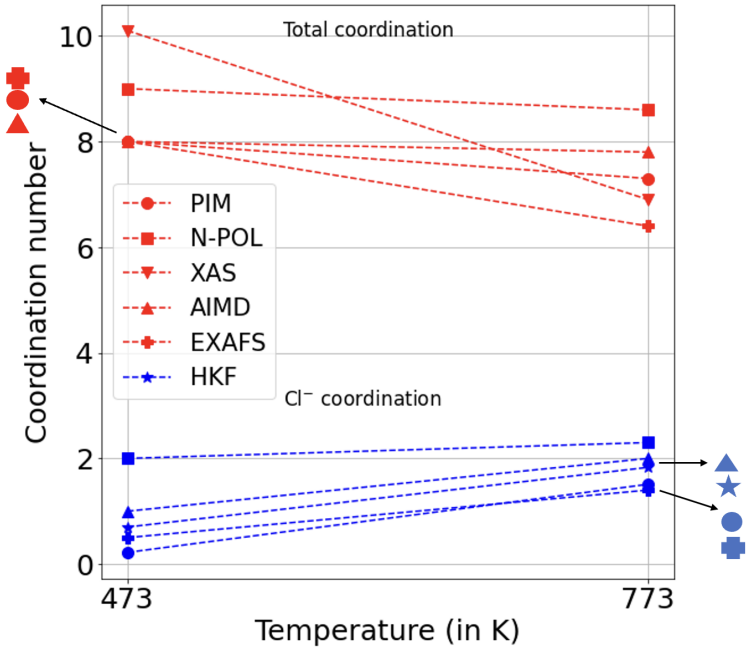

Figure 5.15: Comparison of coordination numbers from PIM, N-POL MD with XAS [254], EXAFS [238], AIMD [238] and HKF model [26] data

$log K^{\infty}_{eq}$ values shown in Table 5.10 and hence follow the same descending order as association constants. $log\beta$ predicted by PIM for reactions 2,3 at 473 K are in better agreement with thermodynamic model than AIMD and N-POL MD. Both the models predict increase in $log\beta$ values of $LaCl^{2+}$ and $LaCl_2^{+}$ with increase in temperature, in agreement with data from HKF model till ~400 °C [27] and AIMD data [238]. Due to the increased stability of La-Cl complexes at higher temperatures, step-wise addition of Cl^- into the coordination sphere of La^{3+} becomes more exothermic at higher temperatures.

The relative stabilities of the metastable CIPs and SShIPs predicted by PIM are in agreement to AIMD data as shown in Figure 5.14. Both predict CIPs as the more stable state at 773 K and SShIPs as the more stable state at 473 K in contrary to N-POL MD that always predicts CIPs as the more stable state at both conditions. However, absolute values of ΔG_{2-1} from PIM are generally lower than those from AIMD. Zhang and Yan [127] also predict similar trends of energy barrier and relative stabilities with a different set of non polarizable pair potential at similar temperature conditions.

From Table 5.11, it may seem that PIM and N-POL MD are more accurate than AIMD in predicting formation constants. However, we do not make such conclusions here because

[1]values are from two the data sets shown in Migdisov et al. [27]

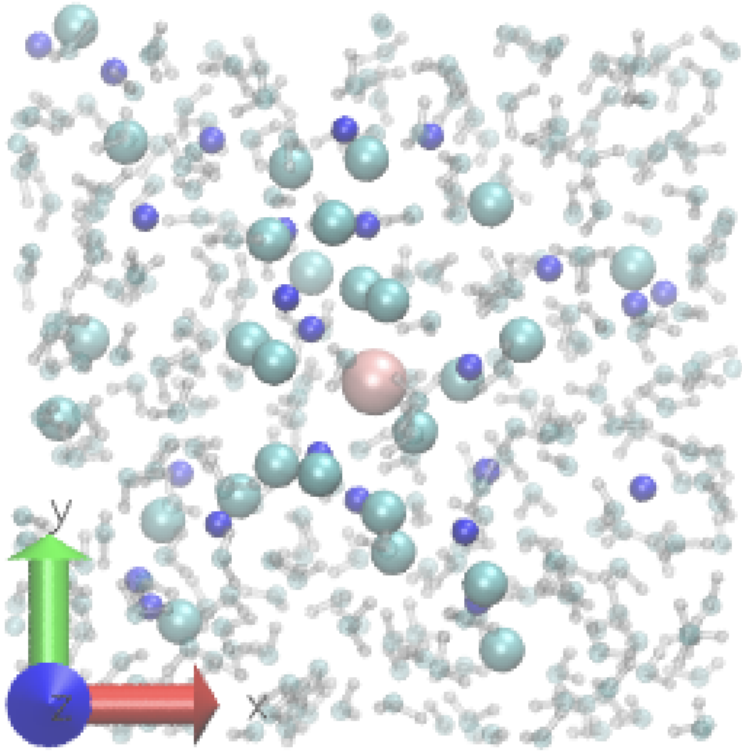

Figure 5.16: Snapshot of La-Cl-Na clusters formed in PIM and N-POL MD simulations in high concentration solutions

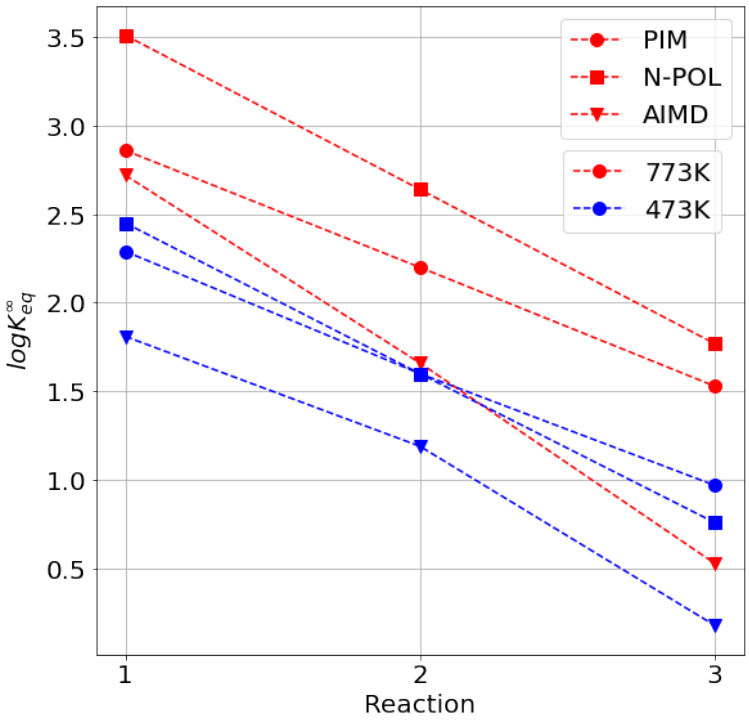

Figure 5.17: Comparison of $logK^{\infty}_{eq}$ of different association reactions from N-POL MD, PIM and AIMD at different conditions

formation constants are derived from the corresponding reaction FES. As discussed above, FES from N-POL MD are unable to predict the relative stabilities of the different metastable states correctly. We do not have any data to prove that FES from PIM are more accurate than their AIMD counterparts.

5.4.2.1 Effect of box size on association constant

MD simulations use periodic boundary conditions to replicate bulk liquid systems. The success of this assumption depends on the size of the simulation box which determines the distance between the particles and their nearest images. A small simulation box would mean lower distances between particles and their images leading to higher interactions between them which is not desirable as this imposes correlations not expected in fluids. To understand the effect of box sizes on calculated values of $logK^{\infty}_{eq}$ and energy barriers, WMetaD simulations were conducted with boxes 1 and 7 in Table 5.4 with the newly fitted PIM. The results are presented in Figure 5.18.

Figure 5.18 shows minor disagreements (maximum difference of $\sim$0.5 $k_B T$ in energy bar-

Table 5.11: Cumulative association constants $log\beta$ obtained from different models

Temperature	Reaction	Method	$log\beta$
773 K	$La^{3+} + Cl^- \longrightarrow LaCl^{2+}$	PIM	2.86
		N-POL	3.51
		AIMD [238]	2.72
	$La^{3+} + 2\,Cl^- \longrightarrow LaCl_2^+$	PIM	5.06
		N-POL	6.15
		AIMD [238]	4.38
	$La^{3+} + 3\,Cl^- \longrightarrow LaCl_3$	PIM	6.59
		N-POL	7.92
		AIMD [238]	4.91
473 K	$La^{3+} + Cl^- \longrightarrow LaCl^{2+}$	PIM	2.29
		N-POL MD	2.45
		AIMD [238]	1.81
		Model [27]	2.29, 2.38[1]
	$La^{3+} + 2\,Cl^- \longrightarrow LaCl_2^+$	PIM	3.89
		N-POL MD	4.05
		AIMD [238]	3.00
		Model [27]	3.86
	$La^{3+} + 3\,Cl^- \longrightarrow LaCl_3$	PIM	4.86
		N-POL MD	4.81
		AIMD [238]	3.18

riers and ∼0.25 log units in association constants) between results from the two simulation boxes. The technique used in calculating association constants in this work boils down to calculating $g^{\infty}(r)$ which is the radial distribution function in the limit of infinite dilution. For highly dilute solutions obtaining $g^{\infty}(r)$ from MD simulations is difficult as sampling deficiency occurs due to rather short simulation times, leading to poor statistics. Therefore the more practical way to do it is to apply Equation 5.16. If it was possible to simulate a 'theoretically' infinitely dilute solution (the simulation box is big enough with adequate number of water molecules and NaCl particles to reach bulk behaviour), $g^{\infty}(r)$ would converge to 1 and hence $\phi(r)$ would converge to 0 at $r \to \infty$, which is the dissociated state in the ideal case. However due to extreme long range nature of Coulomb interactions and limited number of NaCl pairs, this is difficult to achieve even in simulation boxes with edge lengths of ∼30 Å [269]. Hence, the dissociated state is taken to be the limiting continuum behaviour where charged particles interact via screened Coulomb interaction given by, $\phi_{analytical}(r) = \frac{q_i q_j}{4\pi\epsilon_0\epsilon_r r}$. FES obtained from simulation boxes of different sizes are rigidly shifted so that their tails

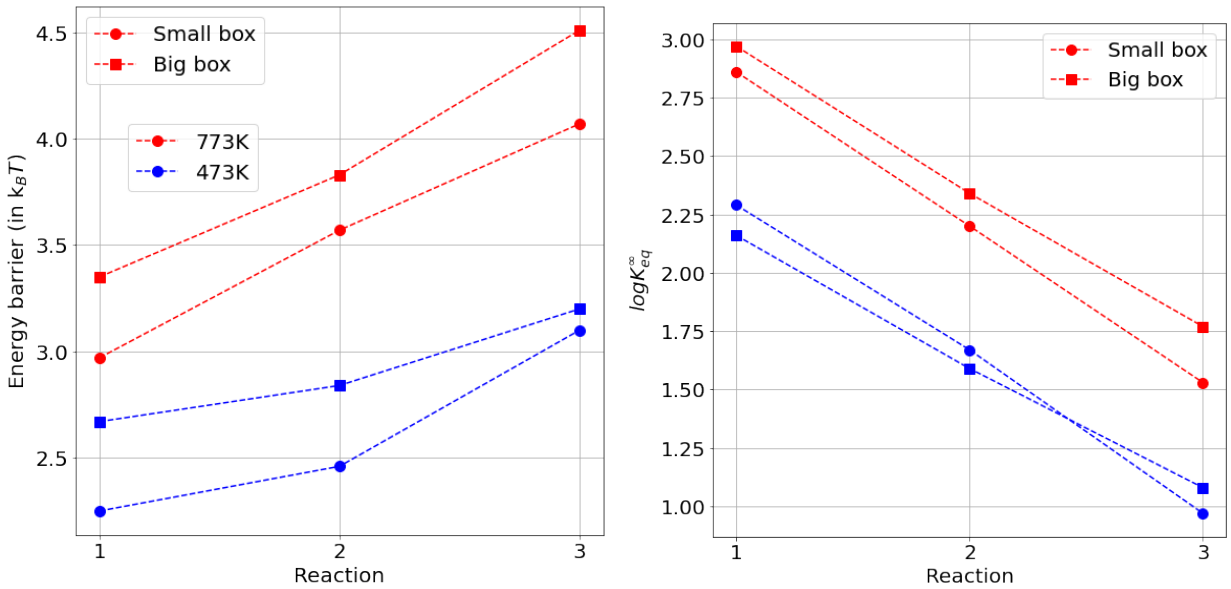

Figure 5.18: Left: Comparison of energy barriers from small and big simulation boxes Right: Comparison of $logK^{\infty}_{eq}$ of association reactions from small and big simulation boxes. Limits of ∼6.30 Å and ∼11 Å were used for small and big boxes respectively

coincide with the analytical solution at long distances as shown in Figure 5.19. The difference in the $logK^{\infty}_{eq}$ values arise due to difference in length of the tail coinciding with the analytical solution. However, once the FES is properly aligned to the analytical solution dependence of $logK^{\infty}_{eq}$ on cutoff distance is weak beyond ∼5 Å (corresponding to SShIP) as shown in Figure 5.20 and also in Aufort et al. [269].

5.5 Conclusion

We fit a new polarizable potential for La^{3+} in Cl^{-} bearing hydrothermal systems from first principle AIMD simulations. Production simulations were performed at 773 K and 473 K to calculate structural and thermodynamic properties of La^{3+} in dilute to concentrated solutions.

Newly fitted PIM interaction potential gives good estimates of La-Cl and La-O distances at the studied conditions. PIM provides better estimates of total coordination and Cl^{-} coordination numbers as compared to N-POL MD in dilute solutions. It also reproduces the increase in La-Cl coordination with increase in temperature observed in experiments. However, the La-O distances predicted by PIM are shorter than experimental data at sim-

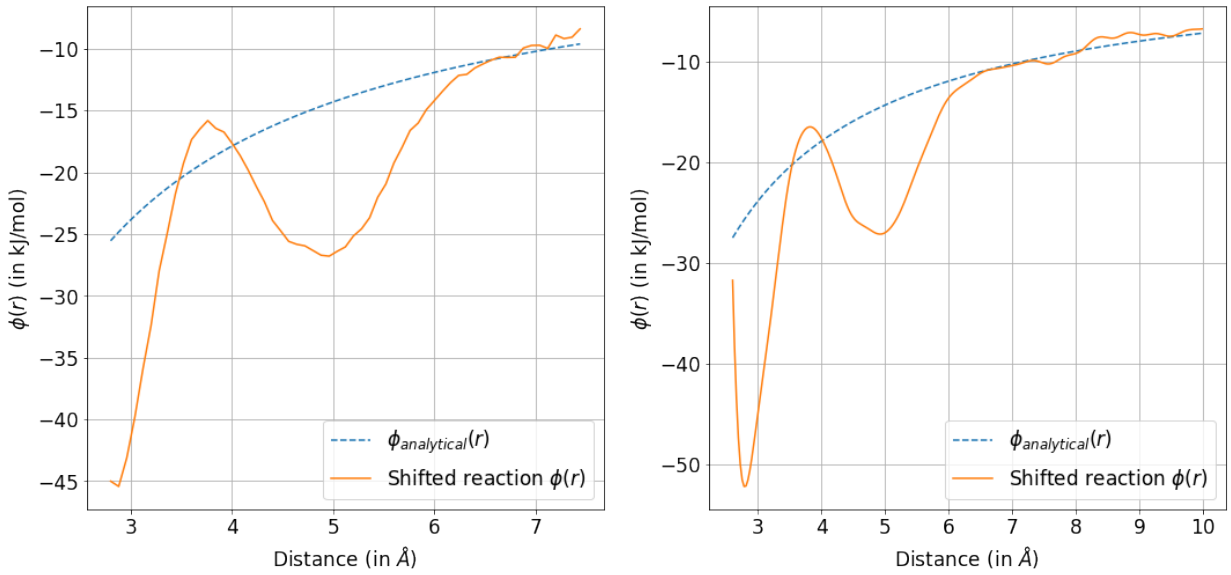

Figure 5.19: $\phi(r)$ obtained from small simulation box (left) and big simulation box (right) aligned to the analytical solution. $\phi(r)$ from larger box shows a longer tail coinciding with the analytical solution

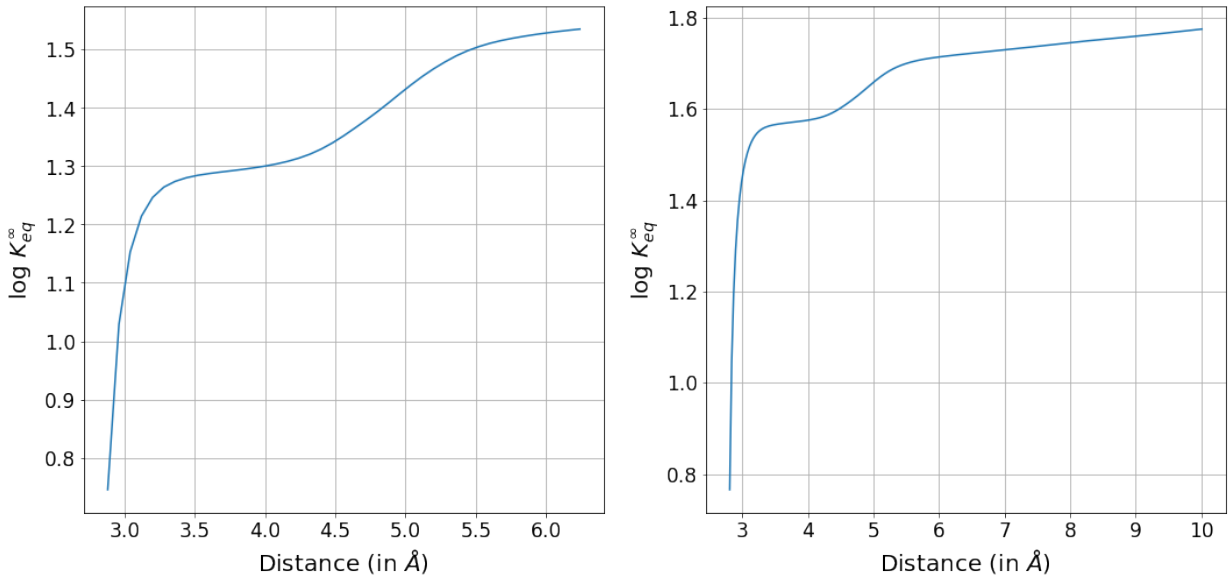

Figure 5.20: Convergence of $logK_{eq}^{\infty}$ in small (left) and big simulation boxes (right)

ilar conditions. In concentrated solutions, both models predict formation of big La-Cl-Na clusters. However, the authenticity of this finding has to be verified by experimental/AIMD simulation data.

Calculation of association constants reveal increasing stability of $LaCl^{2+}$ and $LaCl_2^+$ complexes with increasing temperature. In general formation constants calculated from PIM simulations are closer to AIMD/HKF model data as compared to N-POL MD. The cumulative formation constants predicted by PIM at 473 K are in better agreement with those from HKF model as compared to both AIMD and N-POL MD. This is despite the fact that no energy values are used in fitting the PIM. Relative stabilities of CIPs and SShIPs predicted by PIM are in agreement with AIMD at both the conditions. Altogether, the newly fitted PIM gives more precise structural and thermodynamic insights into dilute La-Cl bearing hydrothermal fluids at both the studied temperature and pressure conditions as compared to simple pair potentials, with reasonable computation cost. Our results underpin the importance of an explicit description ion polarizabilties to retrieve reliable structural and thermodynamic information in hydrothermal systems containing highly polarizable anions (like Cl^-) and cations with high polarization power (like La^{3+}).

Chapter 6

Discussion and future outlook

MD simulations offer valuable and quantitatively reproducible structural and thermodynamic properties of geochemical fluids. AIMD simulations in Chapter 3 show the presence of SO_4^{2-} anions in supercritical fluids containing Na^+ ions. These fluids can therefore mobilise metal ions by forming different sulfate complexes. However, in the absence of Na^+ ions, HSO_4^- anions are present in abundance and metal-bisulfate complexes are expected. Speciation studies of solvents help us delineate the nature and genesis of ore bodies helping in their recovery and extraction. Frequencies of vibrational modes along with the absorption cross-section are frequently used by experimentalists to determine speciation of the fluid under investigation. Using MD simulations 'inverts' the problem because we now have an independent way of determining speciation from MD simulation trajectories. This allows direct assignment of vibrational bands to molecular motions, complementing experimental observations. Mode projection analysis used in Chapter 3 provides a tool to isolate spectroscopically important vibrational modes in complex aqueous fluids which have several closely spaced modes. Since individual ion pairs and their lifetimes can be elucidated from simulation trajectories the effects of contact ion pairs in vibrational spectra can be studied with more clarity. In Chapter 4 we demonstrate the ability of CMD to reproduce experimentally observed trends in electrical conductivity of NaCl solutions in supercritical conditions. Bulk density and ion association are shown to be the main factors controlling electrical conductivity. MD simulations also allow us to provide an explanation for the non linear behaviour of electrical conductivity, from an atomistic scale. An interesting extension of this study would be to calculate electrical conductivity along several geotherms. Since high temperature facilitates partial melting of the wall rocks resulting in a coexisitng rock-fluid-melt system in

lower crustal conditions, theoretical models like the Hashin-Shtrikman upper bound model (HS^+) [272] may be used to obtain bulk conductivity. Such studies can be used to answer important geological questions like the bulk fluid composition forming High Conductivity Zones (HCZs) in subduction zones and lower crust below fold belts [205]. Systematic investigation of conductivity in rock-fluid systems can be made by studying the influences of ion adsorption, porosity and permeability in hydrothermal conditions. Chapter 5 presents a new polarizable interaction potential for La-Cl-H_2O system at supercritical conditions and show its superiority in predicting structural and thermodynamic properties as compared to pairwise interaction potential fitted at room temperature. Interestingly, our new potential also gives accurate results at subcritical conditions. However, it remains to be tested whether this potential can also be used to predict other properties like viscosity and electrical conductivity from ambient to supercritical conditions. Since we can retrieve reliable values of formation constants from PIM simulations, these can be used to fit HKF EOS to obtain distribution of different REE complexes in hydrothermal fluids at conditions not accessible from available experimental data. As discussed earlier, reliable speciation information is invaluable for geochemists and ore geologists. Proper understanding of speciation and thermodynamics of hydrothermal fluids help us delineate geological conditions conducive to the formation of ores. This not only helps in mineral extraction and recovery but also serves as a guide for ore exploration projects.

In different chapters of the thesis, we also address several fundamental issues related to MD simulations and development of new interaction potentials. A class of empirical interaction potentials have their functional forms chosen based on chemical intuition. These potentials are generally fitted to reproduce some target properties of structures in a pre-generated data set or experimental data and hence their transferability and predictive capacities are not guaranteed. Although the chosen functional form is based on the chemical behaviour of the system, numerical accuracy of data generated by using these potentials for conditions and properties not used in their construction should always be analysed critically. This point is studied in detail in Chapters 4 and 5. Chapter 4 shows that although ReaxFF has a complex functional form and is fitted on a wide variety of QC data, its precision in predicting electrical conductivity (property not present in the training set) at supercritical conditions is not good. Infact SPC/E model, with its much simpler functional form and being fitted only on heat of vaporization data, gives better predictions of electrical conductivity at su-

percritical conditions. It remains to be seen in future projects whether refitting the ReaxFF potential with data at supercritical conditions improve the estimations of bulk density and electrical conductivity of NaCl solutions.

Chapter 5 illustrates the issue of transferability of potentials to supercritical conditions. From a methodological perspective, we derive formation constants at infinite dilution directly from the reaction FES. We do not use activity corrections like the Debye-Hückel approach used by many authors [88, 238, 128] to calculate properties at infinite dilution. This is because it is always questionable whether these corrections can be applied to data obtained from microscopic ensembles where there are long ranged interactions in periodic simulation boxes. Another important aspect of calculating properties at infinite dilution is to assess how 'infinitely dilute' the simulated solutions are. It is important to answer this question to establish connection between properties calculated from simulations and thermodynamic models. Obviously an ideal model for infinitely dilute solution would feature a large simulation box with several water molecules and ion pairs so that bulk continuum behaviour is reached at large distances (leading to $g^{\infty}(\mathrm{r})$ converging to 1). However we illustrate and discuss in Chapter 5 that formation constants obtained by integrating over the FES after alignment with the analytical solution has only weak dependencies on the long range behaviour beyond ∼5-6 Å. This observation is important because this method can be used in AIMD simulations also (atleast at high temperatures where SSIPs are not formed due to low static dielectric constant of water) which are generally restricted to small simulation boxes due to high computational cost. However, one of the major shortcomings of PIM is that it uses the non-dissociative DC water model. This impedes usage of PIM in conditions where protolysis of water takes place either at higher temperatures (∼2000 K) or in the presence of species like F^-. These ion-exchange reactions can become important for REE-bearing fluids at subduction zone conditions [88]. Moreover non dissociative forcefields are also not flexible enough to model aqueous systems bearing ions like CO_3^{2-} and SO_4^{2-} as these involve proton exchange reactions (as discussed in Chapter 3). As shown in Chapter 5, PIM predicts extremely high La-Cl CNs in highly concentrated brines. While this prediction remains to be verified through experimental/AIMD studies, unreliable results may be obtained in high concentration brines due to insufficient sampling in the training data. It has to be noted that the La-Cl potential parameters are fitted on force and dipole moment data obtained from the crystalline $LaCl_3$ sub-system where solvation effects and other effects due to the

counter-ions are grossly missing. An attempt was made to include snapshots from AIMD simulations of aqueous La-Cl system in the training data. However, significant under-fitting was observed indicating that the fitted parameters in PIM are not flexible enough to account for crystalline and aqueous phases together. These motivate developing more sophisticated reactive potentials like NNPs and ReaxFF for these systems.

In the recent years, applications of artificial intelligence to predict fluid properties is gaining momentum. Neural Network Potentials (NNPs) [273, 274, 275, 276] are being developed for a wide variety of chemical systems by several research groups around the globe. The predictive capacities of these potentials depend on the quality of the underlying training set which contains representative configurations generated with higher level ab-initio methods. The ab-initio method chosen for training data generation depends on the properties under investigation and the computation resources at hand. To generate high quality reference data with reasonable computation resource, several factors that determine the quality of ab-initio data (like XC functional, basis sets, dispersion corrections) must be properly understood. For example, in Chapter 3 we show that both BLYP and r2SCAN XC functionals predict similar structural properties of sulfur bearing aqueous fluids at high temperatures. So it would be more judicious to use BLYP XC functional for training data generation if we aim to develop a NNP to study structure of such fluids at high temperatures.

Overall, we show that state of the art MD techniques give important and accurate insights into the structural and thermodynamic properties of geochemical fluids at high temperature and pressure. However there are scopes to develop better models whose utility and accuracy spreads over a wide range of thermodynamic conditions. Before such an exercise is undertaken, systematic understanding of the different simulation parameters that affect accuracy, target properties and thermodynamic conditions as well as performance of the solvent model is required. This helps in judicious use of the available computation resources at hand as well as systematic error-handling and parameterization of the interaction model.

Appendix A

Table A.1: Vibrational modes of sulfate species at 298K (except Walrafen et al.[182] where experiments were conducted at 264K) from experiments. The last three experimental results are from aqueous Na_2SO_4 system whereas the remaining are from aqueous H_2SO_4 system. $\upsilon_1(a_1)$ sulfate: symmetric stretch of SO_4^{2-}, $\upsilon_3(f_2)$ sulfate: asymmetric stretch of SO_4^{2-}, $\upsilon_1(a_1)$ bisulfate: symmetric stretch of HSO_4^-, $\upsilon_3(e)$ bisulfate: asymmetric stretch of HSO_4^-, $\upsilon_{SOH}(\mathrm{a_1})/\upsilon_4(\mathrm{a_1})$: S-OH stretching mode

Reference \ Mode	$\upsilon_1(a_1)$ sulfate	$\upsilon_3(f_2)$ sulfate	$\upsilon_1(a_1)$ bisulfate	$\upsilon_3(e)$ bisulfate	$\upsilon_{SOH}(\mathrm{a_1})/\upsilon_4(\mathrm{a_1})$ bisulfate
[277]	977-983	1098-1110	1050-1052	1194-1202	876-898
[122]	983	1110	1051	1190	885
[278]	981	1110	1052	1202	898
[279]	982	-	1040	-	890
[182]	-	-	1035	1165	905
[280]	982	1099	-	1194	887
[281]	980	1100	1050	1200	885
[174]	-	-	1050	1230	885
[282]	-	-	1036	1195	902
[131]	978	-	1048	-	894
[283]	980.5-981.2	-	-	-	-
[284]	980.8-981.4	-	-	-	-
[121]	980	1104	-	-	-

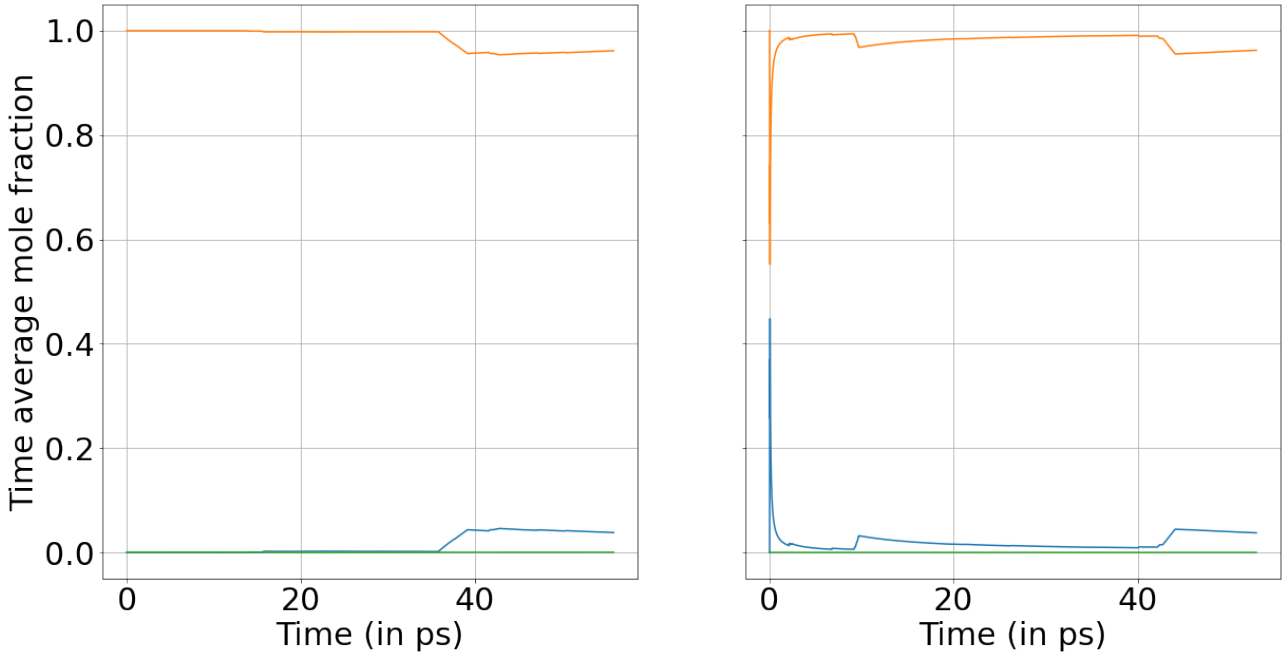

Figure A.1: Time average mole fraction of bisulfate (orange), sulfate (blue) and sulfuric acid (green) from Becke, Lee, Yang, and Parr (BLYP) (left), r2SCAN (right) functionals at ambient conditions in aqueous H_2SO_4 solution

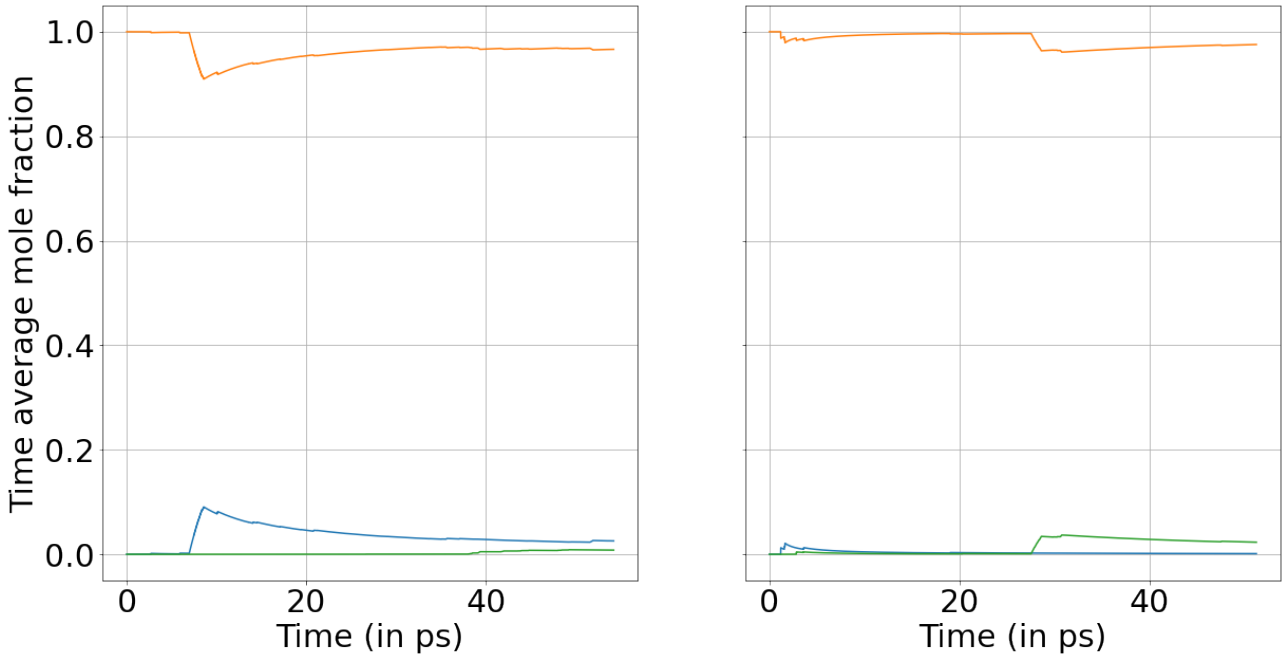

Figure A.2: Time average mole fraction of bisulfate (orange), sulfate (blue) and sulfuric acid (green) from BLYP (left), r2SCAN (right) functionals at 473 K in aqueous H_2SO_4 solution

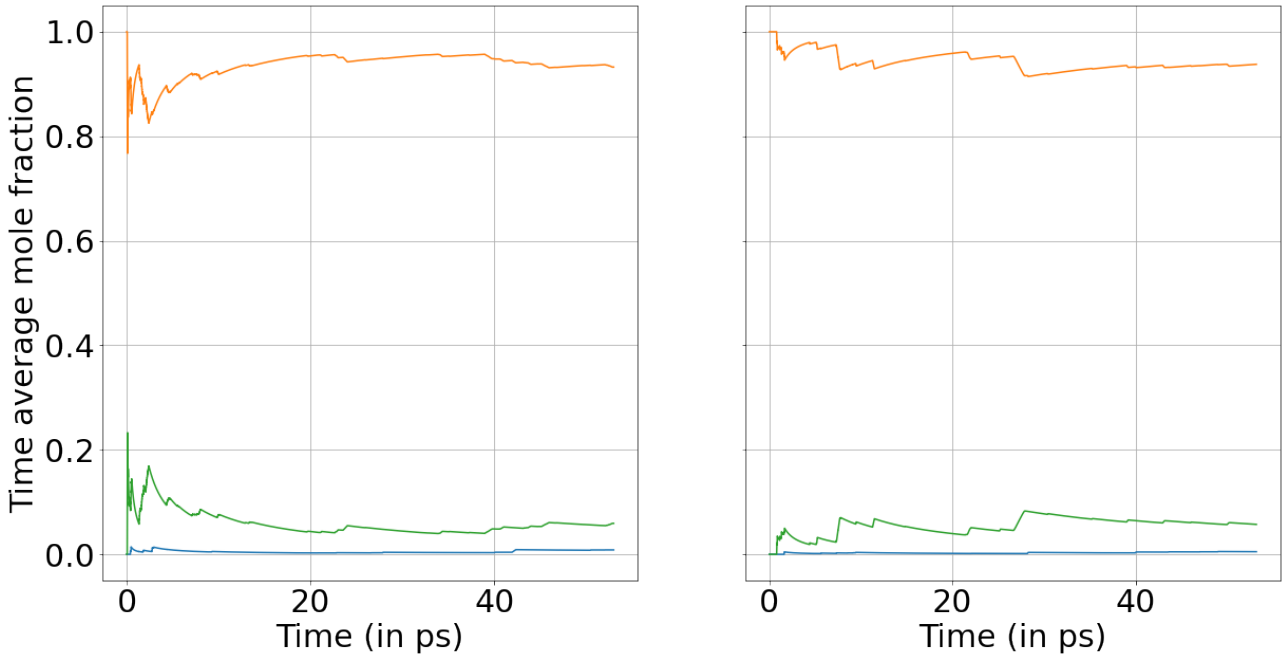

Figure A.3: Time average mole fraction of bisulfate (orange), sulfate (blue) and sulfuric acid (green) from BLYP (left), r2SCAN (right) functionals at 673K in aqueous H_2SO_4 solution

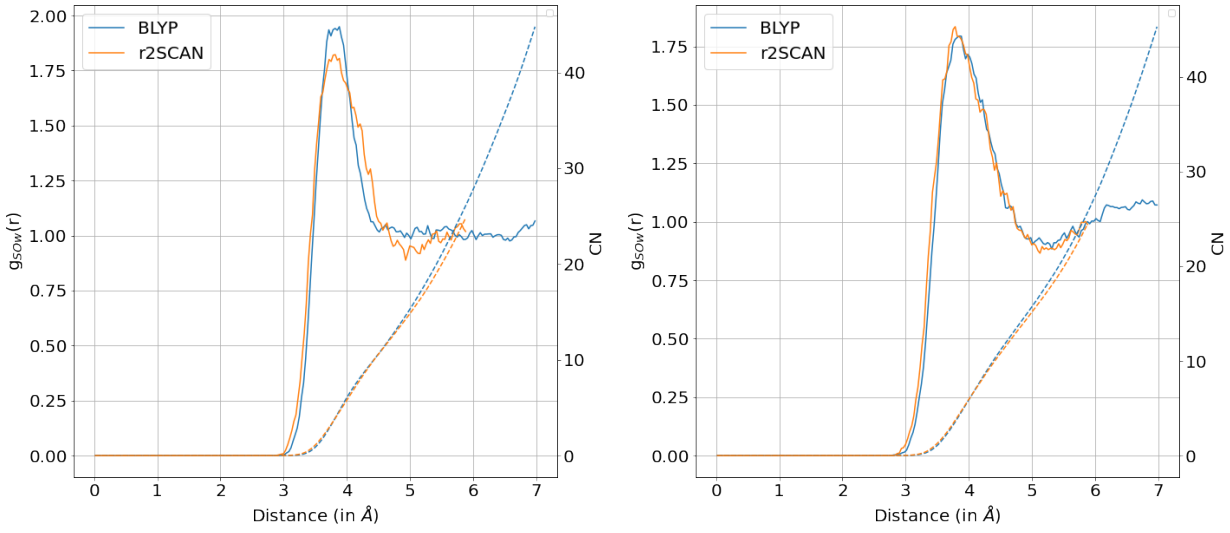

Figure A.4: $g_{SO_w}(r)$ at 473 K (left) and 673 K (right) from 2 functionals in aqueous H_2SO_4 solution. Solid lines represent $g_{ij}(r)$ whereas dashed lines are used to plot Running Coordination Number (CN)

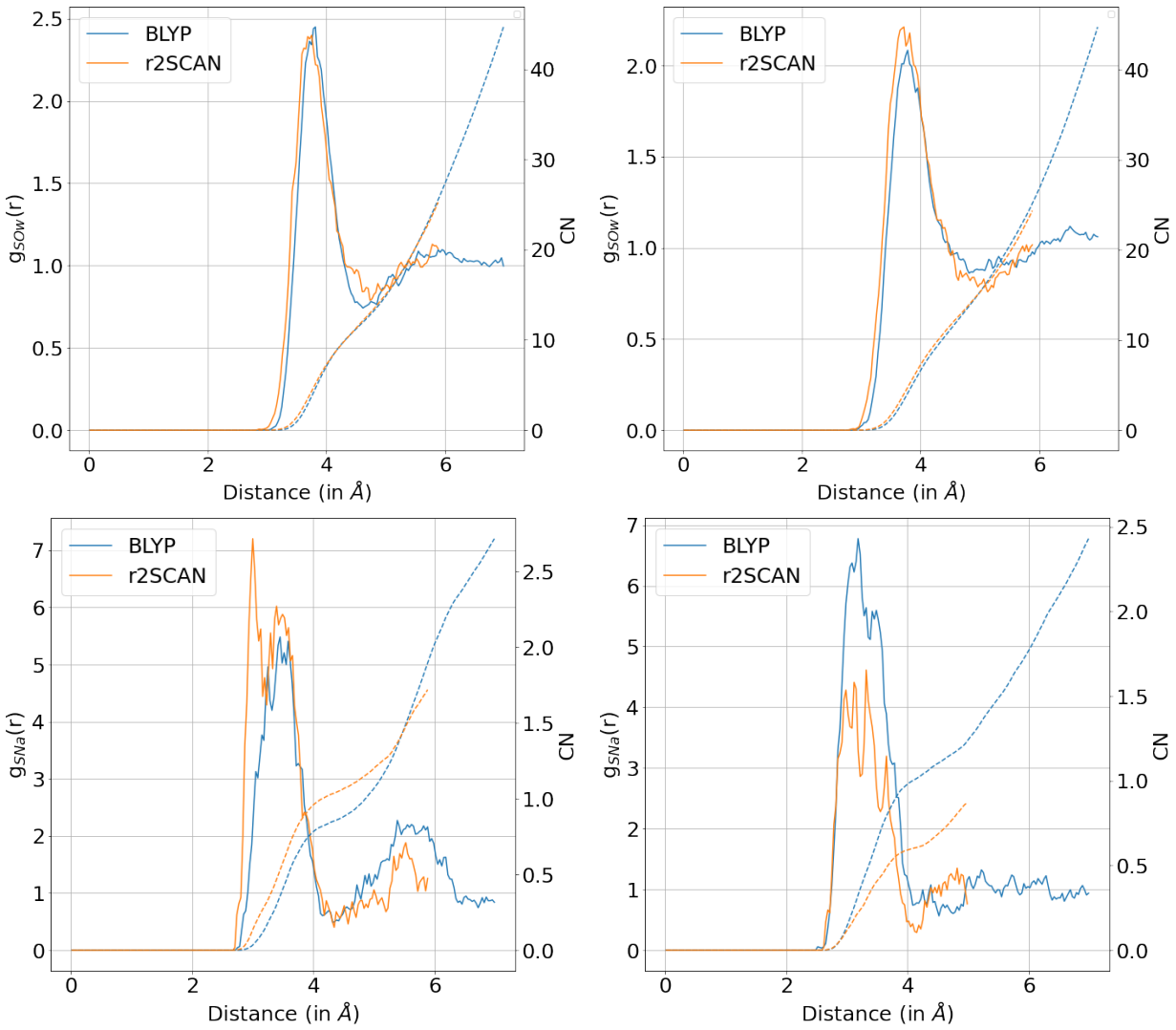

Figure A.5: $g_{SO_w}(r)$, $g_{SNa}(r)$ at 473 K (left) and 673 K (right) from 2 functionals in aqueous Na_2SO_4 solution. Solid lines represent $g_{ij}(r)$ whereas dashed lines are used to plot CN

Table A.2: Vibrational modes of sulfate species (at 298K for bulk phase) from computations along with the levels of theory used (HF: Hartree-Fock, MP: Møller–Plesset, DFT: Density Functional Theory). Data from HF level are scaled by a factor of 0.902 according to Vchirawongkwin et al. [162]

Mode / Reference	$\upsilon_1(a_1)$ sulfate	$\upsilon_3(f_2)$ sulfate	$\upsilon_1(a_1)$ bisulfate	$\upsilon_3(e)$ bisulfate	$\upsilon_{SOH}(\mathrm{a_1})/\upsilon_4(\mathrm{a_1})$ bisulfate
MP2 [150]	-	-	1043-1052	1147-1195	752-910
HF [162]	968	1118	-	-	-
HF [148]	-	-	1028	1175	867
HF [151]	-	-	1037	-	770-850
HF [161]	930	1019-1110	-	-	-
DFT [163]	961-991	1103-1154	-	-	-

Table A.3: Time-averaged mole fraction of sulfur species obtained with different Exchange and Correlation (XC) functionals at different temperatures in aqueous H_2SO_4 solution

Temperature/XC functional	Sulfate	Bisulfate	Acid
Ambient/BLYP	0.038	0.961	0
Ambient/r2SCAN	0.037	0.962	0
473K/BLYP	0.025	0.966	0.008
473K/r2SCAN	0.001	0.975	0.023
673K/BLYP	0.008	0.932	0.059
673K/r2SCAN	0.005	0.937	0.057

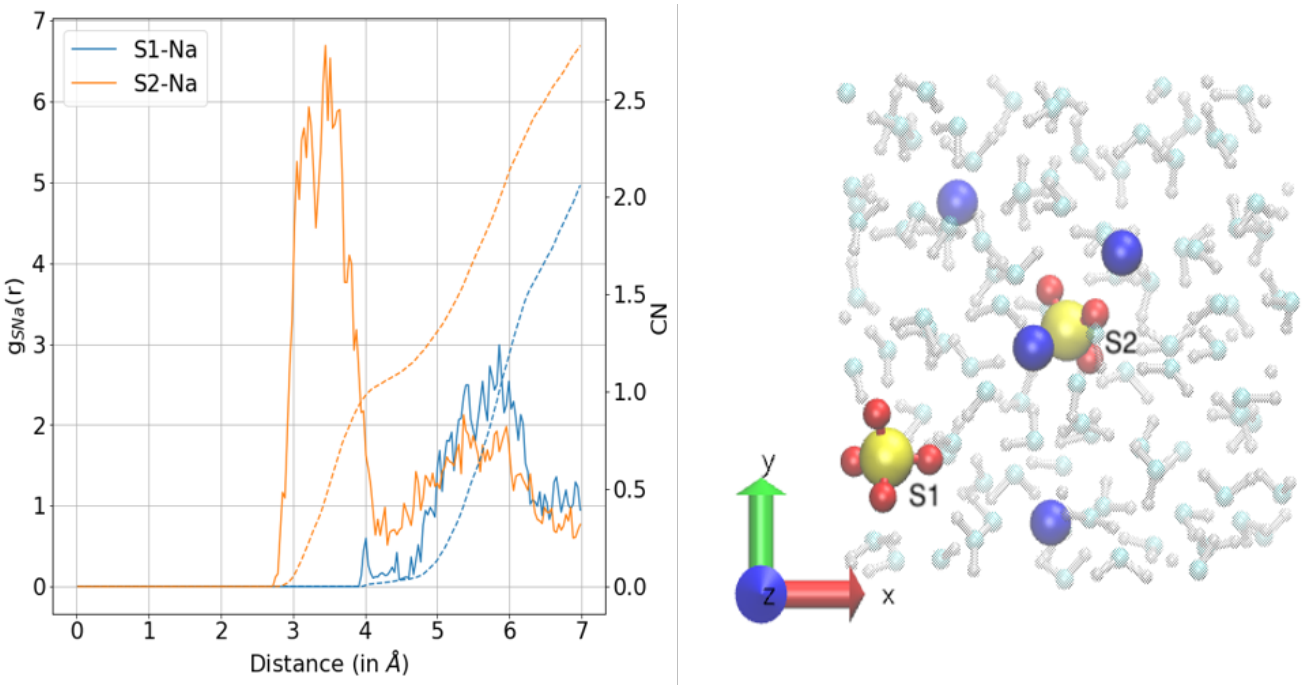

Figure A.6: Pair correlation between individual S atom and Na^+ cations in aqueous Na_2SO_4 solution at 473 K with BLYP functional (left). Snapshot from simulation where S1 refers to the uncomplexed tetrahedra and S2 refers to the complexed tetrahedra (right). Yellow: sulfur, Red: O, Blue: Na, transparent: bulk water molecules

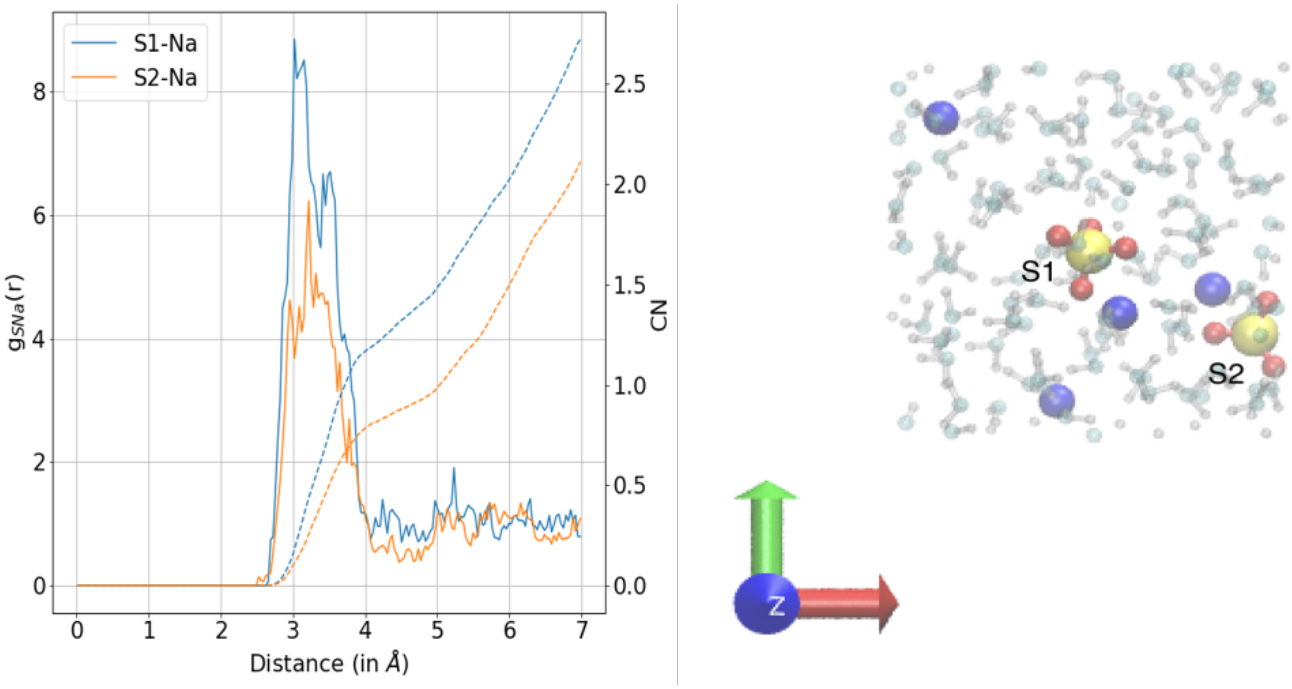

Figure A.7: Pair correlation between individual S atom and Na^+ cations in aqueous Na_2SO_4 solution at 673 K with BLYP functional (left). Snapshot from simulation where S1,S2 refer to complexed sulfate tetrahedra (right). Yellow: sulfur, Red: O, Blue: Na, transparent: bulk water molecules

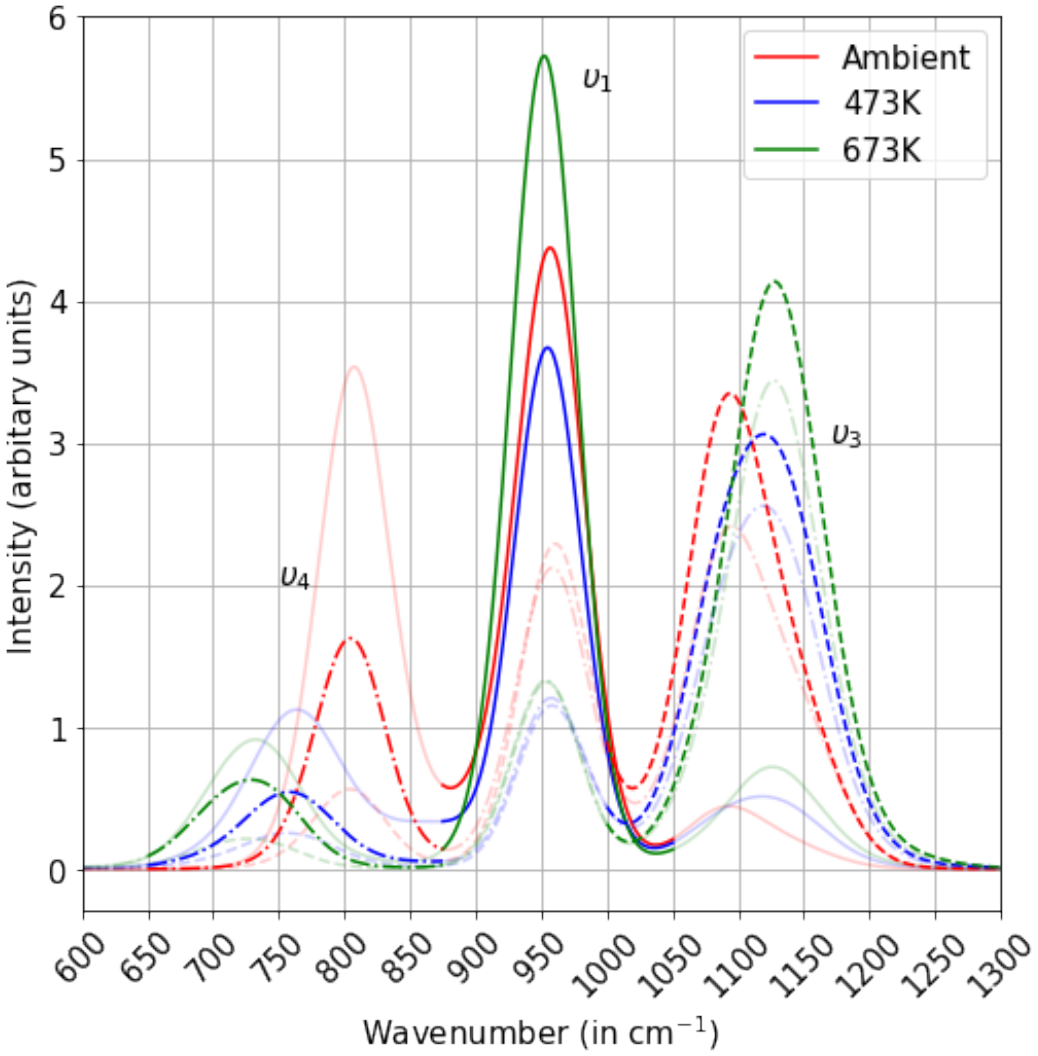

Figure A.8: Quasi-Normal Modes (QNMs) of HSO_4^- ions from BLYP in aqueous H_2SO_4 solution at different studied temperatures. υ_1: solid lines, υ_3: dashed lines, υ_4: dashed-dotted lines

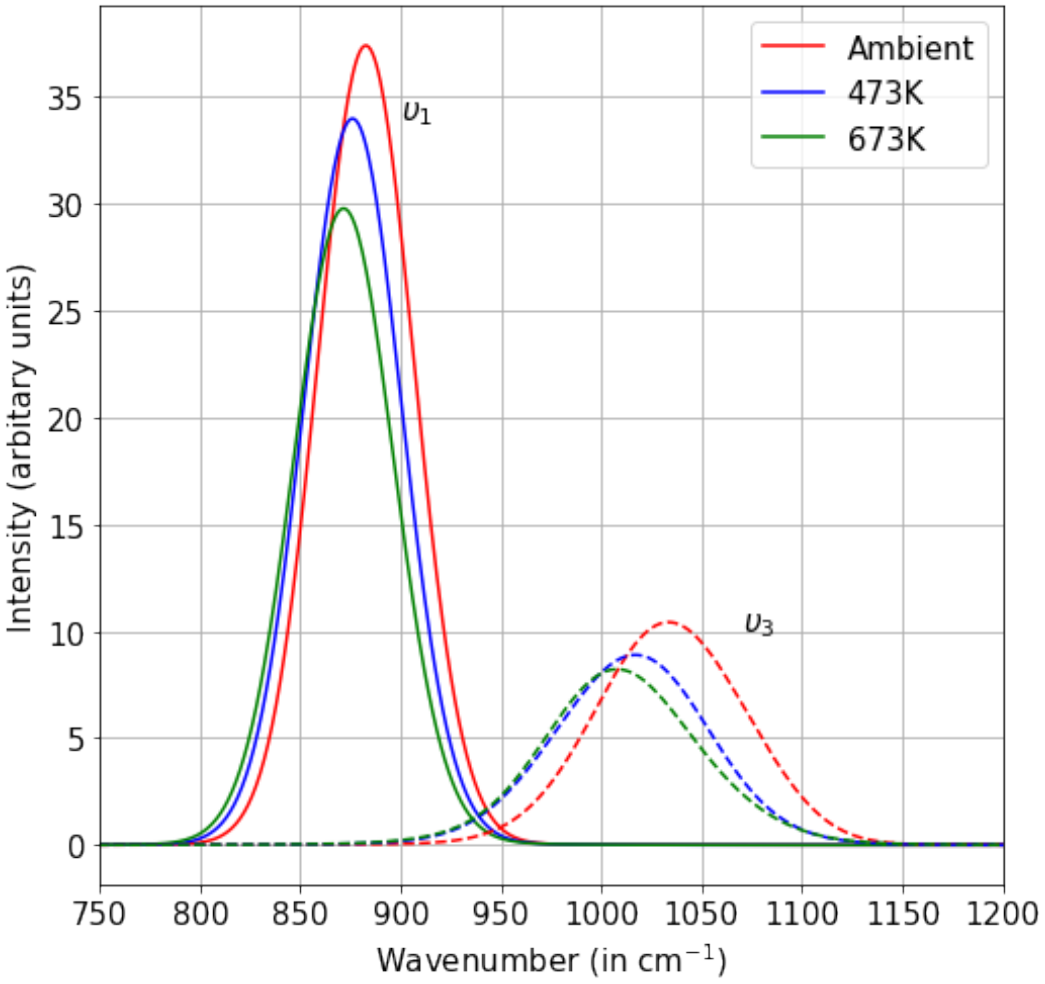

Figure A.9: QNMs of SO_4^{2-} ions from BLYP in aqueous Na_2SO_4 solution at different studied temperatures. υ_1: solid lines, υ_3: dashed lines

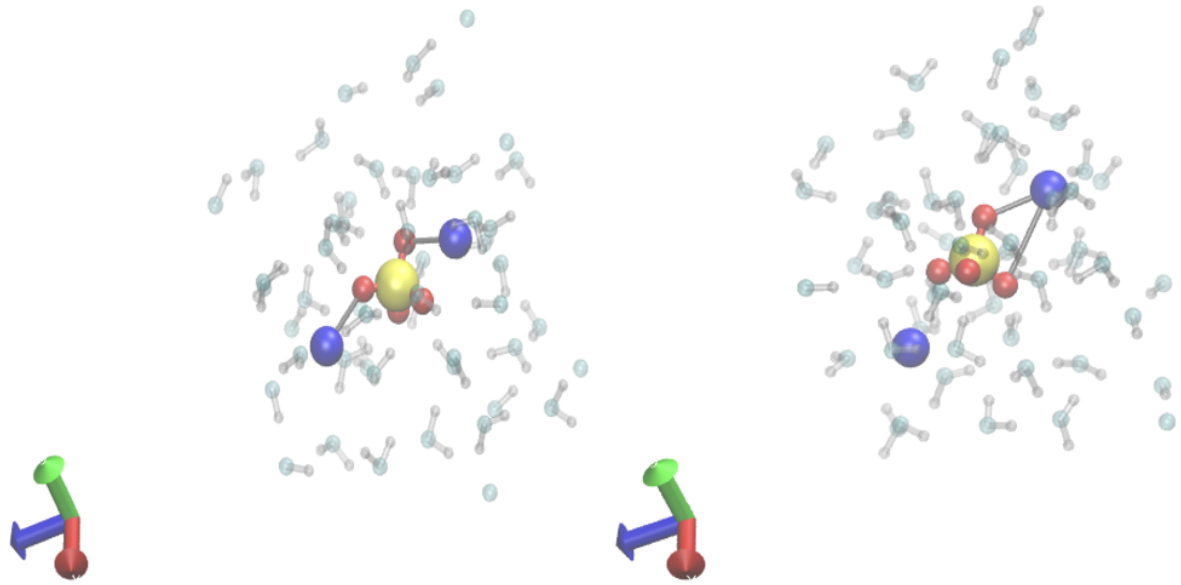

Figure A.10: Snapshots showing monodentate (left) and bidentate (right) ion pairs obtained from aqueous Na_2SO_4 solutions. Yellow: sulfur, Red: O, Blue: Na, transparent: bulk water molecules

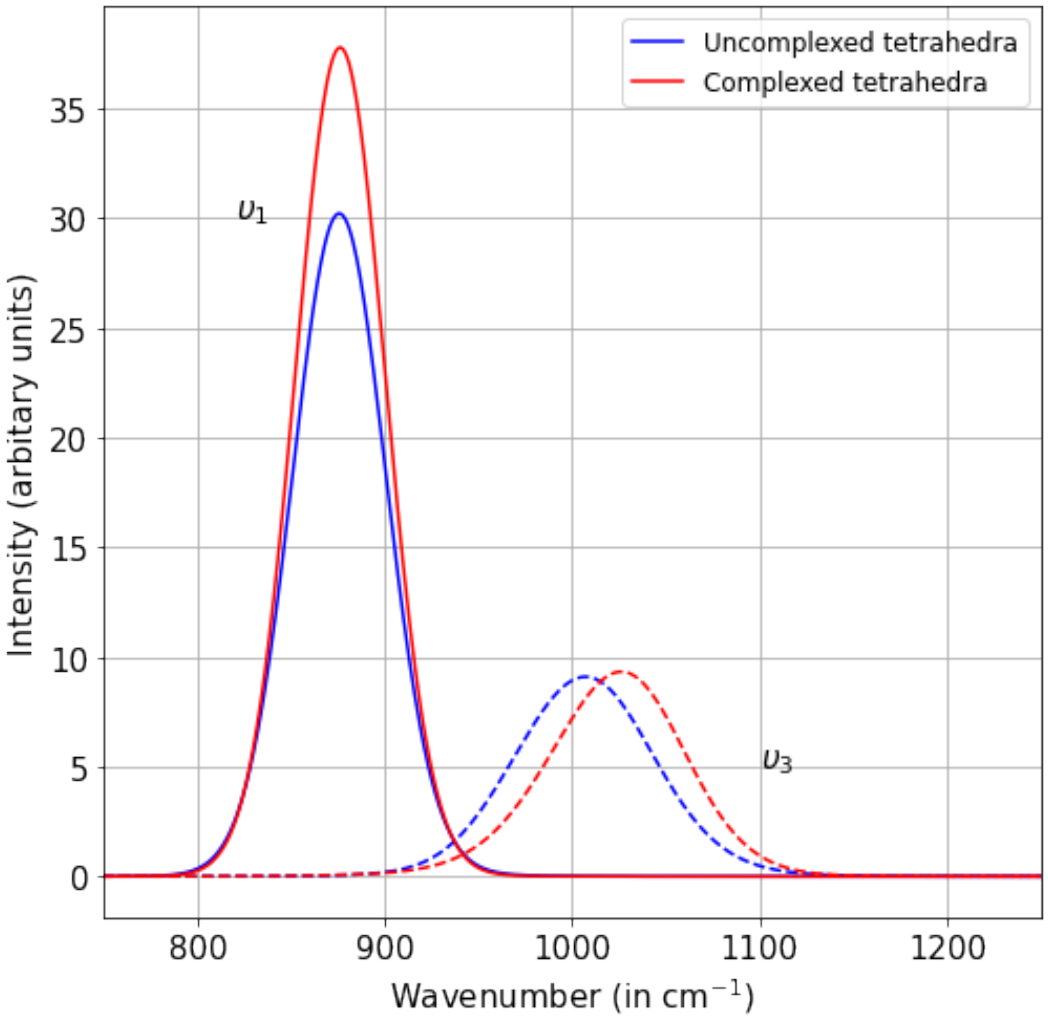

Figure A.11: QNMs of complexed and uncomplexed tetrahedra obtained from aqueous Na_2SO_4 solution at 473 K with BLYP functional

Appendix B

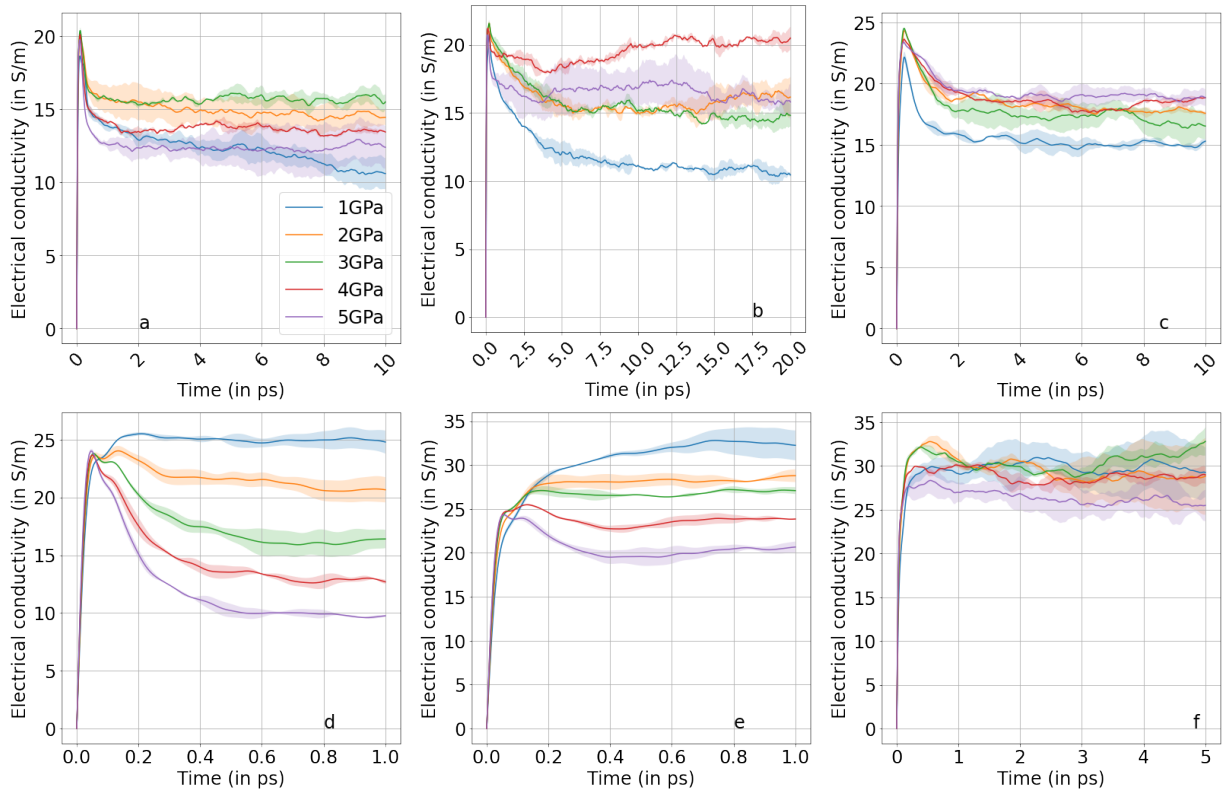

Figure B.1: Electrical conductivity (σ in S/m) of 1.05 m NaCl solution calculated from the ReaxFF (top row: a - 473 K b - 673 K, c - 1073 K) and SPC/E models (bottom row: d - 473 K, e - 673 K, f - 1073 K). Lighter shades have been used to show the range of values obtained by integrating $j(\vec{t})$ from two successive time chunks whereas bold lines have been used to plot the average values

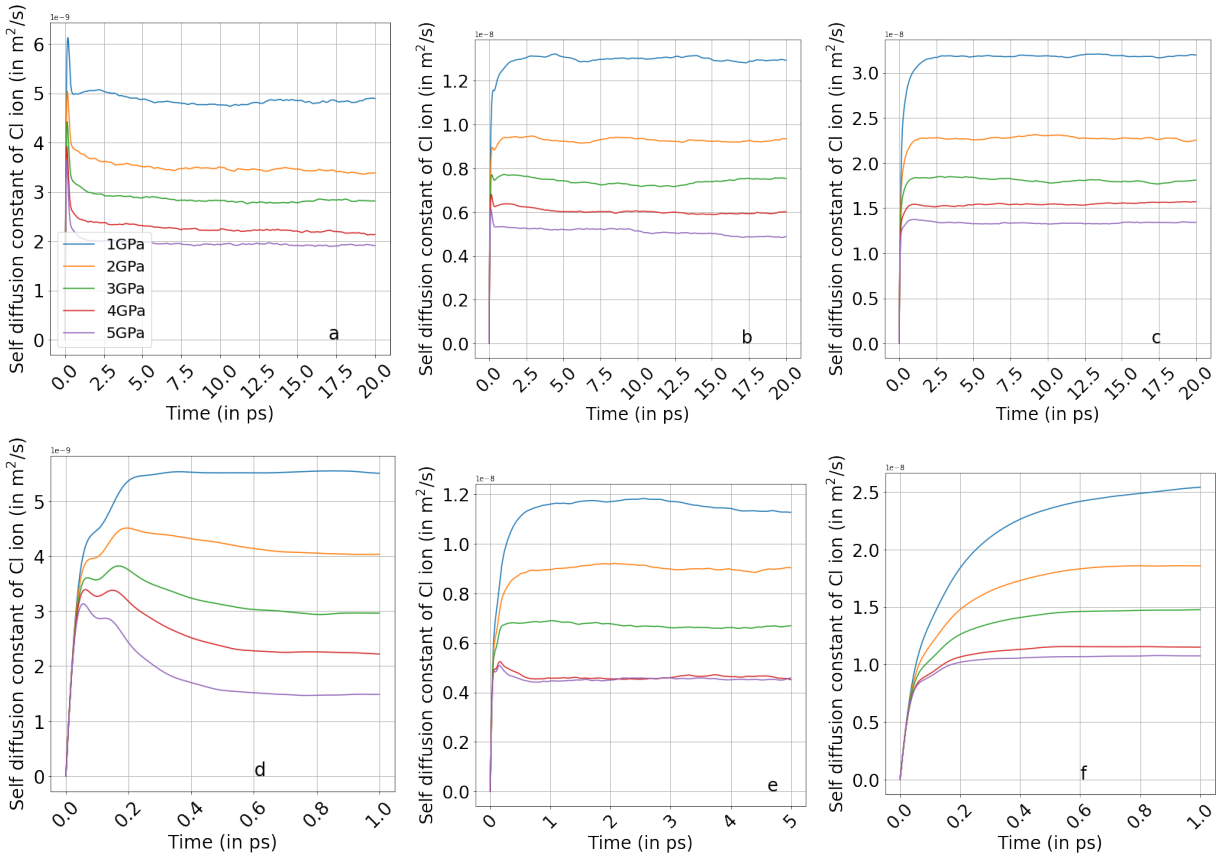

Figure B.2: Convergence of ion self-diffusion coefficients (D_I in 10^{-8} m^2/s) of Cl^- ions obtained from the ReaxFF (top row: a - 473 K b - 673 K, c - 1073 K) and SPC/E (bottom row: d - 473 K, e - 673 K, f - 1073 K) models in 1.05 m brine

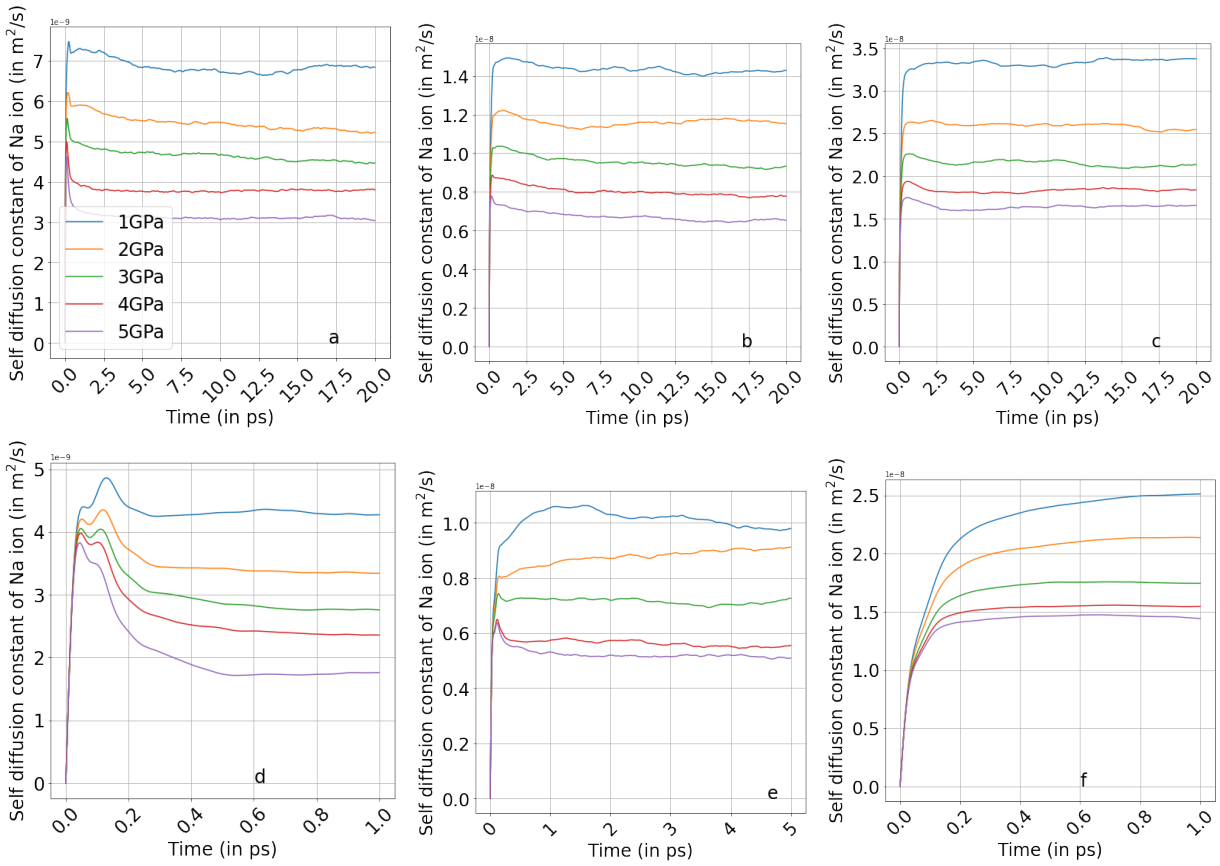

Figure B.3: Convergence of D_I in (10^{-8} m^2/s) of Na^+ ions obtained from the ReaxFF (top row: a - 473 K b - 673 K, c - 1073 K) and SPC/E (bottom row: d - 473 K, e - 673 K, f - 1073 K) models in 1.05 m brine

Table B.1: Comparison of D_I of Na^+,Cl^- ions (in $10^{-9}m^2/s$) obtained by integrating velocity autocorrelation functions (this work) and from Mean Squared Displacement (MSD) of ions [215]

Na^+-(Eq. 4.5)	Na^+-(MSD [215])	Cl^--(Eq. 4.5)	Cl^--(MSD [215])	σ (Eq. 4.1)	σ [215]
0.9	1.1	1.2	1.3	7.5	7.3

Table B.2: D_I of Na^+,Cl^- ions (in 10^{-8} m^2/s) obtained by integrating velocity autocorrelation functions. The first entry in each cell is the D_I of cation whereas the second one is that of the anion

Temperature	Pressure	SPC/E	ReaxFF
473 K	1.0 GPa	0.42/0.55	0.68/0.48
	2.0 GPa	0.33/0.40	0.52/0.37
	3.0 GPa	0.27/0.29	0.44/0.28
	4.0 GPa	0.23/0.22	0.37/0.21
	5.0 GPa	0.17/0.14	0.30/0.19
673 K	1.0 GPa	0.97/1.11	1.42/1.29
	2.0 GPa	0.91/0.90	1.15/0.93
	3.0 GPa	0.72/0.69	0.93/0.75
	4.0 GPa	0.55/0.45	0.77/0.60
	5.0 GPa	0.50/0.45	0.65/0.48
1073 K	1.0 GPa	2.51/2.53	3.37/3.19
	2.0 GPa	2.13/1.85	2.54/2.25
	3.0 GPa	1.74/1.47	2.13/1.80
	4.0 GPa	1.54/1.14	1.84/1.57
	5.0 GPa	1.44/1.07	1.65/1.34

Table B.3: Density of 1.05 m brine (in g/cm^3) obtained from simulations at different conditions and Equation Of State (EOS) [223]

Temperature	Pressure	SPC/E	ReaxFF	EOS
473 K	1.0 GPa	1.19	1.10	1.19
	2.0 GPa	1.31	1.26	1.32
	3.0 GPa	1.40	1.36	1.41
	4.0 GPa	1.47	1.46	1.48
	5.0 GPa	1.53	1.51	1.54
673 K	1.0 GPa	1.08	1.01	1.11
	2.0 GPa	1.23	1.18	1.26
	3.0 GPa	1.33	1.30	1.36
	4.0 GPa	1.40	1.38	1.44
	5.0 GPa	1.46	1.46	1.50
1073 K	1.0 GPa	0.90	0.84	0.94
	2.0 GPa	1.08	1.06	1.13
	3.0 GPa	1.19	1.18	1.25
	4.0 GPa	1.30	1.29	1.35
	5.0 GPa	1.35	1.35	1.42

Table B.4: Comparison of static dielectric constant (ϵ) at different conditions from the SPC/E, ReaxFF models and the Deep Earth Water (DEW) Model [224]

Temperature	Pressure	SPC/E	ReaxFF	DEW Model
473 K	1.0 GPa	53.1	41.4	52.2
	2.0 GPa	59.2	53.5	60.5
	3.0 GPa	62.5	59.1	66.7
	4.0 GPa	73.5	74.2	72.0
	5.0 GPa	75.3	75.1	76.5
673 K	1.0 GPa	26.2	19.4	30.5
	2.0 GPa	33.4	25.9	37.2
	3.0 GPa	38.6	31.5	41.8
	4.0 GPa	42.8	35.4	45.5
	5.0 GPa	44.5	39.0	48.7
1073 K	1.0 GPa	12.1	7.4	12.8
	2.0 GPa	14.3	10.2	16.8
	3.0 GPa	16.8	12.3	19.5
	4.0 GPa	17.7	14.6	21.6
	5.0 GPa	18.5	14.9	23.3

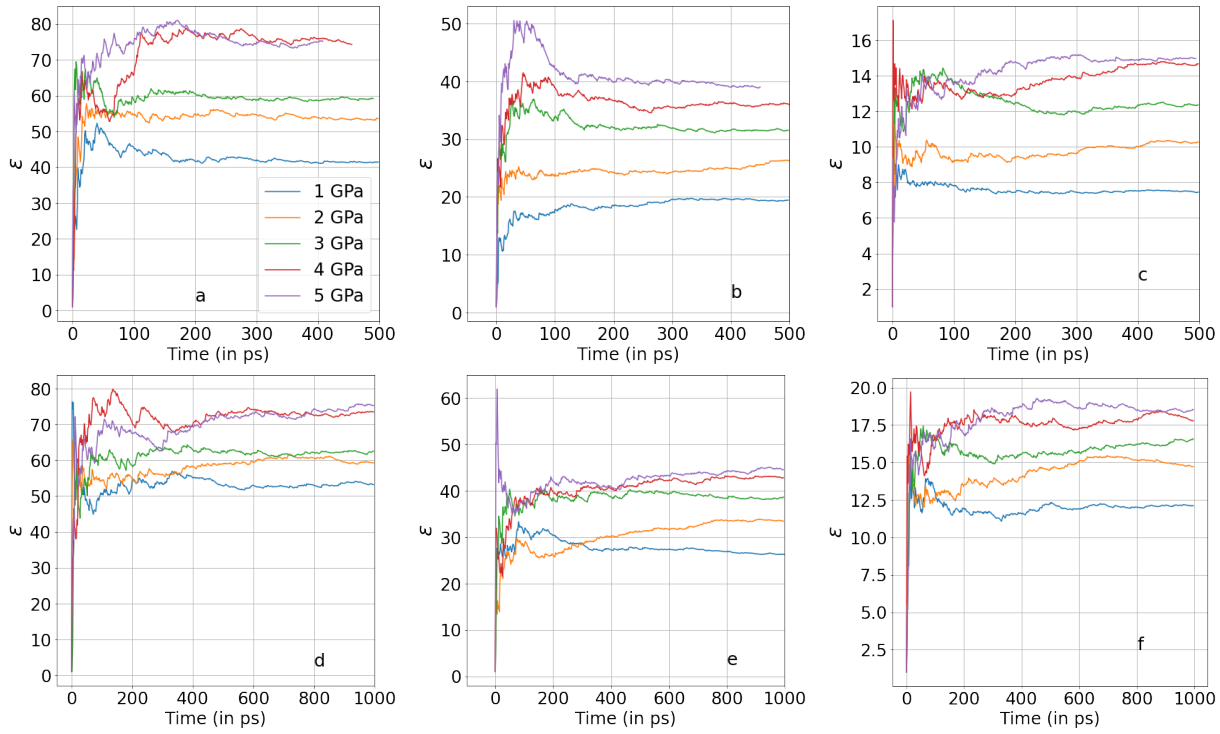

Figure B.4: Convergence of ϵ of water from the ReaxFF (top row: a - 473 K b - 673 K, c - 1073 K) and SPC/E models (bottom row: d - 473 K, e - 673 K, f - 1073 K)

Table B.5: Decomposition of σ (in S/m) along 473 K, 673 K, 1073 K isotherms from the ReaxFF model

Temperature	Pressure	Na-Na-self	Na-Na-cross	Cl-Cl-self	Cl-Cl-cross	Na-Cl
473 K	1.0 GPa	13.55	0.27	6.95	0.43	-10.10
	2.0 GPa	12.98	-0.01	5.77	0.54	-5.78
	3.0 GPa	12.25	-0.53	4.97	-0.15	0.28
	4.0 GPa	10.69	-0.44	4.17	-0.07	-1.75
	5.0 GPa	9.21	-0.59	3.72	0.11	-1.12
673 K	1.0 GPa	18.21	-0.94	12.05	-0.44	-18.95
	2.0 GPa	17.78	0.34	10.01	0.63	-13.11
	3.0 GPa	15.92	0.18	8.68	0.43	-9.50
	4.0 GPa	14.47	0.70	7.33	0.21	-4.29
	5.0 GPa	13.02	-0.90	6.21	0.21	-4.61
1073 K	1.0 GPa	20.95	0.34	14.68	0.59	-20.87
	2.0 GPa	20.62	0.99	12.93	0.60	-17.01
	3.0 GPa	19.82	0.55	11.53	0.56	-13.25
	4.0 GPa	18.99	-0.45	10.75	0.07	-12.82
	5.0 GPa	18.21	-1.57	9.63	0.83	-7.23

Table B.6: Decomposition of σ (in S/m) along 473 K, 673 K, 1073 K isotherms from the SPC/E model

Temperature	Pressure	Na-Na-self	Na-Na-cross	Cl-Cl-self	Cl-Cl-cross	Na-Cl
473 K	1.0 GPa	11.83	-0.36	15.24	-0.62	-1.62
	2.0 GPa	10.12	-0.33	12.21	-0.42	-0.95
	3.0 GPa	8.82	-0.12	9.48	-0.39	0.74
	4.0 GPa	7.85	-0.01	7.39	-0.24	-0.24
	5.0 GPa	6.15	0.13	5.18	-0.29	0.21
673 K	1.0 GPa	18.72	-0.69	20.58	-0.69	-1.40
	2.0 GPa	16.79	-0.68	17.76	-0.86	-1.79
	3.0 GPa	15.33	-0.45	14.59	-0.40	-0.39
	4.0 GPa	13.13	-0.08	10.47	-0.31	-0.35
	5.0 GPa	12.35	-0.24	10.36	-0.30	-0.19
1073 K	1.0 GPa	22.71	-1.10	22.96	-0.24	-9.37
	2.0 GPa	23.25	-0.94	20.29	-0.20	-6.94
	3.0 GPa	21.33	-0.86	18.04	-0.65	-2.73
	4.0 GPa	20.13	-0.37	14.95	-0.29	-1.31
	5.0 GPa	19.22	-0.33	14.30	-0.65	-2.42

Table B.7: Charges on cations and anions obtained from the ReaxFF simulations at different conditions

Temperature	Pressure	Cation	Anion
473 K	1.0 GPa	0.895	-0.761
	2.0,GPa	0.907	-0.755
	3.0 GPa	0.916	-0.751
	4.0 GPa	0.924	-0.747
	5.0 GPa	0.930	-0.745
673 K	1.0 GPa	0.880	-0.752
	2.0 GPa	0.894	-0.745
	3.0 GPa	0.902	-0.741
	4.0 GPa	0.910	-0.737
	5.0 GPa	0.917	-0.733
1073 K	1.0 GPa	0.850	-0.732
	2.0 GPa	0.868	-0.730
	3.0 GPa	0.879	-0.729
	4.0 GPa	0.889	-0.724
	5.0 GPa	0.895	-0.723

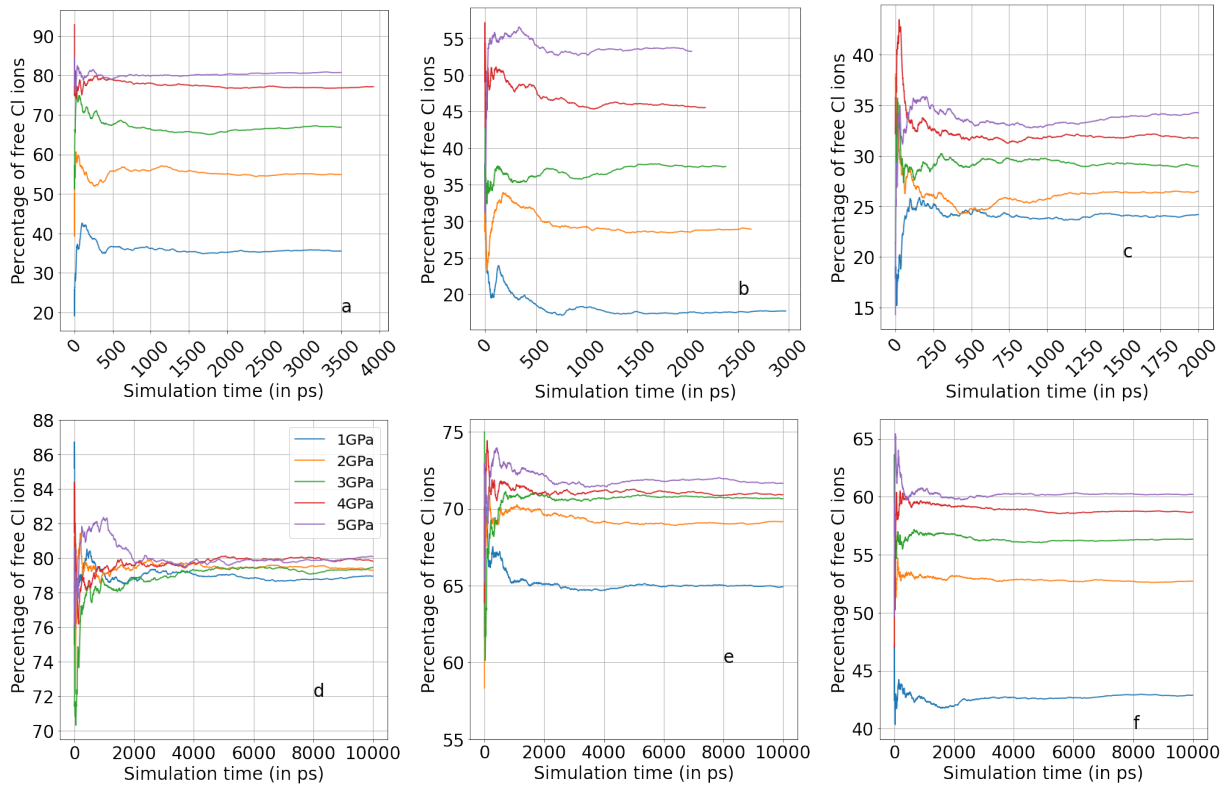

Figure B.5: Time averaged percentage of free Cl ion from the ReaxFF (top row: a - 473 K b - 673 K, c - 1073 K) and SPC/E models (bottom row: d - 473 K e - 673 K, f - 1073 K)

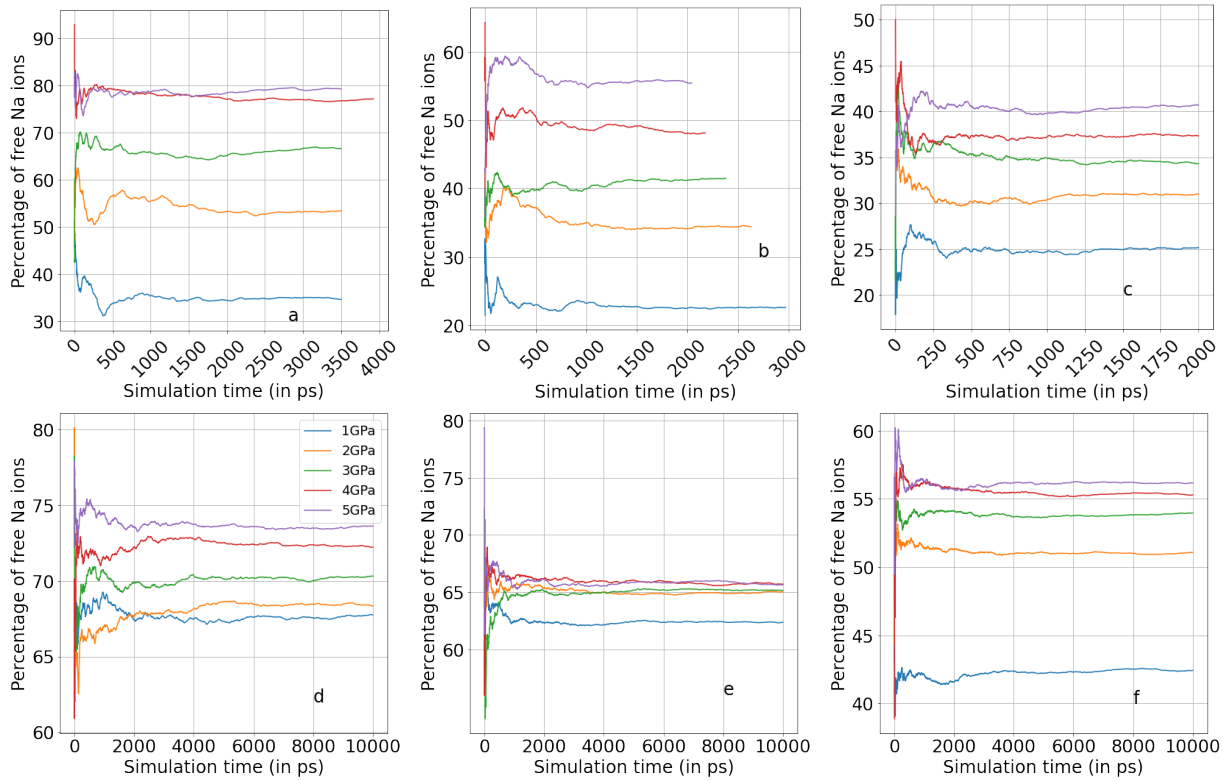

Figure B.6: Time averaged percentage of free Na ion from the ReaxFF (top row: a - 473 K b - 673 K, c - 1073 K) and SPC/E models (bottom row: d - 473 K e - 673 K, f - 1073 K)

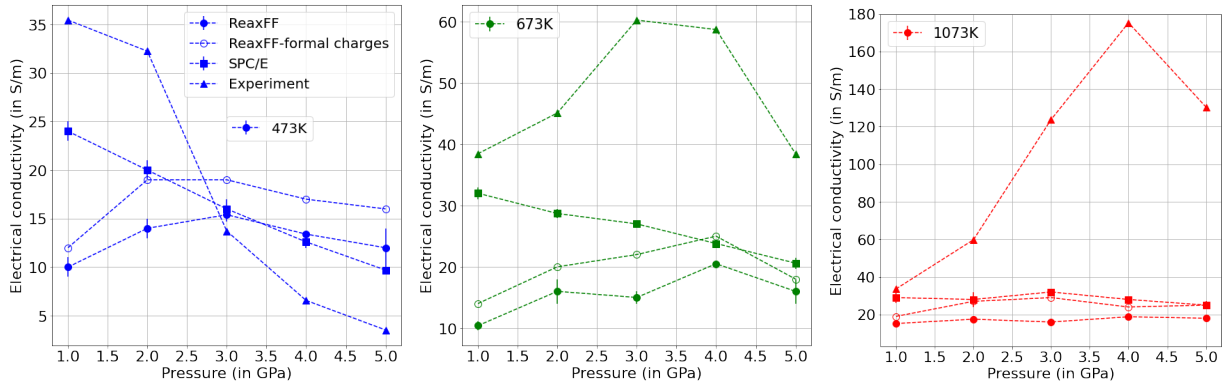

Figure B.7: Comparison of σ along different isotherms obtained with the ReaxFF model with partial charges, ReaxFF model with formal charges, the SPC/E model and experiment [208]

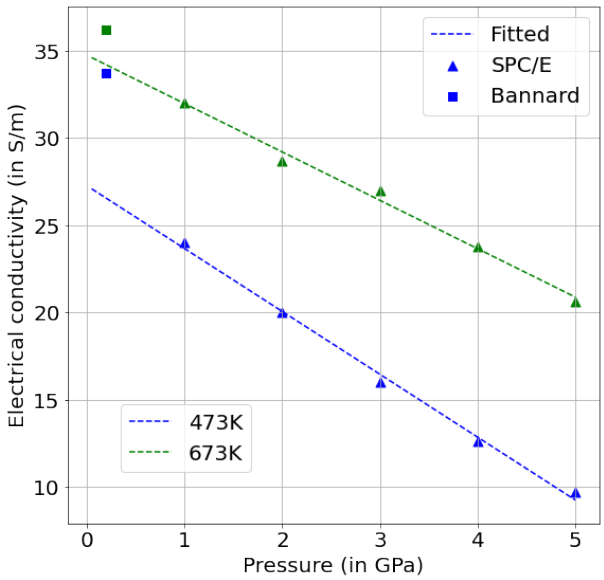

Figure B.8: Comparison of σ calculated in this work and from Bannard [202]. Colour scheme used is same as in Figure B.7

Appendix C

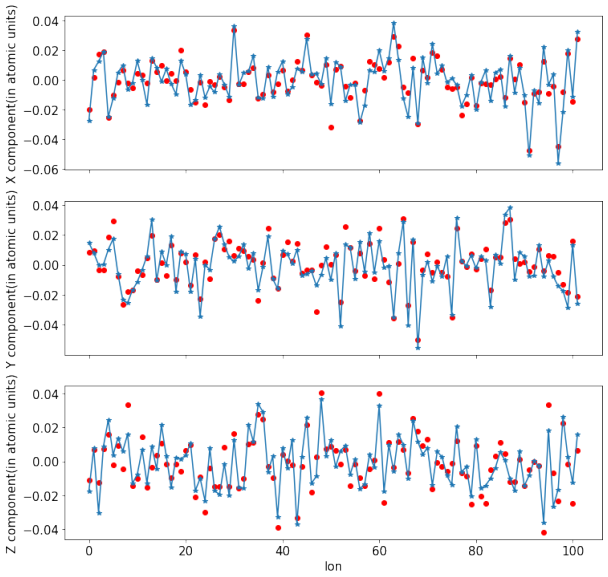

Figure C.1: Comparison of fitted (dots) and computed atomic forces (solid lines) on La^{3+} ion in aqueous La-O subsystem

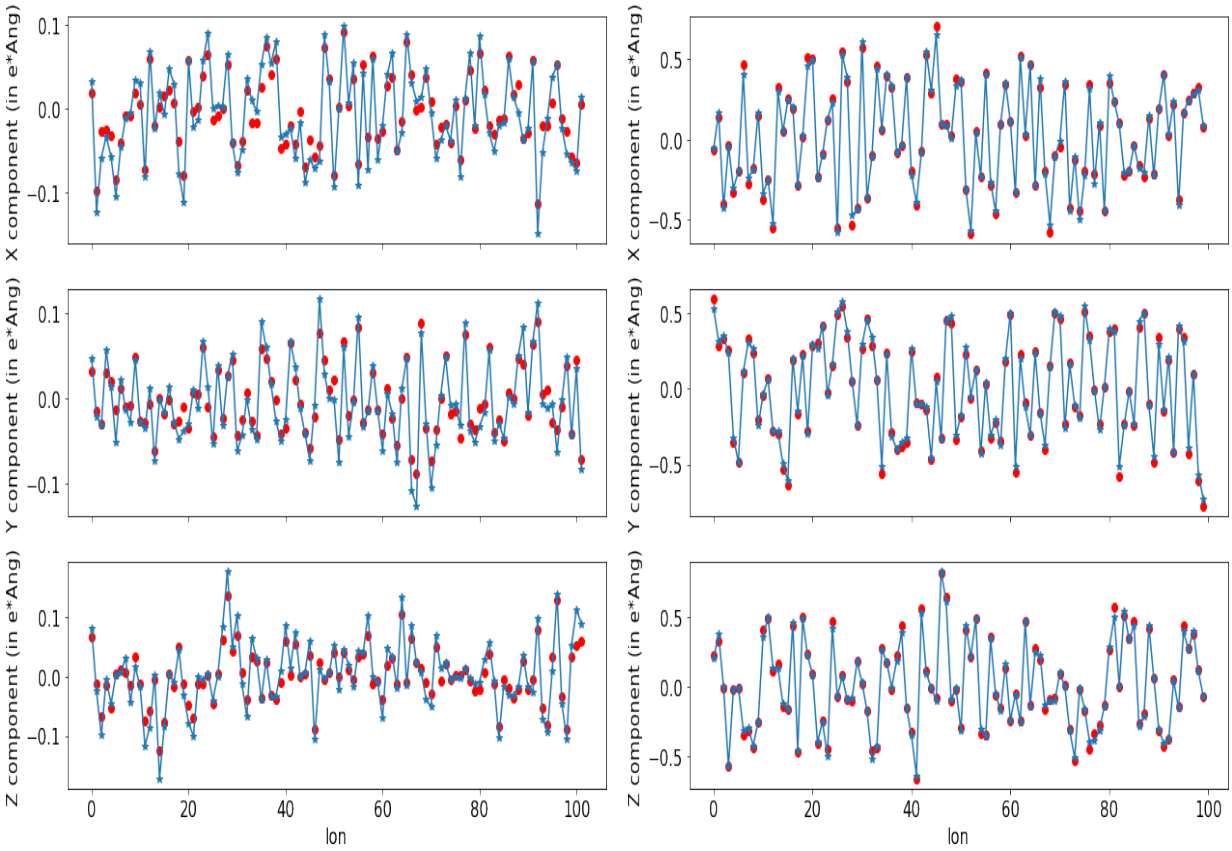

Figure C.2: Comparison of fitted (dots) and computed dipole moments (solid lines) of La^{3+} ion (left) and water molecules (right) in aqueous La-O subsystem

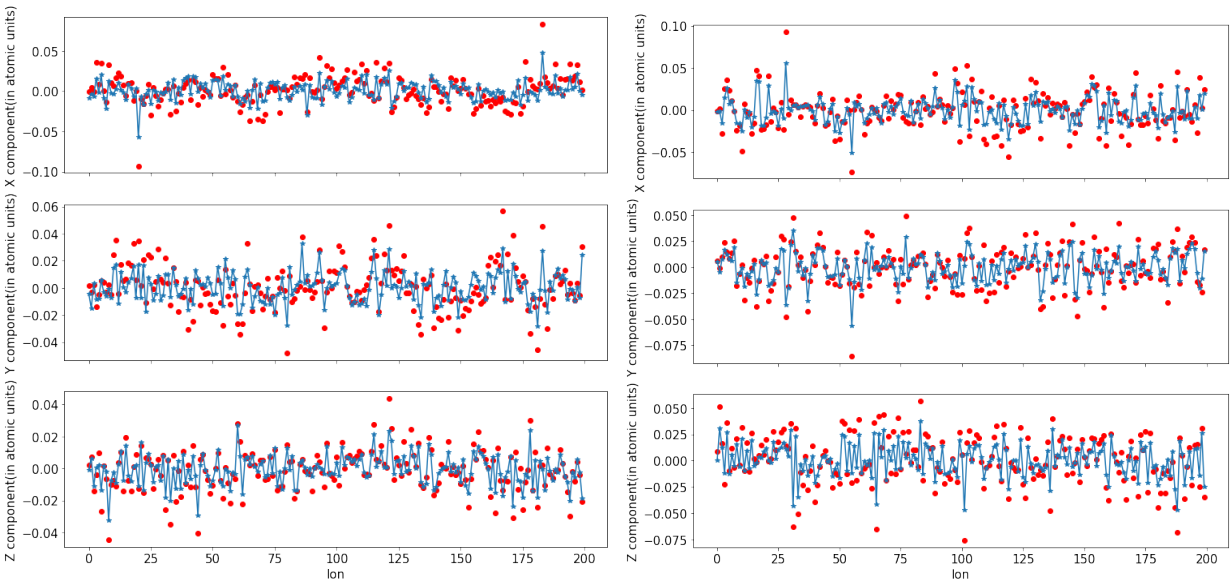

Figure C.3: Comparison of fitted (dots) and computed atomic forces (solid lines) on Cl^{-} ions (left) and La^{3+} ions (right) in crystalline La-Cl subsystem

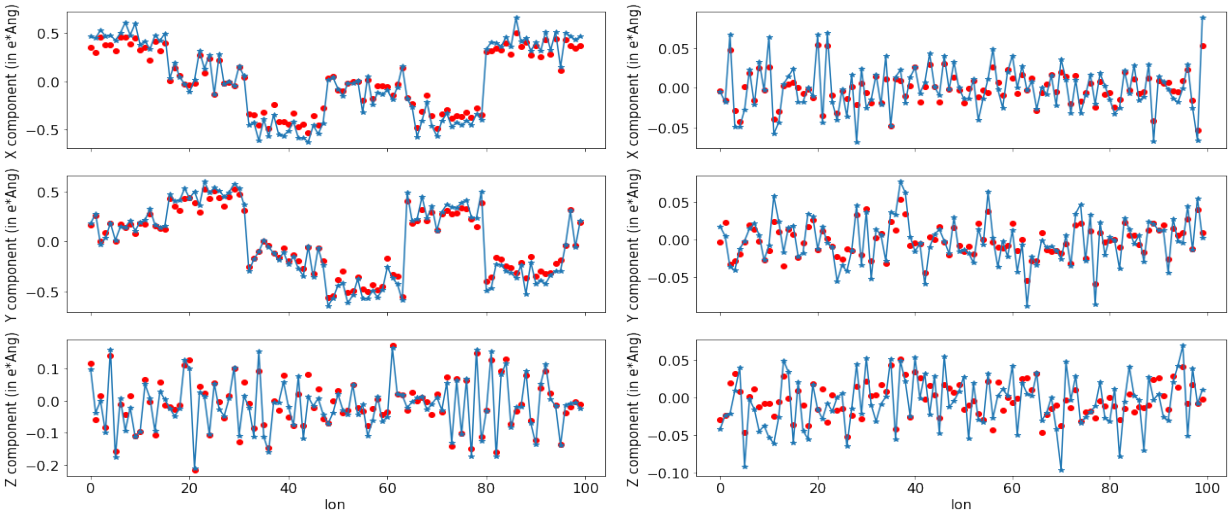

Figure C.4: Comparison of fitted (dots) and computed dipole moments (solid lines) of Cl^- ions (left) and La^{3+} ions (right) in crystalline La-Cl subsystem

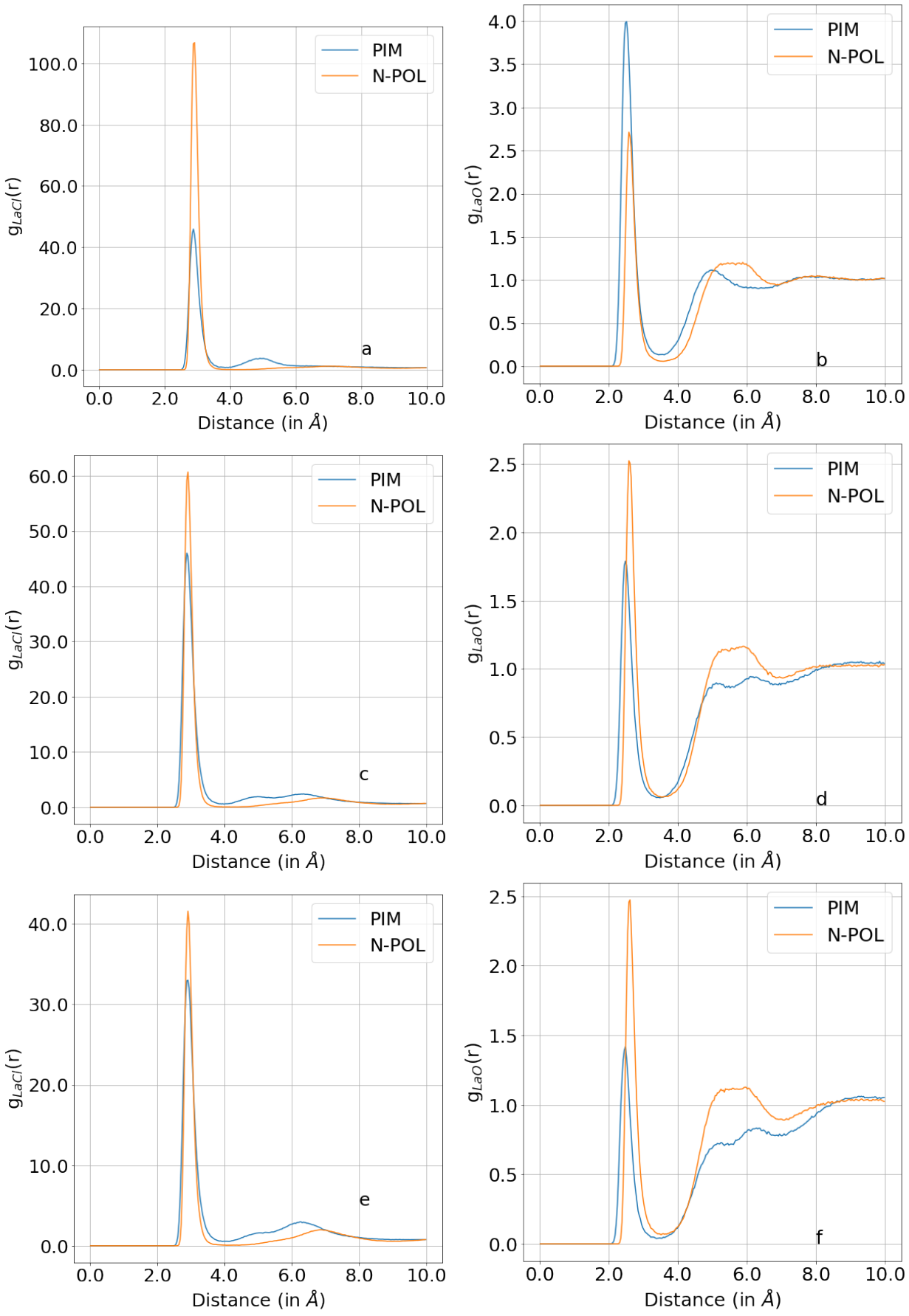

Figure C.5: $g_{LaCl}(r)$ (left column) and $g_{LaO}(r)$ (right column) obtained at 773 K with PIM and N-POL MD with box 2 (a,b), box 3 (c,d) and box 4 (e,f)

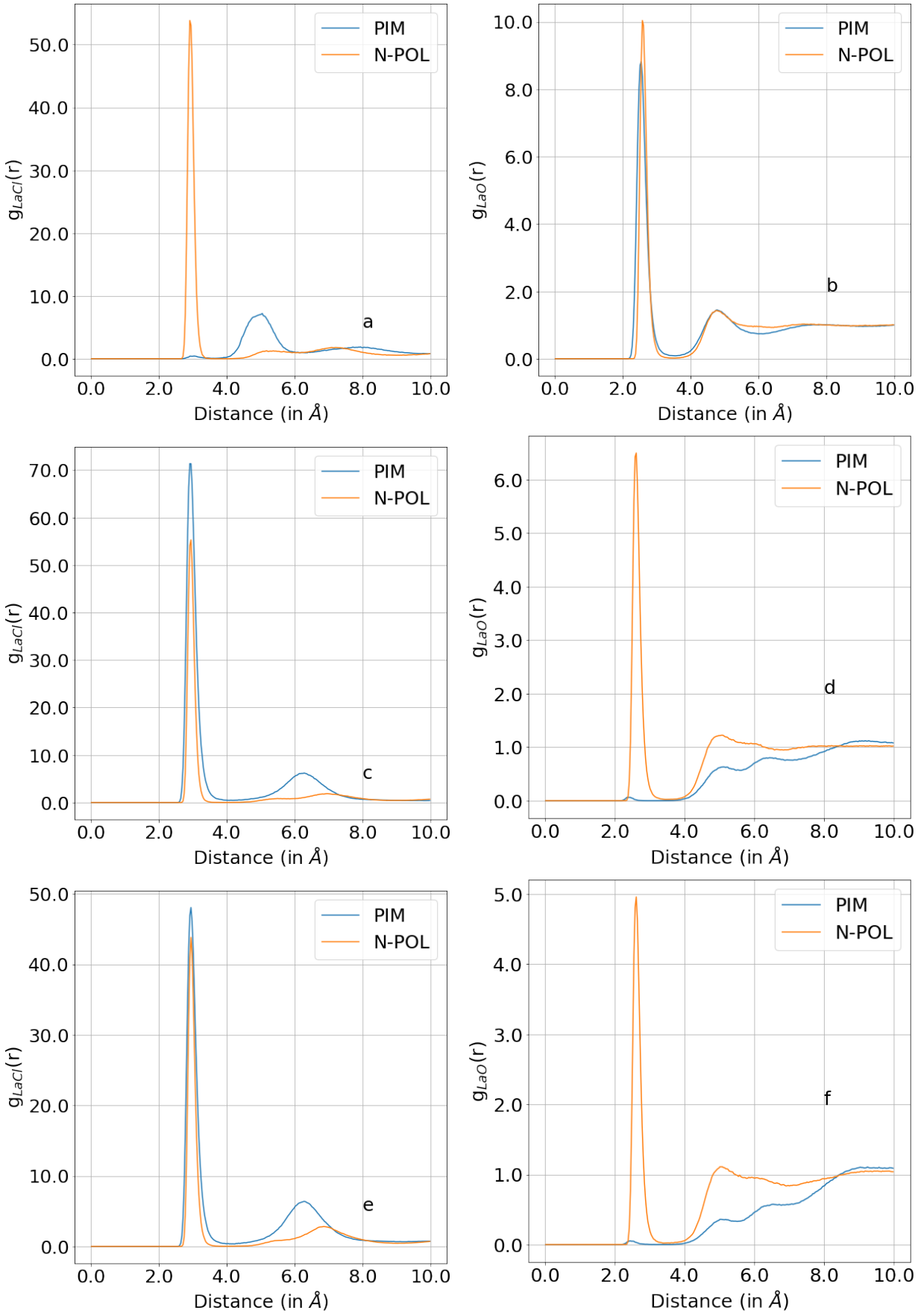

Figure C.6: $g_{LaCl}(r)$ (left column) and $g_{LaO}(r)$ (right column) obtained at 473 K with PIM and N-POL MD with box 2 (a,b), box 3 (c,d) and box 4 (e,f)

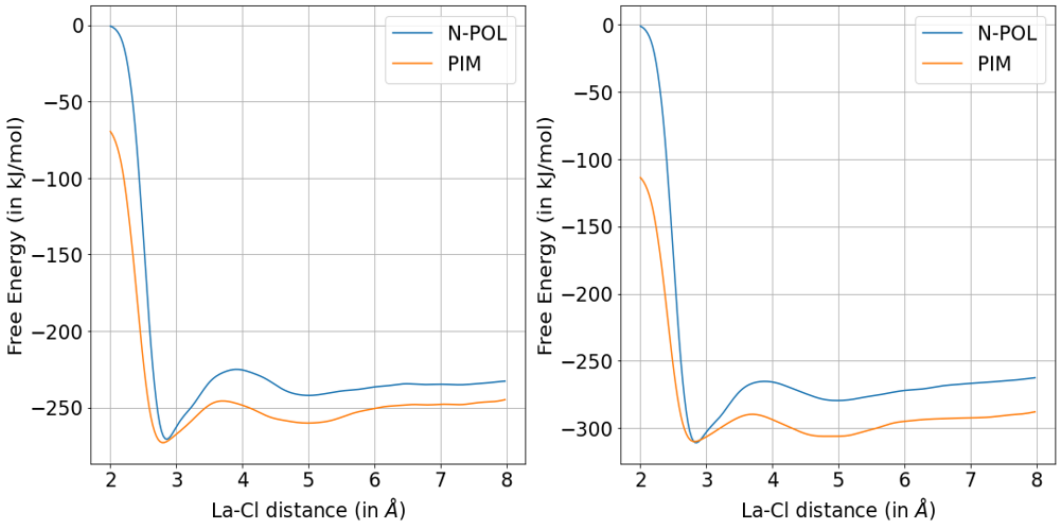

Figure C.7: Left: FES of $LaCl_2^+ + Cl^- \longrightarrow LaCl_3$ reaction from PIM and N-POL MD at 773 K, Right: FES of $La^{3+} + Cl^- \longrightarrow LaCl^+$ reaction from PIM and N-POL MD at 773 K

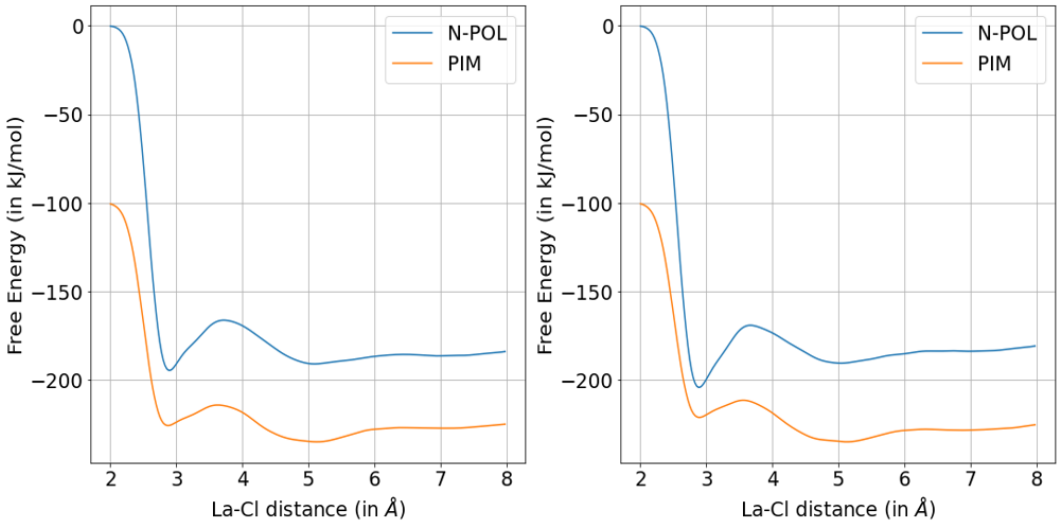

Figure C.8: Left: FES of $LaCl_2^+ + Cl^- \longrightarrow LaCl_3$ reaction from PIM and N-POL MD at 473 K, Right: FES of $La^{3+} + Cl^- \longrightarrow LaCl^+$ reaction from PIM and N-POL MD at 473 K

Bibliography

[1] Craig E. Manning and Maria Luce Frezzotti. "Subduction-Zone Fluids". In: *Elements* 16.6 (Dec. 2020), pp. 395–400. DOI: 10.2138/gselements.16.6.395.

[2] Robert J. Bodnar. "Hydrothermal solutions". In: *Geochemistry*. Dordrecht: Springer Netherlands, 1998, pp. 333–337. ISBN: 978-1-4020-4496-0. DOI: 10.1007/1-4020-4496-8_163. URL: https://doi.org/10.1007/1-4020-4496-8_163.

[3] Christopher German and K. Damm. "Hydrothermal Processes". In: *Treatise on Geochemistry* 6 (Dec. 2003). DOI: 10.1016/B0-08-043751-6/06109-0.

[4] K. L. Von Damm. "SEAFLOOR HYDROTHERMAL ACTIVITY: BLACK SMOKER CHEMISTRY AND CHIMNEYS". In: *Annual Review of Earth and Planetary Sciences* 18.Volume 18, 1990 (1990), pp. 173–204. DOI: https://doi.org/10.1146/annurev.ea.18.050190.001133.

[5] Amy Gartman, Mustafa Yücel, and George Luther. "An Introduction to the Major Chemical Components Released from Hydrothermal Vents". In: May 2014. ISBN: 9780124095489. DOI: 10.1016/B978-0-12-409548-9.09105-3.

[6] Esther M. Schwarzenbach and Matthew Steele-MacInnis. "Fluids in Submarine Mid-Ocean Ridge Hydrothermal Settings". In: *Elements* 16.6 (Dec. 2020), pp. 389–394. DOI: 10.2138/gselements.16.6.389.

[7] Thomas M. McCollom and Jeffrey S. Seewald. "Abiotic Synthesis of Organic Compounds in Deep-Sea Hydrothermal Environments". In: *Chemical Reviews* 107.2 (2007), pp. 382–401. DOI: 10.1021/cr0503660.

[8] Andreas Audétat and Marie Edmonds. "Magmatic-Hydrothermal Fluids". In: *Elements* 16.6 (Dec. 2020), pp. 401–406. DOI: 10.2138/gselements.16.6.401.

[9] Peter Ulmer and Volkmar Trommsdorff. "Serpentine Stability to Mantle Depths and Subduction-Related Magmatism". In: *Science* 268.5212 (1995), pp. 858–861. DOI: 10.1126/science.268.5212.858.

[10] Max W. Schmidt and Stefano Poli. "Experimentally based water budgets for dehydrating slabs and consequences for arc magma generation". In: *Earth and Planetary Science Letters* 163.1 (1998), pp. 361–379. DOI: https://doi.org/10.1016/S0012-821X(98)00142-3.

[11] Kenneth J. Domanik and John R. Holloway. "The stability and composition of phengitic muscovite and associated phases from 5.5 to 11 GPa: Implications for deeply

subducted sediments". In: *Geochimica et Cosmochimica Acta* 60.21 (1996), pp. 4133–4150. DOI: https://doi.org/10.1016/S0016-7037(96)00241-4.

[12] Yong-Fei Zheng et al. "Partial melting, fluid supercriticality and element mobility in ultrahigh-pressure metamorphic rocks during continental collision". In: *Earth-science Reviews - EARTH-SCI REV* 107 (Aug. 2011), pp. 342–374. DOI: 10.1016/j.earscirev.2011.04.004.

[13] Anthony R. Philpotts and Jay J. Ague. *Principles of Igneous and Metamorphic Petrology*. 3rd ed. Cambridge University Press, 2022.

[14] Anne Pommier and Rob L. Evans. "Constraints on fluids in subduction zones from electromagnetic data". In: *Geosphere* 13.4 (June 2017), pp. 1026–1041. DOI: 10.1130/GES01473.1.

[15] Isabelle Chambefort and Andri Stefánsson. "Fluids in Geothermal Systems". In: *Elements* 16.6 (Dec. 2020), pp. 407–411. DOI: 10.2138/gselements.16.6.407.

[16] Inga S. Moeck. "Catalog of geothermal play types based on geologic controls". In: *Renewable and Sustainable Energy Reviews* 37 (2014), pp. 867–882. DOI: https://doi.org/10.1016/j.rser.2014.05.032.

[17] Stephen E. Kesler. "Ore-Forming Fluids". In: *Elements* 1.1 (Jan. 2005), pp. 13–18. DOI: 10.2113/gselements.1.1.13.

[18] Scott A. Wood and Iain M. Samson. "Solubility of Ore Minerals and Complexation of Ore Metals in Hydrothermal Solutions". In: *Techniques in Hydrothermal Ore Deposits Geology*. Society of Economic Geologists, Jan. 1998. ISBN: 9781629490175. DOI: 10.5382/Rev.10.02.

[19] Robert Bodnar et al. "Fluid Inclusions in Hydrothermal Ore Deposits". In: vol. 13. Dec. 2014, pp. 119–142. ISBN: 0-08-098300-6, 978-0-08-098300-4. DOI: 10.1016/B978-0-08-095975-7.01105-0.

[20] C. R. German and William E Seyfried. "Hydrothermal Processes". English (US). In: *The Oceans and Marine Geochemistry*. Vol. 8. Elsevier Inc., Nov. 2013, pp. 191–233. ISBN: 9780080983004. DOI: 10.1016/B978-0-08-095975-7.00607-0.

[21] Wolfgang Bach and G. Fruh-Green. "Alteration of the Oceanic Lithosphere and Implications for Seafloor Processes". In: *Elements* 6 (June 2010), pp. 173–178. DOI: 10.2113/gselements.6.3.173.

[22] Jeffrey C. Alt. "Subseafloor processes in mid-ocean ridge hydrothennal systems". In: *Geophysical Monograph Series* 91 (Jan. 1995), pp. 85–114. DOI: 10.1029/GM091p0085.

[23] Matthew Steele-MacInnis et al. "The role of fluid phase immiscibility in quartz dissolution and precipitation in sub-seafloor hydrothermal systems". In: *Earth and Planetary Science Letters* 321-322 (2012), pp. 139–151. DOI: 10.1016/j.epsl.2011.12.037.

[24] S. E. Drummond and H. Ohmoto. "Chemical evolution and mineral deposition in boiling hydrothermal systems". In: *Economic Geology* 80.1 (Feb. 1985), pp. 126–147. DOI: 10.2113/gsecongeo.80.1.126.

[25] Ralph G. Pearson. "Hard and Soft Acids and Bases". In: *Journal of the American Chemical Society* 85.22 (1963), pp. 3533–3539. DOI: 10.1021/ja00905a001.

[26] A. Migdisov et al. "Hydrothermal transport, deposition, and fractionation of the REE: Experimental data and thermodynamic calculations". In: *Chemical Geology* 439 (2016), pp. 13–42. DOI: https://doi.org/10.1016/j.chemgeo.2016.06.005.

[27] Art. A. Migdisov, A.E. Williams-Jones, and T. Wagner. "An experimental study of the solubility and speciation of the Rare Earth Elements (III) in fluoride- and chloride-bearing aqueous solutions at temperatures up to 300°C". In: *Geochimica et Cosmochimica Acta* 73.23 (2009), pp. 7087–7109. DOI: https://doi.org/10.1016/j.gca.2009.08.023.

[28] Valentina Migliorati et al. "Development of Lennard-Jones and Buckingham Potentials for Lanthanoid Ions in Water". In: *Inorganic Chemistry* 56 (May 2017). DOI: 10.1021/acs.inorgchem.7b00207.

[29] Anthony Williams-Jones, I. Samson, and Gema Olivo. "The Genesis of Hydrothermal Fluorite-REE Deposits in the Gallinas Mountains, New Mexico". In: *Economic Geology* 95 (Mar. 2000), pp. 327–341. DOI: 10.2113/gsecongeo.95.2.327.

[30] Anthony E. Williams-Jones, Artashes A. Migdisov, and Iain M. Samson. "Hydrothermal Mobilisation of the Rare Earth Elements – a Tale of "Ceria" and "Yttria"". In: *Elements* 8.5 (Oct. 2012), pp. 355–360. DOI: 10.2113/gselements.8.5.355.

[31] M. P. Smith and P. Henderson. "Preliminary Fluid Inclusion Constraints on Fluid Evolution in the Bayan Obo Fe-REE-Nb Deposit, Inner Mongolia, China". In: *Economic Geology* 95.7 (Nov. 2000), pp. 1371–1388. DOI: 10.2113/gsecongeo.95.7.1371.

[32] Bernd Lehmann et al. "REE mineralization at Gakara, Burundi: Evidence for anomalous upper mantle in the western Rift Valley". In: *Geochimica et Cosmochimica Acta* 58.2 (1994), pp. 985–992. DOI: https://doi.org/10.1016/0016-7037(94)90520-7.

[33] D.A. Banks et al. “REE composition of an aqueous magmatic fluid: A fluid inclusion study from the Capitan Pluton, New Mexico, U.S.A.” In: *Chemical Geology* 113.3 (1994), pp. 259–272. DOI: https://doi.org/10.1016/0009-2541(94)90070-1.

[34] A. Pommier et al. “Laboratory measurements of electrical conductivities of hydrous and dry Mount Vesuvius melts under pressure”. In: *Journal of Geophysical Research: Solid Earth* 113.B5 (2008). DOI: https://doi.org/10.1029/2007JB005269.

[35] R. Shane McGary et al. “Pathway from subducting slab to surface for melt and fluids beneath Mount Rainier”. In: *Nature* 511.7509 (2014), pp. 338–340. DOI: 10.1038/nature13493.

[36] Leshou Chen et al. “Electrically Conductive Crust in Southern Tibet from INDEPTH Magnetotelluric Surveying”. In: *Science* 274.5293 (1996), pp. 1694–1696. DOI: 10.1126/science.274.5293.1694.

[37] Florian Le Pape et al. “Penetration of crustal melt beyond the Kunlun Fault into Northern Tibet”. In: *Nature Geoscience* 5 (Apr. 2012), pp. 330–335. DOI: 10.1038/ngeo1449.

[38] Alistair C. Hack and Alan B. Thompson. “Density and Viscosity of Hydrous Magmas and Related Fluids and their Role in Subduction Zone Processes”. In: *Journal of Petrology* 52.7-8 (Sept. 2010), pp. 1333–1362. DOI: 10.1093/petrology/egq048.

[39] Daan Frenkel and Berend Smit. “Chapter 1 - Introduction”. In: *Understanding Molecular Simulation (Second Edition)*. Ed. by Daan Frenkel and Berend Smit. Second Edition. San Diego: Academic Press, 2002, pp. 1–6. ISBN: 978-0-12-267351-1. DOI: https://doi.org/10.1016/B978-012267351-1/50003-1.

[40] B. J. Alder and T. E. Wainwright. “Studies in Molecular Dynamics. I. General Method”. In: *The Journal of Chemical Physics* 31.2 (Aug. 1959), pp. 459–466. DOI: 10.1063/1.1730376.

[41] A. Rahman. “Correlations in the Motion of Atoms in Liquid Argon”. In: *Phys. Rev.* 136 (2A 1964), A405–A411. DOI: 10.1103/PhysRev.136.A405.

[42] Jürg Hutter et al. “cp2k: atomistic simulations of condensed matter systems”. In: *WIREs Computational Molecular Science* 4.1 (2014), pp. 15–25. DOI: https://doi.org/10.1002/wcms.1159.

[43] A. P. Thompson et al. “LAMMPS - a flexible simulation tool for particle-based materials modeling at the atomic, meso, and continuum scales”. In: *Comp. Phys. Comm.* 271 (2022), p. 108171. DOI: 10.1016/j.cpc.2021.108171.

[44] Mark James Abraham et al. "GROMACS: High performance molecular simulations through multi-level parallelism from laptops to supercomputers". In: *SoftwareX* 1-2 (2015), pp. 19–25. DOI: https://doi.org/10.1016/j.softx.2015.06.001.

[45] Loup Verlet. "Computer "Experiments" on Classical Fluids. I. Thermodynamical Properties of Lennard-Jones Molecules". In: *Phys. Rev.* 159 (1 1967), pp. 98–103. DOI: 10.1103/PhysRev.159.98.

[46] William H Press et al. *Numerical recipes*. Cambridge University Press, London, England, 1988.

[47] D. Beeman. "Some multistep methods for use in molecular dynamics calculations". In: *Journal of Computational Physics* 20.2 (1976), pp. 130–139. ISSN: 0021-9991. DOI: https://doi.org/10.1016/0021-9991(76)90059-0.

[48] Josh Barnes and Piet Hut. "A hierarchical O(N log N) force-calculation algorithm". In: *Nature* 324.6096 (1986), pp. 446–449. DOI: 10.1038/324446a0.

[49] H. J. C. Berendsen et al. "Molecular dynamics with coupling to an external bath". In: *The Journal of Chemical Physics* 81.8 (Oct. 1984), pp. 3684–3690. DOI: 10.1063/1.448118.

[50] Hans C. Andersen. "Molecular dynamics simulations at constant pressure and/or temperature". In: *The Journal of Chemical Physics* 72.4 (Feb. 1980), pp. 2384–2393. DOI: 10.1063/1.439486.

[51] D. J. Evans and B. L. Holian. "The Nose–Hoover thermostat". In: *The Journal of Chemical Physics* 83.8 (Oct. 1985), pp. 4069–4074. DOI: 10.1063/1.449071.

[52] Giovanni Bussi, Davide Donadio, and Michele Parrinello. "Canonical sampling through velocity rescaling". In: *The Journal of Chemical Physics* 126.1 (Jan. 2007), p. 014101. DOI: 10.1063/1.2408420.

[53] M. Parrinello and A. Rahman. "Crystal Structure and Pair Potentials: A Molecular-Dynamics Study". In: *Phys. Rev. Lett.* 45 (14 1980), pp. 1196–1199. DOI: 10.1103/PhysRevLett.45.1196.

[54] M.P. Allen and D.J. Tildesley. *Computer simulation of liquids*. Oxford University Press, 1989.

[55] J. E. Jones and Sydney Chapman. "On the determination of molecular fields.—I. From the variation of the viscosity of a gas with temperature". In: *Proceedings of the Royal Society of London. Series A, Containing Papers of a Mathematical and Physical Character* 106.738 (1924), pp. 441–462. DOI: 10.1098/rspa.1924.0081.

[56] M B Doran and I J Zucker. "Higher order multipole three-body van der Waals interactions and stability of rare gas solids". In: *Journal of Physics C: Solid State Physics* 4.3 (1971), p. 307. DOI: 10.1088/0022-3719/4/3/006.

[57] J. A. Barker and D. Henderson. "What is "liquid"? Understanding the states of matter". In: *Rev. Mod. Phys.* 48 (4 1976), pp. 587–671. DOI: 10.1103/RevModPhys.48.587.

[58] J. Tersoff. "New empirical approach for the structure and energy of covalent systems". In: *Phys. Rev. B* 37 (12 1988), pp. 6991–7000. DOI: 10.1103/PhysRevB.37.6991.

[59] Sami Tazi et al. "A transferable ab initio based force field for aqueous ions". In: *The Journal of Chemical Physics* 136.11 (2012), p. 114507. DOI: 10.1063/1.3692965.

[60] Mark V. Fedkin et al. "Development of the ReaxFF Methodology for Electrolyte–Water Systems". In: *The Journal of Physical Chemistry A* 123.10 (2019), pp. 2125–2141. DOI: 10.1021/acs.jpca.8b10453.

[61] Adri C. T. van Duin et al. "ReaxFF: A Reactive Force Field for Hydrocarbons". In: *The Journal of Physical Chemistry A* 105.41 (2001), pp. 9396–9409. DOI: 10.1021/jp004368u.

[62] Weiwei Zhang and Adri C. T. van Duin. "Improvement of the ReaxFF Description for Functionalized Hydrocarbon/Water Weak Interactions in the Condensed Phase". In: *The Journal of Physical Chemistry B* 122.14 (2018), pp. 4083–4092. DOI: 10.1021/acs.jpcb.8b01127.

[63] Jan Zielkiewicz. "Structural properties of water: Comparison of the SPC, SPCE, TIP4P, and TIP5P models of water". In: *The Journal of Chemical Physics* 123.10 (Sept. 2005), p. 104501. DOI: 10.1063/1.2018637.

[64] David Sherman and M.D. Collings. "Ion association in concentrated NaCl brines from ambient to supercritical conditions: Results from classical molecular dynamics simulations". In: *Geochemical Transactions* 3 (Nov. 2002), pp. 102–107. DOI: 10.1039/b208671a.

[65] João V. L. Valle et al. "Accuracy of TIP4P/2005 and SPC/Fw Water Models". In: *The Journal of Physical Chemistry B* 128.4 (2024). PMID: 38253517, pp. 1091–1097. DOI: 10.1021/acs.jpcb.3c07044.

[66] H. J. C. Berendsen, J. R. Grigera, and T. P. Straatsma. "The missing term in effective pair potentials". In: *The Journal of Physical Chemistry* 91.24 (1987), pp. 6269–6271. DOI: 10.1021/j100308a038.

[67] David E. Smith and Liem X. Dang. "Computer simulations of NaCl association in polarizable water". In: *The Journal of Chemical Physics* 100.5 (Mar. 1994), pp. 3757–3766. DOI: 10.1063/1.466363.

[68] Jean-Paul Ryckaert, Giovanni Ciccotti, and Herman J.C Berendsen. "Numerical integration of the cartesian equations of motion of a system with constraints: molecular dynamics of n-alkanes". In: *Journal of Computational Physics* 23.3 (1977), pp. 327–341. DOI: https://doi.org/10.1016/0021-9991(77)90098-5.

[69] Wilfried J. Mortier, Swapan K. Ghosh, and S. Shankar. "Electronegativity-equalization method for the calculation of atomic charges in molecules". In: *Journal of the American Chemical Society* 108.15 (1986), pp. 4315–4320. DOI: 10.1021/ja00275a013.

[70] Yun Kyung Shin et al. "Development of a ReaxFF Reactive Force Field for Fe/Cr/O/S and Application to Oxidation of Butane over a Pyrite-Covered Cr_2O_3 Catalyst". In: *ACS Catalysis* 5.12 (2015), pp. 7226–7236. DOI: 10.1021/acscatal.5b01766.

[71] Mengwei Yu et al. "ReaxFF molecular dynamics simulation of nickel catalysed gasification of cellulose in supercritical water". In: *International Journal of Hydrogen Energy* 48.1 (2023), pp. 123–137. DOI: https://doi.org/10.1016/j.ijhydene.2022.09.202.

[72] Hegoi Manzano et al. "Benchmark of ReaxFF force field for subcritical and supercritical water". In: *The Journal of Chemical Physics* 148.23 (June 2018), p. 234503. DOI: 10.1063/1.5031489.

[73] Nabankur Dasgupta et al. "ReaxFF molecular dynamics simulations of electrolyte–water systems at supercritical temperature". In: *The Journal of Chemical Physics* 152.20 (May 2020), p. 204502. DOI: 10.1063/5.0006676.

[74] "What is Density Functional Theory?" In: *Density Functional Theory*. John Wiley Sons, Ltd, 2009. Chap. 1, pp. 1–33. ISBN: 9780470447710. DOI: https://doi.org/10.1002/9780470447710.ch1.

[75] E. Schrödinger. "Quantisierung als Eigenwertproblem". In: *Annalen der Physik* 384.4 (1926), pp. 361–376. DOI: https://doi.org/10.1002/andp.19263840404.

[76] W. Kohn and L. J. Sham. "Self-Consistent Equations Including Exchange and Correlation Effects". In: *Phys. Rev.* 140 (4A 1965), A1133–A1138. DOI: 10.1103/PhysRev.140.A1133.

[77] P. Hohenberg and W. Kohn. "Inhomogeneous Electron Gas". In: *Phys. Rev.* 136 (3B 1964), B864–B871. DOI: 10.1103/PhysRev.136.B864.

[78] A. D. Becke. "Density-functional exchange-energy approximation with correct asymptotic behavior". In: *Phys. Rev. A* 38 (6 1988), pp. 3098–3100. DOI: 10.1103/PhysRevA.38.3098.

[79] Chengteh Lee, Weitao Yang, and Robert G. Parr. "Development of the Colle-Salvetti correlation-energy formula into a functional of the electron density". In: *Phys. Rev. B* 37 (2 1988), pp. 785–789. DOI: 10.1103/PhysRevB.37.785.

[80] James W. Furness et al. "Accurate and Numerically Efficient r2SCAN Meta-Generalized Gradient Approximation". In: *The Journal of Physical Chemistry Letters* 11.19 (2020). PMID: 32876454, pp. 8208–8215. DOI: 10.1021/acs.jpclett.0c02405.

[81] John P. Perdew, Kieron Burke, and Matthias Ernzerhof. "Generalized Gradient Approximation Made Simple". In: *Phys. Rev. Lett.* 77 (18 1996), pp. 3865–3868. DOI: 10.1103/PhysRevLett.77.3865.

[82] 1937 Levine Ira N. *Quantum chemistry*. Seventh edition. Boston : Pearson, [2014], [2014]. URL: https://search.library.wisc.edu/catalog/9910167862202121.

[83] W. J. Hehre, R. F. Stewart, and J. A. Pople. "Self-Consistent Molecular-Orbital Methods. I. Use of Gaussian Expansions of Slater-Type Atomic Orbitals". In: *The Journal of Chemical Physics* 51.6 (Sept. 1969), pp. 2657–2664. DOI: 10.1063/1.1672392.

[84] Mark S. Gordon et al. "Self-consistent molecular-orbital methods. 22. Small split-valence basis sets for second-row elements". In: *Journal of the American Chemical Society* 104.10 (1982), pp. 2797–2803. DOI: 10.1021/ja00374a017.

[85] Joost VandeVondele and Jürg Hutter. "Gaussian basis sets for accurate calculations on molecular systems in gas and condensed phases". In: *The Journal of Chemical Physics* 127.11 (Sept. 2007), p. 114105. DOI: 10.1063/1.2770708.

[86] S. Goedecker, M. Teter, and J. Hutter. "Separable dual-space Gaussian pseudopotentials". In: *Phys. Rev. B* 54 (3 1996), pp. 1703–1710. DOI: 10.1103/PhysRevB.54.1703.

[87] I-Chun Lin et al. "Structure and Dynamics of Liquid Water from ab Initio Molecular Dynamics—Comparison of BLYP, PBE, and revPBE Density Functionals with and without van der Waals Corrections". In: *Journal of Chemical Theory and Computation* 8.10 (2012). PMID: 26593030, pp. 3902–3910. DOI: 10.1021/ct3001848.

[88] J. Stefanski and S. Jahn. "Yttrium speciation in subduction-zone fluids from ab initio molecular dynamics simulations". In: *Solid Earth* 11.3 (2020), pp. 767–789. DOI: 10.5194/se-11-767-2020.

[89] Sandro Jahn and Christian Schmidt. "Speciation in Aqueous $MgSO_4$ Fluids at High Pressures and High Temperatures from ab Initio Molecular Dynamics and Raman Spectroscopy". In: *The Journal of Physical Chemistry B* 114.47 (2010), pp. 15565–15572. DOI: 10.1021/jp101749h.

[90] Christian Schmidt and Sandro Jahn. "Raman spectra of oxidized sulfur species in hydrothermal fluids". In: *Journal of Volcanology and Geothermal Research* 454 (2024), p. 108146. DOI: https://doi.org/10.1016/j.jvolgeores.2024.108146.

[91] John P. Perdew and Karla Schmidt. "Jacob's ladder of density functional approximations for the exchange-correlation energy". In: *AIP Conference Proceedings* 577.1 (July 2001), pp. 1–20. DOI: 10.1063/1.1390175.

[92] Narbe Mardirossian and Martin Head-Gordon. "Thirty years of density functional theory in computational chemistry: an overview and extensive assessment of 200 density functionals". In: *Molecular Physics* 115.19 (2017), pp. 2315–2372. DOI: 10.1080/00268976.2017.1333644.

[93] S. H. Vosko, L. Wilk, and M. Nusair. "Accurate spin-dependent electron liquid correlation energies for local spin density calculations: a critical analysis". In: *Canadian Journal of Physics* 58.8 (1980), pp. 1200–1211. DOI: 10.1139/p80-159.

[94] J. P. Perdew and Alex Zunger. "Self-interaction correction to density-functional approximations for many-electron systems". In: *Phys. Rev. B* 23 (10 1981), pp. 5048–5079. DOI: 10.1103/PhysRevB.23.5048.

[95] John P. Perdew and Yue Wang. "Accurate and simple analytic representation of the electron-gas correlation energy". In: *Phys. Rev. B* 45 (23 1992), pp. 13244–13249. DOI: 10.1103/PhysRevB.45.13244.

[96] D. M. Ceperley and B. J. Alder. "Ground State of the Electron Gas by a Stochastic Method". In: *Phys. Rev. Lett.* 45 (7 1980), pp. 566–569. DOI: 10.1103/PhysRevLett.45.566.

[97] A. D. Becke. "Density functional calculations of molecular bond energies". In: *The Journal of Chemical Physics* 84.8 (Apr. 1986), pp. 4524–4529. DOI: 10.1063/1.450025.

[98] Frank Herman, John P. Van Dyke, and Irene B. Ortenburger. "Improved Statistical Exchange Approximation for Inhomogeneous Many-Electron Systems". In: *Phys. Rev. Lett.* 22 (16 1969), pp. 807–811. DOI: 10.1103/PhysRevLett.22.807.

[99] Karlheinz Schwarz. "On Slater's transition state for ionization energies". In: *Chemical Physics* 7.1 (1975), pp. 100–107. DOI: https://doi.org/10.1016/0301-0104(75)85029-4.

[100] John P. Perdew et al. “Atoms, molecules, solids, and surfaces: Applications of the generalized gradient approximation for exchange and correlation”. In: *Phys. Rev. B* 46 (11 1992), pp. 6671–6687. DOI: 10.1103/PhysRevB.46.6671.

[101] Yingkai Zhang and Weitao Yang. “Comment on “Generalized Gradient Approximation Made Simple””. In: *Phys. Rev. Lett.* 80 (4 1998), pp. 890–890. DOI: 10.1103/PhysRevLett.80.890.

[102] B. Hammer, L. B. Hansen, and J. K. Nørskov. “Improved adsorption energetics within density-functional theory using revised Perdew-Burke-Ernzerhof functionals”. In: *Phys. Rev. B* 59 (11 1999), pp. 7413–7421. DOI: 10.1103/PhysRevB.59.7413.

[103] John P. Perdew et al. “Restoring the Density-Gradient Expansion for Exchange in Solids and Surfaces”. In: *Phys. Rev. Lett.* 100 (13 2008), p. 136406. DOI: 10.1103/PhysRevLett.100.136406.

[104] John P. Perdew. “Density-functional approximation for the correlation energy of the inhomogeneous electron gas”. In: *Phys. Rev. B* 33 (12 1986), pp. 8822–8824. DOI: 10.1103/PhysRevB.33.8822.

[105] A. D. Becke. “Hartree–Fock exchange energy of an inhomogeneous electron gas”. In: *International Journal of Quantum Chemistry* 23.6 (1983), pp. 1915–1922. DOI: https://doi.org/10.1002/qua.560230605.

[106] Axel D. Becke. “A new inhomogeneity parameter in density-functional theory”. In: *The Journal of Chemical Physics* 109.6 (Aug. 1998), pp. 2092–2098. DOI: 10.1063/1.476722.

[107] H.L Schmider and A.D Becke. “Chemical content of the kinetic energy density”. In: *Journal of Molecular Structure: THEOCHEM* 527.1 (2000), pp. 51–61. DOI: https://doi.org/10.1016/S0166-1280(00)00477-2.

[108] John P. Perdew et al. “Accurate Density Functional with Correct Formal Properties: A Step Beyond the Generalized Gradient Approximation”. In: *Phys. Rev. Lett.* 82 (12 1999), pp. 2544–2547. DOI: 10.1103/PhysRevLett.82.2544.

[109] Jianmin Tao et al. “Climbing the Density Functional Ladder: Nonempirical Meta–Generalized Gradient Approximation Designed for Molecules and Solids”. In: *Phys. Rev. Lett.* 91 (14 2003), p. 146401. DOI: 10.1103/PhysRevLett.91.146401.

[110] John P. Perdew et al. “Workhorse Semilocal Density Functional for Condensed Matter Physics and Quantum Chemistry”. In: *Phys. Rev. Lett.* 103 (2 2009), p. 026403. DOI: 10.1103/PhysRevLett.103.026403.

[111] Jianwei Sun, Bing Xiao, and Adrienn Ruzsinszky. "Communication: Effect of the orbital-overlap dependence in the meta generalized gradient approximation". In: *The Journal of Chemical Physics* 137.5 (Aug. 2012), p. 051101. DOI: 10.1063/1.4742312.

[112] Jianwei Sun et al. "Semilocal and Hybrid Meta-Generalized Gradient Approximations Based on the Understanding of the Kinetic-Energy-Density Dependence". In: *The Journal of chemical physics* 138 (Jan. 2013), p. 044113. DOI: 10.1063/1.4789414.

[113] Jianwei Sun, John P. Perdew, and Adrienn Ruzsinszky. "Semilocal density functional obeying a strongly tightened bound for exchange". In: *Proceedings of the National Academy of Sciences* 112.3 (2015), pp. 685–689. DOI: 10.1073/pnas.1423145112.

[114] Jianwei Sun, Adrienn Ruzsinszky, and John P. Perdew. "Strongly Constrained and Appropriately Normed Semilocal Density Functional". In: *Phys. Rev. Lett.* 115 (3 2015), p. 036402. DOI: 10.1103/PhysRevLett.115.036402.

[115] Jianwei Sun et al. "Accurate first-principles structures and energies of diversely bonded systems from an efficient density functional". In: *Nature Chemistry* 8.9 (2016), pp. 831–836. DOI: 10.1038/nchem.2535.

[116] Daniil A. Kitchaev et al. "Energetics of MnO_2 polymorphs in density functional theory". In: *Phys. Rev. B* 93 (4 2016), p. 045132. DOI: 10.1103/PhysRevB.93.045132.

[117] Benoît Roux. "The calculation of the potential of mean force using computer simulations". In: *Computer Physics Communications* 91.1 (1995), pp. 275–282. DOI: https://doi.org/10.1016/0010-4655(95)00053-I.

[118] Alessandro Barducci, Giovanni Bussi, and Michele Parrinello. "Well-Tempered Metadynamics: A Smoothly Converging and Tunable Free-Energy Method". In: *Phys. Rev. Lett.* 100 (2 2008), p. 020603. DOI: 10.1103/PhysRevLett.100.020603.

[119] Eric Darve, David Rodríguez-Gómez, and Andrew Pohorille. "Adaptive biasing force method for scalar and vector free energy calculations". In: *The Journal of Chemical Physics* 128.14 (Apr. 2008), p. 144120. DOI: 10.1063/1.2829861.

[120] Alessandro Barducci, Massimiliano Bonomi, and Michele Parrinello. "Metadynamics". In: *WIREs Computational Molecular Science* 1.5 (2011), pp. 826–843. DOI: https://doi.org/10.1002/wcms.31.

[121] B. Meyer, M. Ospina, and L.B. Peter. "Raman spectrometric determination of oxysulfur anions in aqueous systems". In: *Analytica Chimica Acta* 117 (1980), pp. 301–311. DOI: https://doi.org/10.1016/0003-2670(80)87030-9.

[122] Cathrine E. Lund Myhre et al. "Spectroscopic Study of Aqueous H_2SO_4 at Different Temperatures and Compositions: Variations in Dissociation and Optical Properties".

In: *The Journal of Physical Chemistry A* 107.12 (2003), pp. 1979–1991. DOI: 10.1021/jp026576n.

[123] Tao Wang and Xiaofeng Zhu. "Sulfur transformations during supercritical water oxidation of a Chinese coal". In: *Fuel* 82.18 (2003), pp. 2267–2272. DOI: https://doi.org/10.1016/S0016-2361(03)00167-4.

[124] D. Kirk Nordstrom. "Mine Waters: Acidic to Circmneutral". In: *Elements* 7.6 (Dec. 2011), pp. 393–398. DOI: 10.2113/gselements.7.6.393.

[125] Charles W. Mandeville. "Sulfur: A Ubiquitous and Useful Tracer in Earth and Planetary Sciences". In: *Elements* 6.2 (Apr. 2010), pp. 75–80. DOI: 10.2113/gselements.6.2.75.

[126] Xiaolin Wang et al. "In situ observations of liquid–liquid phase separation in aqueous $MgSO_4$ solutions: Geological and geochemical implications". In: *Geochimica et Cosmochimica Acta* 103 (2013), pp. 1–10. DOI: https://doi.org/10.1016/j.gca.2012.10.044.

[127] Wei Zhang and Tinggui Yan. "A molecular dynamics investigation of La^{3+} and Lu^{3+}-ligand speciation in aqueous solution". In: *Journal of Molecular Liquids* 347 (2022), p. 118367. DOI: https://doi.org/10.1016/j.molliq.2021.118367.

[128] Qiushi Guan et al. "Yttrium speciation in sulfate-rich hydrothermal ore-forming fluids". In: *Geochimica et Cosmochimica Acta* 325 (2022), pp. 278–295. DOI: https://doi.org/10.1016/j.gca.2022.03.011.

[129] Eleanor R. Hughes et al. "The influence of submarine hydrothermal systems on seawater sulfate". In: *Geochimica et Cosmochimica Acta* 344 (2023), pp. 73–89. DOI: https://doi.org/10.1016/j.gca.2023.01.009.

[130] C. Schmidt. "Raman spectroscopic study of a H_2O+Na_2SO_4 solution at 21–600°C and 0.1MPa to 1.1GPa: Relative differential 1-SO_4^{2-} Raman scattering cross sections and evidence of the liquid–liquid transition". In: *Geochimica et Cosmochimica Acta* 73.2 (2009), pp. 425–437. DOI: https://doi.org/10.1016/j.gca.2008.10.019.

[131] Christian Schmidt and Terry M. Seward. "Raman spectroscopic quantification of sulfur species in aqueous fluids: Ratios of relative molar scattering factors of Raman bands of H_2S, HS^-, SO_2, HSO_4^-, SO_4^{2-}, $S_2O_3^{2-}$, S_3^- and H_2O at ambient conditions and information on changes with pressure and temperature". In: *Chemical Geology* 467 (2017), pp. 64–75. DOI: https://doi.org/10.1016/j.chemgeo.2017.07.022.

[132] Quan Wan et al. "Raman Spectra of Liquid Water from Ab Initio Molecular Dynamics: Vibrational Signatures of Charge Fluctuations in the Hydrogen Bond Net-

work". In: *Journal of Chemical Theory and Computation* 9.9 (2013). PMID: 26592405, pp. 4124–4130. DOI: 10.1021/ct4005307.

[133] Sarah Jane Fowler and David M. Sherman. "The nature of NaCl–H_2O deep fluids from ab initio molecular dynamics at 0.5–4.5GPa, 20–800°C, and 1–14m NaCl". In: *Geochimica et Cosmochimica Acta* 277 (2020), pp. 243–264. DOI: https://doi.org/10.1016/j.gca.2020.03.031.

[134] Fiona Sim et al. "Gaussian density functional calculations on hydrogen-bonded systems". In: *Journal of the American Chemical Society* 114.11 (1992), pp. 4391–4400. DOI: 10.1021/ja00037a055.

[135] K. Laasonen, F. Csajka, and M. Parrinello. "Water dimer properties in the gradient-corrected density functional theory". In: *Chemical Physics Letters* 194.3 (1992), pp. 172–174. DOI: https://doi.org/10.1016/0009-2614(92)85529-J.

[136] Thomas D Kühne, Matthias Krack, and Michele Parrinello. "Static and dynamical properties of liquid water from first principles by a novel Car- Parrinello-like approach". In: *Journal of chemical theory and computation* 5.2 (2009), pp. 235–241.

[137] Cui Zhang et al. "First Principles Simulations of the Infrared Spectrum of Liquid Water Using Hybrid Density Functionals". In: *Journal of Chemical Theory and Computation* 7.5 (2011). PMID: 26610134, pp. 1443–1449. DOI: 10.1021/ct2000952.

[138] Stefan Grimme et al. "A consistent and accurate ab initio parametrization of density functional dispersion correction (DFT-D) for the 94 elements H-Pu". In: *The Journal of Chemical Physics* 132.15 (Apr. 2010), p. 154104. DOI: 10.1063/1.3382344.

[139] Michael D. LaCount and François Gygi. "Ensemble first-principles molecular dynamics simulations of water using the SCAN meta-GGA density functional". In: *The Journal of Chemical Physics* 151.16 (Oct. 2019), p. 164101. DOI: 10.1063/1.5124957.

[140] Timothy T. Duignan et al. "Method for Accurately Predicting Solvation Structure". In: *Journal of Chemical Theory and Computation* 16.8 (2020), pp. 5401–5409. DOI: 10.1021/acs.jctc.0c00300.

[141] Timothy T. Duignan et al. "Quantifying the hydration structure of sodium and potassium ions: taking additional steps on Jacob's Ladder". In: *Phys. Chem. Chem. Phys.* 22 (19 2020), pp. 10641–10652. DOI: 10.1039/C9CP06161D.

[142] Akiko Yamaguchi et al. "Hydration structures of barium ions: Ab initio molecular dynamics simulations using the SCAN meta-GGA density functional and EXAFS spectroscopy studies". In: *Chemical Physics Letters* 780 (2021), p. 138945. DOI: https://doi.org/10.1016/j.cplett.2021.138945.

[143] Mark DelloStritto et al. “Aqueous solvation of the chloride ion revisited with density functional theory: impact of correlation and exchange approximations”. In: *Phys. Chem. Chem. Phys.* 22 (19 2020), pp. 10666–10675. DOI: 10.1039/C9CP06821J.

[144] Kyle R. Bryenton et al. “Delocalization error: The greatest outstanding challenge in density-functional theory”. In: *WIREs Computational Molecular Science* 13.2 (2023), e1631. DOI: https://doi.org/10.1002/wcms.1631.

[145] Alex P. Gaiduk, François Gygi, and Giulia Galli. “Density and Compressibility of Liquid Water and Ice from First-Principles Simulations with Hybrid Functionals”. In: *The Journal of Physical Chemistry Letters* 6.15 (2015), pp. 2902–2908. DOI: 10.1021/acs.jpclett.5b00901.

[146] Manel Canales and Elvira Guàrdia. “Computer simulation study of ion-water and water-water hydrogen bonds in sulfuric acid solutions at low temperatures”. In: *Journal of Molecular Liquids* 347 (2022), p. 118351. DOI: https://doi.org/10.1016/j.molliq.2021.118351.

[147] Quan Wan et al. “Electronic Structure of Aqueous Sulfuric Acid from First-Principles Simulations with Hybrid Functionals”. In: *The Journal of Physical Chemistry Letters* 5.15 (2014). PMID: 26277943, pp. 2562–2567. DOI: 10.1021/jz501168p.

[148] Viwat Vchirawongkwin, Chinapong Kritayakornupong, and Bernd M. Rode. “Structural and Dynamical Properties and Vibrational Spectra of Bisulfate Ion in Water: A Study by Ab Initio Quantum Mechanical Charge Field Molecular Dynamics”. In: *The Journal of Physical Chemistry B* 114.35 (2010), pp. 11561–11569. DOI: 10.1021/jp105181n.

[149] Yoong-Kee Choe, Eiji Tsuchida, and Tamio Ikeshoji. “First-principles molecular dynamics study on aqueous sulfuric acid solutions”. In: *The Journal of Chemical Physics* 126.15 (Apr. 2007), p. 154510. DOI: 10.1063/1.2718526.

[150] Tara I. Yacovitch et al. “Infrared Spectroscopy of Hydrated Bisulfate Anion Clusters: $HSO_4^-(H_2O)_{1–16}$”. In: *The Journal of Physical Chemistry Letters* 2.17 (2011), pp. 2135–2140. DOI: 10.1021/jz200917f.

[151] Cory C. Pye. “An ab initio study of the effect of hydration on the vibrational spectrum of hydrogen sulfate”. In: *Computational and Theoretical Chemistry* 1176 (2020), p. 112749. DOI: https://doi.org/10.1016/j.comptc.2020.112749.

[152] Yoong-Kee Choe, Eiji Tsuchida, and Tamio Ikeshoji. “Vibrational analysis of aqueous sulfuric acid: A computational study”. In: *International Journal of Quantum Chemistry* 109.9 (2009), pp. 1984–1990. DOI: https://doi.org/10.1002/qua.22031.

[153] Joachim Reimer, Frédéric Vogel, and Matthew Steele-MacInnis. "Speciation and Structural Properties of Hydrothermal Solutions of Sodium and Potassium Sulfate Studied by Molecular Dynamics Simulations". In: *ChemPhysChem* 17.10 (2016), pp. 1446–1453. DOI: https://doi.org/10.1002/cphc.201600042.

[154] Krzysztof Nieszporek and Jolanta Nieszporek. "Molecular dynamics simulation of an aqueous Na_2SO_4 solution". In: *Annales Universitatis Mariae Curie-Skłodowska, sectio AA – Chemia* 72.2 (2017).

[155] Erik Wernersson and Pavel Jungwirth. "Effect of Water Polarizability on the Properties of Solutions of Polyvalent Ions: Simulations of Aqueous Sodium Sulfate with Different Force Fields". In: *Journal of Chemical Theory and Computation* 6.10 (2010), pp. 3233–3240. DOI: 10.1021/ct100465g.

[156] Viwat Vchirawongkwin, Bernd M. Rode, and Ingmar Persson. "Structure and Dynamics of Sulfate Ion in Aqueous SolutionAn ab initio QMCF MD Simulation and Large Angle X-ray Scattering Study". In: *The Journal of Physical Chemistry B* 111.16 (2007). PMID: 17402778, pp. 4150–4155. DOI: 10.1021/jp0702402.

[157] Pavel Jungwirth, Joseph E. Curtis, and Douglas J. Tobias. "Polarizability and aqueous solvation of the sulfate dianion". In: *Chemical Physics Letters* 367.5 (2003), pp. 704–710. DOI: https://doi.org/10.1016/S0009-2614(02)01782-7.

[158] Joachim Reimer et al. "Ion Association in Hydrothermal Sodium Sulfate Solutions Studied by Modulated FT-IR-Raman Spectroscopy and Molecular Dynamics". In: *The Journal of Physical Chemistry B* 119.30 (2015), pp. 9847–9857. DOI: 10.1021/acs.jpcb.5b03192.

[159] Hao Zhang, Song Wang, and Chia-Chung Sun. "Ab initio investigation on ion-associated species and association process in aqueous Na_2SO_4 and $Na_2SO_4/MgSO_4$ solutions". In: *The Journal of Chemical Physics* 135.8 (Aug. 2011), p. 084309. DOI: 10.1063/1.3622859.

[160] Torsten Wende et al. "Probing the microsolvation of a quaternary ion complex: gas phase vibrational spectroscopy of $(NaSO_4^-)_2(H_2O)_{n=0\text{–}6,8}$". In: *Phys. Chem. Chem. Phys.* 18 (1 2016), pp. 267–277. DOI: 10.1039/C5CP05762K.

[161] Cory C. Pye and Wolfram W. Rudolph. "An ab Initio and Raman Investigation of Sulfate Ion Hydration". In: *The Journal of Physical Chemistry A* 105.5 (2001), pp. 905–912. DOI: 10.1021/jp003253n.

[162] Viwat Vchirawongkwin and Bernd M. Rode. "Solvation energy and vibrational spectrum of sulfate in water – An ab initio quantum mechanical simulation". In: *Chemical Physics Letters* 443.1 (2007), pp. 152–157. DOI: https://doi.org/10.1016/j.cplett.2007.06.040.

[163] Mengzi Zhou et al. "Ab Initio Molecular Dynamics Simulations and Vibrational Frequency Calculations of Species in Liquid-Liquid Phase Separated $MgSO_4$ Solution at 543K". In: *Geofluids* 2024.1 (2024), p. 8852421. DOI: https://doi.org/10.1155/2024/8852421.

[164] Giacomo Miceli, Jürg Hutter, and Alfredo Pasquarello. "Liquid Water through Density-Functional Molecular Dynamics: Plane-Wave vs Atomic-Orbital Basis Sets". In: *Journal of Chemical Theory and Computation* 12.8 (2016), pp. 3456–3462. DOI: 10.1021/acs.jctc.6b00271.

[165] M. Brehm et al. "TRAVIS—A free analyzer for trajectories from molecular simulation". In: *The Journal of Chemical Physics* 152.16 (Apr. 2020), p. 164105. DOI: 10.1063/5.0005078.

[166] Georg Spiekermann et al. "Vibrational mode frequencies of silica species in SiO_2–H_2O liquids and glasses from ab initio molecular dynamics". In: *The Journal of chemical physics* 136 (Apr. 2012), p. 154501. DOI: 10.1063/1.3703667.

[167] Georg Spiekermann et al. "Vibrational properties of silica species in MgO–SiO_2 glasses obtained from ab initio molecular dynamics". In: *Chemical Geology* 346 (2013), pp. 22–33. DOI: https://doi.org/10.1016/j.chemgeo.2012.08.020.

[168] JiXiang Xu, Yan Fang, and Chunhui Fang. "Structure of aqueous sodium sulfate solutions derived from X-ray diffraction". In: *Chinese Science Bulletin* 54 (June 2009), pp. 2022–2027. DOI: 10.1007/s11434-009-0232-1.

[169] Richard J. Gowers and Paola Carbone. "A multiscale approach to model hydrogen bonding: The case of polyamide". In: *The Journal of Chemical Physics* 142.22 (June 2015), p. 224907. DOI: 10.1063/1.4922445.

[170] Alenka Luzar and David Chandler. "Effect of Environment on Hydrogen Bond Dynamics in Liquid Water". In: *Phys. Rev. Lett.* 76 (6 1996), pp. 928–931. DOI: 10.1103/PhysRevLett.76.928.

[171] H. F. M. C. Martiniano and N. Galamba. "Insights on Hydrogen-Bond Lifetimes in Liquid and Supercooled Water". In: *The Journal of Physical Chemistry B* 117.50 (2013), pp. 16188–16195. DOI: 10.1021/jp407768u.

[172] Hossein Ali Karimi-Varzaneh, Paola Carbone, and Florian Müller-Plathe. "Hydrogen Bonding and Dynamic Crossover in Polyamide-66: A Molecular Dynamics Simulation Study". In: *Macromolecules* 41.19 (2008), pp. 7211–7218. DOI: 10.1021/ma8010685.

[173] Lin Lan Zaiwen Yang Shasha Lu. "Twelve-coordinated sulfate hydrogen bonding interactions in water-containing Fe(II) system". In: *Molecular Crystals and Liquid Crystals* 680.1 (2019), pp. 96–104. DOI: 10.1080/15421406.2019.1624400.

[174] G. E. Walrafen and D. M. Dodd. "Infra-red absorption spectra of concentrated aqueous solutions of sulphuric acid. Part 2.—H_2SO_4 and HSO vibrational fundamentals and estimates of (F—H)/T and S for H_2SO_4 gas". In: *Trans. Faraday Soc.* 57 (0 1961), pp. 1286–1296. DOI: 10.1039/TF9615701286.

[175] Yuta Matsumoto et al. "Raman spectroscopic study of aqueous alkali sulfate solutions at high temperature and pressure to yield precipitation". In: *The Journal of Supercritical Fluids* 49.3 (2009), pp. 303–309. ISSN: 0896-8446. DOI: https://doi.org/10.1016/j.supflu.2009.04.004.

[176] A.D. Hammerich, V. Buch, and F. Mohamed. "Ab initio simulations of sulfuric acid solutions". In: *Chemical Physics Letters* 460.4 (2008), pp. 423–431. DOI: https://doi.org/10.1016/j.cplett.2008.06.053.

[177] Tanja van Mourik and Robert J. Gdanitz. "A critical note on density functional theory studies on rare-gas dimers". In: *The Journal of Chemical Physics* 116.22 (June 2002), pp. 9620–9623. DOI: 10.1063/1.1476010.

[178] JoséM. Pérez-Jordá and A.D. Becke. "A density-functional study of van der Waals forces: rare gas diatomics". In: *Chemical Physics Letters* 233.1 (1995), pp. 134–137. DOI: https://doi.org/10.1016/0009-2614(94)01402-H.

[179] Sándor Kristyán and Péter Pulay. "Can (semi)local density functional theory account for the London dispersion forces?" In: *Chemical Physics Letters* 229.3 (1994), pp. 175–180. DOI: https://doi.org/10.1016/0009-2614(94)01027-7.

[180] Majid Rezaei, Sung Sakong, and Axel Groß. "Molecular Modeling of Water-in-Salt Electrolytes: A Comprehensive Analysis of Polarization Effects and Force Field Parameters in Molecular Dynamics Simulations". In: *Journal of Chemical Theory and Computation* 19.17 (2023). PMID: 37528639, pp. 5712–5730. DOI: 10.1021/acs.jctc.3c00171.

[181] Quan Wan, Leonardo Spanu, and Giulia Galli. "Solvation Properties of Microhydrated Sulfate Anion Clusters: Insights from abInitio Calculations". In: *The Journal of Physical Chemistry B* 116.31 (2012). PMID: 22794124, pp. 9460–9466. DOI: 10.1021/jp303624q.

[182] G. E. Walrafen, W.-H. Yang, and Y. C. Chu. "High-Temperature Raman Investigation of Concentrated Sulfuric Acid Mixtures: Measurement of H-Bond ΔH Values between H_3O^+ or $H_5O_2^+$ and HSO_4^-". In: *The Journal of Physical Chemistry A* 106.43 (2002), pp. 10162–10173. DOI: 10.1021/jp021436z.

[183] Francis P. Daly, Chris W. Brown, and Dana R. Kester. "Sodium and magnesium sulfate ion pairing. Evidence from Raman spectroscopy". In: *The Journal of Physical Chemistry* 76.24 (1972), pp. 3664–3668. DOI: 10.1021/j100668a027.

[184] W. W. Rudolph, G. Irmer, and G. T. Hefter. "Raman spectroscopic investigation of speciation in $MgSO_4$(aq)". In: *Phys. Chem. Chem. Phys.* 5 (23 2003), pp. 5253–5261. DOI: 10.1039/B308951G.

[185] Hiroshi Ichihara et al. "A 3-D electrical resistivity model beneath the focal zone of the 2008 Iwate-Miyagi Nairiku earthquake (M 7.2)". In: *Earth, Planets and Space* 66.1 (2014), p. 50. DOI: 10.1186/1880-5981-66-50.

[186] M. Ichiki et al. "An overview of electrical conductivity structures of the crust and upper mantle beneath the northwestern Pacific, the Japanese Islands, and continental East Asia". In: *Gondwana Research* 16.3 (2009), pp. 545–562. DOI: https://doi.org/10.1016/j.gr.2009.04.007.

[187] Wolfgang Soyer and Martyn Unsworth. "Deep electrical structure of the northern Cascadia (British Columbia, Canada) subduction zone: Implications for the distribution of fluids". In: *Geology* 34.1 (Jan. 2006), pp. 53–56. DOI: 10.1130/G21951.1.

[188] Paul W. J. Glover and A. Ádám. "Correlation between crustal high conductivity zones and seismic activity and the role of carbon during shear deformation". In: *Journal of Geophysical Research: Solid Earth* 113.B12 (2008). DOI: https://doi.org/10.1029/2008JB005804.

[189] Xinzhuan Guo, Takashi Yoshino, and Akira Shimojuku. "Electrical conductivity of albite–(quartz)–water and albite–water–NaCl systems and its implication to the high conductivity anomalies in the continental crust". In: *Earth and Planetary Science Letters* 412 (2015), pp. 1–9. DOI: https://doi.org/10.1016/j.epsl.2014.12.021.

[190] Bruno Reynard, Kenji Mibe, and Bertrand Van de Moortèle. "Electrical conductivity of the serpentinised mantle and fluid flow in subduction zones". In: *Earth and Planetary Science Letters* 307.3 (2011), pp. 387–394. DOI: https://doi.org/10.1016/j.epsl.2011.05.013.

[191] John F. Hermance. "The electrical conductivity of materials containing partial melt: A simple model from Archie's law". In: *Geophysical Research Letters* 6.7 (1979), pp. 613–616. DOI: https://doi.org/10.1029/GL006i007p00613.

[192] Jeffery J. Roberts and James A. Tyburczy. "Partial-melt electrical conductivity: Influence of melt composition". In: *Journal of Geophysical Research: Solid Earth* 104.B4 (1999), pp. 7055–7065. DOI: https://doi.org/10.1029/1998JB900111.

[193] R.D. Hyndman and D.W. Hyndman. "Water saturation and high electrical conductivity in the lower continental crust". In: *Earth and Planetary Science Letters* 4.6 (1968), pp. 427–432. DOI: https://doi.org/10.1016/0012-821X(68)90017-4.

[194] R. D. Hyndman and P. M. Shearer. "Water in the lower continental crust: modelling magnetotelluric and seismic reflection results*". In: *Geophysical Journal International* 98.2 (Aug. 1989), pp. 343–365. DOI: 10.1111/j.1365-246X.1989.tb03357.x.

[195] Akira Shimojuku et al. "Electrical conductivity of fluid-bearing quartzite under lower crustal conditions". In: *Physics of the Earth and Planetary Interiors* 198-199 (2012), pp. 1–8. DOI: https://doi.org/10.1016/j.pepi.2012.03.007.

[196] Akira Shimojuku, Takashi Yoshino, and Daisuke Yamazaki. "Electrical conductivity of brine-bearing quartzite at 1GPa: implications for fluid content and salinity of the crust". In: *Earth, Planets and Space* 66.1 (2014), p. 2. DOI: 10.1186/1880-5981-66-2.

[197] Arvin S. Quist. "Ionization constant of water to 800° and 4000 bars". In: *The Journal of Physical Chemistry* 74.18 (1970), pp. 3396–3402. DOI: 10.1021/j100712a017.

[198] William L. Marshall and E. U. Franck. "Ion product of water substance, 0–1000°C, 1–10,000 bars New International Formulation and its background". In: *Journal of Physical and Chemical Reference Data* 10.2 (Apr. 1981), pp. 295–304. DOI: 10.1063/1.555643.

[199] Tatsuhiko Kawamoto et al. "Mantle wedge infiltrated with saline fluids from dehydration and decarbonation of subducting slab". In: *Proceedings of the National Academy of Sciences* 110.24 (2013), pp. 9663–9668. DOI: 10.1073/pnas.1302040110.

[200] Simon M. Peacock. "Fluid Processes in Subduction Zones". In: *Science* 248.4953 (1990), pp. 329–337. DOI: 10.1126/science.248.4953.329.

[201] Fabrice Gaillard, Bruno Scaillet, and Michel Pichavant. "Evidence for present-day leucogranite pluton growth in Tibet". In: *Geology* 32.9 (Sept. 2004), pp. 801–804. DOI: 10.1130/G20577.1.

[202] J. E. Bannard. "Effect of density on the electrical conductance of aqueous sodium chloride solutions". In: *Journal of Applied Electrochemistry* 5.1 (1975), pp. 43–53. DOI: 10.1007/BF00625958.

[203] Arvin S. Quist and William L. Marshall. "Electrical conductances of aqueous sodium chloride solutions from 0 to 800°C and at pressures to 4000 bars". In: *The Journal of Physical Chemistry* 72.2 (1968), pp. 684–703. DOI: 10.1021/j100848a050.

[204] Patience C. Ho, Donald A. Palmer, and Robert E. Mesmer. "Electrical conductivity measurements of aqueous sodium chloride solutions to 600°C and 300 MPa". In: *Journal of Solution Chemistry* 23.9 (1994), pp. 997–1018. DOI: 10.1007/BF00974100.

[205] Ryosuke Sinmyo and Hans Keppler. "Electrical conductivity of NaCl-bearing aqueous fluids to 600°C and 1GPa". In: *Contributions to Mineralogy and Petrology* 172.1 (2016), p. 4. DOI: 10.1007/s00410-016-1323-z.

[206] James K. Fogo, Sidney W. Benson, and Charles S. Copeland. "The Electrical Conductivity of Supercritical Solutions of Sodium Chloride and Water". In: *The Journal of Chemical Physics* 22.2 (Feb. 1954), pp. 212–216. DOI: 10.1063/1.1740032.

[207] James F. Corwin, Robert G. Bayless, and G. E. Owen. "THE CONDUCTIVITY OF DILUTE SODIUM CHLORIDE SOLUTIONS UNDER SUPERCRITICAL CONDITIONS1". In: *The Journal of Physical Chemistry* 64.5 (1960), pp. 641–646. DOI: 10.1021/j100834a028.

[208] Haihao Guo and Hans Keppler. "Electrical Conductivity of NaCl-Bearing Aqueous Fluids to 900°C and 5GPa". In: *Journal of Geophysical Research: Solid Earth* 124.2 (2019), pp. 1397–1411. DOI: https://doi.org/10.1029/2018JB016658.

[209] S.H. Lee et al. "Molecular dynamics simulation of the limiting conductance of NaCl in supercritical water". In: *Chemical Physics Letters* 293.3 (1998), pp. 289–294. DOI: https://doi.org/10.1016/S0009-2614(98)00766-0.

[210] Ali Ghaffari and Ahmad Rahbar-Kelishami. "MD simulation and evaluation of the self-diffusion coefficients in aqueous NaCl solutions at different temperatures and concentrations". In: *Journal of Molecular Liquids* 187 (2013), pp. 238–245. DOI: https://doi.org/10.1016/j.molliq.2013.08.004.

[211] Hiroshi Sakuma and Masahiro Ichiki. "Electrical conductivity of NaCl-H_2O fluid in the crust". In: *Journal of Geophysical Research: Solid Earth* 121.2 (2016), pp. 577–594. DOI: https://doi.org/10.1002/2015JB012219.

[212] Tae Jun Yoon et al. "Electrical conductivity, ion pairing, and ion self-diffusion in aqueous NaCl solutions at elevated temperatures and pressures". In: *The Journal of Chemical Physics* 151.22 (Dec. 2019), p. 224504. DOI: 10.1063/1.5128671.

[213] Alexander P. Lyubartsev and Aatto Laaksonen. "Concentration Effects in Aqueous NaCl Solutions. A Molecular Dynamics Simulation". In: *The Journal of Physical Chemistry* 100.40 (1996), pp. 16410–16418. DOI: 10.1021/jp961317h.

[214] Yilong Pan, Wenjun Yong, and Richard A. Secco. "Electrical Conductivity of Aqueous NaCl at High Pressure and Low Temperature: Application to Deep Subsurface Oceans of Icy Moons". In: *Geophysical Research Letters* 48.17 (2021), e2021GL094020. DOI: https://doi.org/10.1029/2021GL094020.

[215] J. Sala, E. Guàrdia, and J. Martí. "Effects of concentration on structure, dielectric, and dynamic properties of aqueous NaCl solutions using a polarizable model". In: *The Journal of Chemical Physics* 132.21 (June 2010), p. 214505. DOI: 10.1063/1.3429253.

[216] Snehasis Chowdhuri and Amalendu Chandra. "Hydration structure and diffusion of ions in supercooled water: Ion size effects". In: *The Journal of Chemical Physics* 118.21 (June 2003), pp. 9719–9725. DOI: 10.1063/1.1570405.

[217] Samuel Blazquez et al. "Computation of Electrical Conductivities of Aqueous Electrolyte Solutions: Two Surfaces, One Property". In: *Journal of Chemical Theory and Computation* 19.16 (2023), pp. 5380–5393. DOI: 10.1021/acs.jctc.3c00562.

[218] Noam Agmon. "The Grotthuss mechanism". In: *Chemical Physics Letters* 244.5 (1995), pp. 456–462. DOI: https://doi.org/10.1016/0009-2614(95)00905-J.

[219] Melville S. Green. "Markoff Random Processes and the Statistical Mechanics of Time-Dependent Phenomena. II. Irreversible Processes in Fluids". In: *The Journal of Chemical Physics* 22.3 (Mar. 1954), pp. 398–413. DOI: 10.1063/1.1740082.

[220] Ryogo Kubo. "Statistical-Mechanical Theory of Irreversible Processes. I. General Theory and Simple Applications to Magnetic and Conduction Problems". In: *Journal of the Physical Society of Japan* 12.6 (1957), pp. 570–586. DOI: 10.1143/JPSJ.12.570.

[221] Kai-Min Tu, Ryosuke Ishizuka, and Nobuyuki Matubayasi. "Spatial-decomposition analysis of electrical conductivity in concentrated electrolyte solution". In: *The Journal of Chemical Physics* 141.4 (July 2014), p. 044126. DOI: 10.1063/1.4890741.

[222] Joseph C. Fogarty et al. "A reactive molecular dynamics simulation of the silica-water interface". In: *The Journal of Chemical Physics* 132.17 (May 2010), p. 174704. DOI: 10.1063/1.3407433.

[223] Davide Mantegazzi, Carmen Sanchez-Valle, and Thomas Driesner. "Thermodynamic properties of aqueous NaCl solutions to 1073K and 4.5GPa, and implications for dehydration reactions in subducting slabs". In: *Geochimica et Cosmochimica Acta* 121 (2013), pp. 263–290. DOI: https://doi.org/10.1016/j.gca.2013.07.015.

[224] Dimitri A. Sverjensky, Brandon Harrison, and David Azzolini. "Water in the deep Earth: The dielectric constant and the solubilities of quartz and corundum to 60kb and 1200°C". In: *Geochimica et Cosmochimica Acta* 129 (2014), pp. 125–145. DOI: https://doi.org/10.1016/j.gca.2013.12.019.

[225] Athanassios Z. Panagiotopoulos. "Simulations of activities, solubilities, transport properties, and nucleation rates for aqueous electrolyte solutions". In: *The Journal of Chemical Physics* 153.1 (July 2020), p. 010903. DOI: 10.1063/5.0012102.

[226] Jun Soo Kim et al. "Self-Diffusion and Viscosity in Electrolyte Solutions". In: *The Journal of Physical Chemistry B* 116.39 (2012), pp. 12007–12013. DOI: 10.1021/jp306847t.

[227] Raúl Fuentes-Azcatl and Marcia C. Barbosa. "Sodium Chloride, NaCl/: New Force Field". In: *The Journal of Physical Chemistry B* 120.9 (2016). PMID: 26890321, pp. 2460–2470. DOI: 10.1021/acs.jpcb.5b12584.

[228] Raul Fuentes-Azcatl and Marcia Barbosa. "Potassium bromide, KBr/ : New Force Field". In: *Physica A: Statistical Mechanics and its Applications* 491 (Sept. 2017). DOI: 10.1016/j.physa.2017.09.081.

[229] Jicun Li and Feng Wang. "Pairwise-additive force fields for selected aqueous monovalent ions from adaptive force matching". In: *The Journal of Chemical Physics* 143.19 (Nov. 2015), p. 194505. DOI: 10.1063/1.4935599.

[230] Ellen E. Bruce and Nico F. A. van der Vegt. "Does an electronic continuum correction improve effective short-range ion-ion interactions in aqueous solution?" In: *The Journal of Chemical Physics* 148.22 (Mar. 2018), p. 222816. DOI: 10.1063/1.5017101.

[231] Adri C. T. van Duin et al. *A ReaxFF Reactive Force-field for Proton Transfer Reactions in Bulk Water and its Applications to Heterogeneous Catalysis*. Aug. 2023. DOI: 10.1039/9781849734905-00223.

[232] Carlos Vega and Jose L. F. Abascal. "Simulating water with rigid non-polarizable models: a general perspective". In: *Phys. Chem. Chem. Phys.* 13 (44 2011), pp. 19663–19688. DOI: 10.1039/C1CP22168J.

[233] Roger G Skirrow et al. *Critical commodities for a high-tech world: Australia's potential to supply global demand*. Geoscience Australia Canberra, 2013.

[234] I. González-Álvarez et al. "Introduction to the special Issue, insights on carbonatites and their mineral exploration approach: A challenge towards resourcing critical metals". In: *Ore Geology Reviews* 133 (2021), p. 104073. DOI: https://doi.org/10.1016/j.oregeorev.2021.104073.

[235] Emma Sheard et al. "Controls on the Concentration of Zirconium, Niobium, and the Rare Earth Elements in the Thor Lake Rare Metal Deposit, Northwest Territories, Canada". In: *Economic Geology* 107 (Jan. 2012), pp. 81–104. DOI: 10.2113/econgeo.107.1.81.

[236] Joël Brugger et al. "A review of the coordination chemistry of hydrothermal systems, or do coordination changes make ore deposits?" In: *Chemical Geology* 447 (2016), pp. 219–253. DOI: https://doi.org/10.1016/j.chemgeo.2016.10.021.

[237] L Lintjewas and I Setiawan. "Mobility of rare earth element in hydrothermal process and weathering product: a review". In: *IOP Conference Series: Earth and Environmental Science* 118.1 (2018), p. 012076. DOI: 10.1088/1755-1315/118/1/012076.

[238] Qiushi Guan et al. "Speciation and thermodynamic properties of La(III)-Cl complexes in hydrothermal fluids: A combined molecular dynamics and in situ X-ray absorption spectroscopy study". In: *Geochimica et Cosmochimica Acta* 330 (2022), pp. 27–46. DOI: https://doi.org/10.1016/j.gca.2022.02.032.

[239] Magali Duvail et al. "Pair interaction potentials with explicit polarization for molecular dynamics simulations of La^{3+} in bulk water". In: *The Journal of Chemical Physics* 127.3 (July 2007), p. 034503. DOI: 10.1063/1.2751503.

[240] Magali Duvail, Pierre Vitorge, and Riccardo Spezia. "Building a polarizable pair interaction potential for lanthanoids(III) in liquid water: A molecular dynamics study of structure and dynamics of the whole series". In: *The Journal of Chemical Physics* 130.10 (Mar. 2009), p. 104501. DOI: 10.1063/1.3081143.

[241] Riccardo Spezia et al. "Molecular dynamics to rationalize EXAFS experiments: A dynamical model explaining hydration behaviour across the lanthanoid(III) series". In: *Journal of Physics: Conference Series* 190.1 (2009), p. 012056. DOI: 10.1088/1742-6596/190/1/012056.

[242] C. Clavaguéra et al. "Molecular Dynamics Study of the Hydration of Lanthanum(III) and Europium(III) Including Many-Body Effects". In: *The Journal of Physical Chemistry B* 109.16 (2005), pp. 7614–7616. DOI: 10.1021/jp051032h.

[243] Pengyu Ren and Jay W. Ponder. "Consistent treatment of inter- and intramolecular polarization in molecular mechanics calculations". In: *Journal of Computational Chemistry* 23.16 (2002), pp. 1497–1506. DOI: https://doi.org/10.1002/jcc.10127.

[244] Pengyu Ren and Jay W. Ponder. "Polarizable Atomic Multipole Water Model for Molecular Mechanics Simulation". In: *The Journal of Physical Chemistry B* 107.24 (2003), pp. 5933–5947. DOI: 10.1021/jp027815+.

[245] Pengfei Li, Lin Frank Song, and Kenneth M. Jr. Merz. "Parameterization of Highly Charged Metal Ions Using the 12-6-4 LJ-Type Nonbonded Model in Explicit Water". In: *The Journal of Physical Chemistry B* 119.3 (2015), pp. 883–895. DOI: 10.1021/jp505875v.

[246] Alessandra Villa, Berk Hess, and Humberto Saint-Martin. "Dynamics and Structure of Ln(III)Aqua Ions: A Comparative Molecular Dynamics Study Using ab Initio Based Flexible and Polarizable Model Potentials". In: *The Journal of Physical Chemistry B* 113.20 (2009), pp. 7270–7281. DOI: 10.1021/jp8097445.

[247] Humberto Saint-Martin et al. "A mobile charge densities in harmonic oscillators (MCDHO) molecular model for numerical simulations: The water–water interaction". In: *The Journal of Chemical Physics* 113.24 (Dec. 2000), pp. 10899–10912. DOI: 10.1063/1.1324711.

[248] Takashi Ikeda, Masaru Hirata, and Takaumi Kimura. "Hydration structure of Y^{3+} and La^{3+} compared: An application of metadynamics". In: *The Journal of Chemical Physics* 122.24 (July 2005), p. 244507. DOI: 10.1063/1.1940029.

[249] Cyril Terrier et al. "Density functional theory based molecular dynamics study of hydration and electronic properties of aqueous La3+". In: *The Journal of Chemical Physics* 133.4 (July 2010), p. 044509. DOI: 10.1063/1.3460813.

[250] Cesar Beuchat et al. "Hydration of Lanthanide Chloride Salts: A Quantum Chemical and Classical Molecular Dynamics Simulation Study". In: *The Journal of Physical Chemistry B* 114.47 (2010), pp. 15590–15597. DOI: 10.1021/jp105590h.

[251] L. Petit et al. "Molecular Dynamics Study of the Coordination Sphere of Trivalent Lanthanum in a Highly Concentrated LiCl Aqueous Solution: a Combined Classical and Ab Initio Approach". In: *The Journal of Physical Chemistry B* 112.34 (2008), pp. 10603–10607. DOI: 10.1021/jp8017106.

[252] Michael Bühl et al. "Speciation of La(III) Chloride Complexes in Water and Acetonitrile: A Density Functional Study". In: *Inorganic Chemistry* 51.24 (2012), pp. 13396–13407. DOI: 10.1021/ic302255a.

[253] Wolfram W. Rudolph and Gert Irmer. "Hydration and ion pair formation in common aqueous La(iii) salt solutions – a Raman scattering and DFT study". In: *Dalton Trans.* 44 (1 2015), pp. 295–305. DOI: 10.1039/C4DT03003F.

[254] Robert Mayanovic et al. "Steric hindrance and the enhanced stability of light rare-earth elements in hydrothermal fluids". In: *American Mineralogist - AMER MINERAL* 94 (Oct. 2009), pp. 1487–1490. DOI: 10.2138/am.2009.3250.

[255] John C. Tanger and Harold C. Helgeson. "Calculation of the thermodynamic and transport properties of aqueous species at high pressures and temperatures; revised equations of state for the standard partial molal properties of ions and electrolytes". In: *American Journal of Science* 288.1 (1988), pp. 19–98. DOI: 10.2475/ajs.288.1.19.

[256] Johnson R. Haas, Everett L. Shock, and David C. Sassani. "Rare earth elements in hydrothermal systems: Estimates of standard partial molal thermodynamic properties of aqueous complexes of the rare earth elements at high pressures and temperatures". In: *Geochimica et Cosmochimica Acta* 59.21 (1995), pp. 4329–4350. DOI: https://doi.org/10.1016/0016-7037(95)00314-P.

[257] Guillaume Lamoureux et al. “A polarizable model of water for molecular dynamics simulations of biomolecules”. In: *Chemical Physics Letters* 418.1 (2006), pp. 245–249. DOI: https://doi.org/10.1016/j.cplett.2005.10.135.

[258] Liem X. Dang and Tsun-Mei Chang. “Molecular dynamics study of water clusters, liquid, and liquid–vapor interface of water with many-body potentials”. In: *The Journal of Chemical Physics* 106.19 (May 1997), pp. 8149–8159. DOI: 10.1063/1.473820.

[259] K. T. Tang and J. Peter Toennies. “An improved simple model for the van der Waals potential based on universal damping functions for the dispersion coefficients”. In: *The Journal of Chemical Physics* 80.8 (Apr. 1984), pp. 3726–3741. DOI: 10.1063/1.447150.

[260] Jun Wang et al. “Development of Polarizable Models for Molecular Mechanical Calculations. 3. Polarizable Water Models Conforming to Thole Polarization Screening Schemes”. In: *The Journal of Physical Chemistry B* 116.28 (2012), pp. 7999–8008. DOI: 10.1021/jp212117d.

[261] Benjamin Rotenberg et al. “From Localized Orbitals to Material Properties: Building Classical Force Fields for Nonmetallic Condensed Matter Systems”. In: *Phys. Rev. Lett.* 104 (13 2010), p. 138301. DOI: 10.1103/PhysRevLett.104.138301.

[262] Mathieu Salanne et al. “Including many-body effects in models for ionic liquids”. In: *Theoretical Chemistry Accounts* 131.3 (2012), p. 1143. DOI: 10.1007/s00214-012-1143-9.

[263] R.M. Martin. *Electronic Structure: Basic Theory and Practical Methods*. Cambridge University Press, 2004. ISBN: 9780521782852. URL: https://books.google.com/books?id=dmRTFLpSGNsC.

[264] John J. Molina et al. “Ions in solutions: Determining their polarizabilities from first-principles”. In: *The Journal of Chemical Physics* 134.1 (Jan. 2011), p. 014511. DOI: 10.1063/1.3518101.

[265] Carine Clavaguéra and Jean-Pierre Dognon. “Accurate static electric dipole polarizability calculation of +3 charged lanthanide ions”. In: *Chemical Physics - CHEM PHYS* 311 (Apr. 2005), pp. 169–176. DOI: 10.1016/j.chemphys.2004.10.014.

[266] Elizabeth E. Wait et al. “Development of AMOEBA Polarizable Force Field for Rare-Earth La^{3+} Interaction with Bioinspired Ligands”. In: *The Journal of Physical Chemistry B* 127.6 (2023), pp. 1367–1375. DOI: 10.1021/acs.jpcb.2c07237.

[267] Pier Luigi Silvestrelli. “Van der Waals Interactions in DFT Made Easy by Wannier Functions”. In: *Phys. Rev. Lett.* 100 (5 2008), p. 053002. DOI: 10.1103/PhysRevLett.100.053002.

[268] Y. Andersson, D. C. Langreth, and B. I. Lundqvist. "van der Waals Interactions in Density-Functional Theory". In: *Phys. Rev. Lett.* 76 (1 1996), pp. 102–105. DOI: 10.1103/PhysRevLett.76.102.

[269] Julie Aufort, Paolo Raiteri, and Julian D. Gale. "Computational Insights into Mg^{2+} Dehydration in the Presence of Carbonate". In: *ACS Earth and Space Chemistry* 6.3 (2022), pp. 733–745. DOI: 10.1021/acsearthspacechem.1c00389.

[270] A. A. Chialvo et al. "Na^+–Cl ion pair association in supercritical water". In: *The Journal of Chemical Physics* 103.21 (Dec. 1995), pp. 9379–9387. DOI: 10.1063/1.470707.

[271] Thomas Driesner and Christoph A. Heinrich. "The system H_2O–NaCl. Part I: Correlation formulae for phase relations in temperature–pressure–composition space from 0 to 1000°C, 0 to 5000bar, and 0 to 1 X_{NaCl}". In: *Geochimica et Cosmochimica Acta* 71.20 (2007), pp. 4880–4901. DOI: https://doi.org/10.1016/j.gca.2006.01.033.

[272] Z. Hashin and S. Shtrikman. "A Variational Approach to the Theory of the Effective Magnetic Permeability of Multiphase Materials". In: *Journal of Applied Physics* 33.10 (Oct. 1962), pp. 3125–3131. DOI: 10.1063/1.1728579.

[273] Jörg Behler and Michele Parrinello. "Generalized Neural-Network Representation of High-Dimensional Potential-Energy Surfaces". In: *Phys. Rev. Lett.* 98 (14 2007), p. 146401. DOI: 10.1103/PhysRevLett.98.146401.

[274] Jörg Behler. "Neural network potential-energy surfaces in chemistry: a tool for large-scale simulations". In: *Phys. Chem. Chem. Phys.* 13 (40 2011), pp. 17930–17955. DOI: 10.1039/C1CP21668F.

[275] Jörg Behler. "Perspective: Machine learning potentials for atomistic simulations". In: *The Journal of Chemical Physics* 145.17 (Nov. 2016), p. 170901. DOI: 10.1063/1.4966192.

[276] Han Wang et al. "DeePMD-kit: A deep learning package for many-body potential energy representation and molecular dynamics". In: *Computer Physics Communications* 228 (2018), pp. 178–184. DOI: https://doi.org/10.1016/j.cpc.2018.03.016.

[277] Satish C. B. Myneni. "X-Ray and Vibrational Spectroscopy of Sulfate in Earth Materials". In: *Reviews in Mineralogy and Geochemistry* 40.1 (Jan. 2000), pp. 113–172. DOI: 10.2138/rmg.2000.40.2.

[278] W. Rudolph. "Structure and Dissociation of the Hydrogen Sulphate Ion in Aqueous Solution over a Broad Temperature Range: A Raman Study". In: *Zeitschrift für Physikalische Chemie* 194.1 (1996), pp. 73–95. DOI: doi:10.1524/zpch.1996.194.Part_1.073.

[279] Koichi Tomikawa and Hitoshi Kanno. "Raman Study of Sulfuric Acid at Low Temperatures". In: *The Journal of Physical Chemistry A* 102.30 (1998), pp. 6082–6088. DOI: 10.1021/jp980904v.

[280] Jean-Joseph Max, Christophe Ménichelli, and Camille Chapados. "Infrared Titration of Aqueous Sulfuric Acid". In: *The Journal of Physical Chemistry A* 104.12 (2000), pp. 2845–2858. DOI: 10.1021/jp9937398.

[281] Peter W. Faguy, Nebojša S. Marinković, and Radoslav R. Adžić. "An in Situ Infrared Study on the Effect of pH on Anion Adsorption at Pt(111) Electrodes from Acid Sulfate Solutions". In: *Langmuir* 12.2 (1996), pp. 243–247. DOI: 10.1021/la950115u.

[282] R. J. Gillespie and E. A. Robinson. "THE RAMAN SPECTRA OF SULPHURIC, DEUTEROSULPHURIC, FLUOROSULPHURIC, CHLOROSULPHURIC, AND METHANESULPHONIC ACIDS AND THEIR ANIONS". In: *Canadian Journal of Chemistry* 40.4 (1962), pp. 644–657. DOI: 10.1139/v62-100.

[283] Pál Sipos et al. "Raman Spectroscopic Study of Ion Pairing of Alkali Metal Ions with Carbonate and Sulfate in Aqueous Solutions". In: *Australian Journal of Chemistry* 53 (Jan. 2001). DOI: 10.1071/CH00126.

[284] Fernando Rull and Hitoshi Ohtaki. "Raman spectral studies on ionic interaction in aqueous alkali sulfate solutions". In: *Spectrochimica Acta Part A: Molecular and Biomolecular Spectroscopy* 53.5 (1997), pp. 643–653. ISSN: 1386-1425. DOI: https://doi.org/10.1016/S1386-1425(96)01851-3.